PROGRAMA DE DOCTORADO EN MATEMÁTICAS

FACULTAD DE CIENCIAS

DEPARTAMENTO DE ANÁLISIS MATEMÁTICO, ESTADÍSTICA E
INVESTIGACIÓN OPERATIVA Y MATEMÁTICA APLICADA

Mathematical and numerical modelling of dispersive water waves

(Modelado matemático y aproximación numérica de ondas dispersivas)

CIPRIANO ESCALANTE SÁNCHEZ

TESIS DOCTORAL

Directores de la tesis:

Dr. Manuel Jesús Casto Dríaz,   Dr. Tomás Morales de Luna

UNIVERSIDAD DE MÁLAGA

Noviembre 2018

UNIVERSIDAD
DE MÁLAGA

AUTOR: Cipriano Escalante Sánchez

http://orcid.org/0000-0002-7602-5920

UNIVERSIDAD
DE MÁLAGA

D. Manuel Jesús Castro Díaz, Profesor Titular del Departamento de Análisis Matemático, Estadística e Investigación Operativa y Matemática Aplicada de la Universidad de Málaga, y D. Tomás Morales de Luna, Profesor Titular del Departamento de Matemáticas de la Universidad de Córdoba
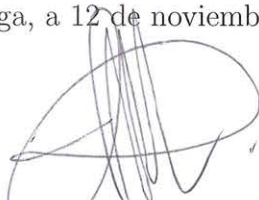
CERTIFICAN:

Que D. Cipriano Escalante Sánchez, Licenciado en Matemáticas, ha realizado en el Departamento de Análisis Matemático, Estadística e Investigación Operativa y Matemática Aplicada de la Universidad de Málaga, bajo nuestra dirección, el trabajo de investigación correspondiente a su Tesis Doctoral, titulado:

Mathematical and numerical modelling of dispersive water waves.

Revisado el presente trabajo, estimamos que puede ser presentado al Tribunal que ha de juzgarlo. Y para que conste a efectos de lo establecido en el artículo octavo del Real Decreto 99/2011, autorizamos la presentación de este trabajo en la Universidad de Málaga.

Málaga, a 12 de noviembre de 2018

Dr. Manuel Jesús Castro Díaz

Dr. Tomás Morales de Luna

Contents

List of Figures

UNIVERSIDAD
DE MÁLAGA

UNIVERSIDAD DE MÁLAGA

Agradecimientos

UNIVERSIDAD
DE MÁLAGA

Es también mi deseo, agradecer a Enrique D. Fernández Nieto y Gladys Narbona Reina, profesores de la Universidad de Sevilla que han contribuido en una parte de los resultados presentados en esta memoria.

Mis más sinceros agradecimientos a Michael Dumbser, de la Universidad de Trento y a Patrick Lynett, de la Universidad del Sur de California, profesores con los que realicé dos estancias de investigación, y contribuyeron en los resultados obtenidos en esta tesis doctoral y en mi formación.

Todo mi agradecimiento a mi familia por su incondicional apoyo.

Gracias a todos.

Introduction

Computational Fluid Mechanics is today one of the most essential tools for the simulation of a multitude of phenomena that take place in our environment. The flow that occurs after a dam break, the circulation of bodies in the water, the behaviour of atmospheric currents, the evolution of a pollutant discharge, erosion and the transport of sediments, tsunamis, among others, are phenomena whose study has a considerable interest since they affect the human being in a decisive way. To reduce the hazards associated with these phenomena such as hurricanes or tsunamis, the prediction is an essential part, and the evaluation of their possible consequences are important goals to be marked since they can help save many lives and reduce material and economic damage. Unfortunately, it is difficult and expensive to perform laboratory studies using scale size models to study such phenomena, due to the global scale of those.

An alternative is to compute numerical simulations of the fluids involved. Tackling such problems requires, in the first place, to trace the theoretical aspects of the physics underlying. Second, it involves developing numerical models that provide reliable predictions of the problems raised and sufficiently in advance to allow the process of decision-making.

According to the theme that concern this thesis, in order to simulate the impact that a tsunami may produce on a coastal zone, it will be necessary to develop models that provide satisfactory results in the propagation of tsunami waves in the ocean, its evolution through the continental shelf towards the nearshore and its impact on the coast. In this context of geophysical flows, these processes have the characteristic of having vertical information that can be negligible compared to the horizontal ones. This circumstance makes it possible to simplify significantly the mathematical formulation of the models to be used for their simulation.

To do that, the three-dimensional Navier-Stokes equations are considered, which are the most general equations of fluid mechanics. These equations may be written in the dimensionless form and simplified under some assumptions:

- the vertical dimension of the domain H is small compared with respect to the wavelength L, that is

$$\mu_1 = \frac{H}{L} \ll 1;$$
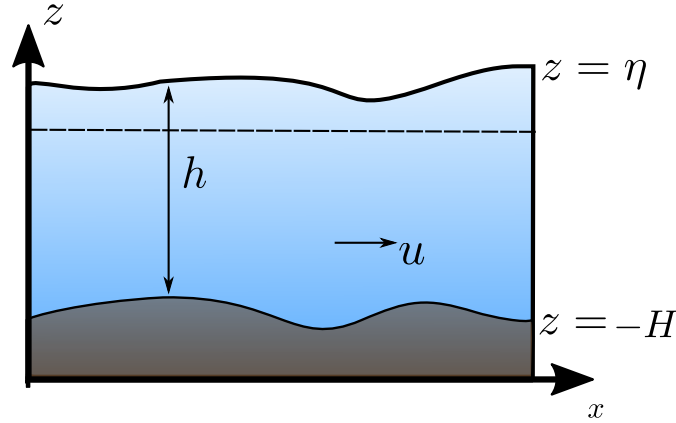
Figure A.1: Fluid across a one-dimensional channel.

- the pressure of the fluid is assumed to be hydrostatic;

- horizontal viscosity terms are neglected.

Under this hypothesis, and after a process of depth-averaging in the vertical direction, one can arrive to a system of non-linear PDE that is called the Nonlinear Shallow-Water Equations, SWE from now on, that reads for one-dimensional domains as

$$\begin{cases} \partial_t h + \partial_x (hu) = 0, \ x \in I \subset \mathbb{R}, \ t > 0, \\[2mm] \partial_t (hu) + \partial_x \left(hu^2 + \frac{1}{2}gh^2 \right) = gh\partial_x H - \tau_b, \end{cases} \tag{0.0.1}$$

where $h(x,t)$ is the positive water height at each point $x \in I$, I a given interval, and time t. $u(x,t)$ is the depth averaged velocity in the x direction. g represents the gravitational constant and $H(x)$ is the still water depth. It is also interesting to define the function $\eta(x,t) = h(x,t) - H(x)$ that describes the free-surface of the fluid measured from the still-water level (see Figure A.1). $\tau_b(x,t)$ parametrizes the bottom friction effects. In the literature one could find different parametrizations of the friction effects and in this thesis a Manning friction law is used given by

$$\tau_b = gh\frac{n^2u|u|}{h^{4/3}} \tag{0.0.2}$$

where n is the Gauckler-Manning coefficient [185]. The system is completed with the corresponding initial conditions and, in the case of bounded domains, with the corresponding boundary conditions.

In fluid dynamics, dispersion of water waves generally refers to frequency dispersion, which means that waves of different wavelengths travel at different phase speeds. Water
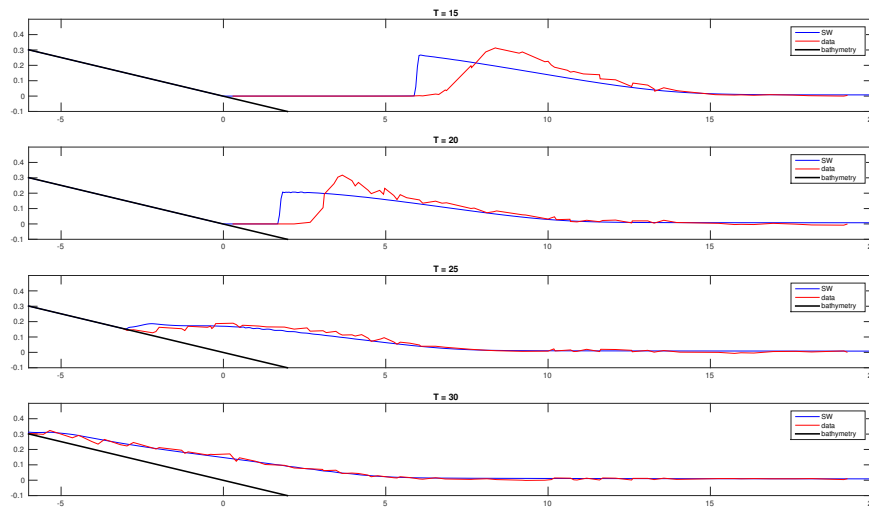
Figure A.2: Comparison of experiments data (red) and simulated ones with SWE at different times during the inundation part.

waves, in this context, are waves propagating on the water surface, with gravity and surface tension as the restoring forces. As a result, water with a free surface is generally considered to be a dispersive medium. However, it is well-known that SWE do not take into account effects associated with dispersive waves.

Figure A.2 illustrate this fact showing snapshots of the evolution of a wave over a plane beach. There one can see how the SWE (in blue) tends to predict faster velocity for the front of the wave when compared with laboratory data (in red). The Stokes linear theory (or Airy wave theory) explain this situation since it states that the speed of wave propagation, or more precisely the phase velocity C_{Airy}, as a quantity that is given in terms of the typical depth H and the local wavenumber k as

$$C^2_{Airy} = gH \frac{\tanh(kH)}{kH},$$

whereas the phase velocity of the system (0.0.5) is given by

$$C^2_{SWE} = gH.$$

The previous relation, which is also called a linear dispersion relation, reveals the dispersive character of the linear water wave theory and that SWE cannot take into account effects associated with dispersive waves. This also explains why the computed numerical simulation in Figure A.2 is shifted, since the speed propagation of the system (0.0.5), C_{SWE}, is faster than the given by the linear theory, C_{Airy}.

Concerning mathematical models able to simulate dispersive water waves, a great effort has been made in recent years in the derivation of relatively simple mathematical models for shallow water flows that include long non-linear water waves, such as Tsunami water waves. The history of non-linear dispersive modelling goes back to the end of the XIX$^{\text{th}}$ century.

In 1834, while conducting experiments to determine the most efficient design for canal boats, J. Scott Russell discovered a phenomenon that he described as the wave of translation. This type of waves move at constant celerity maintaining the same shape. The observations can be found in a technical report for the fourteenth meeting of the British Association for the Advancement of Science (1845) [221]. Nowadays, in fluid dynamics, this type of waves are called Russell's solitary waves or solitary waves. J. Scott Russell spent some time making practical and theoretical investigations of these waves. The problem was that the new observations seemed at contrast with Isaac Newton's and Daniel Bernoulli's theories of hydrodynamics. George Biddell Airy and George Gabriel Stokes had difficulty to accept Scott Russell's experimental observations because the existing water-wave theories could not explain Scott Russell's observations.

It was only later when the first successful theoretical treatment was carried out by Joseph Valentin Boussinesq in 1872 [19], that Russell's observations on solitary waves were accepted as true by some prominent scientists within his lifetime. Afterwards, J. Boussinesq in 1877 [19] proposed the Korteweg de Vries equation, re-derived later by D. Korteweg & G. de Vries (1895). Then, a new generation of 'pioneers' (F. Serre (1953) [227], C.C. Mei & Le Méhauté (1966) [189] and D. Peregrine (1967) [210]) derived modern non-linear dispersive wave models.

One of the most commonly used models that became popular was the system derived by Peregrine [210] in 1967. Equations of motion are derived for long waves in water of varying depth. The equations are for small amplitude waves but do include non-linear terms. They correspond to the Boussinesq equations for water of constant depth. There are two important parameters associated with long waves. One is the ratio of depth to wavelength μ_1, and the other is the ratio of amplitude to depth μ_2. The Peregrine equations were derived under the assumptions of weakly non-linear weakly dispersive waves, that is

$$\mu_1 \ll 1, \ \mu_2 \approx \mu_1^2.$$

The system reads as:

$$\begin{cases} \partial_t h + \partial_x(hu) = 0, \ x \in I \subset \mathbb{R}, \ t > 0, \\ \\ \partial_t (hu) + \partial_x \left(hu^2 + \frac{1}{2} gh^2 \right) = gh\partial_x H + \frac{1}{2} H^2 \partial_{xxt} (uH) - \frac{1}{6} H^3 \partial_{xxt} u - \tau_b. \end{cases} \tag{0.0.3}$$

An asymptotic analysis in the limit $kH \to 0$ shows that the dispersion relation is exact at order $\mathcal{O}(kH)^4$ for the Peregrine system when compared with Airy theory, and therefore it makes a great model for the simulation of long-waves.

As computational power increases, Boussinesq Type Models ([1], [19], [144], [184], [202], [210], [148], [255], [256]) become more accessible. This means that one can use more sophisticated models in order to accurately describe reality, despite the higher computational cost. Two main challenges can be highlighted as overcomed:

- The development of fully non-linear weakly dispersive system derived under the only assumption of $\mu_2 \approx \mu_1^2$ (see for example [144], [168]).

- The improvement of the linear dispersion relation of the derived systems and thus extending the range of validity where models can represent well dispersive water waves. This is, extending the range from moderate to intermediate-deep waters and shallow waters.

The second item above has attracted the attention of the scientific community and can be simply illustrated by a large number of journal papers published on the subject. Attending to the behaviour of the waves, a classification on shallow, intermediate and deep waters is established. Primarily, the second item focus on intermediate waters, that occurs when the typical wavelength L is bounded by $2H$ and $20H$, being H the typical depth. Within this range, it can be demanded much more information on the vertical structure that must be retained when deriving mathematical models. High order Boussinesq equations can offer better dispersive properties. The counterpart is that extremely complex systems with high order derivatives arise (fifth order derivatives in [135]), requiring an equally complex numerical scheme when solving numerically. The complexity increases even more for two space dimensions problems.

However, Madsen and Sorensen (see [184]) fully understanding this problem, found a smart approach for improving dispersive properties without increasing the order of the derivatives appearing in the momentum equation. They propose a system that has received significant attention from the scientific community.

Alternatively, the development of non-hydrostatic pressure models for coastal water waves has been the topic of many studies over the past 30 years. Non-hydrostatic models are capable of solving many relevant features of coastal water waves, such as dispersion, non-linearity, shoaling, refraction, diffraction, and run-up. The central hypothesis in the derivation consists in splitting the pressure into a hydrostatic and a non-hydrostatic part (see Casulli [52]). In this thesis, the non-hydrostatic pressure system derived by Sainte-Marie *et al.* in [21] was numerically approximated. This system can be derived after a standard depth-averaging process from the Euler equations and assuming a constant

vertical profile for the horizontal velocity. The system reads as

$$
\begin{cases}
\partial_t h + \partial_x (hu) = 0, \ x \in I \subset \mathbb{R}, \ t > 0, \\[2mm]
\partial_t (hu) + \partial_x \left(hu^2 + \frac{1}{2} gh^2 + hp \right) = (gh + p_b) \partial_x H - \tau_b, \\[2mm]
\partial_t (hw) + \partial_x (uhw) = p_b, \quad p_b = 2p \\[2mm]
\partial_x u + \dfrac{w - w_b}{h/2} = 0, \quad w_b = -u \partial_x H.
\end{cases}
\tag{0.0.4}
$$

Since the derivation process of the system is similar to the one followed for the SWE, the definition of the variables involved coincides with the ones described in system (0.0.5). The variables w and p are the depth averaged vertical velocity and the depth averaged non-hydrostatic pressure respectively. w_b and p_b account for the vertical velocity and the non-hydrostatic pressure at the bottom, being $p_b = 2p$. The last equation in (0.0.8) accounts for the depth integrated incompressibility condition. The best advantage that presents this non-hydrostatic pressure system is the absence of higher order derivatives and even it has a linear dispersion relation that is similar to the one given by the system (0.0.7).

In this spirit of PDE system with dispersive abilities derived from the assumption of a non-hydrostatic pressure, several works have been developed. To improve the dispersive properties of the systems, the primary trend consists in the use of a multi layer depth averaging approximation. The idea is, given the increasing computational power available, to make systems closer and closer to three-dimensional solvers, i.e. capable of also adequately describing the vertical structure of the flow, leading to distinctive improvements in the non-linear dispersive properties of the model.

In [124], E.D. Fernández-Nieto *et al.* derived a class of multi layer non-hydrostatic pressure system that reduces to the system described in (0.0.8) when the number of layers is set to one. When the number of layer is higher than one, the mathematical model remains extremely simple, in the sense that there are no high derivatives. Moreover, it is shown that when the number of layers tends to infinity, the celerity of the multi layer system tends to the corresponding celerity given by the Airy theory. Due to this reason the non-hydrostatic pressure systems have been considered in this thesis. In particular, one of multi layer systems derived in [124], has been considered in this thesis as the central framework to design numerical schemes to simulate dispersive water waves. Moreover, in this thesis, a novel two-layer non-hydrostatic pressure system with enhanced dispersive properties was proposed in [118] and numerically approximated.

Concerning the nature of the dispersive PDE systems presented above, it is well known that the system (0.0.5) consists on a hyperbolic PDE system. However, the nature of the system (0.0.7), among others Boussinesq and non-hydrostatic systems, differs from a hyperbolic system, and responds instead to a mixed hyperbolic and elliptic problem. Some discussion and theoretical results about existence and uniqueness can be found in [167].

Due to the mixed hyperbolic-elliptic nature of Boussinesq and non-hydrostatic systems, the complexity of the corresponding numerical schemes increases. For example, the incompressibility equation in (0.0.8) adds an extra restriction that makes the system a hyperbolic-elliptic problem. This restriction makes that explicit schemes cannot be applied to the system, since they may have a strong stability condition, or even worse it may result in an unconditionally unstable scheme. Therefore, implicit schemes must be applied and several works can be found in literature (see for example [4], [112], [163], [180], [217], [259] among references therein). Numerical methods applied to non-hydrostatic pressure systems, and even Boussinesq-type systems, typically use a splitting operator (see e.g. [168]) or a projection-correction type schemes (see [4], [63], [112], [118]). Usually, it combines finite volume methods for solving the underlying hyperbolic part in a first step, and finite differences or finite elements for solving the elliptic or non-hydrostatic/dispersive terms in a second step, usually by using staggered grids.

However, there is a nearly recent and alternative strategy to simulate dispersive water waves with hyperbolic PDE systems. In [188], Ricciuto *et al.* proposed a first-order system approach for general one dimensional advection-diffusion-dispersion equations. Similarly, in [147] Brocchini *et al.* obtained a set of dispersive and hyperbolic depth-averaged equations using a hyperbolic approximation of a chosen set of fully nonlinear and weakly dispersive Boussinesq-type equations.

In the same vein, in this thesis a novel first-order hyperbolic depth-averaged system, that can be seen as a modification of the model (0.0.8) for two space dimensions presented in [21], is proposed by Escalante *et al.* in [111]. The novel hyperbolic system is obtained using a hyperbolic reformulation of the original governing PDE (0.0.8) by coupling the divergence constraint of the velocity with the remaining conservation laws at the aid of an evolution equation for the depth-integrated non-hydrostatic pressure, similar to the so-called hyperbolic divergence cleaning introduced in the generalized Lagrangian multiplier approach (GLM) of Munz *et al.* [196], [83] for the Maxwell and the magnetohydrodynamics (MHD) equations. In this work, a formulation is suggested in which the divergence errors of the velocity field are transported at a finite speed that is related to the maximum eigenvalues of the governing PDE system. The augmented hyperbolic system maintains the momentum equations for the horizontal and vertical velocities and still satisfies an energy balance equation, as the original system [21]. Therefore, the final governing PDE system proposed in this dissertation is a system of hyperbolic balance laws and is thus amenable for an explicit discretization via high order numerical schemes.

Higher order methods are desirable due to their improved dissipation and dispersion properties compared to simple second order TVD finite volume schemes. This is particularly important for the accurate propagation of solitary waves over long distances, as it will be also shown later in the numerical results section. In this thesis, two alternatives to discretize the considered PDE systems with high order schemes are chosen:

- High order finite volume methods based on polynomial reconstruction operators.

- High order Discontinuous Galerkin schemes (DG).

Concerning finite volume methods applied to hyperbolic problems, shock-capturing abilities can be exploited. The main difficulty of this technique from a mathematical point of view as well as from the numerical analysis resides in the presence of nonconservative products, which makes difficult the definition of weak solutions. Many interesting problems related to geophysical flow and in particular some of the equations discretized in this dissertation fall into this framework. Then, the nonconservative products are interpreted as Borel measure in the sense introduced by Dal Maso, LeFloch and Murat in [72]. For systems, a family of paths should be chosen. A general framework to numerically solve such systems was introduced by C. Parés in [205], called the path-conservative methods. The choice of this family of paths should be based on the physics of the problem: for instance, it should be based on the viscous profiles corresponding to a regularized system in which some of the neglected terms (e.g. the viscous terms) are taken into account. Unfortunately, the explicit calculations of viscous profiles is in general a difficult task. Some hints of how paths can be chosen is discussed in [38].

The family of generalized Roe schemes introduced in [248] constitutes a particular case of path-conservative numerical method for nonconservative hyperbolic PDE systems. Although the schemes of this family are robust (see, for instance, [14], [30], [208], [205]), they also present, as their conservative counterpart, some drawbacks as their implementation requires the explicit knowledge of the eigenstructure of the intermediate matrices. Sometimes their analytic expression is not available, making Roe schemes computationally expensive. Also, they do not satisfy in general an entropy inequality, as a consequence, an entropy-fix technique has to be added to capture the entropy solution in the presence of smooth transitions (see [154]). It is also well known that the use of incomplete Riemann solvers as Rusanov, Lax-Friedrichs, HLL, etc. allows one to reduce the CPU time required by a Roe solver which resolves all the characteristic fields (see, for instance, [106]). Although when combined with piecewise constant approximation Roe solvers give in general a better resolution of the discontinuities than incomplete Riemann solvers when combined with high order reconstructions the resolution may be indistinguishable. Therefore high order methods based on incomplete Riemann solvers may be more efficient than high order Roe methods.

In this thesis, we use a class of computationally fast first order finite volume solvers: Polynomial Viscosity Matrix (PVM) methods introduced by Castro *et al.* in [40]. This class of incomplete simple Riemann solvers can be applied for general nonconservative hyperbolic systems, defined in terms of viscosity matrices computed by a suitable polynomial evaluation of a Roe linearisation, that overcome these difficulties. PVM schemes can be seen as the natural extension of the one proposed in [84] for balance laws, and, more generally, for nonconservative systems. Moreover, PVM schemes can be extended to high order by following the ideas developed in [25] and to two-dimensional systems following [41], based on a polynomial reconstruction of states.

Another class of high order numerical methods considered in this thesis are the

Discontinuous Galerkin finite element methods which go back to the work by Reed and Hill [214], but it has become particularly famous for the solution of hyperbolic conservation laws thanks to a well-known series of papers by Cockburn and Shu and coworkers, see [68], [67], [66], [69]. In particular, in this dissertation ADER-DG schemes has been adopted, which has been introduced in [97], [93], [91] and which goes back to the family of ADER finite volume schemes by Toro and Titarev [237], [244], [238], [241]. The ADER methodology is based on the approximate solution of the generalized Riemann problem at element interfaces and naturally leads to fully-discrete one-step schemes of arbitrary order of accuracy in both space and time. Due to the well-known Godunov theorem, any better than first order accurate linear scheme is oscillatory and therefore not suitable for the discretization of problems with discontinuities or strong gradients in the solution. Following the ideas introduced in [98], [261], the high order ADER-DG method is supplemented with a suitable *a posteriori* subcell finite volume limiter. The main idea here is to use first an unlimited high order ADER-DG scheme, which produces a so-called candidate solution at the end of each time step. This candidate solution is then checked *a posteriori* against some physical and numerical detection criteria, such as positivity of the solution, the absence of floating point errors and satisfaction of a relaxed discrete maximum principle (DMP). If a cell does not satisfy all these conditions (a so-called troubled cell), the discrete solution is *discarded* and locally *recomputed*, starting again from a valid solution at the old-time level, but using now a more robust scheme on a finer subgrid within the troubled cells. This approach corresponds to an element-local check-pointing and restarting of the solver, but using a more robust and more dissipative scheme after the restart. This new concept of *a posteriori* limiting has been introduced for the first time in the context of finite volume schemes via the MOOD approach, see [64], [88], [89], [173]. For the recomputation of the troubled cells, in principle, any robust finite volume scheme can be used. Here, the family of path-conservative finite volume schemes are employed, which has already been successfully used for the solution of shallow-water type systems in a series of papers, see e.g. [112], [44], [206], [40], [26], [205], [46]. In particular, a robust well-balanced and positive preserving for the water height PVM path-conservative HLL-type Riemann solver [152], [90] is used.

Furthermore, the use of a numerical method that solves correctly stationary solutions is mandatory when the system studied involves perturbations of a steady state, whose amplitude is of the order or bigger than the truncation error of the method. This is the case of a tsunami wave propagating at the ocean: its initial amplitude is small (although the length wave is huge) and it is not always possible to refine the mesh so that the truncation error of the method is lower than this amplitude. In this context a difficulty arises related to the numerical computation of stationary solutions: standard methods that solve correctly systems of conservation laws can fail in solving nonconservative systems when approaching equilibria or near to equilibria solutions. In the context of shallow water equations Bermúdez and Vázquez-Cendón introduced in [14] the condition called *C-property*: a a scheme is said to satisfy this condition if it solves correctly the steady-state

solutions corresponding to water at rest. This the idea of constructing numerical schemes that preserve some equilibria, which are called in general *well-balanced* schemes has been studied by many authors. The design of numerical methods with good properties for conservative or nonconservative problems (systems of balance laws) is a very active front of research: see, for instance, [6], [16], [15], [18], [37], [55], [56], [82], [139], [140], [141], [145], [146], [172], [174], [199], [209], [211], [212], [215], [222], [234], [248], [258], [162], [85], [86], [247], among others.

The simulation of geophysical flows leads to the resolution of problems in significant computational domains, e.g. an oceanic basin when a tsunami simulation, or for significant integration times such the simulation of currents induced by a tidal. In both cases, the simulations present a significant computational effort and as a consequence, efficient implementations are needed to solve these problems in reasonable times.

Frequently, these numerical simulations demand a large computational effort due mainly to big computational domains, the complexity of numerical solution schemes or real-time calculation requirements. Therefore parallel versions of accurate and efficient numerical solvers for high-performance platforms are needed to be able to deal with these simulation scenarios in reasonable times.

Modern *Graphics Processing Units (GPUs)* are highly programmable and massively parallel devices which can be used to accelerate considerably numerical PDE computations in a cost-effective way [22], [159], [251]. They offer hundreds or thousands of processing units optimized for massively performing floating-point operations in parallel and have proven to be useful in the acceleration of numerical schemes which exhibit a lot of exploitable fine-grain parallelism. GPU computing consists of using GPUs together with CPUs to accelerate the solution of compute-intensive science, engineering and enterprise problems. Since the numerical simulation based on PDEs presents a lot of exploitable parallelism, there has been an increasing interest in the acceleration of these simulations using GPU-based computer systems.

There is a widespread use of CUDA-based platforms to accelerate numerical solvers for PDEs [76], [75], [28], [80]. In the PhD thesis [74] and references therein, de la Asunción *et al.* show the adaptation to GPU of the finite volume numerical scheme introduced in [27] to solve the 2D shallow water system. In these references, authors intend to make easier the exploitation of CUDA-enabled platforms to accelerate PDE-based numerical simulations, by providing the suitable CUDA C programming foundations. For this purpose, the authors explain the adaptation to GPU of the finite volume numerical scheme to solve the 2D shallow water system. The CUDA implementation of a first order two-layer shallow water system solver is addressed in [75]. There also exists proposals to implement, using CUDA-enabled GPUs, high order schemes to simulate one-layer systems [47], [131] and to implement first-order schemes for one and two-layer systems on triangular meshes [28]. In [80], several finite volume numerical schemes to solve one-layer shallow water system on structured meshes are tuned to exploit the GPU execution model and efficiently implemented using CUDA C. The distributed implementation of numerical solvers for

cluster of CUDA-based GPUs has been also tackled [78], [77], [79].

The aforementioned numerical solvers implemented on GPU exhibits a computational pattern which is very frequent in the numerical algorithms to solve PDEs and that has been widely used throughout this dissertation. However, a difficulty arises: some of the numerical methods proposed in this dissertation are no longer explicit methods, and relatively big linear systems have to be solved. To do that, we propose some iterative and massively parallel linear solvers to have efficient GPU implementations.

Outline of the thesis:

The outline of this dissertation is the following:

- In Chapter 1 a general overview of the state of the art of the modelling of dispersive systems for the simulation of dispersive water waves is introduced. Two prominent families of dispersive systems can be found nowadays: Boussinesq-type and non-hydrostatic pressure systems. Although in this thesis we will focus on the second class of dispersive systems, two of the most representative and used Boussinesq-type systems are shown in this chapter, and some relations and rewritings as first-order non-hydrostatic pressure PDE systems are established. The multi layer non-hydrostatic pressure system derived by Fernández-Nieto *et al.* in [124] is chosen as the main dispersive model framework for this dissertation. This choice is based on its simplicity and on its good dispersive relation properties which have been introduced and also computed for all the considered systems.

  In this chapter, two novel non-hydrostatic pressure systems, are described: a new two-layer non-hydrostatic pressure system with enhanced dispersive properties; and a new hyperbolic relaxed PDE system that converges to the well-known one-layer system (0.0.8). For both systems, the dispersive properties and its eigenstructure are thoroughly studied.

  At this point, we stress that detailed small-scale wave breaking flow physics is not described by the introduced models, but only the net effect of wave breaking on energy dissipation. This means that we include the breaking mechanism in the depth-integrated equations via a simple sub-scale viscosity model, with a given breaking criteria. To do that efficiently, some breaking mechanism is also proposed.

  Finally, some ideas on the computation of solitary wave for the given systems as well as some comparison are shown.

- In Chapter 2, the theoretical background required for the design of numerical schemes for both one and two dimensional non-conservative hyperbolic systems are stated. Regarding finite volume schemes, the concept of path-conservative scheme and well-balanced scheme, as well as the extension of the numerical schemes to high order, based on the reconstruction of states are given. In particular, the

PVM methods introduced in [48] are described. As an alternative to the high order finite volume based on the reconstruction of states, the finite element ADER Discontinuous Galerkin methods are described supplemented with a suitable *a posteriori* subcell finite volume limiter (see [98], [261], [64]).

- In Chapter 3 the numerical schemes proposed for the given non-hydrostatic pressure systems are fully described. There, different approaches and strategies can be highlighted. On the one hand, we have designed second order finite volume numerical schemes based on a two-step projection-correction technique. At the first step, an explicit finite volume numerical scheme is used for the underlying hyperbolic and hydrostatic part of the system, under a usual CFL condition. Then, in a second step non-hydrostatic terms are taken into account and approximated employing central finite differences. This will involve the inversion of a Poisson-like operator and hence the implicit nature of the numerical scheme. At this step, we have considered both staggered and non-staggered grids for the non-hydrostatic pressure and vertical velocities. On the other hand, a fully explicit and arbitrary high order Discontinuous Garlerkin numerical scheme is proposed for the novel proposed hyperbolic relaxation PDE system, supplemented with a posteriori subcell finite-volume limiter. To allow simulations in real time or faster, an efficient GPU implementation of the numerical method has been carried out in the two-dimensional case and some hints and guidelines on their implementation are given in Appendix E.

- In Chapter 4 the aforementioned numerical schemes for each one of the systems has been applied to idealized academic benchmarks such as the propagation of solitary waves, as well as to more challenging physical situations that involve wave runup on a shore including wave breaking in both one and two space dimensions. In all cases the achieved agreement with analytical solutions or experimental data is excellent, thus showing the validity of both, the proposed mathematical model and the numerical solution algorithm. Experimental data include a wide variety of scenarios: propagation, shoaling, run-up and induced dispersive waves by rigid solid landslides. Finally, some computational times for the two dimensional test cases are shown to evince the sought after efficiency.

- As revealed during the simulation of waves induced by rigid landslide numerical tests, they might be dispersive. In Chapter 5 we measure the influence when considering a non-hydrostatic pressure applied to the simulation of bedload transport. To do that, a new and ongoing work is recalled where a two-layer shallow water type system is proposed to describe bedload sediment transport for strong and weak interactions between the fluid and the sediment. A numerical scheme and some validation and academical tests are shown, providing promising results and good behaviour in low transport rate regimes as well as in many other situations.

- The thesis is rounded-off by some concluding remarks given in Chapter 6.

Publications:

This thesis is based on the following publications:
– Mathematical modelling and numerical methods:

- M. J. Castro, C. Escalante, and T. Morales de Luna. Modelling and simulation of non-hydrostatic shallow flows. In Clément Cancès and Pascal Omnes, editors, *Finite Volumes for Complex Applications VIII - Hyperbolic, Elliptic and Parabolic Problems*, pages 119–126, Cham, 2017. Springer International Publishing.

- C. Escalante, T. Morales, and M.J. Castro. Non-hydrostatic pressure shallow flows: GPU implementation using finite volume and finite difference scheme. *Applied Mathematics and Computation*, (338):631–659, 2018.

- C. Escalante, E.D. Fernández-Nieto, T. Morales, and M.J. Castro. An efficient two–layer non–hydrostatic approach for dispersive water waves. *Journal of Scientific Computing.*, doi.org/10.1007/s10915-018-0849-9, 2018.

- C. Escalante, M. Dumbser, and M.J. Castro. An efficient hyperbolic relaxation system for dispersive water waves and its solution with high order discontinuous Galerkin schemes. *Submitted to Journal of Computational Physics*, 2018.

- C. Escalante, G.Narbona-Reina, E.D. Fernández-Nieto, and T. Morales. A non-hydrostatic bilayer model for bed–load sediment transport that tends to classical SVE models for small morphodynamic time. *Ongoing work*, 2018.

– Experimental validation:

- P.J. Lynett, K. Gately, R. Wilson, L. Montoya, D. Arcas, B. Aytore, Y. Bai, J.D. Bricker, M.J. Castro, K.F. Cheung, C.G. David, G.G. Dogan, C. Escalante, J.M. González-Vida, S.T. Grilli, T.W. Heitmann, J. Horrillo, U. KânoUglu, R. Kian, J.T. Kirby, W. Li, J. Macías, D.J. Nicolsky, S. Ortega, A. Pampell-Manis, Y.S. Park, V. Roeber, N. Sharghivand, M. Shelby, F. Shi, B. Tehranirad, E. Tolkova, H.K. Thio, D. VelioUglu, A.C. Yalçıner, Y. Yamazaki, A. Zaytsev, and Y.J. Zhang. Inter-model analysis of tsunami-induced coastal currents. *Ocean Modelling*, 114:14 – 32, 2017.

- J. Macías, M J. Castro, S. Ortega, C. Escalante, and J.M. González-Vida. Performance benchmarking of tsunami-hysea model for nthmp's inundation mapping activities. *Pure and Applied Geophysics*, 174(8):3147–3183, 2017.

- J. Macías, M. J. Castro, C. Escalante. Performance assessment of tsunami-hysea model for nthmp tsunami currents benchmarking. part I lab data. *Submitted to Coastal Engineering*, 2018.

- J. Macías, C. Escalante, M J. Castro. Multilayer-HySEA model validation for landslide generated tsunamis for rigid slides *Submitted to Ocean Modeling*, 2018.

Introduction (in Spanish)

La mecánica de fluidos geofísicos estudia el comportamiento a gran escala de los flujos de la Tierra, tanto en fase líquida (océanos) como gaseosa (atmósfera). El hecho de que la vida no hubiera podido desarrollarse sin atmósfera ni océanos, explica el tremendo interés que suscita en los científicos el conocimiento de los mecanismos que intervienen en los procesos geofísicos.

Por otro lado, la predicción de desastres naturales como huracanes, tifones, avalanchas, tsunamis... y la evaluación de sus posibles consecuencias son propósitos a tener en cuenta, de cara a disminuir los posibles daños humanos y materiales.

El flujo que se produce tras la rotura de una presa, las corrientes de agua en el mar, la distribución y propagación de un vertido en el mar, la erosión, deposición y transporte de sedimentos, etc... son fenómenos de un enorme interés. Para estos fenómenos, es fundamental la predicción y evaluación de sus posibles consecuencias. Una opción, es la de realizar estudios de laboratorio mediante modelos a escala para estudiar dichos fenómenos. Sin embargo, esta opción puede resultar costosa y poco flexible, en el sentido de que cualquier modificación en los modelos sujetos a estudio, incrementaría aún más el coste de dicho estudio. Otra posibilidad es la considerar simulaciones por ordenador de los fluidos y procesos involucrados.

Para ello, es necesario conocer los principios físicos que están detrás de los fenómenos que se pretenden estudiar. Una vez planteados los problemas, éstos pueden ser complejos e inabordables si se pretenden resolver de forma exacta. Para ello, se trata de desarrollar modelos numéricos que proporcionen aproximaciones fiables de los problemas planteados con la suficiente antelación para permitir una posible toma de decisiones.

Acorde al contexto que concierne a esta tesis, para poder simular el impacto que un tsunami pueda producir en una zona costera, será necesario desarrollar modelos que provean resultados satisfactorios para la propagación de ondas de tipo tsunami en el océano y su evolución desde el talud continental hasta el impacto en costa. En este contexto de fluidos geofísicos, estos procesos tienen la característica de tener información vertical que puede despreciarse, en comparación con la información horizontal. Esta circunstancia hace posible que se pueda simplificar la formulación matemática de los modelos usados para su simulación.

Para ello, las ecuaciones tridimensionales Navier-Stokes, las cuales son las ecuaciones más generales de la mecánica de fluidos, con consideradas. Estas ecuaciones pueden ser

escritas en su forma adimensional y simplificadas bajo ciertas hipótesis:

- la dimensión vertical del dominio H es pequeña en comparación con respecto a la longitud de onda característica L que se presente representar. Esto es:

$$\mu_1 = \frac{H}{L} \ll 1;$$

- se asume la hipótesis de que la presión del fluido es hidrostática;

- los términos de viscosidad horizontal son despreciados.

Bajo estas hipótesis, y tras promediar las ecuaciones en su dimensión vertical, se llega a un sistema no lineal de Ecuaciones en Derivadas Parciales (EDP) comúnmente conocido como las ecuaciones de aguas someras, o según la literatura anglosajona, Shallow-Water Equations (SWE), que en dominios espaciales unidimensionales se escriben como sigue:

$$\begin{cases} \partial_t h + \partial_x(hu) = 0, \ x \in I \subset \mathbb{R}, \ t > 0, \\[2mm] \partial_t(hu) + \partial_x\left(hu^2 + \frac{1}{2}gh^2\right) = gh\partial_x H - \tau_b, \end{cases} \tag{0.0.5}$$

donde $h(x,t)$ representa el espesor de la columna de agua en cada punto $x \in I$, siendo I un intervalo, y t el tiempo. $u(x,t)$ es el promedio de la vertical de la velocidad horizontal. g representa la constante del campo gravitacional y $H(x)$ la topografía. Es también interesante definir la función $\eta(x,t) = h(x,t) - H(x)$ que describe la superficie libre del fluido en cada punto x y cada instante de tiempo t (ver Figura A.1). $\tau_b(x,t)$ parametriza los efectos de fricción con el fondo. En la literatura pueden encontrarse distintas parametrizaciones para los efectos de fricción. En esta tesis se usará una ley de fricción de tipo Manning dada por la expresión

$$\tau_b = gh\frac{n^2 u|u|}{h^{4/3}}, \tag{0.0.6}$$

donde n es el coeficiente de Gauckler-Mannin [185]. El sistema es completado con las correspondientes condiciones iniciales, y en caso de dominios acotados, con las correspondientes condiciones de contorno.

En dinámica de fluidos, es bien sabido que la propagación de las ondas en el agua es un fenómeno dispersivo. Esto quiere decir que ondas de distinta longitud viajan con distinta celeridad. Sin embargo, es bien sabido que las ecuaciones de aguas someras (SWE) no tienen en cuenta estos efectos dispersivos.

La Figura A.2 ilustra este hecho, mostrando capturas de la evolución de una onda aproximándose a una playa. Aquí puede observarse cómo las ecuaciones de aguas someras (en azul) tienden a sobrestimar el tiempo de llegada de la onda a costa cuando se compara

con datos de laboratorio (en rojo). La teoría lineal de Stokes (o la teoría de Airy) explica esta situación ya que establece que la velocidad de propagación, o celeridad C_{Airy}, como una cantidad que viene dada en términos de la profundidad típica H y del número de onda k,

$$C_{Airy}^2 = gH\frac{\tanh(kH)}{kH},$$

mientras que la celeridad del sistema (0.0.5) viene dado por

$$C_{SWE}^2 = gH.$$

La relación anterior, la cual se denomina relación de dispersión lineal para la celeridad, sugiere el carácter dispersivo de la teoría lineal y pone de manifiesto que las ecuaciones de aguas someras no pueden tenerse en cuenta para simular los efectos asociados a las ondas dispersivas en el agua. Este hecho también explica porqué la solución numérica calculada en la Figura A.2 se ve desplazada, ya que la velocidad de propagación del sistema (0.0.5), C_{SWE}, es más rápida que la dada por la teoría lineal C_{Airy}.

En lo que respecta a los modelos matemáticos para simular ondas dispersivas en el agua, un gran esfuerzo se ha realizado en los útimos años en la derivación de modelos matemáticos relativamente sencillos para fluidos someros, válidos para la simulación de ondas con longitudes grandes, como las ondas de tipo tsunami. La historia de los modelos no lineales para la simulación de ondas dispersivas se remonta a principios del siglo XIX.

En 1834, mientras se diseñaban experimentos para determinar el modo más eficiente de diseñar canales en ríos, J. Scott Russel descubrió un fenómeno que el denominó como ondas de traslación ("wave of translation"). Este tipo de ondas se mueven a velocidad constante, preservando además su forma. Las observaciones pueden encontrarse en un "technical report", escrito con motivo del 14 meeting de la asociación "British Association for the Advancement of Science" en 1845 [221]. A día de hoy en dinámica de fluidos, a este tipo de ondas se les denomina "solitones". J. Scott Russell pasó un tiempo realizando investigacioens teóricas y prácticas de este tipo de ondas. El problema era que sus nuevas observaciones parecían contradecir a las más asentadas teorías de Isaac Newton y Daniel Bernoulli en hidrodinámica.

No fue hasta más tarde, cuando el primer resultado teórico exitoso fue llevado a cabo por Joseph Valentin Boussinesq en 1872 [19], que las observaciones de Russel sobre los solitones fueron aceptadas por la comunidad científica. Tras esto, J. Boussinesq en 1877 [19] propuso las ecuaciones de Korteweg de Vries, re-derivadas más tarde por D. Korteweg y G. de Vries (1895). Más tarde, una nueva generación de "pioneros" (F. Serre (1953) [227], C.C. Mei & Le Méhauté (1966) [189] y D. Peregrine (1967) [210]) derivaron nuevos modelos no lineales para ondas dispersivas.

Uno de los modelos más usados y populares fue el sistema de EDPs derivado por Peregrine [210] en 1967. Las ecuaciones de momento son derivadas para ondas de longitud grande y con batimetría no plana. Aunque las ecuaciones son para ondas de amplitud relativamente pequeñas, incluyen términos no lineales. Además, se corresponden con las

ecuaciones derivadas previamente por Boussinesq, cuando se considera una batimetría constante. Hay dos parámetros relevantes asociados a ondas de longitud grande. Uno es el ratio entre la profundidad y la longitud de onda μ_1, y el otro es el ratio entre la amplitud y la profundidad μ_2. Las ecuaciones de Peregrine fueron derivadas bajo las hipótesis

$$\mu_1 \ll 1, \ \mu_2 \approx \mu_1^2.$$

El sistema se escribe como sigue:

$$\begin{cases} \partial_t h + \partial_x(hu) = 0, \ x \in I \subset \mathbb{R}, \ t > 0, \\ \\ \partial_t(hu) + \partial_x\left(hu^2 + \frac{1}{2}gh^2\right) = gh\partial_x H + \frac{1}{2}H^2\partial_{xxt}(uH) - \frac{1}{6}H^3\partial_{xxt}u - \tau_b. \end{cases} \tag{0.0.7}$$

Un análisis asintótico en el límite $kH \to 0$ muestra que la relación de dispersión lineal para la celeridad es exacta hasta orden $\mathcal{O}(kH)^4$ para el sistema de Peregrine comparado con la teoría lineal de Stokes. Esto, hace que el modelo sea apropiado para simulación de ondas con longitud de onda grande.

Mientras la capacidad de cálculo de las modernas computadoras crecía, los modelos de tipo Boussinesq ([1], [19], [144], [184], [202], [210], [148], [255], [256]) se volvían más accesibles desde el punto de vista computacional. Por tanto, se podía empezar a usar modelos más sofisticados que describían mejor la física del problema. Los dos principales retos que surgieron fueron:

- El desarrollo de modelos "fully non-linear weakly dispersive", los cuales se derivan bajo la hipótesis $\mu_2 \approx \mu_1^2$ (véase por ejemplo [144], [168]).

- La mejora de la relación de dispersión lineal de los modelos considerados. De este modo, se podía extender el rango de validez, es decir, el rango donde los modelos pueden describir de forma precisa la física del problema.

El segundo punto anterior, ha atraído la atención de la comunidad científica durante los últimos años. Atendiendo al comportamiento de las ondas, se encuentra la siguiente clasificación: aguas someras, aguas intermedias y aguas profundas. Especialmente el segundo punto mencionado, se centra en la mejora de la relación de dispersión lineal para aguas intermedias, que tiene lugar cuando la longitud de onda típica de las ondas a representar, L, se encuentra aproximadamente entre $2H$ y $20H$, siendo H la profundidad media. En este rango, puede ser muy importante la información vertical que se desprecia cuando se derivan por ejemplo, las ecuaciones de aguas someras. Por tanto, en la derivación de modelos para estos rangos de validez, debe prestarse atención a la estructura vertical de las ecuaciones.

Los modelos de alto orden de tipo Boussinesq pueden ofrecer excelentes propiedades dispersivas. El punto negativo, es que los sistemas son extremadamente complejos,

presentando a su vez derivadas de alto orden (por ejemplo, derivadas de hasta quinto orden aparecen en [135]). A su vez, dichos sistemas requieren de un esquema numérico igualmente complejo cuando se aproximan. La complejidad se incrementa aún más cuando se consideran dominios bidimensionales.

No obstante, Madsen y Sorensen (véase [184]) encontraron una inteligente solución al problema. Los autores propusieron una aproximación que mejoraba de forma sustancial las propiedades dispersivas del modelo de Peregrine, sin incrementar el orden de las derivadas. Ellos propusieron un sistema que a día de hoy se ha convertido en uno de los más conocidos y empleados.

De manera alternativa, el desarrollo de los modelos de presión no hidrostática ha sido también objeto de numerosos estudios científicos durante los últimos 30 años. Los modelos no hidrostáticos son capaces de modelar muchos de los aspectos de interés en el ámbito de ingeniería costera. Estos modelos pueden tener en cuenta los efectos dispersivos, efectos no lineales, shoaling, refracción, difracción, inundación... entre otros. La principal hipótesis empleada durante su derivación consiste en dividir la presión total del fluido y considerarla como la suma de dos contribuciones: hidrostática y no hidrostática (véase Casulli [52]). En esta tesis, el sistema de presión no hidrostática derivado por Sainte-Marie *et al.* en [21] se considera para su aproximación numérica. Este sistema puede ser derivado tras un proceso estándar de integración en vertical de las ecuaciones de Euler, y asumiendo un perfil constante para la velocidad horizontal. El sistema puede escribirse como sigue:

$$\begin{cases} \partial_t h + \partial_x(hu) = 0, \ x \in I \subset \mathbb{R}, \ t > 0, \\[2mm] \partial_t(hu) + \partial_x\left(hu^2 + \frac{1}{2}gh^2 + hp\right) = (gh + p_b)\,\partial_x H - \tau_b, \\[2mm] \partial_t(hw) + \partial_x(uhw) = p_b, \quad p_b = 2p \\[2mm] \partial_x u + \dfrac{w - w_b}{h/2} = 0, \quad w_b = -u\partial_x H. \end{cases} \qquad (0.0.8)$$

Como el proceso de derivación del sistema es similar al seguido para las ecuaciones de aguas someras SWE, la definición de las variables coincide con las descritas para el sistema (0.0.5). Las variables w y p son la velocidad vertical promedio y la presión no hidrostática promedio respectivamente. De igual modo, w_b y p_b denotan la velocidad vertical en el fondo, y la presión no hidrostática en el fondo. La última ecuación en (0.0.8) tiene en cuenta la condición integrada de incompresibilidad. La principal virtud de este sistema no hidrostático radica en su simplicidad, dada la ausencia de derivadas de orden superior. Además, el sistema anterior posee una relación de dispersión lineal que es similar a la del sistema (0.0.7).

Dentro del espíritu de los sistemas de EDPs no hidrostáticos con propiedades dispersivas, pueden encontrarse muchos trabajos. Con el objetivo de mejorar las

propiedades dispersivas del sistema, la principal tendencia que puede encontrarse consiste en el uso de modelos promediados multicapas. La idea es, en vista del reciente incremento de capacidades de los sistemas de computación, derivar sistemas que se encuentren cada vez más y más cerca de los resolvedores tridimensionales. Esto es, modelos que sean capaces de retener más información vertical para poder describir de un modo más preciso la estructura vertical del fluido. De este modo, se llega a una mejor descripción del comportamiento no lineal y de las propiedades dispersivas del experimento de estudio.

En el trabajo [124], E.D. Fernández-Nieto *et al.* derivaron una familia de modelos multicapas con presión no hidrostática. Esta familia de modelos contiene al sistema descrito en (0.0.8) cuando el número de capas es igual a uno. Cuando el número de capas es mayor que uno, el modelo matemático permanece igual de sencillo, en el sentido de que no posee términos con derivadas de orden superior a uno. Otra de sus principales virtudes, radica en el siguiente teorema que fue formalmente demostrado en [124], que establece que cuando el número de capas tiende a infinito, la celeridad del sistema linealizado tiende a la correspondiente celeridad que establece la teoría lineal de Stokes. Debido a esta razón, este sistema de presión no hidrostática ha sido considerado en esta tesis como el marco central de modelos para el diseño de esquemas numéricos para simular ondas dispersivas. Mas aún, en esta tesis un nuevo modelo de presión no hidrostática bicapa con mejoradas propiedades dispersivas es propuesto y aproximado numéricamente en [118].

En cuanto a la naturaleza de los sistemas de EDPs dispersivos presentados aquí, es bien sabido que el sistema (0.0.5) es hiperbólico. Sin embargo, la naturaleza del sistema (0.0.7), entre otros sistemas de tipo Boussinesq y de presión no-hidrostática, responde más bien a sistemas mixtos hiperbólicos-elípticos. Algunos resultados de tipo teóricos sobre existencia y unicidad de soluciones pueden encontrarse en [167].

Debido a la naturaleza hiperbólica-elíptica de los sistemas de tipo Boussinesq y de presión no hidrostática, la complejidad de los correspondientes esquemas numéricos para su discretización aumenta. Por ejemplo, la condición de incompresibilidad en (0.0.8) añade una restricción extra que hace del sistema un problema hiperbólico-elíptico. Esta restricción hace que los esquemas numéricos explícitos no puedan ser aplicados, ya que pueden requerir de una condición de estabilidad fuerte, o incluso peor, puede hacer que los esquemas numéricos resultantes sean incondicionalmente inestables. Por tanto, deben tenerse en cuenta para su discretización esquemas de tipo implícitos (véase por ejemplo [4], [112], [163], [180], [217], [259]). Los métodos numéricos aplicados a los sistemas de presión no-hidrostática, e incluso a los sistemas de tipo Boussinesq, usualmente usan una técnica de tipo "splitting" (véase e.g. [168]) o una técnica de tipo proyección-corrección (véase [4], [63], [112], [118]). Estos esquemas numéricos generalmente combinan resolvedores de volúmenes finitos para resolver el sistema hiperbólico subyacente en un primer paso, y diferencias finitas o elementos finitos para resolver el problema elíptico en un segundo paso, haciendo uso de mallas decaladas ("staggered grids").

Sin embargo, hay una reciente y alternativa estrategia para la simulación de ondas de tipo dispersivas, mediante el uso de sistemas hiperbólicos. En [188], Ricciuto *et al.*

propusieron un sistema de primer orden para problemas generales de tipo advección-difusión-dispersión. En [147] Brocchini *et al.* obtuvieron un conjunto de ecuaciones integradas hiperbólicas usando una técnica de aproximación de tipo relajación.

Siguiendo una línea parecida, en esta tesis se propone un nuevo sistema integrado de primer orden hiperbólico, que puede verse como una modificación del sistema (0.0.8) para dominios bidimensionales presentado en [21]. Este nuevo sistema es propuesto por Escalante *et al.* en [111]. El nuevo sistema hiperbólico es obtenido haciendo uso de una reformulación hiperbólica de las ecuaciones originales (0.0.8). La condición de divergencia se acopla con el resto de leyes de conservación del sistema, siguiendo ideas similares a las aplicadas en [196], [83] para las ecuaciones de Maxwell y las ecuaciones de la magnetohidrodinámica (MHD). En este nuevo trabajo propuesto, una nueva formulación es introducida, donde los errores de la divergencia del campo de velocidades son transportados hacia el exterior del dominio a velocidad finita, relacionada con el máximo de los autovalores del sistema de EDPs. El sistema hiperbólico aumentado continúa satisfaciendo una ley de balance de energías. De la hiperbolicidad del nuevo sistema, se obtiene que esquemas numéricos explícitos y de alto orden pueden desarrollarse de manera eficiente y sencilla.

Los esquemas de alto orden son convenientes debido a sus buenas propiedades mejoradas de disipación y dispersión, en comparación con los esquemas usuales de segundo orden TVD de tipo volúmenes finitos. Esto es particularmente importante cuando se pretende simular la propagación de solitones a grandes distancias en tiempos de integración altos, como se mostrará en esta tesis en la sección de resultados numéricos. En esta tesis, se consideran dos alternativaspara la discretización de alto orden de los sistemas de EDPs estudiados:

- Métodos de volúmenes finitos de alto orden basados en la reconstrucción polinómica de estados.

- Esquemas de alto orden de tipo Discontinuos Galerkin (DG).

En cuanto a los esquemas de tipo volúmenes finitos para problemas hiperbólicos, la principal dificultad que aparece desde un punto de vista matemático así como numérico, reside en la presencia de productos no conservativos, los cuales dificultan la definición de solución débil. Muchos problemas relacionados con los fluidos geofísicos y en particular, algunas de las ecuaciones discretizadas en esta tesis, caen en este marco. Los productos no conservativos son interpretados como medidas de Borel en el sentido introducido por Dal Maso, LeFloch y Murat en [72]. Para sistemas de EDPs, una familia de caminos debe ser elegida. Un marco general para resolver numéricamente estos sistemas fue introducido por C. Parés en [205], con la introducción de los esquemas numéricos camino-conservativos. La elección de una familia de caminos debería estar fundamentada con la física del problema. Algunas notas sobre cómo la familia de caminos debe ser elegida pueden verse en [38]. La familia de los esquemas de Roe generalizados introducidos en [248]

constituye un caso particular de esquema numérico camino-conservativo para sistemas no conservativos de EDPs. Aunque los esquemas de esta familia son robustos (véase por ejemplo [14], [30], [208], [205]), éstos también presentan, así como su correspondiente parte conservativa, algunos problemas ya que en su implementación es necesaria la descomposición espectral de una matriz de Roe. En algunos casos, no puede obtenerse una expresión analítica, haciendo del esquema de Roe una opción computacionalmente ineficiente. De igual modo, estos esquemas no satisfacen en general una desigualdad de entropía, y como consecuencia deben tenerse en cuenta técnicas de tipo "entropy-fix" para capturar las soluciones entrópicas en presencia de transiciones suaves (see [154]). Es también sabido que el uso de resolvedores de Riemann incompletos, tales como Rusanov, Lax-Friedrichs, HLL, etc. permite reducir el coste computacional requerido por un resolvedor de tipo Roe. Aunque cuando se consideran en volúmenes finitos aproximaciones constantes a trozos, los esquemas de Roe proporcionan, en general, una mejor resolución de las discontinuidades en comparación con los resolvedores de Riemann incompletos, cuando estos últimos se combinan con una reconstrucción de alto orden, las diferencias pueden resultar indistinguibles. Es por eso que los resolvedores de Riemann incompletos, combinados con técnicas de reconstrucción de alto orden, pueden resultar más eficientes que métodos de Roe de alto orden.

En esta tesis, usamos una clase de volúmenes finitos de primer orden eficientes: los métodos PVM ("Polynomial Viscosity Matrix") introducidos por Castro *et al.* en [40].

Esta clase de resolvedores de Riemann incompletos, puede aplicarse para sistemas no conservativos hiperbólicos, y están definidos en términos de matrices de viscosidad, las cuales se calculan mediante la evaluación polinómica de una matriz de Roe. Los esquemas de tipo PVM pueden verse como la extensión natural de aquellos métodos presentados en [84] para sistemas de leyes de conservación a sistemas no conservativos. Más aún, los esquemas de tipo PVM pueden extenderse a esquemas numéricos de alto orden, siguiendo las ideas presentadas en [25] y a sistemas bidimensionales siguiendo [41], basadas en reconstrucciones polinómicas de estados.

Otra clase de esquemas numéricos de alto orden considerados en esta tesis, son los esquemas de elementos finitos de tipo "Discontinuous Galerkin" (DG), introducidos originalmente por Reed y Hill [214]. Esta clase de esquemas se han dado a conocer para la resolución numérica de sistemas hiperbólicos de leyes de conservación, gracias a una serie de trabajos publicados por Cockburn, Shu y colaboradores, véase [68], [67], [66], [69].

En particular, en esta tesis los esquemas de tipo ADER-DG introducidos por Dumbser en [97], [93], [91] han sido adoptados. A su vez, éstos trabajos parten de los correspondientes a la familia de esquemas numéricos de volúmenes finitos ADER, introducidos por Toro y Titarev [237], [244], [238], [241]. La metodología ADER está basada en la aproximación de la solución de problemas de Riemann generalizados en las interfaces de los volúmenes de discretización, lo cual lleva a esquemas numéricos de un sólo paso y orden arbitráreo tanto en espacio como en tiempo.

Debido al conocido teorema de Godunov, cualquier esquema lineal de orden mayor que

uno es oscilatorio y, por lo tanto, no es adecuado para la discretización de problemas con discontinuidades o gradientes fuertes en la solución. Siguiendo las ideas introducidas en [98], [261], los esquemas de alto orden ADER-DG se acompañan de una técnica limitadora *a posteriori* de tipo volúmenes finitos en subceldas.

La idea principal consiste en usar primero un esquema de tipo ADER-DG de alto orden sin limitar, el cual produce una denominada solución candidata al final de cada paso de tiempo. Esta solución candidata se verifica *a posteriori* contra algunos valores físicos y criterios de detección numéricos, como la positividad de la solución, la ausencia de errores de punto flotante, etc y se comprueba si satisface cierto principio discreto del supremo relajado (DMP). Si una celda no cumple todas estas condiciones, la solución discreta es *descartada* y localmente *recalculada*, comenzando de nuevo desde una solución válida en el antiguo nivel de tiempo, pero utilizando ahora un esquema más robusto en una sub malla más fina dentro de las celdas con problemas. Este nuevo concepto de limitación *a posteriori* se introdujo por primera vez en el contexto de los esquemas de volúmenes finitos a través del enfoque MOOD, véase [64], [88], [89], [173]. Para el re-cálculo de las celdas con problemas, en principio, se puede usar cualquier esquema de volumen finito robusto. Aquí, se emplea la familia de esquemas de volúmenes finitos camino-conservativos, que ya se han utilizado anteriormente con éxito para la solución de sistemas de tipo de aguas someras en una serie de trabajos, véase por ejemplo [112], [44], [206], [40], [26], [205], [46]. En particular, se usará un esquema camino-conservativo robusto, bien equilibrado y que asegura la positividad de la columna de agua de tipo PVM [90].

Además, el uso de un método numérico que resuelva correctamente las soluciones estacionarias es de vital importancia en algunos casos, como por ejemplo el sistema de aguas someras. En el caso de una onda de tsunami que se propaga en el océano, su amplitud inicial es pequeña (aunque la longitud de onda es enorme) y no siempre es posible refinar la malla para que el error de truncamiento del método sea menor que esta amplitud. En este contexto, surge una dificultad relacionada con el cálculo numérico de las soluciones estacionarias: los métodos estándar que resuelven correctamente los sistemas de leyes de conservación pueden fallar al resolver sistemas no conservativos cuando se acercan a equilibrios o cercanos a las soluciones de equilibrio. En el contexto de aguas someras, Bermúdez y Vázquez-Cendón introdujeron en [14] la condición llamada *propiedad-C*: Se dice que el esquema satisface esta condición si se resuelven correctamente las soluciones de estado estacionario correspondientes al agua en reposo. Esta idea de construir esquemas numéricos que conservan algunos equilibrios, que en general se llaman esquemas numéricos *bien equilibrados*, ha sido estudiado por muchos autores. El diseño de métodos numéricos con buenas propiedades para problemas conservativos o no conservativos es un frente de investigación muy activo: véase, por ejemplo, [6], [16], [15], [18], [37], [55], [56], [82], [139], [140], [141], [145], [146], [172], [174], [199], [209], [211], [212], [215], [222], [234], [248], [258], [162], [85], [86], [247], entre otros.

La simulación de flujos geofísicos conduce a la resolución de problemas en grandes dominios computacionales, por ejemplo, en una cuenca oceánica cuando se realiza

una simulación de tsunami o grandes tiempos de integración, como la simulación de corrientes inducidas por una marea. En ambos casos, las simulaciones presentan un gran esfuerzo computacional y, como consecuencia, se necesitan implementaciones eficientes para resolver estos problemas en tiempos razonables. Por lo tanto, se necesitan versiones paralelas de resolvedores numéricos precisos y eficientes para plataformas de alto rendimiento para poder tratar estos escenarios de simulación en tiempos razonables.

Las modernas *unidades de procesamiento gráfico (GPU)* son dispositivos altamente programables y masivamente paralelos que se pueden usar para acelerar cálculos numéricos (véase [22], [159], [251]). Estos dispositivos ofrecen cientos o miles de unidades de procesamiento optimizadas para realizar de forma masiva operaciones en coma flotante en paralelo, y han demostrado ser eficaces en la aceleración de esquemas numéricos que exhiben una gran cantidad de paralelismo.

Existe un uso generalizado de las plataformas basadas en CUDA para acelerar resolvedores numéricos para EDPs (véase [76], [75], [28], [80]). En la tesis doctoral [74], se muestra la adaptación a GPU del esquema numérico de volúmenes finitos introducido en [27] para resolver el sistema de aguas someras en dominios bidimensionales. En estas referencias, los autores pretenden facilitar la explotación de las plataformas habilitadas por CUDA para acelerar las simulaciones numéricas basadas en EDPs, proporcionando las bases de programación CUDA adecuadas. Para este propósito, los autores explican la adaptación a arquitecturas GPU de los esquemas numéricos de volúmenes finitos para resolver el sistema de aguas someras 2D. Así mismo, se aborda la implementación CUDA de un resolvedor para el sistema bicapa de aguas someras en [75]. También existen propuestas para implementar, usando GPUs, esquemas de alto orden para simular el sistema de aguas someras en [47], [131] y para implementar esquemas de primer orden para los sistemas de una y dos capas en mallas triangulares [28].

Los resolvedores numéricos antes mencionados implementados en GPU exhiben un patrón computacional que es muy frecuente en los algoritmos numéricos para resolver EDPs y que ha sido ampliamente utilizado a lo largo de esta tesis. Sin embargo, surge una dificultad: algunos de los métodos numéricos propuestos en esta tesis no son métodos explícitos, y los sistemas lineales que surgen tienen que ser resueltos de un modo eficiente y paralelo. Para hacer eso, proponemos algunos resolvedores lineales iterativos y masivamente paralelizables para tener implementaciones GPU eficientes.

Resumen abreviado de la tesis:

El resumen abreviado de esta tesis es el siguiente:

- En el Capítulo 1 se presenta una visión general del estado del arte del modelado, y se introducen los principales sistemas dispersivos estudiados en esta tesis. En la actualidad se pueden encontrar dos grandes familias de sistemas dispersivos: los sistemas de tipo Boussinesq y los sistemas de presión no hidrostática. Aunque en esta tesis nos centraremos en la segunda clase de sistemas dispersivos, en este

capítulo se muestran dos de los sistemas de tipo Boussinesq más representativos y usados, y se establecen algunas relaciones y reescrituras como sistemas de EDPs de presión no hidrostática de primer orden. El sistema de presión no hidrostática multicapa derivado por Fernández-Nieto *et al.* en [124] se elige como el principal marco de sistemas dispersivos para esta tesis. Esta elección se basa en su simplicidad y en sus buenas propiedades de relación de dispersión que previamente se han introducido y calculado para todos los sistemas considerados.

En este capítulo, también se describen dos nuevos sistemas de presión no hidrostática: un nuevo sistema de presión no hidrostática de dos capas con propiedades de dispersión mejoradas; y un nuevo sistema de EDPs hiperbólico que converge al sistema de una capa (0.0.8). Para ambos sistemas, las propiedades dispersivas y su estructura espectral se estudian con detalle.

Llegados a este punto, hacemos hincapié en que los modelos introducidos no describen la física subyacente en uno de los procesos que suceden cuando una onda se acerca a costa: la ruptura de la onda o "breaking of the wave". Esto implicará que debamos incluir un mecanismo de tipo breaking en las ecuaciones consideradas. Esto se hará a través de un modelo de viscosidad sencillo, con un criterio de breaking dado, que detectará cuándo y qué ondas son de tipo breaking. Así mismo, algunos mecanismos de breaking novedosos se proponen que más tarde se validarán a través de comparaciones con datos experimentales.

Finalmente, se muestran algunas ideas para el cálculo de solitones para los sistemas dados, así como algunas comparaciones.

- En el Capítulo 2, se establecen los resultados teóricos requeridos para el diseño de esquemas numéricos para sistemas hiperbólicos no conservativos en una y dos dimensiones. En cuanto a los esquemas de volúmenes finitos, se da el concepto de esquemas camino-conservativos y esquemas bien equilibrados, así como la extensión de estos esquemas numéricos a orden superior, basados en la reconstrucción de estados. En particular, se describen los métodos de tipo PVM introducidos en [48]. Como alternativa a los métodos de volúmenes finitos de orden superior basado en la reconstrucción de estados, se describen los métodos ADER-DG complementados a su vez con un limitador de tipo volúmenes finitos *a posteriori* adecuado (ver [98], [64]).

- En el Capítulo 3 los esquemas numéricos propuestos para los sistemas de presión no hidrostática dados se describen completamente. Allí, se pueden destacar diferentes enfoques y estrategias. Por un lado, hemos diseñado esquemas numéricos de volúmenes finitos de segundo orden basados en una técnica de proyección-corrección de dos pasos. En un primer paso, se utiliza un esquema de volúmenes finitos explícito que discretiza la parte hiperbólica e hidrostática subyacente del sistema, bajo una condición de CFL habitual. Luego, en un segundo paso, los términos no

hidrostáticos se toman en cuenta y se aproximan por medio de diferencias finitas centradas. Esto implicará la inversión de un operador de tipo Poisson y de ahí la naturaleza implícita del esquema numérico. En este paso, hemos considerado mallas decaladas y no decaladas para la presión no hidrostática y las velocidades verticales. Por otro lado, se propone un esquema numérico de tipo DG completamente explícito y de alto orden arbitrario para el nuevo sistema de EDPs hiperbólico propuesto, complementado con un limitador de volúmenes finitos a posteriori. Para permitir simulaciones en tiempo real, una implementación eficiente en GPU de los métodos numéricos es llevado a cabo para todos los sistemas bidimensionales, y algunas directrices sobre su implementación son dadas en el Apéndice E.

- En el Capítulo 4 los esquemas numéricos antes mencionados para cada uno de los sistemas se han aplicado a test de referencia académicos tales como la propagación de solitones, así como a situaciones físicas más desafiantes que implican ondas en una zona de costa incluyendo el rompimiento de olas en una y dos dimensiones espaciales. En todos los casos, las comparaciones realizadas con soluciones analíticas o con datos experimentales son excelentes, lo que demuestra la validez del modelo matemático propuesto y del algoritmo para su resolución numérica. Los datos experimentales incluyen una amplia variedad de escenarios: propagación, shoaling, ondas dispersivas inducidas por deslizamientos submarinos de sólidos rígidos, entre otros. Finalmente, algunos tiempos computacionales para los test bidimensionales muestran la eficiencia buscada.

- Tal como se reveló mediante las comparaciones con los datos de laboratorio del test que simulaba ondas inducidas por deslizamientos submarinos rígidos, éstas pueden ser dispersivas. En el Capítulo 5 medimos la influencia al considerar una presión no hidrostática aplicada a la simulación del transporte y arrastre de sedimentos. Para ello, se introduce un trabajo nuevo y que actualmente sigue curso en el que se propone un sistema de dos capas de aguas someras para describir el transporte de sedimentos. Así mismo, se muestra un esquema numérico y algunas pruebas académicas y de validación, que ofrecen resultados prometedores.

- Por último, en el Capítulo 6 se presentan las conclusiones de la tesis y algunas líneas de trabajo futuro.

Chapter 1

Dispersive water waves modelling

Contents

When modelling and simulating geophysical flows, the Non-linear Shallow-Water equations, from now on SWE, is often a good choice as an approximation of the Navier-Stokes equations. Nevertheless, SWE do not take into account the effects associated with dispersive waves. In recent years, a great effort has been made in the derivation of relatively simple mathematical models for shallow water flows that include long non-linear water waves. As computational power increases, Boussinesq type models and non-hydrostatic pressure models ([1], [19], [21], [52], [144], [148], [184], [202], [210], [255], [256], [231], [259]) become more accessible. This means that one can use more sophisticated models to accurately describe reality, despite the higher computational cost. They are capable of solving many relevant features of coastal water waves, such as dispersion, non-linearity, shoaling, refraction, diffraction, and run-up.

This chapter is organized as follows. In Section 1.1, a general overview is presented on the state of the art of the main dispersive systems used during the last years. The genuine system derived by Peregrine and the improvement proposes by Madsen-Sørensen are two of the most representative Boussinesq type systems. A general formulation based on a novel quasi two layer non-hydrostatic pressure system, that collects some of the main Boussinesq type systems, it is also discussed. After that, a class of multi layer non-hydrostatic pressure system derived by E.D. Fernández-Nieto *et al.* in [124] is presented. Later, the particular case when the number of layers is set to one, that corresponds to the system derived originally by Jacques Sainte-Marie *et al.* in [21] is described. Likewise, a simplification of the one layer system, previously introduced by Yamazaki *et al.* in [259] is described. Finally, some basic definitions about the main linear dispersive relations of general interest are given.

In Section 1.2 a new two layer non-hydrostatic pressure system derived by C. Escalante *et al.* in [118] it is described. The system depends on three different free-parameters that are optimized to improve the dispersive relation of the system and can be seen as a modification of one of the models presented in [124] with a correction in the non-hydrostatic pressure profile.

The main drawback when approximating numerically the described dispersive/non-hydrostatic pressure systems is that one has to invert an elliptic operator. This will leads to a restrictive CFL condition for explicit schemes, or even worse, to an unconditionally stable scheme (see [164]). Therefore, implicit schemes must be considered with the consequent loss of efficiency. In Section 1.3 a new and recent technique by C. Escalante *et al.* in [111] is introduced and it is applied to the incompressible non-hydrostatic system derived by Sainte-Marie *et al.* in [21]. The incompressibility equation of the original system proposed in [21] is replaced by an artificial compressibility equation, where errors are transported to the domain boundaries with the maximal admissible speed c following the so-called *Hyperbolic Divergence Cleaning* ideas applied in magneto-hydrodynamic (see [83]). The resulting first-order system formally tends to the proposed in [21] when $c \to \infty$, and it is shown that the system is hyperbolic.

In Section 1.4 some of the main linear dispersion properties of the presented dispersive

and/or non-hydrostatic systems are derived and compared.

In Section 1.5 a discussion on simple wave breaking mechanisms is carried out. At this point, it should be noted that detailed small-scale wave breaking flow physics is not described by the considered model, but only the net effect of wave breaking on energy dissipation. This means that a breaking mechanism is included in the depth-integrated equations via a simple sub-scale viscosity model, with a breaking criterion similar to the one proposed in [219] that allow the dissipation in regions where needed.

Finally in Section 1.6 some aspects concerning solitary waves will be introduced. In this section we provide some basic definitions, as well as analytical solitary wave solutions for the system introduced by Sainte-Marie*et al.* For some other PDE systems where it is not an easy task to find analytical solitary wave solutions, we give a numerical procedure to compute them.

1.1 A general overview on dispersive water waves modelling

The fundamentals of Boussinesq type models are exhibited here, which aims at highlighting the fundamental principles of the modelling, as well as the characteristics of the chosen equations.

The systems that will be considered in this thesis can be formulated for the case of one space dimension as

$$
\begin{cases}
\partial_t U + \partial_x F(U) + B(U)\partial_x U = G(U)\partial_x H + S(U) + \mathcal{T}, \\
\mathcal{I}(U, \partial_x U, H, \partial_x H) = \mathbf{0},
\end{cases}
\tag{GF}
$$

or for the case of two space dimensions as

$$
\begin{cases}
\partial_t U + \nabla \cdot \boldsymbol{F}(U) + \boldsymbol{B}(U) \cdot \nabla U = \boldsymbol{G}(U) \cdot \nabla H + S(U) + \mathcal{T}, \\
\mathcal{I}(U, \nabla U, H, \nabla H) = \mathbf{0},
\end{cases}
\tag{GF-2D}
$$

where in the case of two space dimensions the unknown $U(\boldsymbol{x}, t)$ contains the conserved variables and is defined in $\Omega \times [0, T]$, Ω being a domain of $\mathbb{R}^2$. U takes values in an open convex set $\mathcal{O}$ of $\mathbb{R}^N$; $\boldsymbol{F} = (F_1, F_2)$ is a regular function from $\mathcal{O}$ to $\mathbb{R}^N \times \mathbb{R}^N$ that contains the physical fluxes; $\boldsymbol{B} = (B_1, B_2)$, a regular matrix function from $\mathcal{O}$ to $\mathcal{M}_N \times \mathcal{M}_N(\mathbb{R})$ that contains the nonconservative terms; $\boldsymbol{G} = (G_1, G_2)$, a regular function from $\mathcal{O}$ to $\mathbb{R}^N \times \mathbb{R}^N$ that contains the geometric source terms that accounts the effects of the bottom topography H which is a known function from $\mathcal{O}$ to $\mathbb{R}$; S is a regular function from $\mathcal{O}$ to $\mathbb{R}^N$ containing the source terms that may include friction terms. This formulation allows to represent in a compact form the systems described in this thesis: Boussinesq-type

systems and non-hydrostatic pressure systems, where $\mathcal{T}$ is an operator that contains the dispersive/non-hydrostatic pressure terms depending on

$$\mathcal{T} \equiv \mathcal{T}(U, \nabla U, H, \nabla H) \text{ for Boussinesq-type systems,}$$

$$\mathcal{T} \equiv \mathcal{T}(U, \nabla U, P, \nabla P, H, \nabla H) \text{ for non-hydrostatic pressure-type systems.}$$

For the case of non-hydrostatic pressure systems, $P(\boldsymbol{x}, t)$ accounts for the non-hydrostatic pressure unknowns and is defined in $\Omega \times [0, T]$. This family of systems can not be expressed as a system of balance laws. For example, although $P(\boldsymbol{x}, t)$ is one of the variables of the system, it can not be found an equation in the form $\partial_t P(\boldsymbol{x}, t) + \ldots = 0$. Instead, an extra set of equations that relates P with U are needed. This conditions are expressed by the vector operator $\mathcal{I}$. This set of extra equations contain the incompressibility condition. It relates spatial derivatives of the horizontal velocities, with the vertical velocities that at the same time, are linked with the non-hydrostatic pressures via some vertical momentum equations.

In the subsequent subsection, two of the most popular Boussinesq-type PDE systems will be presented, as well as some of the non-hydrostatic pressure PDE systems that will be discretized in this thesis. Also, some mathematical properties of interest will be analysed.

1.1.1 The non-linear shallow water equations

The non-linear shallow water equations constitute a system of non-linear hyperbolic PDEs. They are derived from the Euler equations assuming a constant vertical profile on the horizontal velocity within the fluid layer, that is also assumed to be incompressible, inviscid and homogeneous.

They are valid for problems in which vertical dynamics can be neglected compared to horizontal effects. As it will be shown, they can not represent dispersive water waves, since the dispersion relation is quite far away from the linear theory for intermediate waters.

The governing equations for one space dimension can be written as a system of conservation laws with geometric source terms that reads as:

$$\begin{cases} \partial_t h + \partial_x \left(hu \right) = 0, \\ \\ \partial_t \left(hu \right) + \partial_x \left(hu^2 + \dfrac{1}{2}gh^2 \right) = gh\partial_x H - \tau_b, \end{cases}$$

where the unknowns (h, hu) takes values in an open convex set of $\mathbb{R}^2$

$$\mathcal{O} = \{(h, hu) \in \mathbb{R}^2, \quad h > 0\},$$

$h = h(x, t)$ being the water depth, $H = H(x)$ the known still water depth. The surface elevation measured from the still-water level is denoted by $\eta = h - H$. Furthermore, t denotes time, g is the gravitational acceleration and u is the depth averaged velocity in the x direction. The bottom friction is included in the equations via an usual Manning-type friction formula for the bottom shear stress that reads

$$\tau_b = ghu\frac{n_m^2|u|}{h^{4/3}}, \tag{1.1.1}$$

where n_m is an empirical bottom friction coefficient (see [185]).

This system can be written as in the general compact form (GF), defining

$$U = \begin{pmatrix} h \\ q \end{pmatrix}, \quad F(U) = \begin{pmatrix} q \\ \dfrac{q^2}{h} + \dfrac{1}{2}gh^2 \end{pmatrix}, \quad G(U) = \begin{pmatrix} 0 \\ gh \end{pmatrix},$$

$$S(U) = -\begin{pmatrix} 0 \\ \tau_b \end{pmatrix}, \quad B(U) = \mathbf{0}, \tag{SWE}$$

$$\mathcal{T} = \mathbf{0}, \quad \mathcal{I} = \mathbf{0},$$

$q = hu$ being the discharge.

Energy balance of the system

An extra conservation law related to the conservation of the energy is verified. The smooth solutions (h, u) of (SWE) satisfies the additional balance law

$$\partial_t E + \partial_x \left(u \left(E + \frac{g}{2}h^2 \right) \right) = -u\tau_b, \tag{1.1.2}$$

where

$$E = \frac{h(u^2)}{2} + \frac{gh(\eta - H)}{2}. \tag{1.1.3}$$

is defined as the mechanical energy.

Note that the contribution to the right hand side

$$-u\tau_b = -u^2 gh\frac{n_m^2|u|}{h^{4/3}} < 0,$$

since $gh\dfrac{n_m^2|u|}{h^{4/3}} > 0$, and this stablish that the friction term with the bottom is the only term in the equations that dissipates energy in a smooth solution. When $n_m = 0$, then the equality (1.1.2) provides a new conservation law verified by the smooth solutions.

Eigenstructure of the system

Let us define

$$J_F = \partial F / \partial U$$

the Jacobian of the flux F with respect to the conserved variables U :

$$J_F = \begin{pmatrix} 0 & 1 \\ C^2 - u^2 & 2u \end{pmatrix}, \quad C = gh.$$

The eigenvalues of the matrix J_F are

$$\lambda_{1,2} = u \pm \sqrt{gh}.$$

A set of linearly independent eigenvectors is given by

$$v_i = \left(1, \lambda_i\right), \ i = 1, 2.$$

The system is strictly hyperbolic if and only if $C > 0$ and $|u| \neq c$.

Governing equations in two space dimensions

The non-linear shallow water equations for bidimensional domains can be written in the general compact form (GF-2D), defining

$$U = \begin{pmatrix} h \\ q_x \\ q_y \end{pmatrix}, \quad F_1(U) = \begin{pmatrix} q_x \\ \dfrac{q_x^2}{h} + \dfrac{1}{2}gh^2 \\ \dfrac{q_x q_y}{h} \end{pmatrix}, \quad F_2(U) = \begin{pmatrix} q_y \\ \dfrac{q_x q_y}{h} \\ \dfrac{q_y^2}{h} + \dfrac{1}{2}gh^2 \end{pmatrix},$$

$$G_1(U) = \begin{pmatrix} 0 \\ gh \\ 0 \end{pmatrix}, \quad G_2(U) = \begin{pmatrix} 0 \\ 0 \\ gh \end{pmatrix}, \quad S(U) = - \begin{pmatrix} 0 \\ \tau_{b,x} \\ \tau_{b,y} \end{pmatrix}, \quad \boldsymbol{B}(U) = \boldsymbol{0},$$

$$\text{(SWE-2D)}$$

$$\mathcal{T} = \boldsymbol{0}, \quad \mathcal{I} = \boldsymbol{0},$$

where $q_u = hu$, $q_v = hv$ are the horizontal discharges, $u(x, y)$ and $v(x, y)$ being the depth averaged velocities in the x and y direction respectively. $\tau_{b,x}$ and $\tau_{b,y}$ contains the

Manning-type friction formula for the bottom shear stress that reads

$$\begin{pmatrix} \tau_{b,x} \\ \tau_{b,x} \end{pmatrix} = gh \frac{n_m^2 \, ||(u,v)||}{h^{4/3}} \begin{pmatrix} u \\ v \end{pmatrix}. \tag{1.1.4}$$

Similarly to the 1D case, for the shallow water equations no extra incompressibility condition is needed, and thus $\mathcal{I} = \mathbf{0}$.

1.1.2 Boussinesq-type systems

In order to retain non-linear dispersive effects from the Navier-Stokes equations, information on the vertical structure of the flow should be included when a new model is derived. The Boussinesq-type wave equations take into account this idea and have prevailed due to their computational efficiency.

The main idea is to include non-hydrostatic effects due to the vertical acceleration of the fluid in the depth-averaging process of the equations. For instance, one can assume that both non-linearity and frequency dispersion are weak and of the same order of magnitude.

Since the early works of Peregrine [210], several improved and enhanced Boussinesq models have been proposed over the years. One may use different approaches to improve non-linear dispersive properties of the model: considering a Taylor expansion of the velocity potential in powers of the vertical coordinate and in terms of the depth-averaged velocity [184] or the particle velocity components (u, w) at a chosen level [202]; including two scalars representing the vertical profile of the non-hydrostatic pressure [160]; using a better flow resolution in the vertical direction with a multi layer approach [176], [178], [257].

In the next subsection two of the most representative Boussinesq type systems proposed by Madsen-Sørensen [184] and Peregrine [210] will be described. The systems can be written for two space dimensions as in (GF-2D).

The underlying system resulting when $\mathcal{T}$, that contains the dispersive terms, are suppressed coincides with the hyperbolic system (SWE-2D) with bottom friction. As in (SWE-2D), $h = h(x, y, t)$ accounts for the water depth; $H = H(x, y)$ for the known still water depth; η for the surface elevation and u and v for the depth averaged velocities in the x and y direction respectively.

In what follows, the Peregrine and the Madsen-Sørensen systems will be described. This systems will be described by (GF-2D) with U, F, B, $S, \mathcal{I}$ defined as in (SWE-2D). They only differ in the definition of the operator $\mathcal{T} \equiv \mathcal{T}(U, \nabla U, H, \nabla H)$.

Peregrine system (1967)

Let us start by introducing the pioneering system derived by Peregrine in [210] which is the dispersive system that has become the most popular. Equations of motion are derived

for long waves in water of varying depth. The equations are for small amplitude waves but do include non-linear terms. When a constant bathymetry is considered, they coincide with the Boussinesq equations [19].

The core of the general procedure to derive the Peregrine system and also in general, to derive a Boussinesq-type system can be summarized as follows (dimensionless variables used):

- Derivation from Euler equations, under the assumption of an irrotational flow:

$$(u, v, w) = \nabla\phi, \ \nabla^2\phi = 0,$$

  where (u, v, w) are the velocity components.

- Makes an asymptotic Taylor expansion and truncation of the potential flow:

$$\phi = \phi_{|b} - \frac{1}{2}(z - z_{|b})^2 \left[\partial_z^2\phi\right]_{|b} + \frac{1}{24}(z - z_{|b})^4 \left[\partial_z^4\phi\right]_{|b} + \ \cdots, \qquad (1.1.5)$$

  where the odd terms in the Taylor expansion are cancelled by using the assumption of irrotational flow.

- Assume the kinematic boundary conditions at the bottom and surface.

- Apply the established power series for the velocity potential in combination with the depth-integrated continuity and momentum equations (Peregrine) or kinematic and dynamic surface boundary conditions.

In the derivation, there are two important parameters associated with long waves. One is the ratio of amplitude to depth μ_1, and the other is the ratio of depth to wavelength μ_2. The Peregrine equations were derived under the assumptions of weakly non-linear weakly dispersive waves, that is

$$\mu_1 \ll 1, \ \mu_2 \approx \mu_1^2,$$

that corresponds to truncation up to second order in the asymptotic Taylor expansion introduced in (1.1.5). The system for two space dimensions can be written in the compact form (GF-2D) by setting in (SWE-2D) $\mathcal{T}$ as

$$\mathcal{T} = \begin{pmatrix} 0 \\ \mathcal{T}_{PER}(U, \nabla U, H, \nabla H) \end{pmatrix} = \begin{pmatrix} 0 \\ \frac{1}{2}H^2\partial_t\nabla\left(\nabla\cdot(H\boldsymbol{u})\right) - \frac{1}{6}H^3\partial_t\nabla\left(\nabla\cdot\boldsymbol{u}\right) \end{pmatrix}, \quad \text{(PER)}$$

where $\boldsymbol{u} = (u, v)$. For Boussinesq-type systems $\mathcal{I} = \boldsymbol{0}$, although it will shown that some of the studied Boussinesq-type systems can be rewritten as a non-hydrostatic pressure system via an incompressibility condition.

Madsen-Sørensen (1992)

Madsen and Sørensen derived a series of interesting papers on dispersive water waves modelling and procedures that later were assumed to be as standard in dispersive water waves modelling.

From the derivation of the Peregrine system, it is clear that a better description of dispersive waves can be achieved by considering a higher order truncation in (1.1.5). However, this leads to a complex system with sums and products of high order derivatives. Madsen and Sørensen, fully understanding this problem, found a smart approach for improving dispersive properties without increasing the order of the derivatives appearing in the momentum equation. In brief, they applied a linear operator

$$L = 1 + \epsilon^2 B H^2 \nabla(H)$$

to the Peregrine system, and they used as well as the linear long-wave approximation

$$\partial_t (h\boldsymbol{u}) + gH\nabla(\eta) \approx 0, \quad \boldsymbol{u} = (u, v)$$

which transforms time derivatives of $h\boldsymbol{u}$, $\boldsymbol{u}$ being the depth-averaged velocities, into spatial derivatives in the free surface η. Some higher derivatives and product of derivatives of the bottom are neglected (see details in [184]). Therefore, extra dispersive terms are obtained, proportional to the free-parameter B, which was chosen to match the $[2, 2]$ Padé approximation of the dispersion relation. These extra terms, however, only contained third-order derivatives such as the original weakly dispersive Peregrine system.

The system for two space dimensions can be written in the compact form (GF-2D) by setting in (SWE-2D) $\mathcal{T}$ as

$$\mathcal{T} = \begin{pmatrix} 0 \\ \mathcal{T}_{MS}(U, \nabla U, H, \nabla H) \end{pmatrix} = \begin{pmatrix} 0 \\ \varphi_1 \\ \varphi_2 \end{pmatrix}, \quad \mathcal{I} = \mathbf{0}, \quad \text{(MS)}$$

where

$$\varphi_1 = \frac{H}{3}\partial_t \left[(3B + 1) H (\partial_{xx}(hu) + \partial_{xy}(hv)) - \partial_x H \left(\partial_x(hu) + \frac{1}{2}\partial_y(hv) \right) - \partial_y H \frac{1}{2}\partial_x(hu) \right]$$

$$+ BgH^2 \left[H (\partial_{xxx}\eta + \partial_{xyy}\eta) + \partial_x H (2\partial_{xx}\eta + \partial_{yy}\eta) - \partial_y H \partial_{xy}\eta \right],$$

$$\varphi_2 = \frac{H}{3}\partial_t \left[(3B + 1) H (\partial_{yy}(hv) + \partial_{xy}(hu)) - \partial_y H \left(\partial_y(hv) + \frac{1}{2}\partial_x(hu) \right) - \partial_x H \frac{1}{2}\partial_y(hv) \right]$$

$$+ BgH^2 \left[H (\partial_{yyy}\eta + \partial_{xxy}\eta) + \partial_y H (2\partial_{yy}\eta + \partial_{xx}\eta) - \partial_x H \partial_{xy}\eta \right].$$

1.1.3   A first order formulation for Boussinesq-type systems

One of the main objectives of this dissertation was to deal with relatively simple PDE systems that can simulate dispersive water waves efficiently. As it can be seen the Boussinesq-type systems are, in the best-case scenario, systems that contain third order derivatives (∂_{xxt}). This will lead to complex numerical schemes, specially when high order derivatives appear in the governing equations. To avoid that, one of the efforts made during this thesis was to write some of the Boussinesq-system as an augmented first order PDE system.

In this subsection, a novel contribution is presented, up to our knowledge, on this dissertation: a procedure to express the equations derived by Peregrine as a first order system of PDEs. The same procedure can also be applied to other Boussinesq systems such as as [1], [184], among others. To illustrate this, let us consider the system (GF-2D) along with (PER) written as a new reformulated augmented first order PDE system

$$
\begin{cases}
\partial_t h + \partial_x \left(hu \right) + \partial_y \left(hv \right) = 0, \\[2mm]
\partial_t \left(hu \right) + \partial_x \left(hu^2 + \dfrac{1}{2}gh^2 + Hp_1 + Hp_2 \right) + \partial_y \left(huv \right) = \\[2mm]
\qquad\qquad\qquad\qquad\qquad \left(gh + 2p_1 + 3p_2 \right) \partial_x H - \tau_{b,x}, \\[2mm]
\partial_t \left(hv \right) + \partial_y \left(hv^2 + \dfrac{1}{2}gh^2 + Hp_1 + Hp_2 \right) + \partial_x \left(huv \right) = \\[2mm]
\qquad\qquad\qquad\qquad\qquad \left(gh + 2p_1 + 3p_2 \right) \partial_y H - \tau_{b,x}, \\[2mm]
\partial_t \left(Hw_1 \right) = 2p_1, \\[2mm]
\partial_t \left(Hw_2 \right) = 2p_1 + 3p_2, \\[2mm]
H\nabla \cdot \boldsymbol{u} + w_1 - w_b = 0, \\[2mm]
H\nabla \cdot \boldsymbol{u} + 2(w_2 - w_b) = 0
\end{cases}
\tag{1.1.6}
$$

$p_i,\ w_i,\ i = 1, 2$ being some arbitrary variables described later depending on

$$
\boldsymbol{u} = (u, v), \quad w_b = -\boldsymbol{u} \cdot \nabla H,
$$

and $\tau_{b,x},\ \tau_{b,y}$ accounts for the friction terms defined in (1.1.4).

Remark 1.1.1. *The considered PDE system* (1.1.6) *only contains first order derivatives as requested.*

Remark 1.1.2. *Attending to a dimensional analysis of the new auxiliary variables defined, it holds:*

$$[p_i] = \frac{m^2}{s^2}, \quad [w_i] = \frac{m}{s}, \quad i = 1, 2,$$

where $[f]$ represents the physical dimension of a given variable f. Thus, p_i can be interpreted as a non-hydrostatic pressure and w_i as a velocity for $i = 1, 2$.

In **Remark** 1.1.4 *a complete reinterpretation, as well as a comparison with other non-hydrostatic pressure systems, is carried out. This constitutes a link between one of the pioneering Boussinesq-type systems with modern non-hydrostatic pressure systems.*

1.1.4 Non-hydrostatic pressure systems. A multi layer approach

In this section one of the multi layer non-hydrostatic pressure models of the family introduced and described by Fernández-Nieto *et al.* in [124] is presented. The final model has some improvements concerning the Boussinesq systems. It is worth to mention that the multi layer approach leads to a first order PDE system. The governing equations satisfy an extra energy conservation law. This is a property that usual Boussinesq-type systems do not satisfy. Another feature to emphasize is that when the number of layer increases, the linear dispersion relation of the linear model converges to the same of Airy's theory. These properties and, in particular, the last one, make multi layer non-hydrostatic pressure systems an ideal framework to simulate dispersive water waves.

The governing equations of the multi layer pressure system derived in [124] are obtained after a process of depth averaging, similar to the derivation process of the shallow water equations. To improve the accuracy, non-material interfaces that separate the fluid into layers with different velocities and pressures are assumed. To do that, some hypothesis on the velocity and pressure profiles are supposed. This will leads to a hierarchy of multi layer systems, depending on the assumption of a linear or quadratic vertical profiles. The main procedure to derive the equations can be summarized as follows:

- The fluid domain is split in the vertical into L layers.

- The Euler equations are depth averaged within each layer.

- The total pressure is decomposed into a sum of hydrostatic and non-hydrostatic pressure.

- The horizontal velocity is assumed to have a piecewise constant vertical profile within each layer.
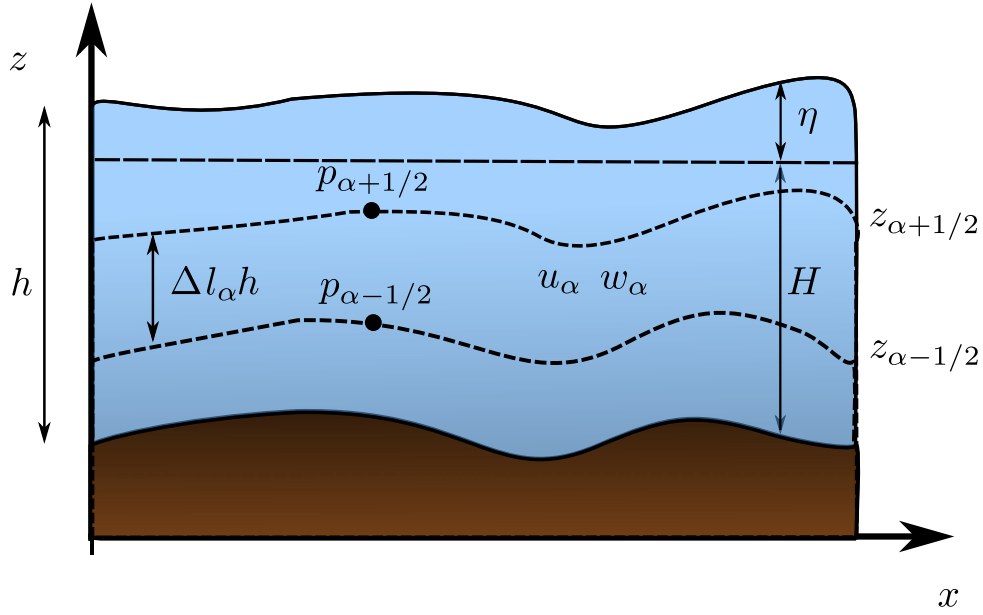
Figure 1.1: Schematic diagram describing the multi layer system

- Due to the above hypothesis on the horizontal velocity, the vertical velocity as well as the non-hydrostatic pressure has a piecewise linear vertical profile within each layer.

- Assume kinematic boundary conditions at the bottom and surface.

The derivation process can be found in [124]. Nevertheless, the derivation for the special case of two layers will be described in this thesis in Subsection 1.2. The governing equations for one-dimensional domains are described in the following.

Given a positive water height $h(x,t)$, it is considered a number of layers $L \geq 1$ and a convex combination $(l_\alpha)_{1 \leq \alpha \leq L}$ such that

$$l_\alpha \in [0,1], \ \sum_{\alpha=1}^{L} l_\alpha = 1.$$

Then it is defined

$$h_\alpha(x,t) = l_\alpha h(x,t) \implies h = \sum_{\alpha=1}^{L} h_\alpha.$$

As depicted on Figure 1.1, the flow is split along the vertical axis into $L \geq 1$ layers denoted by

$$\mathcal{L}_\alpha(x,t) = \left\{ z : z_{\alpha-1/2}(x,t) \leq z \leq z_{\alpha+1/2}(x,t) \right\}, \ \alpha \in \{1,\dots,L\}$$

where

$$z_{\alpha+1/2} = -H + \sum_{\beta=1}^{\alpha} h_\beta,$$

$H(x,t)$ being the bathymetry that can vary in space and time, so that

$$-H = z_{1/2} < z_{3/2} < \ldots < z_{L+1/2} = \eta = h - H, \quad h_\alpha(x,t) = z_{\alpha+1/2}(x,t) - z_{\alpha-1/2}(x,t),$$

where η is the unknown water surface elevation. For the sake of clarity, middle points of layer $\mathcal{L}_\alpha$ are denoted by

$$z_\alpha = \frac{z_{\alpha+1/2} + z_{\alpha-1/2}}{2}.$$

It is shown in [124] that the values of the variables u, w and p, at the virtual interface $z_{\alpha+1/2}$ are given by

$$u_{\alpha+1/2} = \frac{u_\alpha + u_{\alpha+1}}{2}, \quad w_{\alpha+1/2} = \frac{w_\alpha + w_{\alpha+1}}{2}, \quad p_{\alpha+1/2} = \frac{p_\alpha + p_{\alpha+1}}{2}.$$

For a given function $(x, z, t) \to f(x, z, t)$, in the case that it is discontinuous at the interface $z_{\alpha+1/2}$, let us denote

$$f_{\alpha+1/2}^+(x,t) = \lim_{\substack{z \to z_{\alpha+1/2}(x,t) \\ z > z_{\alpha+1/2}(x,t)}} f(x, z, t), \qquad f_{\alpha+1/2}^-(x,t) = \lim_{\substack{z \to z_{\alpha+1/2}(x,t) \\ z < z_{\alpha+1/2}(x,t)}} f(x, z, t),$$

as well as $f_b \equiv f(x, -H(x,t), t), \; f_\eta(x,t) \equiv f(x, \eta(x,t), t)$.

The governing equations for $\alpha \in \{1, \ldots, L\}$ reads

$$\begin{cases} \partial_t h + \partial_x(h\bar{u}) = 0, \; \bar{u} = \sum_{\alpha=1}^{L} l_\alpha u_\alpha, \\[2ex] \partial_t(h_\alpha u_\alpha) + \partial_x(h_\alpha u_\alpha^2 + \frac{1}{2}gh_\alpha^2 + h_\alpha p_\alpha) + u_{\alpha+1/2}\Gamma_{\alpha+1/2} - u_{\alpha-1/2}\Gamma_{\alpha-1/2} \\[2ex] \qquad\qquad + \partial_x z_{\alpha-1/2}p_{\alpha-1/2} - \partial_x z_{\alpha+1/2}p_{\alpha+1/2} = gh_\alpha \partial_x H \\[2ex] \partial_t(h_\alpha w_\alpha) + \partial_x(h_\alpha u_\alpha w_\alpha) + w_{\alpha+1/2}\Gamma_{\alpha+1/2} - w_{\alpha-1/2}\Gamma_{\alpha-1/2} = p_{\alpha-1/2} - p_{\alpha+1/2}, \\[2ex] \partial_x u_{\alpha+} \dfrac{w_{\alpha+1/2}^- - w_\alpha}{h_\alpha/2} = 0, \\[2ex] w_{\alpha+1/2}^+ + \partial_t H - u_{\alpha+1}\partial_x z_{\alpha+1/2} + \sum_{\beta=1}^{\alpha} \partial_x(h_\beta u_\beta) = 0, \end{cases}$$

$$\text{(NH-L)}$$

where u_α, w_α and p_α are the horizontal and vertical depth averaged velocities as well as the depth-averaged non-hydrostatic pressure respectively at the layer $\mathcal{L}_\alpha(x,t)$.

Note that

$$w^+_{\alpha+1/2} - w^-_{\alpha+1/2} = \partial_x z_{\alpha+1/2} \left(u_{\alpha+1} - u_\alpha \right),$$

is a jump condition that a weak solution which is discontinuous at $z = z_{\alpha+1/2}(x,t)$ must verify. The hypothesis on the total pressure of vanishing at the free surface as well as the kinematic boundary condition at the free surface leads to

$$p_{L+1/2} = 0, \quad w^-_{L+1/2} = \partial_t \eta + u_L \partial_x \eta.$$

Terms $\Gamma_{\alpha\pm1/2}$ accounts for mass transfer and appears as a contribution of the surface integral during the depth averaging process:

$$\Gamma_{\alpha+1/2} = \sum_{\beta=\alpha+1}^{L} \partial_x \left(h_\beta(u_\beta - \bar{u}) \right).$$

The last two equations describe some extra conditions that transcribe the free divergence constraint.

The governing PDE satisfies an extra energy conservation law. Let us denote the mechanical energy to the semi-discrete level

$$E_\alpha = h_\alpha \frac{u_\alpha^2 + w_\alpha^2}{2} + g h_\alpha z_\alpha.$$

If $(h, u_\alpha, w_\alpha, p_\alpha)$ are smooth solutions to (NH-L), then it holds

$$\partial_t \sum_{\alpha=1}^{L} E_\alpha + \partial_x \left(\sum_{\alpha=1}^{L} u_\alpha \left(E_\alpha + g h_\alpha \left(\eta - z_\alpha \right) + h_\alpha p_\alpha \right) \right) = \left(gh + p_{1/2} \right) \partial_t H.$$

1.1.5 One layer non-hydrostatic pressure systems

The multi layer pressure system introduced above has some attractive mathematical properties concerning with the linear dispersion relations. As it was mentioned, it can be shown that when the number of layers tends to infinity, the celerity or phase speed dispersion relation converges to the one given by the linear theory. However, in practice and when the system is applied to simulate complex events that include large computational domains, the computational time grow too quickly when considering 3 or more layers.

Following the spirit of this dissertation of considering relatively simple systems to simulate dispersive water waves, some special cases will be examined. The first one is related to the case of considering one layer, that corresponds to the system deduced in [21] by Sainte-Marie *et al.* firstly. After, a simplification of this one layer system derived in [259] by Yamazaki *et al.* is considered. This system, which is relatively simple will be one of the non-hydrostatic pressure systems that have been discretized and validated along this dissertation in the subsequent chapters.

The one layer case (Sainte-Marie *et al.*)

A special case of the previously described multi layer non-hydrostatic pressure is when the number of layers is set to one. This is the case of the non-hydrostatic pressure system that was derived previously by Sainte-Marie *et al.* in [21]. The governing equations for one space dimension read

$$
\begin{cases}
\partial_t h + \partial_x \left(hu \right) = 0, \\[2ex]
\partial_t \left(hu \right) + \partial_x \left(hu^2 + \dfrac{1}{2}gh^2 + hp \right) = \left(gh + p_b \right) \partial_x H - \tau_b, \\[2ex]
\partial_t \left(hw \right) + \partial_x \left(uhw \right) = p_b, \quad p_b = 2p, \\[2ex]
\partial_x u + \dfrac{w - w_b}{h/2} = 0, \quad w_b = -\partial_t H - u\partial_x H,
\end{cases}
$$

where $h = h(x,t)$ is the water depth and $H = H(x)$ is the known still water depth. The surface elevation measured from the still-water level is denoted by $\eta = h - H$. Furthermore, t denotes time, g is the gravitational acceleration; u is the depth averaged velocity in the x direction; w is the depth averaged vertical velocity; w_b denotes the vertical velocity at the bottom that it was obtained from a no-penetration boundary condition and takes into account the dependence on time of the bathymetry H. τ_b denotes the friction with the bottom given by (1.1.1). Finally p denotes the depth averaged non-hydrostatic pressure and p_b denotes the non-hydrostatic pressure at the bottom. Note that in the vertical direction, the following relation holds

$$
p_b = 2p.
$$

This system can be written in the general compact form (GF), defining

$$
U = \begin{pmatrix} h \\ q_u \\ q_w \end{pmatrix}, \quad F(U) = \begin{pmatrix} q \\ \dfrac{q^2}{h} + \dfrac{1}{2}gh^2 \\ \dfrac{q_u q_w}{h} \end{pmatrix}, \quad G(U) = \begin{pmatrix} 0 \\ gh \\ 0 \end{pmatrix},
$$

$$
S(U) = - \begin{pmatrix} 0 \\ \tau_b \\ 0 \end{pmatrix}, \quad B(U) = \mathbf{0},
\tag{NH-1L}
$$

$$
\mathcal{T}(U, \partial_x U, p, \partial_x p, H, \partial_x H) = - \begin{pmatrix} 0 \\ h\partial_x p + p\partial_x\,(2\eta - h) \\ -2p \end{pmatrix},
$$

$$
\mathcal{I}(U, \partial_x U, H, \partial_x H) = h\partial_x q_u - q_u \partial_x\,(2\eta - h) + 2q_w + 2h\partial_t H,
$$

$q_u = hu$, $q_w = hw$ being the horizontal and vertical discharges respectively. The incompressibility condition $\mathcal{I}$ has been multiplied by h^2 in order to express the system in terms of the conserved quantities h, q_u and q_w.

A simplified one layer non-hydrostatic pressure system (Yamazaki *et al.*)

Under a similar hypothesis to the one assumed by Sainte-Marie *et al.* in [21], Yamazaki *et al.* derived in [259] a relatively simple non-hydrostatic pressure system. The equations are derived after a process of depth averaging from the Euler equations. Thus, a linear vertical profile is assumed for the non-hydrostatic pressure and vertical velocity, as well as a constant vertical profile for the horizontal velocity. The difference resides in a simplification carried out with the convective terms on the vertical velocity equation which are neglected. Thus a simpler system arises. This simplified system has been numerically solved in [112] (see Subsections 3.1 and 3.2), and validated through laboratory and field experiments in [157],[182] (See Chapter 4).

The governing equations for one space dimensions of the system derived in [259] read

$$
\begin{cases}
\partial_t h + \partial_x (hu) = 0, \\[2mm]
\partial_t (hu) + \partial_x \left(hu^2 + \dfrac{1}{2} gh^2 + hp \right) = (gh + p_b) \partial_x H - \tau_b, \\[2mm]
\partial_t w = \dfrac{p_b}{h}, \quad p_b = 2p, \\[2mm]
\partial_x u + \dfrac{w - w_b}{h/2} = 0, \quad w_b = -\partial_t H - u \partial_x H,
\end{cases}
$$

whereas in the description of the variables of the system (NH-1L), $h = h(x,t)$ is the water depth and $H = H(x)$ is the known still water depth. $\eta = h - H$ denotes the surface elevation measured from the still-water level. Furthermore, t denotes time, g is the gravitational acceleration; u is the depth averaged velocity in the x direction; w is the depth averaged vertical velocity; w_b denotes the vertical velocity at the bottom that it was obtained from a no-penetration boundary condition and takes into account the dependence on time of the bathymetry H. τ_b denotes the friction with the bottom given by (1.1.1). Finally p denotes the depth averaged non-hydrostatic pressure and p_b denotes the non-hydrostatic pressure at the bottom. Note that in the vertical direction, the following relation holds

$$
p_b = 2p.
$$

This system is of interest due to its simplicity on the vertical velocity equations. In this thesis, this PDE system is considered and discretized on a staggered mesh for the vertical velocity as well as for the non-hydrostatic pressure in Subsections 3.1 and 3.2. Due to that, although this system can be written as in the general formulation (GF) and in a similar manner as in (NH-1L), it is convenient to introduce the following rewriting of the system:

$$
\begin{cases}
\partial_t U + \partial_x F(U) = G(U)\partial_x H + S(U) + \\[2mm]
\qquad\qquad\qquad\qquad + \mathcal{T}(U, \partial_x U, p, \partial_x p, H, \partial_x H), \\[2mm]
\partial_t w = 2\dfrac{p}{h}, \\[2mm]
\mathcal{I}(U, \partial_x U, H, \partial_x H, w) = 0,
\end{cases}
\qquad \text{(YAM)}
$$

where

$$U = \begin{pmatrix} h \\ q \end{pmatrix}, \quad F(U) = \begin{pmatrix} hu \\ \dfrac{q^2}{h} + \dfrac{1}{2}gh^2 \end{pmatrix}, \quad G(U) = \begin{pmatrix} 0 \\ gh \end{pmatrix},$$

$$S(U) = - \begin{pmatrix} 0 \\ \tau_b \end{pmatrix}, \quad \mathcal{T}(U, \partial_x U, p, \partial_x p, H, \partial_x H) = - \begin{pmatrix} 0 \\ h\partial_x p + p\partial_x (2\eta - h) \end{pmatrix},$$

$$\mathcal{I}(U, \partial_x U, H, \partial_x H, w) = h\partial_x q - q\partial_x (2\eta - h) + 2hw + 2h\partial_t H,$$

and $q = hu$ denotes the discharge.

Remark 1.1.3. *Let us notice that the vertical momentum equation of the system* (YAM)

$$\partial_t w = \frac{p_b}{h},$$

can be written by using the mass equation $\partial_t h + \partial_x (hu) = 0$, *as follows*

$$\partial_t (hw) + \partial_x (uhw) = \frac{p_b}{h} + hu\partial_x w,$$

and thus, the system (YAM) *can be written as*

$$\begin{cases} \partial_t h + \partial_x (hu) = 0, \\\\ \partial_t (hu) + \partial_x \left(hu^2 + \dfrac{1}{2}gh^2 + hp \right) = (gh + p_b)\,\partial_x H - \tau_b, \\\\ \partial_t (hw) + \partial_x (uhw) = \dfrac{p_b}{h} + hu\partial_x w, \quad p_b = 2p, \\\\ \partial_x u + \dfrac{w - w_b}{h/2} = 0, \quad w_b = -\partial_t H - u\partial_x H, \end{cases} \tag{1.1.7}$$

Energy balance of the systems

Similar to the multi layer non-hydrostatic pressure system described in Subsection 1.1.4, an extra balance law related to the conservation of the energy is verified. The smooth solutions (h, u, w, p) of (NH-1L) satisfy the additional balance law

$$\partial_t E + \partial_x \left(u \left(E + gh^2 + hp \right) \right) = (gh + p_b)\,\partial_t H - u\tau_b, \tag{1.1.8}$$

where

$$E = h\frac{u^2 + w^2}{2} + gh\frac{\eta - H}{2} \tag{1.1.9}$$

is the mechanical energy. In absence of friction with the bottom as well as for $\partial_t H = 0$, the above balance law becomes a new conservation law for the smooth solutions of the system.

On the contrary, due to the simplification made with the convective terms during the derivation of the system (YAM), then it holds

$$\partial_t E + \partial_x \left(u \left(E + gh^2 + hp \right) \right) = \left(gh + p_b \right) \partial_t H - u\tau_b + huw\partial_x w, \tag{1.1.10}$$

where E is defined as in (1.1.9). Thus, it can not be found a similar extra energy conservation law for the system (YAM) in absence of friction and for $\partial_t H = 0$.

Eigenstructure of the underlying hydrostatic system

Let us define for the systems (NH-1L) and (YAM) the underlying hydrostatic system that results from removing the non-hydrostatic contribution $\mathcal{T}$ along with the incompressibility condition $\mathcal{I}$. It is easy to check that both hydrostatic systems coincide with the system (SWE) previously defined. Thus, the underlying hydrostatic system for both non-hydrostatic pressure systems coincides and is strictly hyperbolic (see Section 1.1.1).

Governing equations in two space dimensions of the system (YAM)

The extension of the system (YAM) for bidimensional domains can be written as

$$\begin{cases} \partial_t U + \nabla \cdot \boldsymbol{F}(U) = \boldsymbol{G}(U) \cdot \nabla(H) + S(U) + \\ \qquad\qquad\qquad + \mathcal{T}(U, \nabla U, p, \nabla p, H, \nabla H), \\ \partial_t w = 2\dfrac{p}{h}, \\ \\ \mathcal{I}(U, \nabla U, H, \nabla H, w) = 0, \end{cases} \tag{YAM-2D}$$

where

$$
U = \begin{pmatrix} h \\ q_x \\ q_y \end{pmatrix}, \quad F_1(U) = \begin{pmatrix} q_x \\ \dfrac{q_x^2}{h} + \dfrac{1}{2}gh^2 \\ \dfrac{q_x q_y}{h} \end{pmatrix}, \quad F_2(U) = \begin{pmatrix} q_y \\ \dfrac{q_x q_y}{h} \\ \dfrac{q_y^2}{h} + \dfrac{1}{2}gh^2 \end{pmatrix},
$$

$$
G_1(U) = \begin{pmatrix} 0 \\ gh \\ 0 \end{pmatrix}, \quad G_2(U) = \begin{pmatrix} 0 \\ 0 \\ gh \end{pmatrix}, \quad S(U) = -\begin{pmatrix} 0 \\ \tau_{b,x} \\ \tau_{b,y} \end{pmatrix}
$$

$$
\mathcal{T}(U, \nabla(U), H, \nabla(H)) = -\begin{pmatrix} 0 \\ h\partial_x p + p\partial_x (2\eta - h) \\ h\partial_y p + p\partial_y (2\eta - h) \end{pmatrix}
$$

$$
\mathcal{I}(U, \nabla U, H, \nabla H, w) = h\nabla \cdot \boldsymbol{q} - \boldsymbol{q} \cdot \nabla (2\eta - h) + 2hw + 2h\partial_t H, \quad \boldsymbol{q} = (q_x, q_y).
$$

$q_x = hu$, $q_y = hv$ being the discharges and $\tau_{b,x}$, $\tau_{b,y}$ account for the friction terms defined in (1.1.4).

Remark 1.1.4. *Let us assume in the rewriting of the Peregrine system as a first order PDE system (1.1.6) a flat bottom. Then one has*

$$
w_1 = 2w_2, \quad p_1 = -3p_2,
$$

and let us define

$$
w := w_2, \quad p := -2p_2.
$$

Then the system reduces to

$$
\begin{cases}
\partial_t h + \partial_x \left(hu \right) + \partial_y \left(hv \right) = 0, \\[2mm]
\partial_t \left(hu \right) + \partial_x \left(hu^2 + \frac{1}{2}gh^2 + Hp \right) + \partial_y \left(huv \right) = -\tau_{b,x}, \\[2mm]
\partial_t \left(hv \right) + \partial_y \left(hv^2 + \frac{1}{2}gh^2 + Hp \right) + \partial_x \left(huv \right) = -\tau_{b,y}, \\[2mm]
H \partial_t \left(w \right) = \frac{3}{2}p, \\[2mm]
H \nabla \cdot \boldsymbol{u} + 2w = 0.
\end{cases}
$$

Replacing H by h in the third and fourth equations of the above system, it yields

$$
\begin{cases}
\partial_t h + \partial_x \left(hu \right) + \partial_y \left(hv \right) = 0, \\[2mm]
\partial_t \left(hu \right) + \partial_x \left(hu^2 + \frac{1}{2}gh^2 + Hp \right) + \partial_y \left(huv \right) = -\tau_{b,x}, \\[2mm]
\partial_t \left(hv \right) + \partial_y \left(hv^2 + \frac{1}{2}gh^2 + Hp \right) + \partial_x \left(huv \right) = -\tau_{b,y}, \\[2mm]
\partial_t \left(w \right) = \frac{3}{2}\frac{p}{h}, \\[2mm]
h \nabla \cdot \boldsymbol{u} + 2w = 0.
\end{cases}
\qquad (1.1.11)
$$

Let us reinterpret w and p in (1.1.11) as the depth integrated vertical velocity and the depth-integrated non-hydrostatic pressure by similitude with system (YAM-2D). Also, let us reinterpret $\frac{3}{2}p$ as the non-hydrostatic pressure at the bottom. Thus, the system (1.1.11) only differs from the system (YAM-2D) on the relation between the non-hydrostatic pressure at the bottom and its depth-averaged value which is:

$$
p_b = \frac{3}{2}p.
$$

Moreover, by substituting the vertical velocity equation in (1.1.11)

$$
\partial_t w = \frac{3}{2}\frac{p}{h}
$$

by

$$\partial_t (hw) + \partial_x(uhw) + \partial_y(vhw) = \frac{3}{2}p$$

then the system coincides with the Green-Naghdi system for flat bottom, that was firstly written as a non-hydrostatic pressure system in [21]. It can be proved that the Serre-Green-Naghdi system satisfies an energy conservation law given by:

$$\partial_t E + \partial_x \left(u \left(E + gh^2 + hp \right) \right) + \partial_y \left(v \left(E + gh^2 + hp \right) \right) = 0,$$

where

$$E = h\frac{u^2 + v^2 + \frac{2}{3}w^2}{2} + gh\frac{\eta - H}{2}$$

is the mechanical energy.

Thus, this procedure of converting the Boussinesq-type system of Peregine into a non-hydrostatic pressure system can be seen as a way to improve the mathematical properties of the Peregine system, since an energy conservation law can be fulfilled when $\nabla H = 0$, and to reduce the order of derivatives, since it is written as a first order PDE system. Furthermore, a link between one of the most popular Boussinesq-type systems and the non-hydrostatic pressure modelling framework has been established.

1.1.6   Linear dispersion relation

In this subsection, the main concepts concerning the dispersive relations of PDE systems are presented. In particular, the linear dispersion relation of the phase velocity, the group velocity, and the linear shoaling. This constitutes a standard study of PDE systems for dispersive water waves modelling. The two first properties are related to the propagation of dispersive wave trains, and the latter with shoaling processes. This can occur when waves arrive at the continental shelf, from intermediate to shallow waters.

To obtain the linear dispersion properties of the systems studied during this dissertation, the equations are linearised around the lake at rest steady state solution. An asymptotic expansion

$$f = f^{(0)} + \epsilon f^{(1)} + \mathcal{O}(\epsilon^2), \tag{1.1.12}$$

is considered, where f denotes a generic variable of the system. The resulting linearised model for the perturbations, which is obtained after neglecting $\mathcal{O}(\epsilon^2)$ terms, is considered. After that, A Stokes-type Fourier analysis is carried out looking for first-order solutions of the form

$$f(x,t) = f_0 e^{i(\omega t - kx)}, \tag{1.1.13}$$

where ω is the angular frequency and k is the local wave-number. Since the resulting system is linear, it is possible to find an exact non-trivial solution. This constitutes an standard procedure to study systems that model dispersive water wavers (see [176], [184], [226]).

Phase velocity

The phase velocity of a wave is the rate at which the phase of the wave propagates in space. This is the velocity at which the phase of any one frequency component of the wave travels. For such a component, any given phase of the wave (for example, the crest) will appear to travel at the phase velocity. The phase velocity is defined as $C = \omega/k$. Following the process detailed above, the phase velocity can be obtained for any given PDE system studied in this dissertation. It can be compared to the exact phase velocity given by the linear theory (Airy wave theory):

$$C_{Airy}^2 = gH \frac{\tanh(kH)}{kH}, \tag{1.1.14}$$

where k denotes the local wave-number.

Group velocity

The group velocity of a wave is the velocity with which the overall shape of the wave's amplitudes (known as the modulation or envelope of the wave) propagates through space. The group velocity is obtained essentially taking the derivative concerning the wave-number k from the linear dispersion relation

$$G_{Airy} = C_{Airy} + k\partial_k C_{Airy},$$

and a reference formula can also be obtained

$$G_{Airy} = \frac{1}{2}\left(1 + \frac{2kH}{\sinh(2kH)}\right)C_{Airy}. \tag{1.1.15}$$

Linear shoaling

Madsen & Sørensen introduced the linear shoaling gradient γ as another quantity to measure the applicability of Boussinesq equations (see [184]):

$$\frac{\partial_x \eta}{\eta} = -\gamma \frac{\partial_x H}{H}.$$

Here the shoaling gradient γ is a function of the wave number k and H and it relates the effect of compactness or shoaling that waves suffers when approaching to the coast. The shoaling gradient γ can be determined using the concept of the constancy of the energy flux, which is a valid assumption before of the breaking of the wave:

$$\partial_x \left(\eta^2 C_g\right) = 0,$$

and thus,

$$\frac{\partial_x \eta}{\eta} = -\frac{1}{2}\frac{\partial_x C_g}{C_g}.$$

Given the group velocity, it can be seen that

$$\frac{\partial_x C_g}{C_g} = S_1 \frac{\partial_x(kH)}{kH}$$

where S_1 is a function to be determined such that the equality holds. Taking the derivative of the dispersive relation with respect to x gives

$$\frac{\partial_x k}{k} = S_2 \frac{\partial_x H}{H},$$

where, again, S_2 is another function to be determined. Finally, the linear shoaling gradient of a given system under consideration is given by:

$$\gamma = \frac{1}{2} S_1 \left(1 + S_2\right).$$

Again, a reference formula can be obtained from the linear theory, which is given by:

$$\gamma_{Airy} = kH \tanh(kH) \frac{\left(1 - kH \tanh(kH)\right)\left(1 - \tanh^2(kH)\right)}{\left(\tanh(kH) + kH\left(1 - \tanh^2(kH)\right)\right)^2}. \tag{1.1.16}$$

1.2 A novel two layer non-hydrostatic system with enhanced dispersive properties

In [118] a new two layer-averaged system derived from Euler equations was considered by C. Escalante *et al.* In this work a two layer depth-integrated non-hydrostatic system is proposed with improved dispersion relations. This improvement is obtained employing three free parameters: two of them related to the representation of the pressure at the interface and a third one that controls the relative position of the interface concerning the total height. These parameters are then optimized to improve the dispersive properties of the resulting system. The optimized model shows good linear wave characteristics up to $kH \approx 10$, that can be improved for long waves. The central hypothesis for the derivation is the assumption of a constant vertical profile of the horizontal velocity within each layer. This corresponds to the assumption of a shallow water regime as it is usual when deriving non-hydrostatic multi layer systems.

The proposed two layer system can be seen as a modification of one of the models presented in [124] with a correction in the non-hydrostatic pressure profile. This will lead to a system that improves the main dispersive properties of the other two layer non-hydrostatic pressure systems proposed in the literature (see for instance [71]). Moreover, it improves the dispersive properties of some multi layer systems with 5 layers (see for instance [10]). It is worth mentioning that the resulting system is a model which is less expensive from the computational point of view while keeping good dispersive relations.

Thus, the final model can be applied to intermediate waters for a wide range of waves for a kH up to 10.

In the subsequent subsection, part of the work carried out in [118] is described: the derivation of the subsequent system as well as the mathematical study concerning to the dispersive properties; the study on the hyperbolicity of an underlying part of the final system.

1.2.1   Derivation of the system

This model is obtained by setting a non-material interface that separates two layers with different velocity and pressure. In the deduction of the equations, it is assumed that the horizontal velocity has a piecewise constant vertical profile, by while the vertical velocity and the non-hydrostatic counterpart pressure are piecewise linear, the three unknowns being discontinuous at the interface. For the sake of clarity, the equations are deduced for one-dimensional horizontal domains, although a similar process can be followed for two space dimensions.

The Euler system restricted to the (x, z) plane reads

$$
\begin{cases}
\partial_x u + \partial_z w = 0, & \text{(1.2.1a)} \\[2mm]
\partial_t u + \partial_x \left(u^2 + p_T \right) + \partial_z \left(uw \right) = 0, & \text{(1.2.1b)} \\[2mm]
\partial_t w + \partial_x \left(uw \right) + \partial_z \left(w^2 + p_T \right) = -g, & \text{(1.2.1c)}
\end{cases}
$$

where x and z denote the horizontal Ox and the vertical Oz axis respectively. This system is considered for

$$t > t_0, \ x \in \mathbb{R}, \ -H(x,t) \leq z \leq \eta(x,t),$$

where η is the unknown water elevation, H is the bathymetry that can vary in space and time, u and w are the horizontal and vertical velocities. The water height is $h = \eta + H$. The model is completed with boundary conditions at the free surface

$$
\begin{cases}
\partial_t \eta(x,t) + u(x, \eta(x,t), t) \partial_x \eta(x,t) - w(x, \eta(x,t), t) = 0, & \text{(1.2.2a)} \\[2mm]
p_T((x, \eta(x,t), t)) = p^{atm}, & \text{(1.2.2b)}
\end{cases}
$$

where p^{atm} is the atmospheric pressure. At the bottom, no-penetration boundary condition is imposed

$$u(x, -H(x,t), t) \partial_x H + w(x, -H(x,t), t) + \partial_t H = 0. \tag{1.2.3}$$

The total pressure p_T is supposed to be decomposed into a sum of a hydrostatic and non-hydrostatic part:

$$p_T = p^{atm} + g(\eta - z) + p \tag{1.2.4}$$

where $p(x, z, t)$ is the non-hydrostatic pressure. Hereinafter, the atmospheric pressure will be supposed to be zero and the non-hydrostatic pressure is assumed to vanish at the free surface

$$p(x, \eta(x,t), t) = 0. \qquad (1.2.5)$$

Given a positive water height $h(x,t)$, $l_1, l_2 \in [0,1]$ are considered such that $l_1 + l_2 = 1$, and the fluid is decomposed along the vertical axis into two virtual layers of height

$$h_\alpha = l_\alpha h, \ \alpha = 1, 2.$$

In what follows, $\alpha = 1$ stands for the lower layer and $\alpha = 2$ for the upper one (see Figure 1.2). Let us denote

$$\mathcal{L}_1(x,t) = \{z : -H(x,t) \le z \le z_I(x,t)\}, \ \mathcal{L}_2(x,t) = \{z : z_I(x,t) \le z \le \eta(x,t)\},$$

where $z_I(x,t) = h_1 - H$. z_α will denote the level of the middle point of the layers:

$$z_1(x,t) = \frac{z_I - H}{2}, \qquad z_2(x,t) = \frac{z_I + \eta}{2}.$$

For a given function $(x, z, t) \to f(x, z, t)$, let us denote

$$f_{I^+}(x,t) = \lim_{\substack{z \to z_I(x,t) \\ z > z_I(x,t)}} f(x,z,t), \qquad f_{I^-}(x,t) = \lim_{\substack{z \to z_I(x,t) \\ z < z_I(x,t)}} f(x,z,t),$$

as well as $f_b \equiv f(x, -H(x,t), t)$, $f_\eta(x,t) \equiv f(x, \eta(x,t), t)$.

As it was mentioned before, to derive the model a given vertical profile on the unknowns of the problem is assumed. First, a piecewise constant profile of the horizontal velocity is considered. Denoting $u_1(x,t)$ and $u_2(x,t)$ the horizontal velocities at layers $\mathcal{L}_1(x,t)$ and $\mathcal{L}_2(x,t)$, respectively. This is the main hypothesis for the derivation of the model, which corresponds to a shallow water regime. In fact, taking $p = 0$ in (1.2.4) and $l_1 = 1$, the SWE can be deduced in the same way.

From previous assumption and the incompressibility condition (1.2.1a), the vertical velocity has a piecewise linear profile. Let us recall that, using the notation introduced before, its limits at the interface level $z = z_I(x,t)$ are denoted by $w_{I^\pm}$. The vertical velocity at the bottom and the free surface are denoted by w_b and w_η, respectively.

Finally, a piecewise linear profile of the non-hydrostatic pressure is also considered. Thus, it can be determined from atmospheric pressure value, which is supposed to be zero, and its limits at the interface or bottom. Thus $p_\eta = 0$, and denote its limits at the interface level $z = z_I(x,t)$ by $p_{I^\pm}$, and the pressure at the bottom, $p_b(x,t)$. It is also denoted by $p_1(x,t)$ and $p_2(x,t)$ the non-hydrostatic pressure part evaluated at the middle level of the corresponding layer, that is,

$$p_1(x,t) = p(x, z_1(x,t), t), \qquad p_2(x,t) = p(x, z_2(x,t), t).$$
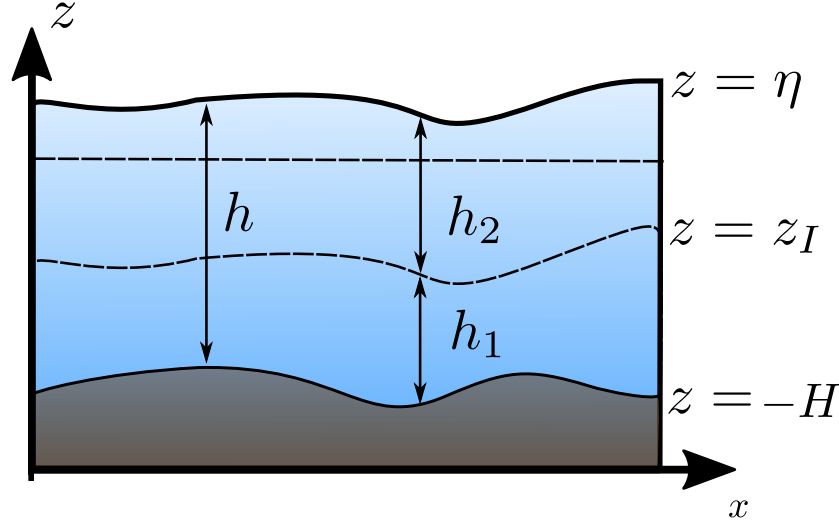
Figure 1.2: Bilayer setting

From the incompressibility condition (1.2.1a), a weak solution which is discontinuous at $z = z_I(x,t)$ must verify the following jump condition (see [121], [124])

$$w_{I+} - w_{I-} = (u_2 - u_1)\,\partial_x z_I. \tag{1.2.6}$$

Let us denote by w_1 and w_2 the vertical velocity at the middle level of the corresponding layer, that is,

$$w_1(x,t) = w(x, z_1(x,t), t), \qquad w_2(x,t) = w(x, z_2(x,t), t).$$

Then, the incompressibility condition (1.2.1a) inside each layer reads,

$$\begin{cases} \partial_x u_1 + 2\dfrac{w_1 - w_b}{h_1} = 0, & \text{(1.2.7a)} \\[3mm] \partial_x u_2 + 2\dfrac{w_2 - w_{I+}}{h_2} = 0. & \text{(1.2.7b)} \end{cases}$$

The integration over each layer of the incompressibility equation (1.2.1a), combined with conditions (1.2.2a), (1.2.3), gives the mass equations at each layer,

$$\begin{cases} \partial_t h_1 + \partial_x (h_1 u_1) = -\left(w_{I-} - (\partial_t z_I + u_1 \partial_x z_I)\right), & \text{(1.2.8a)} \\[3mm] \partial_t h_2 + \partial_x (h_2 u_2) = \left(w_{I+} - (\partial_t z_I + u_2 \partial_x z_I)\right). & \text{(1.2.8b)} \end{cases}$$

Let us define

$$\begin{cases} \Gamma_{I-} = w_{I-} - \partial_t z_I - u_1 \partial_x z_I, \\[3mm] \Gamma_{I+} = w_{I+} - \partial_t z_I - u_2 \partial_x z_I. \end{cases}$$

Using the jump condition (1.2.6), $\Gamma_{I^+} = \Gamma_{I^-}$ and it is defined

$$\Gamma_I = \frac{w_{I^+} + w_{I^-}}{2} - \partial_t z_I - \frac{u_1 + u_2}{2} \partial_x z_I.$$

Then equation (1.2.8) becomes

$$\begin{cases} \partial_t h_1 + \partial_x (h_1 u_1) = -\Gamma_I, & \text{(1.2.9a)} \\[2mm] \partial_t h_2 + \partial_x (h_2 u_2) = \Gamma_I. & \text{(1.2.9b)} \end{cases}$$

Thus, Γ_I can be interpreted as an approximation of the mass transfer across the interface z_I. Moreover, by combining equations (1.2.9a) and (1.2.9b) is obtained:

$$\Gamma_I = l_1 \partial_x (h_2 u_2) - l_2 \partial_x (h_1 u_1). \tag{1.2.10}$$

Following the procedure described in [124], and taking into account the piecewise linear discontinuous profile of non-hydrostatic pressure, the following horizontal momentum equations are obtained

$$\partial_x (h_1 u_1) + \partial_x (h_1 u_1^2 + h_1 p_1) + \frac{u_1 + u_2}{2} \Gamma_I - p_b \partial_x H - p_{I^-} \partial_x z_I = -g h_1 \partial_x \eta. \tag{1.2.11}$$

$$\partial_x (h_2 u_2) + \partial_x (h_2 u_2^2 + h_2 p_2) - \frac{u_1 + u_2}{2} \Gamma_I + p_{I^+} \partial_x z_I = -g h_2 \partial_x \eta. \tag{1.2.12}$$

Note that the gradients of p_1 and p_2 appear because the assumption of the linear profile for the pressure inside each layer. The following vertical momentum equations are also deduced,

$$\partial_x (h_1 w_1) + \partial_x (h_1 u_1 w_1) + \frac{w_1 + w_2}{2} \Gamma_I + p_{I^-} - p_b = 0. \tag{1.2.13}$$

$$\partial_x (h_2 w_2) + \partial_x (h_2 u_2 w_2) - \frac{w_1 + w_2}{2} \Gamma_I - p_{I^+} = 0. \tag{1.2.14}$$

In this work the unknowns are

$$p_b \text{ and } p_I := p_{I^-},$$

for the non-hydrostatic pressure. To close the system, it is supposed that

$$p_{I^+} = \gamma_1 p_b + \gamma_2 p_I, \ \ \gamma_1 + \gamma_2 \neq 0, \tag{1.2.15}$$

and therefore, due to the assumption on the non-hydrostatic vertical profile:

$$p_1 = \frac{p_b + p_I}{2}, \ \ p_2 = \frac{\gamma_1 p_b + \gamma_2 p_I}{2}.$$

The underlying reason to assume this discontinuity for the non-hydrostatic pressure is to introduce an artificial set of free parameters, which will help to improve the dispersive properties of the system (see Section 1.2.3).

Remark 1.2.1. *Notice that for $\gamma_1 = 0$, $\gamma_2 = 1$ the original system derived in [124], is recovered and for $\gamma_1 = 1$, $\gamma_2 = \dfrac{\delta}{\delta - 2}$ the approach*

$$p_{I+} - p_{I-} = \delta(p_2 - p_1).$$

The case $\gamma_1 + \gamma_2 = 0$ is avoided (see Subsection 1.3.4 and Appendix D).

To sum up, collecting all the equations described before, the system reads as:

$$
\begin{cases}
\partial_t h + \partial_x \left(l_1 h u_1 + l_2 h u_2 \right) = 0, \\[2mm]
\partial_t \left(l_1 h u_1 \right) + \partial_x \left(l_1 h u_1^2 + l_1 h p_1 \right) + \frac{u_1 + u_2}{2} \Gamma_I - p_b \partial_x H - p_I \partial_x z_I = -g l_1 h \partial_x \eta, \\[2mm]
\partial_t \left(l_1 h u_2 \right) + \partial_x \left(l_2 h u_2^2 + l_2 h p_2 \right) - \frac{u_1 + u_2}{2} \Gamma_I + (\gamma_1 p_b + \gamma_2 p_I) \partial_x z_I = -g l_2 h \partial_x \eta, \\[2mm]
\partial_t \left(l_1 h w_1 \right) + \partial_x \left(l_1 h u_1 w_1 \right) + \frac{w_1 + w_2}{2} \Gamma_I = p_b - p_I, \\[2mm]
\partial_t \left(l_2 h w_2 \right) + \partial_x \left(l_2 h u_2 w_2 \right) - \frac{w_1 + w_2}{2} \Gamma_I = \gamma_1 p_b + \gamma_2 p_I, \\[2mm]
\partial_x u_1 + 2 \dfrac{w_1 - w_b}{l_1 h} = 0, \\[2mm]
\partial_x u_2 + 2 \dfrac{w_2 - w_{I+}}{l_2 h} = 0,
\end{cases}
\tag{1.2.16}
$$

where

$$
\begin{cases}
w_{I+} = u_2 \partial_x z_I - \partial_x \left(l_1 h u_1 \right) - \partial_t H, \\[2mm]
w_b = -u_1 \partial_x H - \partial_t H.
\end{cases}
\tag{1.2.17}
$$

The system depends on the parameters $(l_1, \gamma_1, \gamma_2)$, which need to be chosen. This will be done following a criterion that improve the dispersive relations of the system. Note that the proposed system has the same number of variables as when considering a continuous pressure, that is $p_{I+} - p_{I-} = 0$, that are

$$h, \ u_\alpha, w_\alpha, p_I, p_b$$

and therefore the computational cost of the improved model will be the same than the original one proposed in [124].

System (1.2.16) can be written in the general and compact form (GF) for one dimensional domains with bottom friction terms as

$$
\begin{cases}
\partial_t U + \partial_x F(U) + B(U)\partial_x U = G(U)\partial_x H + S(U) + \\
\qquad\qquad\qquad\qquad + \mathcal{T}(U, \partial_x U, P, \partial_x P, H, \partial_x H), \qquad \text{(NH-2L)} \\
\mathcal{I}(U, \partial_x U, H, \partial_x H) = \mathbf{0},
\end{cases}
$$

defining

$$
U = \begin{pmatrix} h \\ q_{u,1} \\ q_{u,2} \\ q_{w,1} \\ q_{w,2} \end{pmatrix}, \quad
F(U) = \begin{pmatrix} l_1 q_{u,1} + l_2 q_{u,2} \\ \dfrac{q_{u,1}^2}{h} + \dfrac{1}{2} g h^2 \\ \dfrac{q_{u,2}^2}{h} + \dfrac{1}{2} g h^2 \\ \dfrac{q_{u,1} q_{w,1}}{h} \\ \dfrac{q_{u,2} q_{w,2}}{h} \end{pmatrix}, \quad
G(U) = \begin{pmatrix} 0 \\ gh \\ gh \\ 0 \\ 0 \end{pmatrix}, \quad
S(U) = - \begin{pmatrix} 0 \\ \tau_{1,b} \\ 0 \\ 0 \\ 0 \end{pmatrix}
$$

where

$$
q_{u,\alpha} = h u_\alpha, \ q_{w,\alpha} = h w_\alpha, \ \alpha = 1, 2
$$

are the horizontal and vertical discharges. The Manning friction term only appears at the equation concerning to the lower layer and is given by

$$
\tau_{1,b} = g q_{u,1} \frac{n_m^2 |u_1|}{h^{4/3}}.
$$

$B(U)$ is a matrix function such that $B(U)\partial_x U$ involves the nonconservative products related to the mass transfer across interfaces that appear in the momentum equations

$$
B(U) = \begin{pmatrix}
0 & 0 & 0 & 0 & 0 \\
0 & -l_2 \dfrac{u_1 + u_2}{2} & l_2 \dfrac{u_1 + u_2}{2} & 0 & 0 \\
0 & l_1 \dfrac{u_1 + u_2}{2} & -l_1 \dfrac{u_1 + u_2}{2} & 0 & 0 \\
0 & -l_2 \dfrac{w_1 + w_2}{2} & l_2 \dfrac{w_1 + w_2}{2} & 0 & 0 \\
0 & l_1 \dfrac{w_1 + w_2}{2} & -l_1 \dfrac{w_1 + w_2}{2} & 0 & 0
\end{pmatrix}.
$$

Note that the corresponding equations for the horizontal and vertical momentum at the layer $\mathcal{L}_\alpha$, have been divided by l_α. The limit case $l_1 = 1$, $l_2 = 0$ corresponds to the one layer model presented in [21]. For the sake of simplicity, $l_\alpha \in (0, 1)$ is assumed.

Finally, the non-hydrostatic terms are given by

$$
P = \begin{pmatrix} p_b \\ \\ p_I \end{pmatrix}, \; \mathcal{T}(U, \partial_x U, P, \partial_x P, H, \partial_x H) = - \begin{pmatrix} 0 \\ \partial_x(hp_1) - p_b\partial_x H/l_1 - p_I\partial_x z_I/l_1 \\ \partial_x(hp_2) + (\gamma_1 p_b + \gamma_2 p_I)\partial_x z_I/l_2 \\ (p_I - p_b)/l_1 \\ -(\gamma_1 p_b + \gamma_2 p_I)/l_2 \end{pmatrix},
$$

where

$$
p_1 = \frac{p_b + p_I}{2}, \; p_2 = \frac{\gamma_1 p_b + \gamma_2 p_I}{2},
$$

and

$$
\mathcal{I}(U, \partial_x U, H, \partial_x H) = \begin{pmatrix} l_1 h\partial_x q_{u,1} - 2q_{u,1}\partial_x z_1 + 2q_{w,1} + 2h\partial_t H \\ \\ 2l_1 h\partial_x q_{u,1} + l_2 h\partial_x q_{u,2} - 2q_{u,2}\partial_x z_2 + 2q_{w,2} + 2h\partial_t H \end{pmatrix}. \quad (1.2.18)
$$

Operator (1.2.18) contains the incompressibility condition for each layer, and it is obtained multiplying equations (1.2.7a) and (1.2.7b) by $l_1 h^2$ and $l_2 h^2$ respectively. Equations (1.2.17) have been used as well. This allows to write the full two layer system in terms of discharges.

The nature of the continuous problem corresponds to a mix-problem. It consists of a hyperbolic system with a restriction, given by an incompressibility condition (1.2.18). Moreover, using the incompressibility condition, the system can be expressed as a set of three equations (mass equation, u_1–momentum equation, u_2–momentum equation) in terms on the variables h, H, u_1, u_2 in which high order derivative terms, ∂_{xxt}, appear. The expression of the system in terms of velocities is avoided in this thesis since the expressions are too tedious to write. Moreover, one of the objectives of the proposed dissertation is to avoid the presence of high order derivatives. However, in the next subsection, the hyperbolicity of the underlying hydrostatic part is studied.

1.2.2 Hyperbolicity of the underlying hydrostatic system

Let us define the underlying hydrostatic system of (NH-2L) given by

$$\partial_t U + \partial_x F(U) + B(U)\partial_x U = G(U)\partial_x H, \qquad (\text{SWE-2L})$$

where U, F, B and G are defined in (NH-2L) In this subsection, it is shown that the system (SWE-2L) is hyperbolic for every $l_1 \in (0,1)$, and an approximation of the eigenvalues is given.

Hyperbolicity

To prove the hyperbolicity, let us consider the system (SWE-2L) in quasi-linear form

$$\partial_t U + \mathcal{A}\partial_x U = G(U)\partial_x H, \qquad (1.2.19)$$

where $\mathcal{A} = J_F + B$, J_F being the Jacobian matrix of the flux F. The characteristic polynomial of the matrix $\mathcal{A}$ is given by

$$\mathcal{P}(\lambda, l_1) = \frac{1}{2} (u_1 - \lambda)(u_2 - \lambda)\mathcal{Q}(\lambda, l_1),$$

$\mathcal{Q}(\lambda, l_1)$ being a third order polynomial on λ given by

$$\mathcal{Q}(\lambda, l_1) = f(\lambda) - R(l_1),$$

$$f(\lambda) = (3u_1 - u_2 - 2\lambda)\left((u_2 - \lambda)^2 - gh\right), \ R(l_1) = l_1 K, \ K = (u_1 - u_2)\left((u_1 - u_2)^2 - 4gh\right).$$

For the sake of simplicity on the notation, the dependence on U is not written explicitly. Let us study the hyperbolicity of the hydrostatic system. It is easy to check that

$$\lambda_1 = u_1, \ \lambda_2 = u_2$$

are eigenvalues of the system for every $l_1 \in (0,1)$. It remains to check if the cubic polynomial $\mathcal{Q}(\lambda, l_1)$ has three distinct roots.

In the following it is shown that the cubic polynomial has always three different roots for every $l_1 \in [0,1]$, and in particular for every $l_1 \in (0,1)$ as requested. A sketch of the proof:

1. Let us remark that $\mathcal{Q}$ is a cubic polynomial on λ satisfying

$$\mathcal{Q}(-\infty, l_1) = +\infty, \ \mathcal{Q}(\infty, l_1) = -\infty.$$

2. Note that $f(\lambda)$ is a cubic polynomial that does not depend on l_1. Moreover, it has two local extrema given by the roots of $f'(\lambda)$:

$$\lambda^{\pm} = \frac{u_1 + u_2}{2} \pm \sqrt{\frac{gh}{3} + \left(\frac{u_1 - u_2}{2}\right)^2}.$$

3. A sufficient and necessary condition for the existence of three real and distinct roots of the cubic polynomial $\mathcal{Q}(\lambda, l_1)$ is that:

$$f(\lambda^-) < R(l_1) \text{ and } f(\lambda^+) > R(l_1).$$

4. Note that when $l_1 = 0$, the polynomial $\mathcal{Q}(\lambda, 0)$ has three roots:

$$\lambda_3 = \frac{3u_1 - u_2}{2}, \ \lambda_{4,5} = u_2 \pm \sqrt{gh},$$

and thus $f(\lambda^-) < R(0)$ and $f(\lambda^+) > R(0)$.

Similarly, when $l_1 = 1$, the polynomial $\mathcal{Q}(\lambda, 1)$ has three roots:

$$\lambda_3 = \frac{-u_1 + 3u_2}{2}, \ \lambda_{4,5} = u_1 \pm \sqrt{gh},$$

and therefore $f(\lambda^-) < R(1)$ and $f(\lambda^+) > R(1)$.

Thus, assuming that $K \geq 0$, then $R(1) \geq R(l_1) \geq R(0)$ and therefore

$$f(\lambda^+) > R(1) \geq R(l_1),$$

$$f(\lambda^-) < R(0) \leq R(l_1).$$

Assuming that $K \leq 0$, then $R(1) \leq R(l_1) \leq R(0)$ and therefore

$$f(\lambda^+) > R(0) \geq R(l_1),$$

$$f(\lambda^-) < R(1) \leq R(l_1).$$

This concludes the proof.

A first order approximation for the eigenvalues

In the case of $l_1 = \frac{1}{2}$, the eigenvalues can be computed explicitly and are given by:

$$\lambda_1 = u_1, \ \lambda_2 = u_2, \ \lambda_3 = \frac{u_1 + u_2}{2}, \ \lambda_{4,5} = \frac{u_1 + u_2}{2} \pm \sqrt{gh + \frac{3}{4}(u_1 - u_2)^2}.$$

Taking advantage on this fact, two approximations for the eigenvalues of the system (SWE-2L) for any $l_1 \in (0, 1)$ are given:

• For a first approach, let us denote the eigenvalues that depends on l_1 as

$$\lambda_1(l_1) = u_1, \ \lambda_2(l_1) = u_2,$$

as the known eigenvalues for any $l_1 \in (0, 1)$, and

$$\lambda_3(l_1), \ \lambda_4(l_1), \ \lambda_5(l_1)$$

as the eigenvalues that are roots of the cubic polynomial $\mathcal{Q}(\lambda, l_1)$. The following approximation of the eigenvalues, that gives the exact roots of the cubic polynomial $\mathcal{Q}(\lambda, l_1)$ for $l_1 \in \{0, 1/2, 1\}$ is proposed:

$$\lambda_3(l_1) \approx \widetilde{\lambda}_3(l_1) = \left(\frac{3}{2} - 2l_1\right) u_1 + \left(2l_1 - \frac{1}{2}\right) u_2,$$

$$\lambda_{4,5}(l_1) \approx \widetilde{\lambda_{4,5}}(l_1) = l_1 u_1 + l_2 u_2 \pm \sqrt{gh + 3l_1 l_2 \left(u_1 - u_2\right)^2}.$$

- Another approach for the eigenvalues is proposed in the following. Since $\lambda(l_1)$ is a root of $\mathcal{Q}(\lambda, l_1)$, then

$$\mathcal{Q}(\lambda(l_1), l_1) = 0,$$

and deriving with respect to l_1 it yields

$$\lambda'(l_1) = \frac{\left((u_1 - u_2)^2 - 4gh\right) (u_1 - u_2)}{2 \left(gh - 3u_1 u_2 + 3 \left(u_1 + u_2 - \lambda(l_1)\right) \lambda(l_1)\right)}.$$

Thus, an approximation is given for the eigenvalues that are roots of $\mathcal{Q}(\lambda, l_1)$ with the first order approximation

$$\lambda_i(l_1) \approx \widetilde{\lambda}_i = \lambda_i(1/2) + \lambda'_i(1/2)(l_1 - 1/2), \ i \in \{3, 4, 5\},$$

that can be explicitly computed, since $\lambda_i(1/2)$ are known:

$$\lambda_3(l_1) \approx \widetilde{\lambda}_3 = \frac{u_1 + u_2}{2} + (u_1 - u_2)(1 - 2l_1) \frac{gh - \frac{1}{4}(u_1 - u_2)^2}{gh + \frac{3}{4}(u_1 - u_2)^2} + \mathcal{O}(l_1^2),$$

$$\lambda_{4,5}(l_1) \approx \widetilde{\lambda_{4,5}} = \frac{u_1 + u_2}{2} \pm \sqrt{gh + \frac{3}{4}(u_1 - u_2)^2} +$$

$$+ (u_1 - u_2)\left(l_1 - \frac{1}{2}\right) \frac{gh - \frac{1}{4}(u_1 - u_2)^2}{gh + \frac{3}{4}(u_1 - u_2)^2} + \mathcal{O}(l_1^2)$$

This procedure is more rigorous than the previous one and lead to a more sophisticated expressions of the approximated eigenvalues.

An upper and lower bounds for maximum and minimum eigenvalues

Since the three roots of the cubic polynomial $\mathcal{Q}(\lambda, l_1)$ in λ are determined by the abscissas of the intersection points between the cubic polynomial $f(\lambda)$ and the line $R(l_1)$, then the maximum and minimum roots of the polynomial $\mathcal{Q}(\lambda, l_1)$ are in the set defined by the roots of $\mathcal{Q}(\lambda, l_1)$ for $l_1 = 0$ and $l_1 = 1$.

The roots $\lambda_i(l_1)$ of $\mathcal{Q}(\lambda, l_1)$ for $l_1 = 0$ and $l_1 = 1$ are:

$$\lambda_{3,4}(0) = u_2 \pm \sqrt{gh}, \ \lambda_5(0) = \frac{1}{2}(3u_1 - u2),$$

$$\lambda_{3,4}(1) = u_1 \pm \sqrt{gh}, \ \lambda_5(1) = \frac{1}{2}(3u_2 - u1),$$

Note that the analysis carried out in this subsection is only valid if $l_1 \in (0, 1)$, since for the particular cases of $l_1 = 0$ and $l_1 = 1$ the number of equations of the system is reduced, as well as the degree of the characteristic polynomial $\mathcal{P}$. However, it can be checked that when $l_1 = 0$, the roots of the resulting underlying hydrostatic system are $\lambda_{3,4}(0)$ and for $l_1 = 1$, the roots are $\lambda_{3,4}(1)$. Therefore, for $l_1 \in (0, 1)$ the following inequalities for the maximum and minimum of the eigenvalues holds

$$\min(|u_1| - \sqrt{gh}, |u_2| - \sqrt{gh}) \leq \min(\lambda_i) \leq \max(\lambda_i) \leq \max(|u_1| + \sqrt{gh}, |u_2| + \sqrt{gh}).$$

This means that the maximum and minimal speed of propagation of the underlying hydrostatic system are bounded by the maximum and minimal celerities of each layer.

1.2.3   Linear dispersion relation

In this subsection, the dispersion relations of the integrated two layer system (1.2.16) are deduced as usual (see Subsection 1.1.6 and references [61], [168],[176], [184], [226]).

Remark that the studied dispersive relations are dependent on the parameters $(l_1, \gamma_1, \gamma_2)$. Later the aforementioned $(l_1, \gamma_1, \gamma_2)$ parameters will be chosen through examination of the derived dispersive relations following the standard procedure on such topics (see [176], [184], [226]).

Phase velocity

The equations are linearised around the lake at rest steady state solution, and the asymptotic expansion (1.1.12) and flat bathymetry are considered. The linearised version of system (NH-2L) reads

$$
\begin{cases}
\partial_t \eta^{(1)} + H\partial_x \left(l_1 u_1^{(1)} + l_2 u_2^{(1)} \right) = 0, \\[2ex]
\partial_t U^{(1)} + g\partial_x \eta^{(1)} I_2 + \dfrac{1}{2} A_1 \partial_x P^{(1)} = 0, \\[2ex]
H\partial_t W^{(1)} + A_2 P^{(1)} = 0, \\[2ex]
HA_3 \partial_x U^{(1)} + 2W^{(1)} = 0,
\end{cases}
\tag{1.2.20}
$$

being

$$
U^{(1)} = \begin{pmatrix} u_1^{(1)} \\ u_2^{(1)} \end{pmatrix}, \ W^{(1)} = \begin{pmatrix} w_1^{(1)} \\ w_2^{(1)} \end{pmatrix}, \ P^{(1)} = \begin{pmatrix} p_b^{(1)} \\ p_I^{(1)} \end{pmatrix},
$$

$$
I_2 = \begin{pmatrix} 1 & 0 \\ 0 & 1 \end{pmatrix}, \ A_1 = \begin{pmatrix} 1 & 1 \\ \gamma_1 & \gamma_2 \end{pmatrix}, \ A_2 = \begin{pmatrix} -1/l_1 & 1/l_1 \\ -\gamma_1/l_2 & -\gamma_2/l_2 \end{pmatrix}, \ A_3 = \begin{pmatrix} l_1 & 0 \\ 2l_1 & l_2 \end{pmatrix}.
$$

Assuming $\gamma_1 + \gamma_2 \neq 0$, then after some algebraic manipulations, the system (1.2.20) can be expressed in terms of $\eta^{(1)}$, $U^{(1)}$ and its derivatives,

$$
\begin{cases}
\partial_t \eta^{(1)} + H\partial_x \left(l_1 u_1^{(1)} + l_2 u_2^{(1)} \right) = 0, \\[2ex]
\partial_t U^{(1)} + g\partial_x \eta^{(1)} I_2 + \dfrac{1}{4} H^2 A_1 A_2^{-1} A_3 \partial_{xxt} U^{(1)} = 0.
\end{cases}
\tag{1.2.21}
$$

A Stokes-type Fourier analysis is carried out looking for first-order solutions of the form

$$
\eta^{(1)}(x,t) = \eta_0 e^{i(\omega t - kx)}, \ U^{(1)}(x,t) = \begin{pmatrix} u_1 \\ u_2 \end{pmatrix} e^{i(\omega t - kx)},
\tag{1.2.22}
$$

where η_0 is the wave amplitude, ω is the cyclic frequency and k the wave number. By substituting (1.2.22) into (1.2.21), yield the linear system

$$
\left(\begin{array}{cc|c} & & g \\ & \Lambda & \\ & & g \\ \hline l_1 H & l_2 H & -C \end{array} \right) \begin{pmatrix} u_1 \\ u_2 \\ \eta_0 \end{pmatrix} = \begin{pmatrix} 0 \\ 0 \\ 0 \end{pmatrix},
\tag{1.2.23}
$$

where C is the wave celerity defined by $C = \omega/k$ and

$$\Lambda = -C \left(I_2 + \frac{1}{4} (kH)^2 A_1 A_2^{-1} A_3 \right).$$

Looking for non-trivial solutions, the matrix of the linear system (1.2.23) must be singular, and yields the linear dispersion relation

$$\frac{C^2}{gH} = \frac{1 + N_1 (kH)^2}{1 + D_1 (kH)^2 + D_2 (kH)^4}. \tag{1.2.24}$$

Since $l_2 = 1 - l_1$, the coefficients $N_0,\ N_1,\ D_0,\ D_1,\ D_2$ are solely functions of $l_1,\ \gamma_1,\ \gamma_2$ given by

$$\begin{cases} N_1 = \dfrac{l_1 l_2(-\gamma_1 - \gamma_2 + 2(\gamma_2 - 1)l_1 + 2)}{4(\gamma_1 + \gamma_2)}, \\[3mm] D_1 = \dfrac{\gamma_1 + \gamma_2 + 2(\gamma_2 - 2)l_1^2 - 2l_1(\gamma_1 + \gamma_2 - 2)}{4(\gamma_1 + \gamma_2)}, \quad D_2 = \dfrac{l_1^2 l_2^2(\gamma_1 - \gamma_2)}{16(\gamma_1 + \gamma_2)}. \end{cases}$$

Remark 1.2.2. *If the relation $\gamma_1 + \gamma_2 = 0$ holds, then regarding the linear vertical velocity equation in (1.2.20), one has that P can not be uniquely expressed in terms of $\partial_t W$, due to the fact that A_2 is a singular matrix. According to this, it is assumed that $\gamma_1 + \gamma_2 \neq 0$, and thus the matrix A_2 has an inverse A_2^{-1}.*

Remark 1.2.3. *It is of interest the writing of the linearised system in the form given in (1.2.21). Therefore, the system can be written in terms of $h = \eta + H, H, u_1, u_2$. This procedure can be generalized and applied to the original system (NH-2L), leading to a compact formulation free of vertical velocities and non-hydrostatic variables, as well as its corresponding equations. The counterpart is that higher order derivatives will appear.*

Group velocity and linear shoaling

The group velocity G and the linear shoaling gradient γ can be obtained from the linear dispersion relation of the phase velocity (1.2.24) following the guidelines given in Subsection 1.1.6. The determination of these dispersion relations are performed on a computer using symbolic calculation. The resulting expression are tedious and will not be given here. Nevertheless, some figures are shown in Subsection 1.4 for the group velocity and linear shoaling gradient comparing with the linear theory as well as with the dispersion relation of other PDE systems.

Dispersive optimization

For the studied dispersion relations, i.e. wave celerity, group velocity and linear shoaling, a reference formula can be derived from the Airy theory (see Subsection 1.1.6). Now, the most accurate set of parameters l_1, γ_1 and γ_2 , in a sense that will be described later, will be chosen in this section attending to the previous formulae. For this analysis, a representation of the overall error, including errors in wave celerity, group velocity and shoaling, is sought. It is worth to mention that C, C_{Airy}, G, G_{Airy}, γ and γ_{Airy} are in fact solely functions of kH, l_1, γ_1, γ_2. Then for a given $s > 0$, one can consider the integral on kH

$$\Delta_s(l_1, \gamma_1, \gamma_2) := \int_0^s \frac{1}{kH} \left(\frac{|C - C_{Airy}|}{|C_{Airy}|} + \frac{|G - G_{Airy}|}{|C_{Airy}|} + \frac{|\gamma - \gamma_{Airy}|}{|\gamma_{Airy}|} \right) \, dkH, \qquad (1.2.25)$$

that accounts for the linear dispersion error given by the described two layer system when compared with the Airy theory. Therefore this error is minimized defining

$$(l_1^{(s)}, \gamma_1^{(s)}, \gamma_2^{(s)}) := \arg \min_{\substack{(l_1^*, \gamma_1^*, \gamma_2^*) \\ l_1^* \in (0,1) \\ \gamma_1 + \gamma_2 \neq 0}} \left[\Delta_s(l_1^*, \gamma_1^*, \gamma_2^*) \right].$$

When simulating dispersive water waves, errors at low wave numbers k are more relevant than errors at high wave numbers, since the equations are largely used to simulate shallow water flows. Due to that, as in [178], the sum of the relative errors is divided by kH inside the integral (1.2.25). Then, the proposed election of $(l_1^{(s)}, \gamma_1^{(s)}, \gamma_2^{(s)})$ minimizes properly the sum of the relative errors of wave celerity, group velocity and linear shoaling, with respect to the reference formulae in a range of $kH \in [0, s]$. The integral is approximated numerically via Gaussian quadrature points, avoiding the singularity at $kH = 0$. The arg min function is approximated by using an iterative method for non-linear optimization.

Attending to the range of applicability, two set of parameters are obtained. The first one is

$$(l_1^{(5)}, \gamma_1^{(5)}, \gamma_2^{(5)}) = (0.4929, -0.1530, 1.1192), \qquad (l_1^{(5)}, \gamma_1^{(5)}, \gamma_2^{(5)})$$

and a second choice for an extended range is

$$(l_1^{(15)}, \gamma_1^{(15)}, \gamma_2^{(15)}) = (0.7194, 0.1386, 0.7305). \qquad (l_1^{(15)}, \gamma_1^{(15)}, \gamma_2^{(15)})$$

Similarly, it is also denoted

$$(l_1^{(2L)}, \gamma_1^{(2L)}, \gamma_2^{(2L)}) = (1/2, 0, 1), \qquad (l_1^{(2L)}, \gamma_1^{(2L)}, \gamma_2^{(2L)})$$

the coefficients corresponding to the original two layer system proposed in [124].

An alternative procedure to the optimal choice of the free-parameters is the following: as the equations are largely used to simulate shallow water flows, the linear analysis is

supplemented with an asymptotic analysis in the limit $kH \to 0$. To do that, the resulting Taylor expansion of the phase velocity (1.2.24) is compared with the one coming from the Airy theory at order $\mathcal{O}(kH)^4$:

$$\frac{C_{Airy}^2}{gH} = 1 - \frac{1}{3}(kH)^2 + \mathcal{O}(kH)^4,$$

$$\frac{C^2}{gH} = 1 - \frac{\gamma_1 + \gamma_2 - l_1(\gamma_1 + \gamma_2 + l_1(\gamma_1 + \gamma_2 - 2(\gamma_2 - 1)l_1) - 2)}{4(\gamma_1 + \gamma_2)}(kH)^2 + \mathcal{O}(kH)^4,$$

which coincides for

$$\gamma_1 = \frac{3l_1(1 - l_1)(2 - \gamma_2 - 2(\gamma_2 - 1)l_1) - \gamma_2}{3l_1(l_1 + 1) + 1}. \tag{1.2.26}$$

Note that the original two layer non-hydrostatic system derived in [124], which corresponds to the election of $l_1 = \dfrac{1}{2}$ and $\gamma_1 = 0, \ \gamma_2 = 1$, verify at order $\mathcal{O}(kH)^4$:

$$\frac{C_{2L}^2}{gH} = 1 - \frac{5}{16}(kH)^2 + \mathcal{O}(kH)^4.$$

Thus, our proposed system can satisfy up to order $\mathcal{O}(kH)^4$ the Airy theory by setting γ_1 as in (1.2.26). The parameters l_1 and γ_2 are still free parameters, and a similar tuning as the one explained in this subsection can be made in order improve the linear dispersive relation for higher values of kH.

The numerical results shown in this dissertation are computed with the two set of parameters given by $(l_1^{(5)}, \gamma_1^{(5)}, \gamma_2^{(5)})$ and $(l_1^{(15)}, \gamma_1^{(15)}, \gamma_2^{(15)})$. In Subsection 1.4 some comparisons are shown.

1.2.4   Governing equations in two space dimensions

Following a similar procedure than the one presented in Section 1.2.1, the resulting x, y, z momentum equations as well as the two incompressibility equations inside each layer derived for two space dimensions can be written in the general and compact form (GF-2D) for two dimensional domains with bottom friction terms as

$$\begin{cases} \partial_t U + \nabla \cdot \boldsymbol{F}(U) + \boldsymbol{B}(U) \cdot \nabla U = \boldsymbol{G}(U) \cdot \nabla H + S(U) + \mathcal{T}, \\ \mathcal{I}(U, \nabla U, H, \nabla H) = \boldsymbol{0}, \end{cases} \tag{NH-2L2D}$$

defining

$$U = \left(h, \ q_{x,1}, \ q_{y,1}, \ q_{x,2}, \ q_{y,2}, \ q_{w,1}, \ q_{w,2} \right),$$

$$F_1(U) = \left(l_1 q_{x,1} + l_2 q_{x,2}, \ \frac{q_{x,1}^2}{h} + \frac{1}{2}gh^2, \ \frac{q_{x,1}q_{y,1}}{h}, \ \frac{q_{x,2}^2}{h} + \frac{1}{2}gh^2, \ \frac{q_{x,2}q_{y,2}}{h}, \ \frac{q_{x,1}q_{w,1}}{h}, \ \frac{q_{x,2}q_{w,2}}{h} \right)^T,$$

$$F_2(U) = \left(l_1 q_{y,1} + l_2 q_{y,2}, \ \frac{q_{x,1}q_{y,1}}{h}, \ \frac{q_{y,1}^2}{h} + \frac{1}{2}gh^2, \ \frac{q_{x,2}q_{y,2}}{h}, \ \frac{q_{y,2}^2}{h} + \frac{1}{2}gh^2, \ \frac{q_{y,1}q_{w,1}}{h}, \ \frac{q_{y,2}q_{w,2}}{h} \right)^T,$$

$$G_1(U) = \left(0, \ gh, \ gh, \ 0, \ 0, \ 0, \ 0 \right)^T,$$

$$G_2(U) = \left(0, \ 0, \ 0, \ gh, \ gh, \ 0, \ 0 \right)^T,$$

$$S(U) = - \left(0, \ \tau_{1,bx}, \ \tau_{1,by}, \ 0, \ 0, \ 0, \ 0 \right)^T$$

being
$$\boldsymbol{q}_\alpha = (q_{x,\alpha}, q_{y,\alpha}) = (hu_\alpha, hv_\alpha), \ q_{w,\alpha} = hw_\alpha, \ \alpha = 1, 2$$

the horizontal and vertical discharges. The Manning friction term only appears at the equation concerning to the lower layer and is given by

$$\tau_{1,bx} = gq_{x,1}\frac{n_m^2|(u_1, v_1)|}{h^{4/3}}, \quad \tau_{1,by} = gq_{y,1}\frac{n_m^2|(u_1, v_1)|}{h^{4/3}}.$$

$\boldsymbol{B}(U)$ is a matrix function such that $\boldsymbol{B}(U) \cdot \nabla(U)$ involves the nonconservative products related to the mass transfer across interfaces that appear in the momentum equations

$$\boldsymbol{B}(U) = \begin{pmatrix} 0 & 0 & 0 & 0 & 0 & 0 & 0 \\ 0 & -l_2\dfrac{u_1 + u_2}{2} & l_2\dfrac{u_1 + u_2}{2} & 0 & 0 & 0 & 0 \\ 0 & l_1\dfrac{u_1 + u_2}{2} & -l_1\dfrac{u_1 + u_2}{2} & 0 & 0 & 0 & 0 \\ 0 & 0 & 0 & -l_2\dfrac{v_1 + v_2}{2} & l_2\dfrac{v_1 + v_2}{2} & 0 & 0 \\ 0 & 0 & 0 & l_1\dfrac{v_1 + v_2}{2} & -l_1\dfrac{v_1 + v_2}{2} & 0 & 0 \\ 0 & -l_2\dfrac{w_1 + w_2}{2} & l_2\dfrac{w_1 + w_2}{2} & -l_2\dfrac{w_1 + w_2}{2} & l_2\dfrac{w_1 + w_2}{2} & 0 & 0 \\ 0 & l_1\dfrac{w_1 + w_2}{2} & -l_1\dfrac{w_1 + w_2}{2} & l_1\dfrac{w_1 + w_2}{2} & -l_1\dfrac{w_1 + w_2}{2} & 0 & 0 \end{pmatrix}.$$

Note that the corresponding equations for the horizontal and vertical momentum at the layer $\mathcal{L}_\alpha$, have been divided by l_α. The limit case $l_1 = 1$, $l_2 = 0$ corresponds to the extension to bidimensional domains one layer model described in [4]. For the sake of simplicity, it is assumed that $l_\alpha \in (0, 1)$.

Finally, the non-hydrostatic terms are given by

$$
P = \begin{pmatrix} p_b \\ \\ p_I \end{pmatrix}, \ \mathcal{T}(U, \nabla U, P, \nabla P, H, \nabla H) = - \begin{pmatrix} 0 \\ \partial_x \left(h p_1 \right) - p_b \partial_x H / l_1 - p_I \partial_x z_I / l_1 \\ \partial_y \left(h p_1 \right) - p_b \partial_y H / l_1 - p_I \partial_y z_I / l_1 \\ \partial_x \left(h p_2 \right) + (\gamma_1 p_b + \gamma_2 p_I) \partial_x z_I / l_2 \\ \partial_y \left(h p_2 \right) + (\gamma_1 p_b + \gamma_2 p_I) \partial_y z_I / l_2 \\ (p_I - p_b) / l_1 \\ - (\gamma_1 p_b + \gamma_2 p_I) / l_2 \end{pmatrix},
$$

and

$$
\mathcal{I}(U, \nabla U, H, \nabla H) =
$$

$$
\begin{pmatrix} l_1 h \nabla \cdot \boldsymbol{q}_1 - 2 \boldsymbol{q}_1 \cdot \nabla (z_1) + 2 q_{w,1} + 2 h \partial_t H \\ \\ 2 l_1 h \nabla \cdot \boldsymbol{q}_1 + l_2 h \nabla \cdot \boldsymbol{q}_2 - 2 \boldsymbol{q}_2 \cdot \nabla (z_2) + 2 q_{w,2} + 2 h \partial_t H \end{pmatrix}. \tag{1.2.27}
$$

Operator (1.2.27) contains the incompressibility condition for each layer, and similarly to what is done for the case of one dimensional domains, is obtained multiplying the incompressibility conditions at each layer $\mathcal{L}_\alpha$ by $l_\alpha h^2$. This allows to write the full two layer system in terms of discharges.

1.3   A hyperbolic relaxation non-hydrostatic pressure system

In [111], up to our knowledge, a novel set of first-order hyperbolic equations was proposed that can model dispersive non-hydrostatic free surface flows. The governing PDE system is obtained by making a hyperbolic approximation of the non-hydrostatic free-surface flow model (NH-1L) recently derived by Sainte-Marie *et al.* in [21], which describes the propagation of dispersive waves in shallow waters, and which satisfies an extra energy conservation law.

The hyperbolic system is obtained using a hyperbolic reformulation of the original governing PDE (NH-1L). The divergence constraint of the velocity is coupled with the remaining conservation laws at the aid of an evolution equation for the depth-integrated non-hydrostatic pressure. This technique is similar to the so-called hyperbolic divergence

cleaning introduced in the generalized Lagrangian multiplier approach (GLM) of Munz *et al.* [196], [83] for the Maxwell and the magnetohydrodynamics (MHD) equations. A formulation is suggested in which the divergence errors of the velocity field are transported at a finite speed that is related to the maximum eigenvalues of the governing PDE system. The augmented hyperbolic system maintains the momentum equations for the horizontal and vertical velocities and still satisfies an energy balance equation, as the original system (NH-1L). The idea is also similar to the method of artificial compressibility that can be used for the numerical solution of the incompressible Navier-Stokes equations.

The final governing PDE system proposed is a system of hyperbolic balance laws, and it is thus amenable for discretization via high order numerical schemes. Higher order methods are desirable due to their improved dissipation and dispersion properties compared to simple second order TVD finite volume schemes. This is particularly important for the accurate propagation of solitary waves over long distances, as it will be also shown later in the numerical results section.

The derivation of the subsequent system as well as the mathematical study concerning to the dispersive properties; the study on the hyperbolicity; the proposed numerical scheme that it will be presented in Chapter 3; a breaking mechanism to model breaking waves; and the numerical tests, were proposed in [111].

1.3.1 Governing equations

The non-hydrostatic system (NH-1L) derived by Sainte-Marie *et al.* in [21] is modified as

$$
\begin{cases}
\partial_t h + \partial_x (hu) = 0, & \text{(1.3.1a)} \\[2ex]
\partial_t (hu) + \partial_x \left(hu^2 + \frac{1}{2} gh^2 + hp \right) = (gh + 2p)\, \partial_x H - \tau_b, & \text{(1.3.1b)} \\[2ex]
\partial_t (hw) + \partial_x (uhw) = 2p, & \text{(1.3.1c)} \\[2ex]
\partial_t (hp) + \partial_x (uhp) + hc^2 \left(\partial_x u + \frac{w - w_b}{h/2} \right) = 0, \quad w_b = -u\partial_x H - \partial_t H & \text{(1.3.1d)}
\end{cases}
$$

where $c = \alpha\sqrt{gH_0}$ is a given constant celerity, H_0 being a typical average still water depth and $\alpha > 1$. The approximation is based on a modified system in which the divergence constraint on the velocity field is coupled with the other conservation laws following the ideas of the so-called hyperbolic divergence cleaning applied in the context of the generalized Lagrangian multiplier (GLM) method for the magnetohydrodynamics equations put forward in [83], [196]. A formulation is suggested in which the divergence

errors are transported with a finite speed c. In the subsequent section The hyperbolicity of the augmented system is studied and proved also that, the augmented system satisfies an additional energy conservation law. For hyperbolic systems with convex extensions, the reader is referred also to the pioneering work of Godunov and Romenski, [136], [137], [220, 138], who derived a theoretical framework on symmetric hyperbolic and thermodynamically compatible (SHTC) systems that are all endowed with such an extra conservation law.

This modified system (NHyp) can be written in compact matrix-vector form as in (GF) defining

$$
U = \begin{pmatrix} h \\ q_u \\ q_w \\ q_p \end{pmatrix}, \quad
F(U) = \begin{pmatrix} q_u \\ \dfrac{q_u^2}{h} + \dfrac{1}{2}gh^2 + q_p \\ \dfrac{q_u q_w}{h} \\ \dfrac{q_u q_p}{h} + c^2 q_u \end{pmatrix}, \quad
G(U) = \begin{pmatrix} 0 \\ gh + 2p \\ 0 \\ -2c^2 u \end{pmatrix},
$$

$$
S(U) = -\begin{pmatrix} 0 \\ \tau_b \\ -2p \\ 2c^2(w + \partial_t H) \end{pmatrix}, \quad
B(U) = \begin{pmatrix} 0 & 0 & 0 & 0 \\ 0 & 0 & 0 & 0 \\ 0 & 0 & 0 & 0 \\ -c^2\dfrac{q_u}{h} & 0 & 0 & 0 \end{pmatrix},
$$
$$\text{(NHyp)}$$

$$
\mathcal{T} = \mathbf{0}, \quad \mathcal{I} = \mathbf{0},
$$

where $q_u = hu, \; q_w = hw, \; q_p = hp$.

Remark 1.3.1. *Following the spirit of Remark* 1.1.3*, a hyperbolic relaxation system can*

be considered for the system (YAM) *in the following form*

$$
\begin{cases}
\partial_t h + \partial_x (hu) = 0, \\[2mm]
\partial_t (hu) + \partial_x \left(hu^2 + \dfrac{1}{2}gh^2 + hp \right) = (gh + 2p)\,\partial_x H - \tau_b, \\[2mm]
\partial_t (hw) + \partial_x (uhw) = 2p + hu\partial_x w, \\[2mm]
\partial_t (hp) + \partial_x (uhp) + hc^2 \left(\partial_x u + \dfrac{w - w_b}{h/2} \right) = 0, \quad w_b = -u\partial_x H - \partial_t H
\end{cases}
\tag{1.3.2}
$$

1.3.2 Energy balance of the system (NHyp)

The proposed system (NHyp) satisfies the additional balance law

$$
\partial_t E + \partial_x \left(u \left(E + \dfrac{g}{2}h^2 + hp \right) \right) = (gh + 2p)\partial_t H - u\tau_b,
\tag{1.3.3}
$$

where

$$
E = \frac{h(u^2 + w^2)}{2} + \frac{gh(\eta - H)}{2} + \frac{hp^2}{2c^2}.
\tag{1.3.4}
$$

Proof. As it is usually done, by adding $(u \cdot$ (1.3.1b) $+ w \cdot$ (1.3.1c)$)$, and using the mass conservation equation (1.3.1a), one has

$$
\partial_t \widetilde{E} + \partial_x \left(u \left(\widetilde{E} + \dfrac{g}{2}h^2 + hp \right) \right) = hp \left(\partial_x u + \dfrac{w + u\partial_x H}{h/2} \right) + (gh + 2p)\partial_t H - u\tau_b,
$$

where

$$
\widetilde{E} = \frac{h(u^2 + w^2)}{2} + \frac{gh(\eta - H)}{2}.
$$

For the original system (NH-1L), one has $\left(\partial_x u + \dfrac{w + u\partial_x H}{h/2} \right) = 0$, and thus the energy equality (1.3.3). For the proposed model, it can be easily checked by using the mass conservation equation (1.3.1a), that the following equality holds:

$$
\partial_t \left(hp^2 \right) + \partial_x \left(hup^2 \right) + 2c^2 hp \left(\partial_x u + \dfrac{w + u\partial_x H}{h/2} \right) = 0.
\tag{1.3.5}
$$

Thus,

$$
hp \left(\partial_x u + \dfrac{w + u\partial_x H}{h/2} \right) = -\frac{1}{2c^2} \left(\partial_t \left(hp^2 \right) + \partial_x \left(hup^2 \right) \right)
$$

and the relation (1.3.3) completes the proof. $\qquad\square$

Remark 1.3.2. *Note that when $c \to \infty$, the original system (NH-1L) is recovered along with the energy balance (1.1.8).*

Remark 1.3.3. *Note that when $c = 0$, and for an initial condition $w_0 = p_0 = 0$, the classical shallow-water system (SWE) is recovered.*

1.3.3 Eigenstructure of the system (NHyp)

The system (NHyp) written in quasi-linear form read as

$$\partial_t U + A(U)\partial_x U = G(U)\partial_x H + S(U), \tag{1.3.6}$$

with

$$A(U) = J_F(U) + B(U),$$

where $J_F = \partial F/\partial U$ is the Jacobian of the flux F with respect to the conserved variables U. The eigenvalues of the matrix $A(U)$ are

$$\lambda_{1,2} = u, \ \lambda_{3,4} = u \pm C_e$$

where $C_e = \sqrt{gh + p + c^2}$. A set of linearly independent eigenvectors is given by

$$\boldsymbol{v}_1 = \left(1, \ u, \ 0, \ -gh\right), \qquad \boldsymbol{v}_2 = \left(0, \ 0, \ 1, \ 0\right),$$

$$\boldsymbol{v}_{3,4} = \left(1, \ w\left(p + c^2\right)\lambda_{3,4}, \ p + c^2, \ 0\right). \tag{1.3.7}$$

1.3.4 Linear dispersion relation

In this subsection, the dispersion relations of the proposed system (NHyp) are deduced as usual (see Subsection 1.1.6 and references [61], [168], [176], [184], [226]).

Phase velocity

Assuming that both η and u are very small perturbation of a lake at rest steady state, and flat bathymetry, the linearised version of system (1.2.16) reads

$$\begin{cases} \partial_t \eta^{(1)} + H\partial_x u^{(1)} = 0, \\\\ \partial_t u^{(1)} + g\partial_x \eta^{(1)} + \partial_x p^{(1)} = 0, \\\\ H\partial_t w^{(1)} - 2p^{(1)} = 0, \\\\ H\partial_t p^{(1)} + Hc^2\partial_x u^{(1)} + 2c^2 w^{(1)} = 0. \end{cases} \tag{1.3.8}$$

A Stokes-type Fourier analysis is carried out looking for first-order solutions of the form

$$\eta^{(1)}(x,t) = \eta_0 e^{i(\omega t - kx)}, \; u^{(1)}(x,t) = u_0 e^{i(\omega t - kx)},$$

$$w^{(1)}(x,t) = w_0 e^{i(\omega t - kx)}, \; p^{(1)}(x,t) = p_0 e^{i(\omega t - kx)}, \tag{1.3.9}$$

where ω is the angular frequency and k is the wave number. By substituting (1.3.9) into (1.3.8), yield the linear system

$$\begin{pmatrix} -\omega & Hk & 0 & 0 \\ gk & -\omega & 0 & k \\ 0 & 0 & H\omega & -2i \\ 0 & -c^2 Hk & 2ic^2 & H\omega \end{pmatrix} \cdot \begin{pmatrix} \eta_0 \\ u_0 \\ w_0 \\ p_0 \end{pmatrix} = \mathbf{0}. \tag{1.3.10}$$

Assuming $c^2 = \alpha^2 gH$ and looking for non-trivial solutions, then the matrix of the linear system (1.2.23) must be singular, yielding the linear dispersion relation

$$(kH)^2 \frac{C_p^2}{gH}\left(\frac{C_p^2}{gH} - 1\right) + 4\alpha^2\left(1 - \frac{C_p^2}{gH}\left(1 + \frac{1}{4}(kH)^2\right)\right) = 0, \tag{1.3.11}$$

where $C_p = \dfrac{\omega}{k}$ is the phase velocity. Note that for $\alpha^2 \to \infty$, the linear dispersion relation of the original system (NH-1L) is recovered:

$$\frac{C_J^2}{gH} = \frac{1}{J(kH)}, \qquad J(kH) = 1 + \frac{1}{4}(kH)^2.$$

From (1.3.11),

$$\frac{(C_p^2)^{\pm}}{gH} = \left(\frac{J(kH) + \gamma}{2} \mp \sqrt{\left(\frac{J(kH) + \gamma}{2}\right)^2 - \gamma}\right)^{-1}, \qquad \gamma = \left(\frac{kH}{2\alpha}\right)^2. \tag{1.3.12}$$

The phase velocities C_p^+ and C_p^- are called the rapid and slow phase velocity, respectively. The velocity C_p^+ is always larger than the one of system (NHyp). It does not have any physical meaning and describes the evolution of artificial high-frequency waves related to the modification of the system.

Figure 1.3 shows the error of the phase velocities C_p^- for several values of α, and for the original system (NH-1L), with respect to the phase velocity given by the Airy theory in a range of $kH \in [0, 3]$. This interval is chosen according to the range in which the original weakly non-linear weakly dispersive system [21] shows a good match with respect to the linear theory of Stokes. It can be stated that for a value of $c = 5\sqrt{gH}$, the linear

dispersion relation of the proposed hyperbolic system is very close to the original one. Moreover, Figure 1.4 shows that the absolute value of the relative error in phase celerity with respect to the original system (NH-1L) is less than 2.6 percent for $\alpha = 3$.
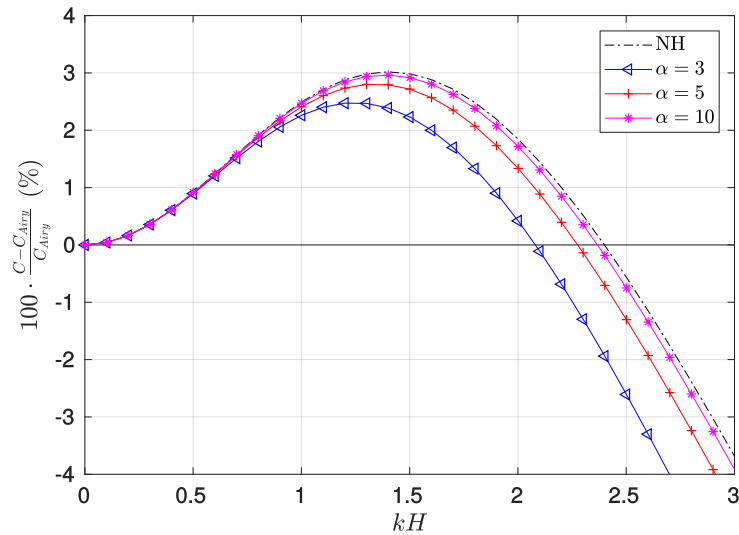
Figure 1.3: Relative error of the phase velocities with respect to the Airy theory for the original system (NH-1L) (black) and for the new hyperbolic approach (NHyp) using $\alpha = 3$ (blue), $\alpha = 5$ (red) and $\alpha = 10$ (magenta).
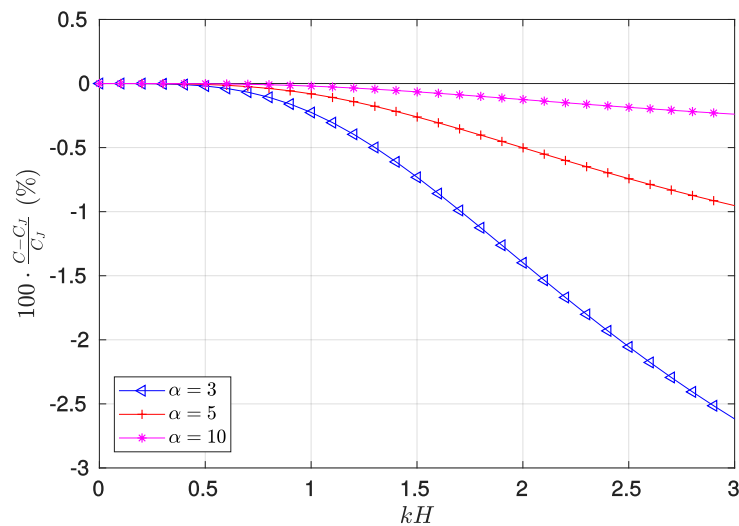
Figure 1.4: Relative error of the phase velocity C_p^- of the new hyperbolic system (NHyp) with respect to the original dispersive system (NH-1L) for $\alpha = 3$ (blue), $\alpha = 5$ (red) and $\alpha = 10$ (magenta).

Group velocity and linear shoaling

The group velocity G and the linear shoaling gradient γ can be obtained from the linear dispersion relation of the phase velocity (1.3.11) following the guidelines given in Subsection 1.1.6. The determination of these dispersion relations are performed on a computer using symbolic calculation. The resulting expressions are tedious and will not be given here. Nevertheless, some graphics are shown in Subsection 1.4 for the group velocity and linear shoaling gradient comparing with the linear theory as well as with the dispersion relation of other PDE systems.

1.3.5 Governing equations in two space dimensions

The corresponding governing equations of the original system (NH-1L) for two-dimensional domains can be found in [4]. The extension for two-dimensional domains of the system (NHyp) can be written as in the general compact form (GF-2D), defining

$$
U = \begin{pmatrix} h \\ q_x \\ q_y \\ q_w \\ q_p \end{pmatrix}, \quad
F_1(U) = \begin{pmatrix} q_x \\ \dfrac{q_x^2}{h} + \dfrac{1}{2}gh^2 + q_p \\ \dfrac{q_x q_y}{h} \\ \dfrac{q_x q_w}{h} \\ \dfrac{q_x q_p}{h} + c^2 q_x \end{pmatrix}, \quad
F_2(U) = \begin{pmatrix} q_y \\ \dfrac{q_x q_y}{h} \\ \dfrac{q_y^2}{h} + \dfrac{1}{2}gh^2 + q_p \\ \dfrac{q_y q_w}{h} \\ \dfrac{q_y q_p}{h} + c^2 q_y \end{pmatrix},
$$

$$
G_1(U) = \begin{pmatrix} 0 \\ gh \\ 0 \\ 0 \\ -2c^2 q_x \end{pmatrix}, \quad
G_2(U) = \begin{pmatrix} 0 \\ 0 \\ gh \\ 0 \\ -2c^2 q_y \end{pmatrix}, \tag{NHyp-2D}
$$

$$S(U) = - \begin{pmatrix} 0 \\ \tau_{b,x} \\ \tau_{b,y} \\ -2p \\ 2c^2(\dfrac{q_w}{h} + \partial_t H) \end{pmatrix}, \quad \boldsymbol{B}(U) = \begin{pmatrix} 0 & 0 & 0 & 0 & 0 \\ 0 & 0 & 0 & 0 & 0 \\ 0 & 0 & 0 & 0 & 0 \\ 0 & 0 & 0 & 0 & 0 \\ -c^2\dfrac{q_x + q_y}{h} & 0 & 0 & 0 & 0 \end{pmatrix},$$

$$\mathcal{T} = \boldsymbol{0}, \quad \mathcal{I} = \boldsymbol{0},$$

being $q_x = hu$, $q_y = hv$, $q_w = hw$ the discharges, $q_p = hp$ and $\tau_{b,x}$, $\tau_{b,y}$ accounts for the friction terms defined in (1.1.4).

1.4   A comparison of the linear dispersion properties of the described systems

In this section, the main linear dispersive properties of the described systems to model dispersive water waves are compared.

To do that, the linear dispersion relations for the described systems are tagged with the corresponding labels given by: Non-linear shallow water system (SWE); Peregrine system (PER); Madsen-Sørensen system (MS); Multi layer non-hydrostatic pressure systems (NH–kL) for a multi layer system with a number of $k \geq 1$ layers; One layer non-hydrostatic pressure (and Yamazaki *et al.*) system (NH-1L); two layer non-hydrostatic pressure system (NH-2L) from C. Escalante *et al.*; The hyperbolic relaxation system from C. Escalante *et al.* (NHyp).

Note that the same linear dispersion relations are obtained for the systems (NH-1L) and (YAM), since the same linearised systems are obtained, and the tag (NH-1L) will be used.

The linear study for the first four systems enumerated above were carried out in their respective references (see, e.g. [124], [184], [210]). The fifth case corresponds to the particular case of 1 layer of the multi layer system. The sixth and seventh systems were detailed in the Subsection 1.2.3 and 1.3.4 respectively.

The expressions of the phase velocities for the aforementioned systems are given in Tables 1.1 and 1.2. The last two columns contains $Er_C(s)$ that means the maximum relative error of the phase velocities with respect to the Airy in a range $kH \in [0, s]$ in

percent:

$$Er_C(s) = 100 \cdot \max_{kH \in [0,s]} \left(\frac{|C(kH) - C(kH)_{Airy}|}{|C(kH)_{Airy}|} \right).$$

Figures 1.5, 1.6, 1.7 and Table 1.1 summarized the results for the one layer systems. The (MS) equations achieve the better results concerning to systems with 1 layer. The system shows relative error in a range of $kH \in [0,3]$ for the phase velocity that is less than 2 % and for the group velocity less than 5 %. It also presents good shoaling properties within this range. Nevertheless, the one layer system (NH-1L) is less complex and also achieves good errors in the linear dispersive relations studied for smaller values of kH. The systems (SWE) and (PER) only provides good errors in the linear dispersion relations for smaller values of $kH \ll 1$. The hyperbolic approximation made in the system (NHyp) also show excellent results compared with respect the original system (NH-1L), both for the phase and group velocities as well as the shoaling gradient.

Figures 1.8, 1.9, 1.10 and Table 1.2 summarized the results for the multi layer systems. The results verified that better results are obtained for multi layer systems with higher number of layers. It is remarkable the good shoaling gradient that the (NH-5L) can achieved for large values of kH.

Attending to the results of the new two layer system, the first set of parameters $(l_1^{(5)}, \gamma_1^{(5)}, \gamma_2^{(5)})$ leads to an excellent agreement with the Airy theory for kH up to 5. The percentage errors in phase celerity is less than 0.09% and for the group velocity is less than 2% for smaller kH. Linear shoaling is reproduced very well in this range also. Another choice for an extended range of kH is $(l_1^{(15)}, \gamma_1^{(15)}, \gamma_2^{(15)})$ that ensures a percentage error for the celerity less than 1.24% for kH up to 15. For the group velocity this choice provides an error less than 6% for kH up to 10. The comparison with the standard two layer approximation corresponding to the choice $(l_1^{(2L)}, \gamma_1^{(2L)}, \gamma_2^{(2L)})$ shows that although the second optimization $(l_1^{(15)}, \gamma_1^{(15)}, \gamma_2^{(15)})$ does not seem to improve the errors with respect to $(l_1^{(2L)}, \gamma_1^{(2L)}, \gamma_2^{(2L)})$, it ensures reasonable errors for an extended range of kH.

Let us remark that the two layer model proposed in this thesis presents a good agreement for linear shoaling gradient with just two layers. To have similar results, at least five layers are needed for multi layer models like the one presented in [10]. Moreover, the results for the phase velocity with parameters $(l_1^{(15)}, \gamma_1^{(15)}, \gamma_2^{(15)})$ show that the two layer obtains a smaller relative error for kH up to 15, when compared with the two layer system proposed in [71]. This means that the model proposed here can achieve better dispersive properties than models that have similar o even more computational complexity.

One layer Systems – Phase velocity – Errors for kH up to 3,5			
Model	Phase velocity	$Er_C(3)$	$Er_C(5)$
(SWE)	gH	73.63 %	123.61 %
(PER)	$gH\dfrac{1}{1+\frac{1}{3}(kH)^2}$	13.18 %	26.80 %
(MS) $(B=1/21)$	$gH\dfrac{1+B(kH)^2}{1+(B+\frac{1}{3})(kH)^2}$	1.43 %	2.02 %
(NH-1L)	$gH\dfrac{1}{1+\frac{1}{4}(kH)^2}$	3.02 %	16.95 %
(NHyp)	$\left(\dfrac{J(kH)+\gamma}{2}+\sqrt{\left(\dfrac{J(kH)+\gamma}{2}\right)^2-\gamma}\right)^{-1}$	4.60 % $(\alpha=5)$	18.16 % $(\alpha=10)$

Table 1.1: Phase velocity expressions for the given Boussinesq and one layer systems and maximum of the relative error $Er_C(s)$ compared with the Airy theory for different ranges of $kH \in [0, s]$
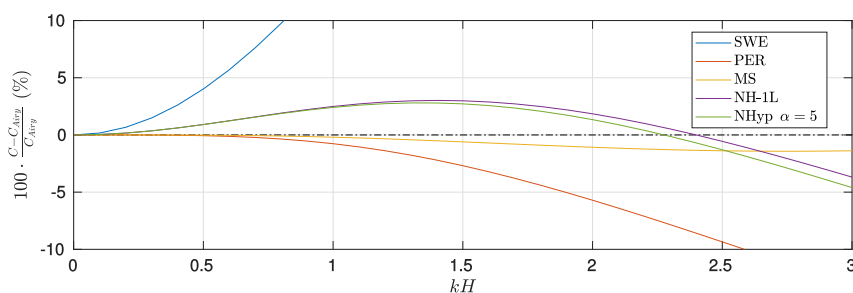
Figure 1.5: Relative error of the phase velocities with respect to the Airy theory for the described one layer systems

Multi layer Systems – Phase velocity – Errors for kH up to 5,15			
Model	Phase velocity	$Er_C(5)$	$Er_C(15)$
(NH-2L) $(l_1^{(2L)}, \gamma_1^{(2L)}, \gamma_2^{(2L)})$	$gH\dfrac{1 + \frac{(kH)^2}{16}}{1 + \frac{3(kH)^2}{8} + \frac{(kH)^4}{256}}$	0.71 %	10.67 %
(NH-2L) $(l_1^{(5)}, \gamma_1^{(5)}, \gamma_2^{(5)})$	$gH\dfrac{1 + N_1\,(kH)^2}{1 + D_1\,(kH)^2 + D_2\,(kH)^4}$	0.09 %	13.01 %
(NH-2L) $(l_1^{(15)}, \gamma_1^{(15)}, \gamma_2^{(15)})$	$gH\dfrac{1 + N_1\,(kH)^2}{1 + D_1\,(kH)^2 + D_2\,(kH)^4}$	1.24 %	1.24 %
(NH-3L)	$gH\dfrac{1 + \frac{5(kH)^2}{54} + \frac{(kH)^4}{1296}}{1 + \frac{5(kH)^2}{12} + \frac{5(kH)^4}{432} + \frac{1(kH)^6}{46656}}$	0.31 %	0.62 %
(NH-5L)	$gH\dfrac{1 + \frac{3(kH)^2}{25} + \frac{63(kH)^4}{2510^3} + \frac{3(kH)^6}{2510^4} + \frac{(kH)^8}{1010^7}}{1 + \frac{9(kH)^2}{20} + \frac{21(kH)^4}{1010^2} + \frac{21(kH)^6}{1010^4} + \frac{9(kH)^8}{2010^6} + \frac{(kH)^{10}}{1010^9}}$	0.11 %	0.11 %

Table 1.2: Phase velocity expressions for the given multi layer systems and maximum of the relative error $Er_C(s)$ compared with the Airy theory for different ranges of $kH \in [0, s]$
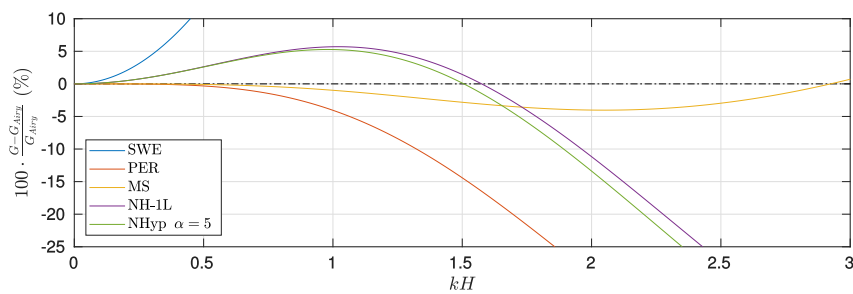
Figure 1.6: Relative error of the group velocities with respect to the Airy theory for the described one layer systems
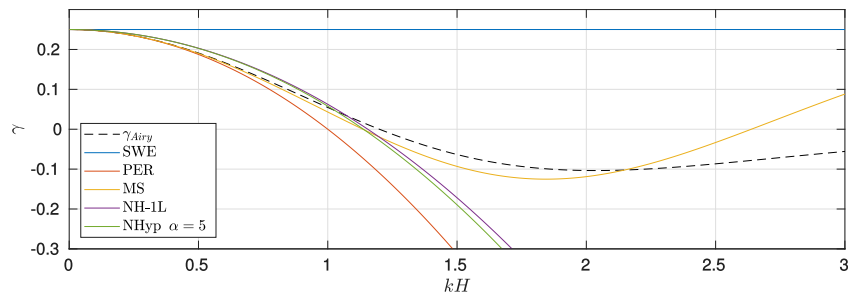
Figure 1.7: Comparison with the reference shoaling gradient with respect to the Airy theory for the described one layer systems
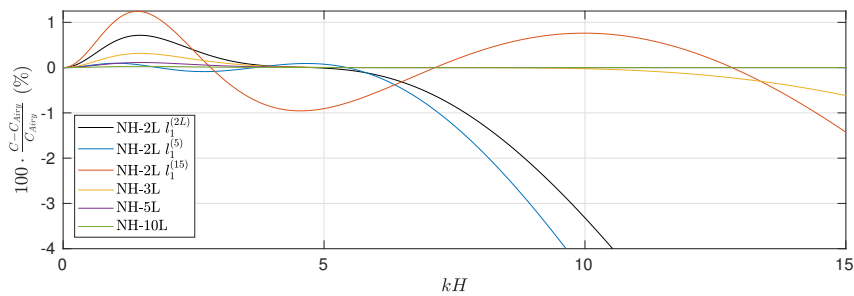
Figure 1.8: Relative error of the phase velocities with respect to the Airy theory for the described multi layer systems
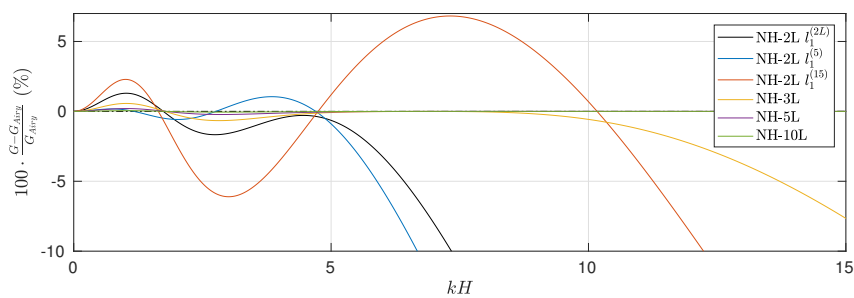
Figure 1.9: Relative error of the group velocities with respect to the Airy theory for the described multi layer systems
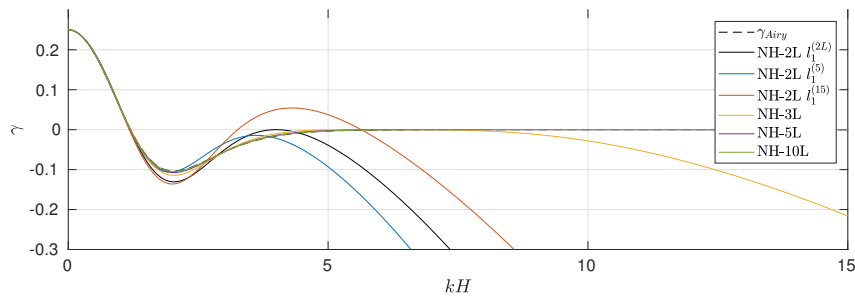
Figure 1.10: Comparison with the reference shoaling gradient with respect to the Airy theory for the described multi layer systems

1.5 Breaking waves modelling

As pointed in [219], in shallow water, complex events can be observed related to turbulent processes. One of these processes corresponds to the breaking of waves near the coast. As it will be seen in the numerical tests proposed in this work, the models presented here cannot describe this process without an additional term which allows the model to dissipate the required amount of energy on such situations. When breaking processes occur, mostly close to shallow areas, two different approaches are usually employed when dispersive Boussinesq-type models are considered.

Close to the coast where breaking starts, the SWE propagates breaking bores at the correct speed, since kH is small, and dissipation of the breaking wave is also well reproduced. Due to that, the simplest way to deal with breaking waves, when considering dispersive systems, consists in neglecting the dispersive part of the equation. This means to force the non-hydrostatic pressure to be zero where breaking occurs. Due to that, this technique has the advantage that only a breaking criterion is needed to stop and start it. However, the main disadvantage is that the grid-convergence is not ensured when the mesh is refined, and global and costly breaking criteria should be taken into account (see [163]).

The other strategy, that will be adopted in this dissertation, consists in the dissipation of breaking bores with a diffusive term. Again, breaking criteria to switch on/off the dissipation is needed. Usually, an eddy viscosity approach (see [219]) solves the matter, where an empirical parameter is defined, based on a quasi-heuristic strategy to determine when the breaking occurs. The main difficulty that presents this mechanism is that usually the diffusive term must be discretized implicitly due to the high order derivatives from the diffusion. Otherwise, it will lead to a severe restriction on the CFL number. As a consequence, an extra linear system has to be solved, losing efficiency. In any case, this challenge is overcome by C. Escalante *et al.* in [112] for the one layer non-hydrostatic system derived in [259], and a natural extension of this procedure for the two layer case was given by C. Escalante *et al.* in [118]. In this section the two breaking criteria will be

described for the one layer non-hydrostatic pressure systems (YAM-2D), (NHyp-2D). An extension of this technique is proposed for the case of two layer system (NH-2L).

A breaking mechanism for the one layer non-hydrostatic pressure systems

One space dimension

For the sake of clarity, the breaking mechanism is described for the system (NH-1L) in one space dimension. Later, the extension of the procedure for two dimensional domains for the system (YAM-2D) and (NHyp-2D) will be given. Let us consider a simple and well-known eddy viscosity approach similar to the one introduced in [219], by adding a diffusive term in the horizontal momentum equation of system (NH-1L):

$$
\begin{cases}
\partial_t h + \partial_x (hu) = 0, \\[2mm]
\partial_t (hu) + \partial_x \left(hu^2 + \frac{1}{2}gh^2 + hp \right) = (gh + 2p)\,\partial_x H - \tau_{b,x} + \partial_x \left(\nu h \partial_x u \right), \\[2mm]
\partial_t (hw) + \partial_x (uhw) = 2p, \\[2mm]
\partial_x u + \dfrac{w - w_b}{h/2} = 0, \quad w_b = -\partial_t H - u\partial_x H,
\end{cases}
$$

ν being the eddy viscosity

$$
\nu = Bh|\partial_x(hu)|, \quad B = 1 - \frac{\partial_x(hu)}{U_1}, \tag{1.5.1}
$$

where

$$
U_1 = B_1\sqrt{gh}, \ U_2 = B_2\sqrt{gh},
$$

denote the flow speeds at the onset and termination of the wave-breaking process and B_1, B_2 are calibration coefficients that should be fixed through laboratory experiments (see [219]). Wave energy dissipation associated with breaking begins when $|\partial_x(hu)| \geq U_1$ and continues as long as $|\partial_x(hu)| \geq U_2$. The proposed definition of the viscosity ν requires a positive value of B. To satisfies that, for negative values of B, the viscosity ν is set to zero.

It is a known fact that using an explicit scheme for a parabolic equation requires a time step restriction of type $\Delta t = \mathcal{O}(\Delta x^2)$. The breaking mechanism has this nature and this would mean a too restrictive time step. This is the reason for choosing an implicit discretization of this term. This can be solved by considering an implicit discretization

of the eddy viscosity term, evaluating the term $\partial_x (\nu h \partial_x u)$ at the right-hand side of the momentum discrete equation in (NH-1L). The implicit discretization involves solving an extra tridiagonal linear system, leading to a loss of efficiency.

In [112] a new efficient treatment of the eddy viscosity term was present by C. Escalante *et al.* for depth averaged non-hydrostatic models. To do that, the horizontal momentum equation is rewritten as

$$\partial_t (hu) + \partial_x \left(hu^2 + \frac{1}{2}gh^2 + hp - \nu h \partial_x u \right) = (gh + 2p) \partial_x H - \tau_{b,x} \qquad (1.5.2)$$

and define

$$p = \widetilde{p} + \nu \partial_x u. \qquad (1.5.3)$$

Thus, replacing p by $\widetilde{p} + \nu u_x$, the system can be rewritten as

$$\begin{cases} \partial_t h + \partial_x (hu) = 0, \\\\ \partial_t (hu) + \partial_x \left(hu^2 + \frac{1}{2}gh^2 + h\widetilde{p} \right) = (gh + 2\widetilde{p}) \partial_x H - \tau_{b,x} + 2\nu \partial_x u \partial_x H, \\\\ \partial_t (hw) + \partial_x (uhw) = 2\widetilde{p} + 2\nu \partial_x u, \\\\ \partial_x u + \dfrac{w - w_b}{h/2} = 0, \quad w_b = -\partial_t H - u \partial_x H. \end{cases} \qquad (1.5.4)$$

Note that the terms $2\nu \partial_x u_x \partial_x H$, in the horizontal momentum equation, and $2\nu \partial_x u$, in the vertical velocity equation, are essentially first order derivatives of u, and can be discretized explicitly without the aforementioned severe restriction on the CFL condition. That gives us an efficient discretization of the eddy viscosity terms.

Moreover, since the incompressibility equation in (1.5.4) holds, then one has that

$$2\nu \partial_x u = 4\nu \frac{w_b - w}{h}.$$

Since it is of interest in this dissertation to obtain relatively simple systems, a simplification on the breaking mechanism described in (1.5.4) is proposed by assuming a mild slope bottom for the breaking terms, that is

$$\partial_x H \approx 0, \quad \partial_t H \approx 0, \text{ and thus, } w_b \approx 0.$$

Therefore in order to take into account the simplified breaking mechanism on the

system (NH-1L), only the source term $S(U)$ has to be modified as follows

$$S(U) = -\begin{pmatrix} 0 \\ \tau_b \\ \mathcal{R}_{br} \end{pmatrix} \tag{1.5.5}$$

$\mathcal{R}_{br}$ being

$$\mathcal{R}_{br} = -4B|\partial_x(hu)|w, \quad B = 1 - \frac{\partial_x(hu)}{U_1}. \tag{1.5.6}$$

In Chapter 4 numerical experiments and comparisons with laboratory data will show that breaking waves can be accurately described with this simple and efficient breaking mechanism.

Due to the form of the breaking terms, they can be discretized as the friction with the bottom terms appearing at the horizontal momentum equation, τ_b. In this thesis this terms will be discretized in a semi-implicit manner.

Note that following the same procedure, a similar breaking mechanism can be introduced for the system (NHyp) modifying the source term

$$S(U) = -\begin{pmatrix} 0 \\ \tau_b \\ -2p + \mathcal{R}_{br} \\ 2c^2(w + \partial_t H) \end{pmatrix}, \tag{1.5.7}$$

and similarly for the system (YAM) replacing the vertical velocity equation by

$$\partial_t w = 2\frac{p}{h} + \mathcal{R}_{br},$$

being $\mathcal{R}_{br}$ the term defined in (1.5.6)

Remark 1.5.1. *Reinterpretation of the eddy viscosity approach:*

- *Let us consider the vertical component of the stress-tensor*

$$\tau_{zz} = 2\widetilde{\nu}(x, z, t)\partial_z W(x, z, t),$$

where $\widetilde{\nu}(x, z, t)$ is a positive function and W is the vertical velocity. Now, following the same process carried out in [259] to depth-average the vertical momentum equation from Euler equations. To do so, let us integrate the vertical component of the stress-tensor along $z \in [-H, \eta]$:

$$\int_{-H}^{\eta} \partial_z \tau_{zz} \ dz = 2 \int_{-H}^{\eta} \partial_z \widetilde{\nu} \partial_z W + \widetilde{\nu} \partial_{zz} W \ dz.$$

Due to the assumption of a linear vertical profile for the vertical velocity W, then $\partial_{zz}W = 0$ and $\partial_z W$ does not depend on z and thus

$$\int_{-H}^{\eta} \partial_z \tau_{zz} \, dz = 2\varsigma \partial_z W,$$

where $\varsigma = \int_{-H}^{\eta} \partial_z \widetilde{\nu}$ is the eddy viscosity. Using again the linearity of the vertical profile for W, and the no-penetration boundary condition:

$$\partial_z W = \frac{w - w_b}{h/2}, \qquad w = \frac{1}{h}\int_{-H}^{\eta} W \, dz.$$

Using the incompressible condition: $\dfrac{w - w_b}{h/2} = -\partial_x u$. Thus,

$$\int_{-H}^{\eta} \partial_z \tau_{zz} \, dz = -4\varsigma u_x.$$

Finally, it remains to choose a closure for ς in the system with the described depth-averaged vertical component of the stress-tensor.

- *Note that seting*

$$\varsigma = -\frac{1}{2}\nu,$$

where ν is the eddy viscosity described in (1.5.4), then coincides with the same term $2\nu\partial_x u$ introduced in the vertical momentum equation in (1.5.4).

Two space dimension

A new, simple and efficient breaking mechanism can be considered for two dimensional domains following the procedure presented in Remark 1.5.1. The same process as in [21] is used, to depth-average the vertical component of the stress-tensor. Due to the linearity on the vertical profile of the vertical velocity within the fluid layer, it is defined:

$$\boldsymbol{\mathcal{R}_{br}} = \int_{-H}^{\eta} \partial_z \tau_{zz} \, dz = 2\int_{-H}^{\eta} \partial_z \widetilde{\nu}\partial_z W + \widetilde{\nu}\partial_{zz}W \, dz = 2\varsigma\partial_z W,$$

where $\varsigma = -\int_{-H}^{\eta} \partial_z \widetilde{\nu}$ is the eddy viscosity. Using the incompressibility condition from (YAM-2D):

$$\boldsymbol{\mathcal{R}_{br}} = 4\varsigma\frac{w - w_b}{h}, \; w_b = -u\partial_x H - v\partial_x H - \partial_t H.$$

In this dissertation, as in [112], [219] and inspired in the definition of ς in Remark 1.5.1, ς is choosen to be

$$\varsigma = -\frac{1}{2}B|\partial_x(hu) + \partial_y(hv)|,$$

where B is a coefficient related to the breaking criteria. Following a natural and simpler extension of the criteria proposed by [219],

$$B = 1 - \frac{\partial_x(hu) + \partial_y(hv)}{U_1},$$

wave energy dissipation associated with breaking begins when $|\partial_x(hu) + \partial_y(hv)| \geq U_1$ and continues as long as $|\partial_x(\partial_x(hu) + \partial_y(hv)| \geq U_2$, where

$$U_1 = B_1\sqrt{gh}, \qquad U_2 = B_2\sqrt{gh},$$

denote the flow speeds at the onset and termination of the wave-breaking process and B_1, B_2 are calibration coefficients that should be calibrated through laboratory experiments. In this work, as in [112], [219], $B_1 = 0.5$ and $B_2 = 0.15$ for all the test cases studied.

Similarly to the case of one dimensional domains, a simplification is made by assuming a mild slope bottom for the breaking terms, that is

$$\nabla H \approx 0, \quad \partial_t H \approx 0, \text{ and thus, } w_b \approx 0.$$

Therefore the breaking mechanism considered consists in adding at the right hand side of the vertical equation of the systems (YAM-2D) or (NHyp-2D), the term:

$$\boldsymbol{\mathcal{R}_{br}} = -4B|\partial_x(hu) + \partial_y(hv)|w, \quad B = 1 - \frac{\partial_x(hu) + \partial_y(hv)}{U_1}. \tag{1.5.8}$$

A breaking mechanism for the two layer non-hydrostatic pressure system (NH-2L)

Although the generalization of the breaking mechanism presented above to the case of the two layer system straightforward, in [118] C. Escalante *et al.* designed an ad-hoc breaking mechanism for the case of the two layer non-hydrostatic pressure system (NH-2L). To do so, following the same ideas as for the case of the one layer system, let us consider the vertical component of the stress-tensor

$$\tau_{zz} = 2\widetilde{\nu}\partial_z w,$$

where $\widetilde{\nu}(x, z, t)$ is a positive function. The same process as in Subsection 1.2.1 is used to depth-average the vertical component of the stress-tensor. By taking into account the incompressibility condition and that the vertical velocity has a linear profile within each layer:

$$\int_{\mathcal{L}_\alpha} \partial_z \tau_{zz} \, dz = -\varsigma_\alpha h_\alpha \partial_x u_\alpha, \tag{1.5.9}$$

where $\varsigma_\alpha = \int_{\mathcal{L}_\alpha} \partial_z \widetilde{\nu}$.

Now the system is closed defining $\varsigma_\alpha(x,t)$. In the subsequent, ς_α are computed assuming the equations in one space domains, to better clarify the procedure. To do so, it is observed that the linear combination of the non-hydrostatic pressures, p_b and p_I appearing at the right hand side of the vertical equations, can be expressed in terms of u_α and its derivatives $\partial_{xx} u_\alpha, \partial_{xt} u_\alpha, \partial_x u_\alpha$ and $\partial_t u_\alpha$. The proposed election of ς_α in this work is based on the idea of cancelling those aforementioned $\partial_x u_\alpha$ terms with $-\varsigma_\alpha h_\alpha \partial_x u_\alpha$. The procedure is detailed in Appendix A. The following definition is proposed:

$$
\begin{cases}
\varsigma_1 = w_1 - 3u_1 \partial_x H + 2\partial_t H, \\[2ex]
\varsigma_2 = w_2 + 3u_2 \partial_x z_I + 2\partial_t H.
\end{cases}
\tag{1.5.10}
$$

Note that the deduced breaking terms are essentially first order derivatives of u_1, u_2, and can be discretized explicitly, as in the spirit of the case for the one-layer systems.

Finally, a breaking criteria to switch on/off the dissipation is needed. Following a natural and simpler extension of the criteria proposed by [219] and used in the case of the one layer system, wave energy dissipation associated with breaking begins when $|\partial_x(l_1 h u_1 + l_2 h u_2)| \geq U_1$ and continues as long as $|\partial_x(l_1 h u_1 + l_2 h u_2)| \geq U_2$, where

$$
U_1 = B_1 \sqrt{gh}, \qquad U_2 = B_2 \sqrt{gh},
$$

denote the flow speeds at the onset and termination of the wave-breaking process and B_1, B_2 are calibration coefficients that should be calibrated through laboratory experiments. In this work, as in [219] $B_1 = 0.5$ and $B_2 = 0.15$ for al the test cases studied.

Note that the breaking criteria to switch on/off the dissipation is a simplified version of the one proposed in [219], that includes some improvements such as: taking into account a residence time for the activation/deactivation of the criteria to accounting a continuous dissipation; or computing in the breaking criteria $|\partial_x(hu)|$ as $\frac{1}{2}(|\partial_x(hu)| + \partial_x(hu))$ which would automatically become zero on the back of the crest of the wave.

The breaking mechanism proposed in this work can be considered with this improved breaking criteria given in [219], as well as the one proposed in [163], which are more sophisticated and expensive.

Nevertheless, although a fast and straightforward breaking criterion has been chosen, the numerical tests in Chapter 4 will show that this technique performs adequately. Moreover, the simple breaking mechanism considered in this work: corrects the classical overshoot that dispersive models present for the run-up of waves (see Fig. 4.10); ensures the grid convergence even if breaking mechanism is switching on/off during the experiment (see Fig. 4.13). Although the simple breaking criterion does not detect hydraulic jumps, is observed that the proposed system without the breaking dissipation can handle well

with hydraulic jumps. In any case, a more sophisticated breaking detector that reveals hydraulic jumps can be considered as well.

1.6   Solitary waves

In this section, some details about solitary waves are given. These are waves that propagate without any temporal evolution in shape or size over a flat bottom. The wave has one global peak and decays far away from it. Solitary waves arise in many contexts, including the elevation of the surface of the water which is the case of our interest in this thesis. Solitary waves are believed to model some essential aspects of the coastal effects of tsunamis well (see [233]).

John Scott Russell made the initial observation of a solitary wave in shallow water. According to Russell's empirical formula, the speed equals $\sqrt{g(A + H_0)}$, where A is the amplitude of the peak of the solitary wave above the surface of the undisturbed water. As Bullough has shown in [23], Russell's approximated speed and the true speed of solitary waves observed in nature only differ by a term of $\mathcal{O}(A^2/H^2)$.

In general, it is not an easy task to derive an analytical expression for solitary waves. As it will be shown, the derivation of analytical solitary wave solutions involves solving an ordinary differential equation (ODE), which a priori may be difficult. There are several methods to find analytic expressions for solitary wave solutions of nonlinear PDEs. There are two straightforward methods, namely the direct integration method and the tanh-method (see [149],[11]).

In this subsection, we show an analytical expression for solitary waves for the non-hydrostatic pressure system (NH-1L), that can be found in [21]. This solitary wave solutions coincides with the approximated expressions given in the literature for system (YAM) as it can be seen in [259],[112] and references therein.

In this dissertation, we give a general procedure to compute numerically solitary wave solutions for some of the studied PDE systems by using a high order ODE solver. In particular, we will show some solitary solutions for the system (NHyp).

Later, an important class of solitary waves corresponding to ones that are solutions for the Euler equations are introduced. Since it is well known, no explicit expressions for solitary waves for Euler equations are known, and an interesting procedure to compute them numerically presented in [65],[104] will be employed.

Finally, some comparisons between the presented solitary waves for the non-hydrostatic pressure systems and the Euler equations will be shown. This comparison will show a significant mismatch between both solutions, specially for bigger amplitudes.

1.6.1   Analytical solitary wave solution for the system (NH-1L)

A family of solitary wave solutions for the system (NH-1L) is described in [21]. Given a flat bottom $H = H_0$, and an amplitude A, there exists a family of solitary wave solutions

for the system (NH-1L) given by

$$
\begin{cases}
h = H_0 + A \cdot \text{sech}^2 \left(\dfrac{x - C_e t}{l} \right), \\[2mm]
u = C_e \left(1 - \dfrac{d}{h} \right), \\[2mm]
w = -\dfrac{A C_e d}{l h} \, \text{sech} \left(\dfrac{x - C_e t}{l} \right) \text{sech}' \left(\dfrac{x - C_e t}{l} \right), \\[2mm]
p = \dfrac{A C_e^2 d^2}{2 l^2 h^2} \left((2H_0 - h) \left(\text{sech}' \left(\dfrac{x - C_e t}{l} \right) \right)^2 + \right. \\[2mm]
\left. \quad + h \, \text{sech} \left(\dfrac{x - C_e t}{l} \right) \text{sech}'' \left(\dfrac{x - C_e t}{l} \right) \right)
\end{cases}
\tag{1.6.1}
$$

where f' denotes the derivative of the function f. When finding such solitary wave solutions, some integration constant arise when the tanh-method (see [11]) is used. In order to satisfies the asymptotic conditions

$$
U'', \; U' \to 0, \; U \to \left(H_0, \; 0, \; 0, 0 \right)^t, \quad \text{when } \xi \to \pm\infty, \text{ and } U \text{ being } (h, u, w, p)^t,
$$

the following relations arise:

$$
C_e = \frac{l}{d} \sqrt{ \frac{g H_0^3}{l^2 - H_0^2} }, \quad l = H_0 \sqrt{ \frac{A + H_0}{A} }.
$$

Here, C_e denote the wave speed. l is related with the wavelength: due to the asymptotic behaviour, the wavelength can not be defined in a proper way. However, it is commonly accepted ([233]) that a measure of the wavelength of a solitary wave is the distance between the point x_f on the front and the tail x_t where the height is 1 % of the maximum, i.e., $\eta(x_f, t = 0) = \eta(x_t, t = 0) = A/100$. Then, one can consider $x_t = -3l$, $x_f = 3l$ and thus the wavelength is $6l$. Finally, d (m) is a parameter that controls the celerity.

During this dissertation, we will consider the family of solitary waves (1.6.1) depending on the amplitude A and the depth H_0. We will always choose d to be $d = H_0$, and thus one always has

$$
C_e = \sqrt{g(A + H_0)},
\tag{1.6.2}
$$

that corresponds with the celerity given by Russel and Bullough ([23],[221]).

1.6.2 Solitary wave solutions for the system (NHyp)

In this section we give a procedure to find solitary wave solutions of the hyperbolic system (NHyp). As pointed out in (1.3.6), the governing PDE system for a flat bottom

can be written in quasi-linear form

$$\partial_t U + A(U)\partial_x U = S(U),$$

where we also like to stress the dependency of A on the relaxation parameter $c = \alpha\sqrt{gH_0}, H_0 = 1$. During this subsection, we will use $\alpha = 1$ and $\alpha = 3$, to show the differences, and to provide numerical solitary waves for the value of the parameter $\alpha = 3$ that will be used in Chapter 4.

Let us consider a solitary wave moving along the $x-$axis at a constant velocity C_e. We look for solutions in the form $U(\xi)$, with $\xi = \dfrac{x - c_e t}{l}$. Hence, the time derivative is given by $\partial_t U = -\dfrac{C_e}{l}U'$ and the space derivative is $\partial_x U = \dfrac{1}{l}U'$, where the prime symbol denotes differentiation with respect to ξ. For these type of solitary wave solutions, the original PDE system reduces to the nonlinear ODE system

$$(A(U) - C_e I)\, U' = l \cdot S(U),$$

I being the identity matrix. The matrix $A(U) - C_e I$ is invertible provided that C_e is not an eigenvalue of $A(U)$. Therefore we finally get the ODE system

$$\begin{cases} U'(\xi) = l \cdot (A(U(\xi)) - C_e I)^{-1} S(U(\xi)), & \xi \in [0, D] \\ \\ U(0) = U_0. \end{cases} \quad (1.6.3)$$

D a large enough real number. A numerical method will be employed in this dissertation to solve this ODE system. To do that, the nonlinear ODE system is solved very accurately in a numerical way using *tenth order* version of the time DG method presented in this thesis (see Chapter 2) and using a very small time step of $\Delta\xi = 10^{-3}$. In what follows, we will consider this highly accurate numerical solution of the ODE system (1.6.3) as exact solution of the problem. This technique of using a *tenth order* version of the time DG method has been widely used by other authors (see e.g. [155]).

Let us construct a particular solitary wave solution by solving the ODE system (1.6.3) over a flat bottom $H = H_0$, with

$$C_e = \sqrt{g(A + H_0)}, \quad l = H_0\sqrt{\dfrac{A + H_0}{A}}.$$

as in (1.6.2). Let us consider the initial data

$$U(0) = \left(H_0 + 10^{-9}, \ 10^{-9}, \ 10^{-9}, 10^{-9}\right)^t.$$

One can checked numerically that the described procedure leads to a solitary wave in the form of Figure 1.11 that fulfils the asymptotic conditions

$$U'', \ U' \to 0, \quad \text{when } \xi \to \pm\infty$$

and

$$U \to \left(H_0,\ 0,\ 0, 0\right)^t \text{ when } \xi \to -\infty, \quad U \to \left(A + H_0,\ 0,\ 0, 0\right)^t \text{ when } \xi \to \infty.$$

Since we look for a numerical solution satisfying the typical asymptotic conditions

$$U'',\ U' \to 0,\ U \to \left(H_0,\ 0,\ 0, 0\right)^t, \text{ when } \xi \to \pm\infty,$$

we proceed as follows:

- First, we find the first point $\xi_M \in [0, D]$ where the numerical solution reach the maximum for the variable $\eta = h - H_0$.

- Then, we consider the ascending part of the solitary wave as the computed numerical solution for $\xi \in [0, \xi_M]$.

- The descending part of the solitary wave is construct by symmetry from $\xi = \xi_M$ to $\xi = 2\xi_M$.
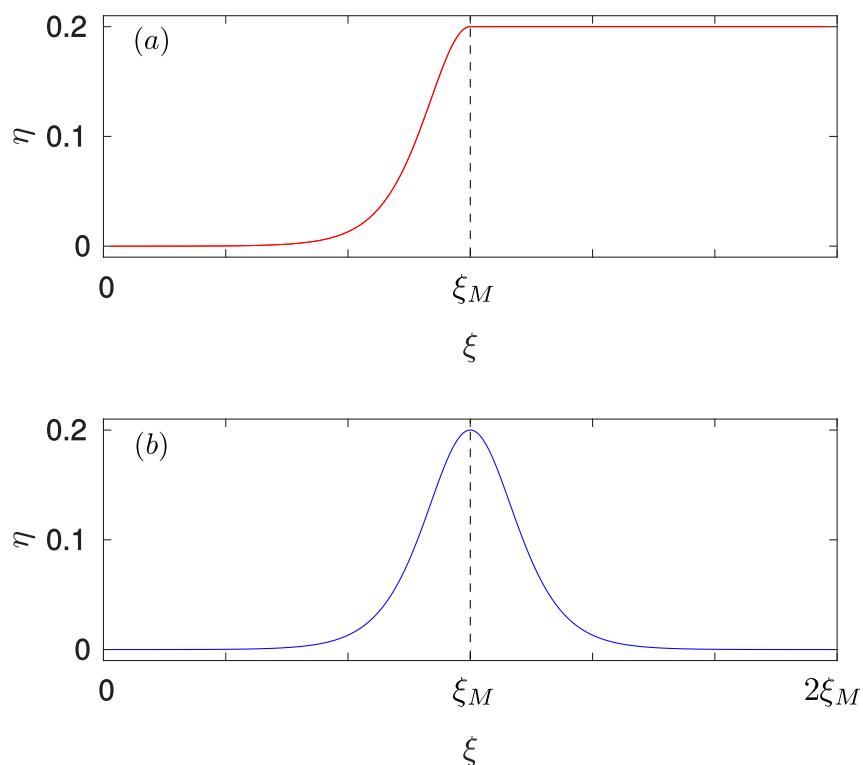
Figure 1.11: In (a) the numerical solution obtained after solve (1.6.3). In (b) the considered solitary wave after connect the ascending part with a symmetrical descending part.
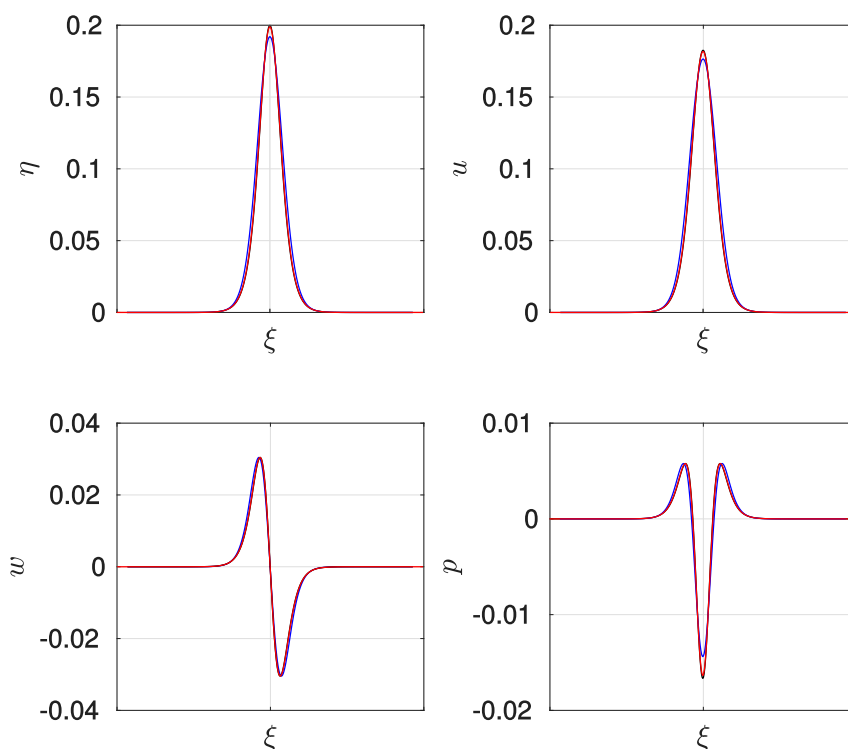
Figure 1.12: In black line the exact solution (1.6.1)-1.6.2 for the system (NH-1L). In blue the computed solution for the system (NHyp) with $\alpha = 1$ In red the computed solution for the system (NHyp) with $\alpha = 3$

Figures 1.12–1.13 show the computed solitary waves for $A = 0.2$ and $A = 0.6$ and for a relaxation parameter $c = \alpha\sqrt{gH_0}$, $\alpha = 1$ and 3. Figures 1.12–1.13 also show a comparison with the exact solitary wave given in (1.6.1) for the system (NH-1L). The comparison shows that even for the smaller value of the relaxation parameter α, the numerically computed solution for the system (NHyp) and the exact for the system (NH-1L) are in a perfect match.

Therefore, the solitary wave solution given in (1.6.1) can also be considered as an approximated solitary wave solution for the system (NHyp), and in practice, we will use it along this dissertation.

Remark 1.6.1. *An approximated expression of a solitary wave solution for the system (YAM) is given by (1.6.1)-(1.6.2). Note that although this is not an exact solution, it coincides with the approximated expressions given in the literature for this system (see [259, 112] and references therein).*
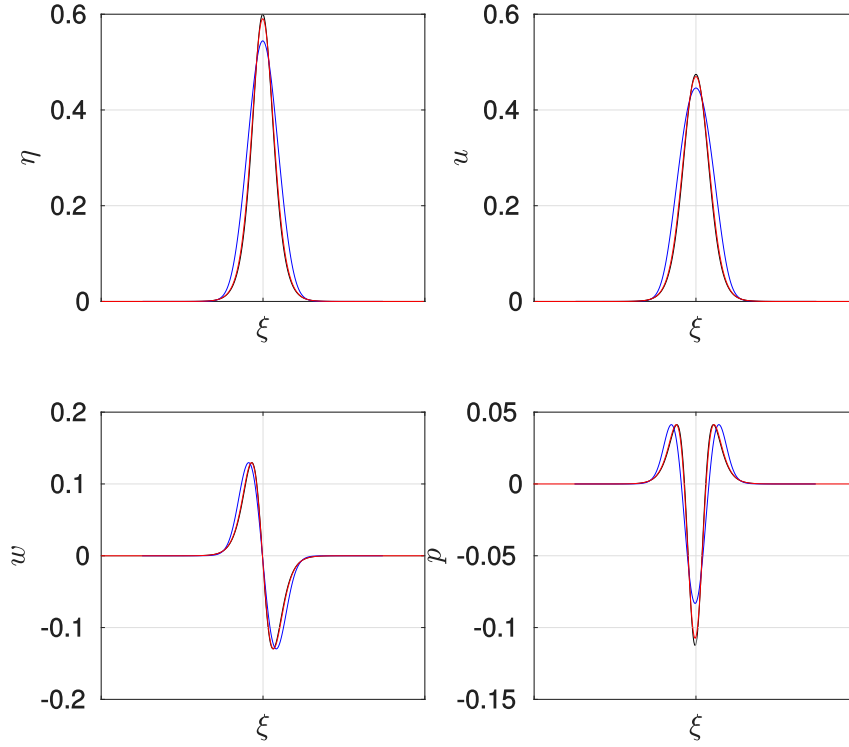
Figure 1.13: In black line the exact solution (1.6.1) for the system (NH-1L). In blue the computed solution for the system (NHyp) with $\alpha = 1$ In red the computed solution for the system (NHyp) with $\alpha = 3$

1.6.3   Solitary wave solutions for the Euler system

In order to compute solitary waves for the Euler equations (1.2.1), we use the numerical method presented in [65],[104]. The tool given in [65] provides the free-surface $\eta_E = h_E - H$, and profiles at a given level $z \in [-H, \eta_E]$, for horizontal and vertical velocities $u_E(x, z)$, $w_E(x, z)$, as well as for the total pressure $p_{T,E}(x, z)$.

Since we want to compare this solutions with the ones previously described for the non-hydrostatic pressure systems, let us split the vertical domain into L layers as in Subsection 1.1.4 and let us denote,

$$u_{E,\alpha} = \frac{1}{h_E} \int_{\mathcal{L}_\alpha} u_E \; dz, \quad w_{E,\alpha} = \frac{1}{h_E} \int_{\mathcal{L}_\alpha} w_E \; dz,$$

$$(1.6.4)$$

$$p_{E,\alpha} = \frac{1}{h_E} \int_{\mathcal{L}_\alpha} p_{T,E} - g\,(\eta - z) \; dz, \quad \alpha \in \{1, \ldots, L\}$$

the depth-averaged horizontal and vertical velocities as well as the non-hydrostatic pressure within the layer $\mathcal{L}_\alpha$. To compute the above integrals, we use a third order
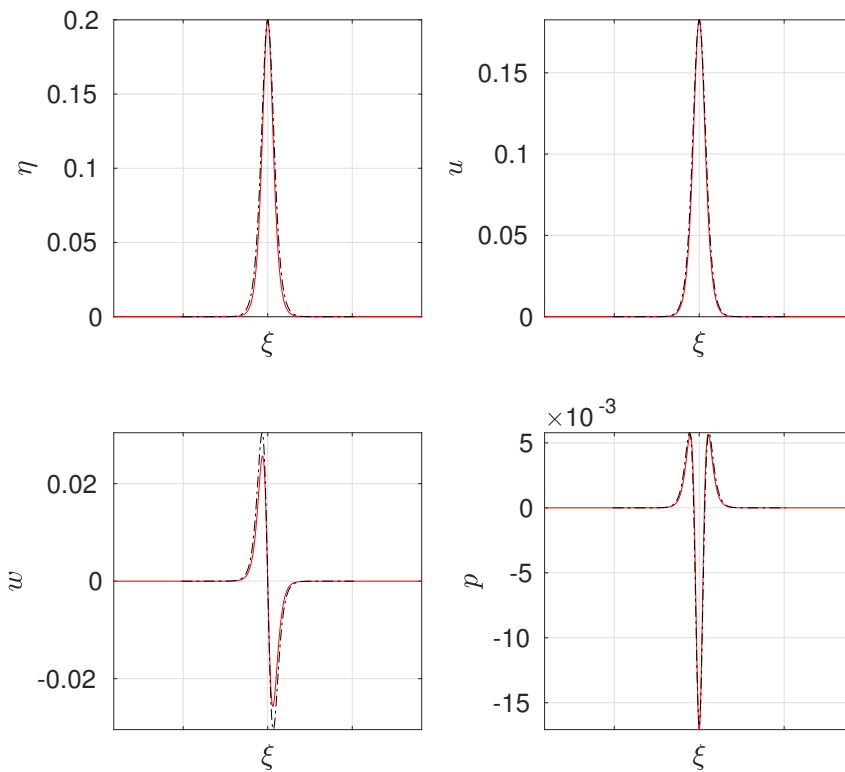
Figure 1.14: Comparison between Eulerian solitary wave (1.6.4) with $L = 1$ (in black) and solitary wave defined by (1.6.1) and (1.6.2) (in red) of amplitude $A = 0.2$.

Gaussian quadrature formula.

Figures 1.14–1.15 show two Eulerian solitary waves of amplitudes $A = 0.2$ and $A = 0.6$ computed using (1.6.4) with $L = 1$. A comparison with the solitary waves defined by (1.6.1)-(1.6.2) for the system (NH-1L) is shown, revealing important differences specially for bigger amplitudes. Moreover, Figure 1.16 show the vertical profile of the function $z \to p_{E,\alpha}(x = 0, z)$ being $x = 0$, the point such that $h_E(x = 0) = A = 0.6$, and $\alpha \in \{1, \ldots, L\}$, $L = 20$. The computed vertical profile does not appears to be linear, in contrast with the assumption of a linear vertical profile for the non-hydrostatic pressure of the described one-layer systems. Thus, it can be stated from these observations that the one-layer systems can not capture well the physics of a non-linear Eulerian solitary wave of bigger amplitudes.

Moreover, in Section 4.1, the computed Eulerian solitary waves (1.6.4) with $L = 1$ are used as initial condition for the system (NH-1L). This proves numerically the poor behaviour of the one layer systems when dealing with Eulerian solitary waves of big amplitudes.

Notwithstanding, in Section 4.1 we will show that the two-layer system can simulate correctly this kind of solitary waves of big amplitudes.
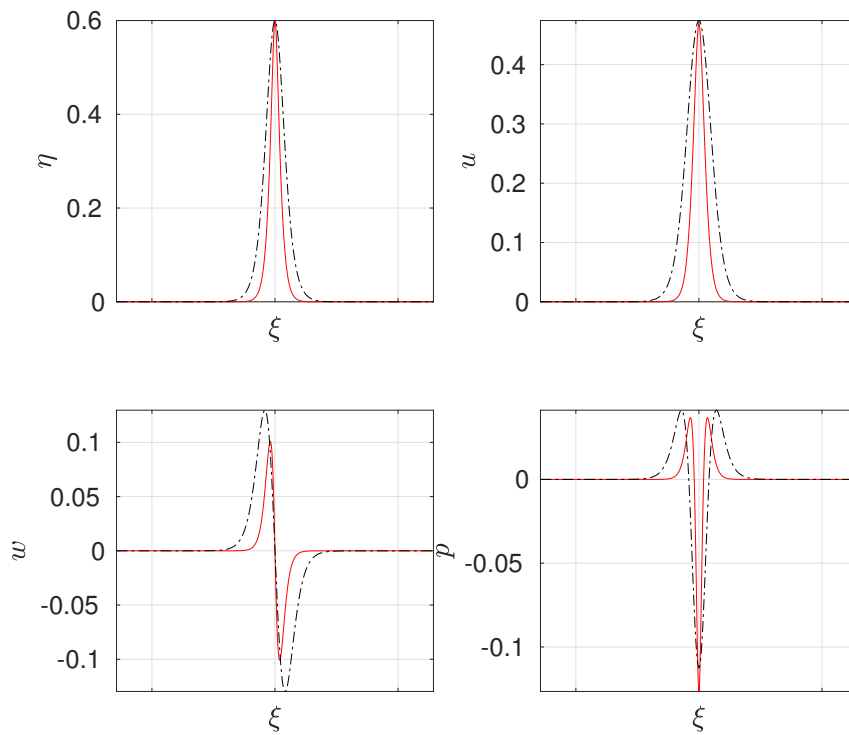
Figure 1.15: Comparison between Eulerian solitary wave (1.6.4) with $L = 1$ (in black) and solitary wave defined by (1.6.1) and (1.6.2) (in red) of amplitude $A = 0.6$.
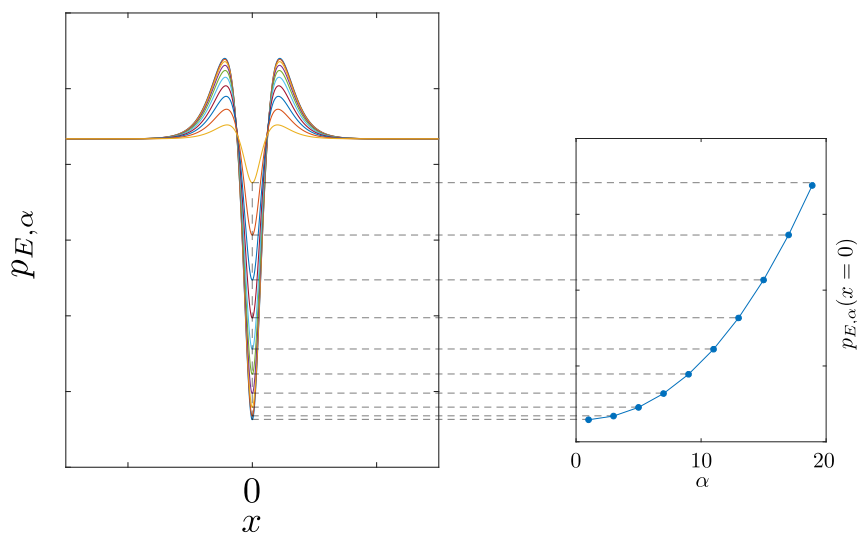
Figure 1.16: Non-hydrostatic pressure profile of the Eulerian solitary wave (1.6.4) with $L = 20$. Left figure shows the non-hydrostatic pressure for layers $\alpha = 1, 3, 5, \ldots, 19$. Right figure shows an interpolation of the vertical profile of p_E at the point $x = 0$.

Chapter 2

Finite volume and Discontinuous Galerkin methods

Contents

2.1   Introduction

In this chapter we describe a general methodology for developing high order well-balanced schemes for hyperbolic systems with nonconservative products and/or source terms that,

for the case of one dimensional domains, read as:

$$\partial_t U + \partial_x F(U) + B(U)\partial_x U = G(U)\partial_x \sigma \qquad (2.1.1)$$

where the unknown $U(x,t)$ is defined in $\Omega \times [0,T]$, Ω being a domain of $\mathbb{R}$, and takes values on an open convex subset $\mathcal{O}$ of $\mathbb{R}^N$; F and G are regular functions from $\mathcal{O}$ to $\mathbb{R}^N$; B is a regular matrix function from $\mathcal{O}$ to $\mathcal{M}_{N \times N}(\mathbb{R})$; and $\sigma(x)$ is a known function from $\mathbb{R}$ to $\mathbb{R}$. In the case of two dimensional domains the general hyperbolic system with nonconservative products and/or source terms reads as:

$$\partial_t U + \nabla \cdot \boldsymbol{F}(U) + \boldsymbol{B}(U) \cdot \nabla U = \boldsymbol{G}(U) \cdot \nabla \sigma \qquad (2.1.2)$$

where in this case the unknown $U(\boldsymbol{x},t)$ is defined in $\Omega \times [0,T]$, Ω being a domain of $\mathbb{R}^2$, and takes values in an open convex set $\mathcal{O}$ of $\mathbb{R}^N$; $\boldsymbol{F} = (F_1, F_2)$ is a regular function from $\mathcal{O}$ to $\mathbb{R}^N \times \mathbb{R}^N$; $\boldsymbol{B} = (B_1, B_2)$ is a regular matrix function from $\mathcal{O}$ to $\mathcal{M}_{N \times N} \times \mathcal{M}_{N \times N}(\mathbb{R})$; $\boldsymbol{G} = (G_1, G_2)$ is a regular function from $\mathcal{O}$ to $\mathbb{R}^{2N}$; and $\sigma(\boldsymbol{x})$ is a known function from $\mathbb{R}^2$ to $\mathbb{R}$.

PDE systems of this form appear in many fluid models in different contexts: shallow water models, mutliphase flow models, gas dynamic, or in this dissertation, accounts for the hydrostatic/non-dispersive part of the general formulation in one space dimension (GF) and in two space dimension (GF-2D).

Note that, the general formulations (GF) and (GF-2D) may contains source terms $S(U)$, that are not taken into account by (2.1.1) and (2.1.2) respectively. This source terms can be stiff such as frictions terms, and for the case of the systems described in this thesis, can also include breaking or in the case of the system (NHyp), some non-hydrostatic terms. Although the numerical methods described within this Chapter, can be extended to consider such source terms, we will treat them in a semi-implicit manner, as it will be described in Chapter 3. Only in the case of Discontinuous Galerkin schemes (DG), presented in Section 2.4, they will be treated in a different way.

The main difficulty of systems of the form (2.1.1) both from the theoretical and the numerical points of view comes from the presence of nonconservative products (when $B \neq 0$ or $G \neq 0$ and σ is discontinuous) that does not make sense in the distributional framework when the solution U develops discontinuities.

There are several mathematical theories allowing to formalize the notion of weak solution for a nonconservative system: Volpert [253], Colombeau [54], Dal Maso-LeFloch-Murat [72]. We briefly recall Dal Maso-LeFloch-Murat theory [72] to define weak solutions of nonconservative systems and how it has been used to establish the notion of path-conservative schemes. We show that, under this framework, it is possible to extend to the nonconservative case many well-known numerical schemes that are commonly used for system of conservation laws. Moreover, their extension to high order can be done as well. We briefly point out the difficulties related to the right definition of weak solution.

The use of a well-balanced numerical method is mandatory when the system studied involves perturbations of a steady state, whose amplitude is of the order or bigger than

the truncation error of the method. This is the case of a tsunami wave propagating at the ocean: its initial amplitude is small (although the lengthwave is huge) and it is not always possible to refine the mesh so that the truncation error of the method is lower than this amplitude. Another difficulty related to that is the numerical computation of stationary solutions: standard methods that solve correctly systems of conservation laws can fail in solving (2.1.1) when approaching equilibria or near to equilibria solutions. In the context of shallow water equations, Bermúdez and Vázquez-Cendón introduced in [14] the condition called *C-property*: a scheme is said to satisfy this condition if it solves correctly the steady-state solutions corresponding to water at rest. This idea of constructing numerical schemes that preserve some equilibria, which are called in general *well-balanced* schemes, has been studied by many authors. The design of numerical methods with good properties for problems of the form (2.1.1) or the particular cases corresponding to $B = 0$ (systems of balance laws) is a very active front of research: see, for instance, [6], [16], [15], [18], [37], [55], [56], [82], [139], [140], [141], [145], [146], [172], [174], [199], [209], [211], [212], [215], [222], [234], [248], [258], [162], [85], [86], [247] among others.

As it will be seen, the strategy to obtain well-balanced methods has a close relation with the difficulty related to the definition of the nonconservative products appearing in the system.

In this chapter, we briefly recall the main theoretical results concerning path-conservative schemes and show its usefulness to state a general framework to design finite volume numerical methods for systems of the form (2.1.1)- (2.1.2).

As it will be seen in Section 2.2, the framework of path-conservative schemes makes it possible to extend to the nonconservative case many well-known numerical methods for systems of conservation laws in a natural way. A class of efficient first order path-conservative schemes, namely *Polinomial Viscosity Methods*, is briefly described. The extension to high order of the discussed schemes is also introduced, by using reconstruction operators. Finally, we analyze the well-balanced property of the numerical methods. Then, in Section 2.3 we briefly recall the ideas given in the Section 2.2 for the case of PDEs over two space dimension. Finally, in Section 2.4 a different branch of numerical schemes in described: Discontinuous Galerkin schemes. There, we described the ADER Discontinuous Galerkin schemes that can be applied to any system of the form (2.1.1)-(2.1.2), along with an a posterior subcell finite volume limiter strategy.

2.2 Finite volume path-conservative schemes in one space dimension

Let us consider first order quasi-linear PDE systems:

$$\partial_t W + \mathcal{A}(W)\partial_x W = \mathbf{0}, \quad x \in \Omega \subset \mathbb{R}, \ t > 0, \tag{2.2.1}$$

with initial condition

$$W(x,0) = W_0(x) \quad x \in \Omega \subset \mathbb{R}, \tag{2.2.2}$$

in which the unknown $W(x,t)$ is defined in $\Omega \times [0,T]$, Ω being a domain of $\mathbb{R}$, and takes values on an open convex subset $\mathcal{O}$ of $\mathbb{R}^M$, and

$$W \in \Omega \mapsto \mathcal{A}(W) \in \mathcal{M}_{M \times M}(\mathbb{R})$$

is a smooth locally bounded map. The system is supposed to be strictly hyperbolic, i.e. for all $W \in \Omega \times [0,T]$ the matrix $\mathcal{A}(W)$ has M real and distinct eigenvalues

$$\lambda_1(W) < \cdots < \lambda_M(W),$$

and $\mathcal{A}(W)$ is thus diagonalizable. Any system (2.1.1) may be rewritten in the form (2.2.1) by considering σ as an unknown and by adding the equation $\partial_t \sigma = 0$. Then:

$$W = (U, \ \sigma)^T,$$

and $\mathcal{A}(W)$ is the matrix whose block structure is as follows:

$$\mathcal{A}(W) = \left(\begin{array}{c|c} A(U) & -G(U) \\ \hline 0 & 0 \end{array} \right),$$

where $A(U) = J_F(U) + B(U)$, $J_F(U)$ being the Jacobian matrix of the flux function F, U in an open convex set on $\mathbb{R}^N$, $N = M - 1$.

In order to design finite volume methods for systems of the form (2.2.1), we may proceed, as it is done for systems of conservation laws, by integrating the equation in an arbitrary space-time rectangle $[a,b] \times [t_0, t_1]$:

$$\int_a^b W(x,t_1) \, dx = \int_a^b W(x,t_0) \, dx - \int_{t_0}^{t_1} \int_a^b \mathcal{A}(W(x,t)) \partial_x W(x,t) \, dx \, dt. \tag{2.2.3}$$

The difficulty comes from the fact that the last integrand may be discontinuous and it is expected to be a measure involving Dirac's deltas at the discontinuities. Under some hypotheses of regularity for $\mathcal{A}$, the theory introduced by Dal Maso, LeFloch, and Murat [72] allows to define the product $\mathcal{A}(W)\partial_x W$ for functions W with bounded variation, provided a family of Lipschitz continuous paths $\Phi : [0,1] \times \Omega \times \Omega \to \Omega$ is prescribed, which must satisfy certain regularity and compatibility conditions. In particular

$$\Phi(0; W_L, W_R) = W_L, \qquad \Phi(1; W_L, W_R) = W_R, \tag{2.2.4}$$

and

$$\Phi(s; W, W) = W. \tag{2.2.5}$$

According to this theory, given a function $W(x)$ with bounded variation, the product $\mathcal{A}(W)\partial_x W$ is defined as a locally bounded measure. This measure coincides with the

distributional derivative in the special case of a conservative product, for which $\mathcal{A}(W)$ is the Jacobian matrix for some function $F(W)$. The interested reader is addressed to [72] for a rigorous and complete presentation of this theory.

In practice, the family of paths can be interpreted as a tool to give a sense to the last integral appearing in (2.2.3) for piecewise smooth functions W. More precisely, given a bounded variation function $W : [a, b] \to \mathbb{R}^M$, we define:

$$
\fint_a^b \mathcal{A}(W(x)) \partial_x W(x) \, dx = \int_a^b \mathcal{A}(W(x)) \partial_x W(x) \, dx
$$
$$
+ \sum_l \int_0^1 \mathcal{A}(\Phi(s; W_l^-, W_l^+)) \partial_s \Phi(s; W_l^-, W_l^+) \, ds. \quad (2.2.6)
$$

In this definition, W_l^- and W_l^+ represent, respectively, the limits of W to the left and right of its lth discontinuity (remember that the set of discontinuities of a bounded variation function is countable). Observe that, in (2.2.6), the family of paths has been used to determine the weight of the Dirac measures placed at the discontinuities of W.

According to this definition of integral, a weak solution can be defined as a function satisfying

$$
\int_a^b W(x, t_1) \, dx = \int_a^b W(x, t_0) \, dx - \int_{t_0}^{t_1} \fint_a^b \mathcal{A}(W(x, t)) \partial_x W(x, t) \, dx \, dt, \quad (2.2.7)
$$

for every space-time rectangle $[a, b] \times [t_0, t_1]$.

Once the notion of integral of the nonconservative product has been stated and proceeding as in the conservative case, it is easy to check that, across a discontinuity, weak solutions have to satisfy the generalized Rankine-Hugoniot condition:

$$
\xi(W^+ - W^-) = \int_0^1 \mathcal{A}(\Phi(s; W^-, W^+)) \partial_s \Phi(s; W^-, W^+) \, ds, \quad (2.2.8)
$$

where ξ is the speed of propagation of the discontinuity, and W^- and W^+ are the left and right limits of the solution at the discontinuity. If $\mathcal{A}(W)$ is the Jacobian matrix for some function $F(W)$, (2.2.8) reduces to the standard Rankine-Hugoniot condition:

$$
\xi(W^+ - W^-) = F(W^+) - F(W^-), \quad (2.2.9)
$$

independently of Φ.

As it happens for systems of conservation laws, in order to have uniqueness of solution, an entropy condition has to be added to the notion of weak solution: let us assume that (2.2.1) is equipped with an entropy pair $(\mathcal{H}, Q)$, i.e, a convex function $\mathcal{H} : \Omega \to \mathbb{R}$ and a function $Q : \Omega \to \mathbb{R}$ such that $\nabla Q(W) = \nabla \mathcal{H}(W) \cdot \mathcal{A}(W)$. Then, a weak solution is said to be an *entropy solution* if it satisfies the inequality

$$
\partial_t \mathcal{H}(W) + \partial_x Q(W) \leq 0, \quad (2.2.10)
$$

in the sense of distributions.

Therefore, it is clear that the concept of weak solution strongly depends on the chosen family of paths, which is a priori arbitrary. The crucial question is thus how to choose the "good" family of paths. The answer to this question is not easy and it will be discussed in Section 2.2.1. Meanwhile, let us assume that the family of paths, and thus the definition of weak solution, has been chosen.

2.2.1   Path-conservative numerical schemes

In order to discretize the system, computing cells $I_i = [x_{i-1/2}, x_{i+1/2}]$ are considered, whose size Δx is supposed to be constant for simplicity. Let us also suppose that $x_{i+1/2} = i\Delta x$ and we denote by $x_i = (i - 1/2)\Delta x$ the center of the cell I_i. Let Δt be the constant time step and define $t_n = n\Delta t$. Let us denote by W_i^n the approximation of the cell average of the weak solution at the cell I_i at time t_n provided by the scheme. The initial cell values are thus given by:

$$W_i^0 = \frac{1}{\Delta x} \int_{x_{i-1/2}}^{x_{i+1/2}} W_0(x)\, dx. \tag{2.2.11}$$

From (2.2.7), the cell averages of weak solutions satisfy the equality:

$$\frac{1}{\Delta x} \int_{I_i} W(x, t_{n+1})\, dx = \frac{1}{\Delta x} \int_{I_i} W(x, t_n)\, dx - \frac{\Delta t}{\Delta x} \frac{1}{\Delta t} \int_{t_n}^{t_1} \fint_{I_i} \mathcal{A}(W)\partial_x W\, dx\, dt, \tag{2.2.12}$$

In the following let us relax the notation in time by denoting $W(x_i, t_n) = W_i^n$. According to Parés [205], we consider thus numerical methods of the form:

Definition 1. *Given a family of paths Φ, a numerical scheme is said to be Φ-conservative if it can be written under the form:*

$$W_i^{n+1} = W_i^n - \frac{\Delta t}{\Delta x}\big(\mathcal{D}_{i-1/2}^+ + \mathcal{D}_{i+1/2}^-\big), \tag{2.2.13}$$

where

$$\mathcal{D}_{i+1/2}^\pm = \mathcal{D}^\pm\big(W_i^n, W_{i+1}^n\big),$$

$\mathcal{D}^-$ and $\mathcal{D}^+$ being two continuous functions from Ω^2 to Ω satisfying

$$\mathcal{D}^\pm(W, W) = 0 \quad \forall W \in \Omega, \tag{2.2.14}$$

and

$$\mathcal{D}^-(W_L, W_R) + \mathcal{D}^+(W_L, W_R) = \int_0^1 \mathcal{A}\big(\Phi(s; W_L, W_R)\big)\partial_s\Phi(s; W_L, W_R)\, ds, \tag{2.2.15}$$

for every set $\{W_L, W_R\} \subset \Omega$.

Remark 2.2.1. *The notion of path-conservative is a generalization of that of conservative method for a system of conservation laws in the following sense: if $\mathcal{A}(W)$ is the Jacobian of a flux function F, then (2.2.15) reduces to*

$$\mathcal{D}^-(W_L, W_R) + \mathcal{D}^+(W_L, W_R) = F(W_R) - F(W_L). \tag{2.2.16}$$

Therefore, we can define

$$\mathcal{F}(W_L, W_R) = \mathcal{D}^-(W_L, W_R) + F(W_L), \tag{2.2.17}$$

or, equivalently,

$$\mathcal{F}(W_L, W_R) = F(W_R) - \mathcal{D}^+(W_L, W_R). \tag{2.2.18}$$

Then, (2.2.14) leads to

$$\mathcal{F}(W, W) = F(W)$$

so that $\mathcal{F}$ is a numerical flux consistent with F, and using (2.2.17)-(2.2.18) in (2.2.13), it can be easily checked that the numerical method can be rewritten as the conservative method:

$$W_i^{n+1} = W_i^n - \frac{\Delta t}{\Delta x}\big(\mathcal{F}_{i+1/2} - \mathcal{F}_{i-1/2}\big), \tag{2.2.19}$$

with

$$\mathcal{F}_{i+1/2} = \mathcal{F}\big(W_i^n, W_{i+1}^n\big).$$

Due to this, if the system (2.2.1) involves some conservation laws (as it happens with the mass equations in the one or the two-layer shallow water system) a path-conservative method will be conservative for these equations. The same happens if a linear combination of some of the equations gives a conservation law.

Finally, let us remark that path-conservative schemes have been successfully applied to many different problems, besides the shallow-water or multi layer shallow-water models. For instance, they have been applied to Saint Venant-Exner [50], turbidity currents [192], Ripa model [224], two-modes shallow-water system [31], Baer-Nunziato model [100], Pitman-Le model [209], Savage-Hutter models [119], Bingham shallow-water system [120], blood flow [194], two-phase flows [195], among others.

Convergence and choice of paths

In [33] a negative result of convergence for path-conservative numerical methods was given together with several numerical examples. Later, a new example was given in [2]. These results have led in many cases to an oversimplified picture according to which path-conservative methods do not converge. The goal of this paragraph is to shed some light in this rather involved aspect of the convergence failure and to show that this is due to the mathematical nature of nonconservative systems.

The experience proves that path-conservative numerical methods converge with the expected order of accuracy and, under the adequate CFL condition, with the same stability property as their conservative counterparts. The difficulty comes from the fact that the limits of numerical solutions may differ from the *correct* ones. Nevertheless, as it has been mentioned, weak solutions of nonconservative systems may be defined in infinitely many ways. Then, what does *the correct weak solutions* mean?

In many cases, mathematical models based on hyperbolic system are the vanishing diffusion and/or dispersion limit of a family of PDE system involving higher order terms. In order to fix the ideas, let us suppose that we have a system of the form (2.2.1) which is the vanishing diffusion limit of

$$\partial_t W + \mathcal{A}(W)\partial_x W = \varepsilon R \partial_{xx} W, \tag{2.2.20}$$

where R is a positive definite matrix. Then, the adequate notion of weak solution (and thus the correct choice of the family of paths) should be consistent with the *traveling waves* of the regularized system: see [170]. Remember that a traveling wave

$$W_\epsilon(x,t) = V\left(\frac{x - \sigma t}{\epsilon}\right), \tag{2.2.21}$$

is a solution of (2.2.20) satisfying

$$\lim_{\xi \to -\infty} V(\xi) = W^-, \quad \lim_{\xi \to +\infty} V(\xi) = W^+, \quad \lim_{\xi \to \pm\infty} V'(\xi) = 0.$$

If there exists a traveling wave of speed σ linking the states W^-, W^+, the limit when ϵ tends to 0 of W_ϵ,

$$W(x,t) = \begin{cases} W^- & \text{if } x < \sigma t \\ W^+ & \text{if } x > \sigma t \end{cases}$$

should be an admissible weak solution of the nonconservative hyperbolic system. An easy computation shows that V has to solve

$$-\sigma V' + A(V)V' = RV''. \tag{2.2.22}$$

By integrating (2.2.22) from $-\infty$ to ∞ and taking into account the boundary conditions, we obtain the jump condition

$$\int_{-\infty}^{\infty} A(V(\xi))V'(\xi)\, d\xi = \sigma(W^+ - W^-).$$

If this jump condition is compared with the generalized Rankine-Hugoniot condition (2.2.8), it is clear that the good choice for the path connecting the states W^- and W^+ would be, after a reparametrization, the viscous profile.

Observe that, while for systems of conservation laws, the jump condition reduces to the standard Rankine-Hugoniot one regardless of the form of the diffusion term, now the jump condition depends explicitly of the viscous profile that, in turns, depend of the specific choice of the matrix R.

This observation is the key point to understand the fact that many numerical methods fail in converging to the correct weak solutions: the limits of the numerical solutions satisfy a jump condition which is related to the *numerical viscosity* of the method and not to the physically relevant one. Of course, this phenomenon affects to any numerical method in which the small scale effects (the vanishing diffusion and/or dispersion) are not taken into account, regardless of whether it is path-conservative or not. For instance, even the Godunov method based on the right weak solutions of the Riemann problems fails, in general, to converge to the right solution: this is due to the numerical viscosity introduced in the averaging step.

In order to overcome this difficulty, one could use viscosity-free methods based on Random Choice, as Glimm, or front-tracking methods; or methods based on the equivalent equation; or use methods that control the entropy losses across discontinuities like nonlinear projection methods; or methods based on kinetic relations (see [171] and the references therein).

Unfortunately, many of these techniques are very difficult or very costly to apply to complex nonconservative systems as the two-layer shallow water model.

Let us conclude with some remarks:

- The difficulties of convergence to the right weak solutions is not always present. For instance, in systems of balance laws with continuous σ there is no ambiguity in the definition of weak solution and all the numerical methods discussed in Chapter 3 converge to them.

- The computation of viscous profiles may be a very difficult task. In that case, the family of straight segments is a sensible choice, as their corresponding jump conditions give a third order approximation of the physically correct ones [49].

- In many cases, the numerical results provided by different numerical methods are very close to each other, although all of them may be far from the right weak solutions. This fact is in good agreement with the results obtained in [57] according to which the Hugoniot curve coincides up to third order (in the amplitude of the shock) when the matrix of the system and the viscosity matrix commute.

2.2.2   Some path-conservative schemes: Roe and PVM methods

In this subsection, we present some examples of path-conservative systems for the system (2.2.1) that we will use throughout this dissertation.

Roe methods

Roe methods are based on the following extension of a Roe linearization to the nonconservative case introduced in [248]:

Definition 2. *Given a family of paths Φ, a function $\mathcal{A}_\Phi \colon \Omega \times \Omega \mapsto M_{M \times M}(\mathbb{R})$ is called a* Roe linearization *if it verifies the following properties:*

- *for each $W_L, W_R \in \Omega$, $\mathcal{A}_\Phi(W_L, W_R)$ has M distinct real eigenvalues,*

- *$\mathcal{A}_\Phi(W, W) = \mathcal{A}(W)$ for every $W \in \Omega$,*

- *for any $W_L, W_R \in \Omega$,*

$$\mathcal{A}_\Phi(W_L, W_R) \cdot (W_R - W_L) = \int_0^1 \mathcal{A}(\Phi(s; W_L, W_R)) \partial_s \Phi(s; W_L, W_R)\, ds. \quad (2.2.23)$$

Once the linearization has been chosen, the corresponding Roe scheme can be written as a path-conservative scheme in the form (2.2.13) with

$$\mathcal{D}^\pm(W_L, W_R) \;\; = \;\; \mathcal{A}_\Phi^\pm(W_L, W_R) \cdot (W_R - W_L),$$

where, as usual,

$$\mathcal{A}_\Phi^\pm(W_L, W_R) = \frac{1}{2}\big(\mathcal{A}_\Phi(W_L, W_R) \pm |\mathcal{A}_\Phi(W_L, W_R)|\big), \quad (2.2.24)$$

where

$$|\mathcal{A}_\Phi(W_L, W_R)| = K_\Phi(W_L, W_R) \cdot |L_\Phi(W_L, W_R)| \cdot K_\Phi(W_L, W_R)^{-1}. \quad (2.2.25)$$

Here, $|L_\Phi(W_L, W_R)|$ is the diagonal matrix whose coefficients are the absolute value of the eigenvalues of $\mathcal{A}_\Phi(W_L, W_R)$ and $K_\Phi(W_L, W_R)$ a $M \times M$ matrix whose columns are associated eigenvectors.

Using this expression, the numerical method can be rewritten as follows:

$$W_i^{n+1} = W_i^n - \frac{\Delta t}{2\Delta x}\big(\mathcal{A}_\Phi(W_{i-1}^n, W_i^n)(W_i^n - W_{i-1}^n) + \mathcal{A}_\Phi(W_i^n, W_{i+1}^n)(W_{i+1}^n - W_i^n)\big)$$

$$- \frac{\Delta t}{2\Delta x}\big(\big|\mathcal{A}_\Phi(W_{i-1}^n, W_i^n)\big|(W_i^n - W_{i-1}^n) - \big|\mathcal{A}_\Phi(W_i^n, W_{i+1}^n)\big|(W_{i+1}^n - W_i^n)\big). \quad (2.2.26)$$

In this form, it is clear that the second term in the right-hand side is a centered approximation of $\mathcal{A}(W)\partial_x W$ and the third term is the numerical viscosity.

Let us discuss now the application of Roe methods to systems of the form (2.2.1). Let us denote the path written as

$$\Phi = \begin{pmatrix} \Phi_U \\ \\ \Phi_\sigma \end{pmatrix}.$$

Following [208], we consider linearizations of the form:

$$\mathcal{A}_\Phi(W_L, W_R) = \left(\begin{array}{c|c} A_\Phi(W_L, W_R) & -G_\Phi(W_L, W_R) \\ \hline 0 & 0 \end{array} \right),$$

where

$$A_\Phi(W_L, W_R) = J_F(U_L, U_R) + B_\Phi(W_L, W_R), \tag{2.2.27}$$

$J_F(U_L, U_R)$ being a Roe linearization of the Jacobian of the flux F in the usual sense:

$$J_F(U_L, U_R) \cdot (U_R - U_L) = F(U_R) - F(U_L); \tag{2.2.28}$$

$B_\Phi(W_L, W_R)$ a matrix satisfying:

$$B_\Phi(W_L, W_R) \cdot (U_R - U_L) = \int_0^1 B(\Phi(s; W_L, W_R)) \partial_s \Phi_U(s; W_L, W_R) \, ds, \tag{2.2.29}$$

and $G_\Phi(W_L, W_R)$ a vector satisfying

$$G_\Phi(W_L, W_R) \cdot (U_R - U_L) = \int_0^1 G(\Phi(s; W_L, W_R)) \partial_s \Phi_\sigma(s; W_L, W_R) \, ds, \tag{2.2.30}$$

where it has been used that $\Phi = \left(\Phi_U, \ \Phi_\sigma \right)^t$. An easy calculation shows that, if (2.2.28)-(2.2.30) are satisfied, then (2.2.27) is a Roe linearization, provided that $A_\Phi(W_L, W_R)$ has N real distinct not vanishing eigenvalues:

$$\lambda_1(W_L, W_R) < \cdots < \lambda_N(W_L, W_R).$$

Finally, taking into account the structure of the matrices $\mathcal{A}_\Phi$ and $|\mathcal{A}_\Phi|$, as well as the Roe property (2.2.28), the numerical scheme (2.2.13) can be written in terms of the variable U as follows

$$U_i^{n+1} = U_i^n - \frac{\Delta t}{\Delta x} \left(D_{i-1/2}^+ + D_{i+1/2}^- \right),$$

where skipping the notation in time:

$$D_{i+1/2}^\pm \big(W_i, W_{i+1} \big) = \frac{1}{2} \big(F(U_{i+1}) - F(U_i) + B_{i+1/2}(U_{i+1} - U_i) - G_{i+1/2}(\sigma_{i+1} - \sigma_i) \big)$$
$$\pm \frac{1}{2} \big| A_{i+1/2} \big| \big(U_{i+1} - U_i - A_{i+1/2}^{-1} G_{i+1/2}(\sigma_{i+1} - \sigma_i) \big) \big), \quad (2.2.31)$$

and $A_{i+1/2} = A_\Phi(W_i, W_{i+1}), \ B_{i+1/2} = B_\Phi(W_i, W_{i+1}), \ G_{i+1/2} = G_\Phi(W_i, W_{i+1})$.

Polynomial viscosity methods

Besides the Roe methods, some other strategies can be used to construct path-conservative numerical schemes. The computation of the particular decomposition of Roe methods, requires the explicit knowledge of the eigenvalues and eigenvectors of the intermediate matrix. When an easy analytic expression is not available, as it is the case for the multi layer shallow water system or other geophysical models, the eigenvalues and eigenvectors of the matrix have to be numerically calculated at every intercell and at every time step, which is computationally expensive. The same difficulty arises in the Osher-Solomon solver [32, 203].

We present here some ideas introduced in [35], [43] and [48] to obtain numerical methods based on decomposition (2.2.24) of Roe matrices that overcomes this difficulty. The idea is to replace (2.2.24) by:

$$\widehat{\mathcal{A}}_\Phi^\pm(W_L, W_R) = \frac{1}{2}\left(\mathcal{A}_\Phi(W_L, W_R) \pm \mathcal{Q}_\Phi(W_L, W_R)\right), \qquad (2.2.32)$$

where

$$\mathcal{Q}_\Phi(W_L, W_R) = \left(\begin{array}{c|c} Q_\Phi(W_L, W_R) & Q_\Phi(W_L, W_R)A_\Phi^{-1}(W_L, W_R)G_\Phi(W_L, W_R) \\ \hline 0 & 0 \end{array}\right).$$

The expression of the corresponding numerical method is like (2.2.26) replacing the absolute value of the intermediate matrix by an approximation $\mathcal{Q}_\Phi$, easier to compute, that plays the role of viscosity matrix.

Note that different numerical schemes can be obtained when choosing $\mathcal{Q}_\Phi$. For instance, a rough approximation is given by the local Lax-Friedrichs (or Rusanov) method, in which:

$$Q_\Phi(W_L, W_R) = \max(|\lambda_i(W_L, W_R)|, i = 1, \ldots, N)I, \qquad (2.2.33)$$

I being the identity matrix. Remark that the definition of $Q_\Phi(W_L, W_R)$ only requires an estimation of the largest wave speed in absolute value. However, this approach gives excessive numerical diffusion for the waves corresponding to the lower eigenvalues. Alternatively, the choice

$$\mathcal{Q}_\Phi(W_L, W_R) = |A_\Phi(W_L, W_R)|,$$

corresponds to the Roe scheme, which needs the knowledge of the eigenstructure of the matrix A_Φ that might result expensive.

The strategy is then to consider viscosity matrices of the form

$$Q_\Phi(W_L, W_R) = f(A_\Phi(W_L, W_R)), \qquad (2.2.34)$$

where, $f : \mathbb{R} \mapsto \mathbb{R}$ satisfies the following properties:

(f_1) $f(x) \geq 0, \forall x \in \mathbb{R}$,

(f_2) $f(x)$ is *easy* to evaluate,

(f_3) the graph of $f(x)$ is *close* to the graph of $|x|$.

Moreover, if

(f_4) $f(0) > 0$

no entropy-fix techniques are required to avoid the appearance of non-entropy discontinuities at the numerical solutions.

The stability of the scheme is strongly related to the definition of the function $f(x)$. In particular, let

$$\lambda_{1,i+1/2} < \cdots < \lambda_{N,i+1/2},$$

be the eigenvalues of $A_\Phi(W_i, W_{i+1})$, i.e. $\lambda_{j,i+1/2} \equiv \lambda_j(W_i, W_{i+1})$, $j = 1, \ldots, N$, and assume that an usual CFL condition holds:

$$\frac{\Delta t}{\Delta x} \max_{i,j} |\lambda_{j,i+1/2}| \leq 1, \tag{2.2.35}$$

then the resulting scheme is L^∞-stable if $f(x)$ verifies the following condition [48]:

$$f(x) \geq |x|, \quad \forall\, x \in [\lambda_{1,i+1/2}, \lambda_{N,i+1/2}], \ \forall\, i \in \mathbb{Z}, \tag{2.2.36}$$

i.e., the graph of the function $f(x)$ must be above the one corresponding to the absolute value function in the interval containing the eigenvalues.

At the beginning of the eighties, Harten, Lax and van Leer [151] proposed to choose f as the linear polynomial $p(x)$ that interpolates $|x|$ at the smallest and largest eigenvalue, which results in a considerable improvement of the local Lax-Friedrichs method. This idea, which is on the basis of the HLL method, has been improved by several authors later (see [245] for a review).

Degond *et al.* in [84] constructed a simple approximation of $|A|$ by means of a polynomial that approximates $|x|$ without interpolation of the absolute value function at the exact eigenvalues. This approach has been extended to a general framework in [48], where the so-called PVM (Polynomial Viscosity Matrix) methods are defined in terms of viscosity matrices based on general polynomial evaluations of a Roe matrix. The idea is to consider viscosity matrices of the form:

$$\mathcal{Q}_\Phi(W_i, W_{i+1}) = P_r^{i+1/2}(\mathcal{A}_\Phi(W_i, W_{i+1}),$$

where $P_r^{i+1/2}(x)$ is a polynomial of degree r.

A number of well-known schemes can be redefined as a PVM method: this is the case for Roe, Lax-Friedrichs, Rusanov, HLL [151], FORCE [240], MUSTA [130],[242], etc. (see

Scheme	Polynomial	Coefficients
Lax-Friedrichs	$P_0(x) = \alpha_0$	$\alpha_0 = \dfrac{\Delta x}{\Delta t}$
HLL	$P_1(x) = \alpha_0 + \alpha_1 x$	$\alpha_0 = \dfrac{\lambda_{N,i+1/2}\|\lambda_{1,i+1/2}\| - \lambda_{1,i+1/2}\|\lambda_{N,i+1/2}\|}{\lambda_{N,i+1/2} - \lambda_{1,i+1/2}}$ $\alpha_1 = \dfrac{\|\lambda_{N,i+1/2}\| - \|\lambda_{1,i+1/2}\|}{\lambda_{N,i+1/2} - \lambda_{1,i+1/2}}$
FORCE	$P_2(x) = \alpha_0 + \alpha_2 x^2$	$\alpha_0 = \dfrac{\Delta x}{2\Delta t}, \ \alpha_2 = \dfrac{\Delta t}{2\Delta x}$

Table 2.1: Some well-known solvers as PVM schemes

[48] for details). The numerical scheme introduced in [84] and the Krylov-Riemann solver recently introduced in [246] can be viewed as particular case of PVM scheme as well. In Table 2.1 we show the polynomial corresponding to Lax-Friedrichs, HLL and FORCE schemes.

The numerical scheme for a PVM method can be expressed in the form (2.2.31) for the variables U_i with

$$D_{i+1/2}^{\pm}(W_i, W_{i+1}) = D_{i+1/2}^{\pm}(U_i, \sigma_i, U_{i+1}, \sigma_{i+1}) =$$
$$\frac{1}{2}\big(F(U_{i+1}) - F(U_i) + B_{i+1/2}(U_{i+1} - U_i) - G_{i+1/2}(\sigma_{i+1} - \sigma_i)\big)$$
$$\pm \frac{1}{2}Q_{i+1/2}\big(U_{i+1} - U_i - A_{i+1/2}^{-1}G_{i+1/2}(\sigma_{i+1} - \sigma_i))\big), \quad (2.2.37)$$

where $Q_{i+1/2} = P_r^{i+1/2}(A_{i+1/2})$.

Besides the interpretation of known numerical methods as PVM, this framework allows the derivation of new ones. For instance, in [125] a numerical method based on a polynomial that interpolates three values (the largest and lowest eigenvalues and the maximum of the intermediate ones) has been derived. This numerical method gives excellent results for the two-layer shallow water model. Another interesting family of PVM schemes based on *Chebyshev polynomials*, which provide optimal uniform approximations to the absolute value function has been proposed in [43].

We will consider the following notation for PVM methods. We will denote PVM-$l(S_0, \ldots, S_k)$ for a numerical scheme whose viscosity matrix $Q_{i+1/2}$ is defined by a polynomial of degree l whose coefficients depends on $S_0, \ldots, S_k$. In practice, the parameters $S_0, \ldots, S_k$ are related with the approximations of some of the wave speeds. For example, Lax-Friedrichs corresponds to PVM-$0(S_0)$, being $S_0 = \dfrac{\Delta x}{\Delta t}$, where Δt is related with the maximum of the propagation speed of the waves through the CFL condition.

Definition 3. *A numerical method PVM is said to be upwind if*

$$P_r^{i+1/2}(\mathcal{A}_{i+1/2}) = \begin{cases} \mathcal{A}_{i+1/2}, & \text{if } \lambda_{1,i+1/2} > 0, \\ -\mathcal{A}_{i+1/2}, & \text{if } \lambda_{N,i+1/2} < 0, \end{cases}$$

and we denote as PVM-U.

Thus, if

$$P_r^{i+1/2}(x) = \begin{cases} x, & \text{if } \lambda_{1,i+1/2} > 0, \\ -x, & \text{if } \lambda_{N,i+1/2} < 0, \end{cases}$$

then the resulting PVM method is upwind.

Notice that the term

$$C = Q_{i+1/2} A_{i+1/2}^{-1} G_{i+1/2}, \tag{2.2.38}$$

in (2.2.37) can be interpreted as the up-winding part of the source term discretization. This term makes no sense if any of the eigenvalues of $A_{i+1/2}$ vanishes. One way to deal with this kind of resonant problems has been proposed in [134].

In the subsequent paragraphs, we present the PVM methods that will be used along this thesis. For the sake of simplicity, we will suppress the dependency on the index $i+1/2$ appearing on the polynomial as well as on its coefficients. Thus, we will denote $P_r(x)$ instead of $P_r^{i+1/2}$, and α_j instead of $\alpha_j^{i+1/2}$.

- **PVM-1U(S_L, S_R) or HLL method**

  Let us consider in this section a PVM method defined with a polynomial of degree 1, this is (See Figure 2.1),
  $$P_1(x) = \alpha_0 + \alpha_1 x. \tag{2.2.39}$$

  In order to define the coefficients α_0 y α_1 let us impose the following two conditions:

  $P_1(S_L) = |S_L|$ y $P_1(S_R) = |S_R|$, where S_L (respectively S_R) is an approximation of the minimum (respectively maximum) of the wave speeds. A possibility is to take $S_L = \lambda_{1,i+1/2}, S_R = \lambda_{N,i+1/2}$, although a simple choice has been proposed by Davis [73], as follows:

  $$S_L = \min(\lambda_{1,i+1/2}, \lambda_{1,i}), \quad S_R = \max(\lambda_{N,i+1/2}, \lambda_{N,i+1}),$$

  being $\lambda_{i,1} < \cdots < \lambda_{i,N}$ the eigenvalues of the matrix $\mathcal{A}_\Phi(W_i, W_i)$. This enforces the entropy preserving property of the scheme. After some algebraic manipulations, it yields

  $$\alpha_0 = \frac{S_R|S_L| - S_L|S_R|}{S_R - S_L}, \quad \alpha_1 = \frac{|S_R| - |S_L|}{S_R - S_L}. \tag{2.2.40}$$
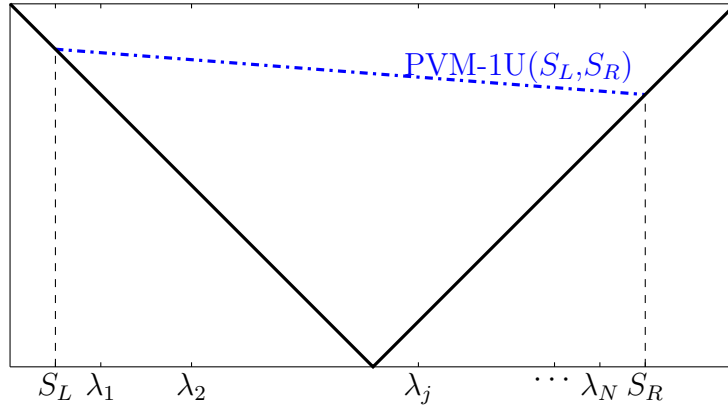
Figure 2.1: Polynomial associated to the method PVM-1U(S_L, S_R).

Remark 2.2.2. *Note that if $S_L > 0 \Rightarrow P_1(x) = x$ and if $S_R < 0 \Rightarrow P_1(x) = -x$. Then, the resulting method is upwind.*

Remark 2.2.3. *If we are in the case of a system of conservation laws ($B = 0$ y $G = 0$), the the flux is conservative and the PVM method coincides with the usual HLL scheme [152]. Thus, the described PVM-1U(S_L, S_R) scheme gives a natural generalization of the HLL method for nonconservative problems.*

- **PVM-2U(S_L, S_R, S_{int}) method or IFCP**

This method was proposed by E. Fernández *et al.* in [125] for the resolution of the two layer shallow water system. In [223], C. Sánchez-Linares *et al.* describe a generalisation for general case of nonconservative systems.

To do that, let us consider a polynomial of degree 2

$$P_2(x) = \alpha_0 + \alpha_1 x + \alpha_2 x^2, \tag{2.2.41}$$

and let us impose the following conditions:

$$P_2(S_L) = |S_L|, \ P_2(S_R) = |S_R| \text{ and } P_2(S_{int}) = |S_{int}|,$$

where S_L (respectively S_R) is an approximation of the minimum (respectively maximum) wave speeds and S_{int} is defined as

$$S_{int} = \mathcal{S}_{ext} \cdot \max\{|\lambda_{2,i+1/2}|, ..., |\lambda_{N-1,i+1/2}|\},$$

being

$$\mathcal{S}_{ext} = \begin{cases} \text{sgn}(S_R + S_L), & \text{if } (S_R + S_L) \neq 0, \\ 1, & \text{otherwise.} \end{cases} \tag{2.2.42}$$

The coefficients α_j, $j = 0, 1, 2$ are given by:

$$
\begin{aligned}
\alpha_0 &= \delta_L\, S_R\, S_{int} + \delta_R\, S_L S_{int} + \delta_{int}\, S_L\, S_R, \\
\alpha_1 &= -S_L(\delta_R + \delta_{int}) - S_R(\delta_L + \delta_{int}) - S_{int}(\delta_L + \delta_R), \\
\alpha_2 &= \delta_L + \delta_R + \delta_{int},
\end{aligned}
\tag{2.2.43}
$$

where

$$
\delta_L = \frac{|S_L|}{(S_L - S_R)(S_L - S_{int})}, \quad \delta_R = \frac{|S_R|}{(S_R - S_L)(S_R - S_{int})},
$$

$$
\delta_{int} = \frac{|S_{int}|}{(S_{int} - S_L)(S_{int} - S_R)}.
$$

Remark 2.2.4. *In [223], it shown that the IFCP scheme is linearly L^∞-stable under the usual CFL condition.*

2.2.3   High order finite volume schemes based on reconstruction of states

The goal of this section is to present the general expression of a high order method for (2.2.1) based on the use of a first order path-conservative numerical scheme and a reconstruction operator.

Let us denote by $\overline{W}_i(t)$ the exact cell average of the solution W of (2.2.1) over the cell I_i at time t,

$$
\overline{W}_i(t) = \frac{1}{\Delta x} \int_{x_{i-1/2}}^{x_{i+1/2}} W(x, t)\, dx.
$$

The following equation can be easily obtained from (2.2.1):

$$
\overline{W}_i' = -\frac{1}{\Delta x} \int_{x_{i-1/2}}^{x_{i+1/2}} \mathcal{A}(W(x, t)) \partial_x W(x, t)\, dx.
\tag{2.2.44}
$$

Let us consider a first order path-conservative numerical scheme (2.2.13) and a reconstruction operator of order s, i.e. an operator that associates to a given sequence $\{W_i\}$ two new sequences $\{W_{i+1/2}^-\}$, $\{W_{i+1/2}^+\}$ in such a way that, whenever

$$
W_i = \frac{1}{\Delta x} \int_{I_i} W(x)\, dx \quad \forall\, i \in \mathbb{Z}
$$

for some smooth function W, then

$$
W_{i+1/2}^\pm = W(x_{i+1/2}) + O\left(\Delta x^s\right) \quad \forall\, i \in \mathbb{Z}.
$$

In practice, the reconstructed states $W_{i+1/2}^{\pm}$ are calculated as follows; given a sequence $\{W_i\}$ of values at the cells, an approximation function is calculated at every cell I_i using the values W_j at a given *stencil*,

$$P_i(x) = P_i(x; W_{i-l}, \ldots, W_{i+r}),$$

with l, r two natural numbers. The reconstructions $W_{i+1/2}^{\pm}$ are then calculated by taking the limits of these functions at the intercells:

$$\lim_{x \to x_{i-1/2}^+} P_i(x) = W_{i-1/2}^+, \qquad \lim_{x \to x_{i+1/2}^-} P_i(x) = W_{i+1/2}^-. \qquad (2.2.45)$$

Following [207], we consider the semi-discrete method:

$$W_i' = -\frac{1}{\Delta x}\left(\mathcal{D}_{i-1/2}^+ + \mathcal{D}_{i+1/2}^- + \int_{I_i} \mathcal{A}[P_i(x)]\partial_x P_i(x)\,dx\right), \qquad (2.2.46)$$

where $\mathcal{D}_{i+1/2}^{\pm}$ are evaluated in $W_{i+1/2}^{\pm}(t)$

$$\mathcal{D}_{i+1/2}^{\pm} = \mathcal{D}^{\pm}(W_{i+1/2}^-(t), W_{i+1/2}^+(t)), \qquad (2.2.47)$$

where $\{W_{i+1/2}^{\pm}(t)\}$ represent the reconstructed states associated to $\{W_i(t)\}$, and

$$P_i(x) \equiv P_i(x; W_{i-l}(t), \ldots, W_{i+r}(t)). \qquad (2.2.48)$$

In (2.2.46) the approximation functions are used to approximate the regular part of the weak integral in (2.2.44) and the terms $\mathcal{D}_{i-1/2}^{\pm}$ are used again to split the Dirac measures corresponding to the discontinuities at the intercells.

The semi-discrete method (2.2.46) in terms of the variable U_i can be written, similarly to (2.2.37), as:

$$U_i' = -\frac{1}{\Delta x}\left(D_{i-1/2}^+(U_{i-1/2}^-, \sigma_{i-1/2}^-, U_{i-1/2}^+, \sigma_{i-1/2}^+) + D_{i+1/2}^-(U_{i+1/2}^-, \sigma_{i+1/2}^-, U_{i+1/2}^+, \sigma_{i+1/2}^+)\right)$$

$$- \frac{1}{\Delta x}\left(\int_{I_i} \partial_x F[P_{i,U}(x)] + B[P_{i,U}(x)]\partial_x P_{i,U}(x) - G[P_{i,U}(x)]\partial_x P_{i,\sigma}(x)\,dx\right). \quad (2.2.49)$$

$P_{i,U}(x)$ and $P_{i,\sigma}(x)$ being the reconstruction of U and σ in the cell i respectively. In practice, the integral terms in (2.2.49) are numerically approached with a 1D quadrature formula.

Notice that (2.2.49) is a system of ordinary differential equations to be solved by using a high order numerical solver with good properties. In practice the TVD Runge-Kutta schemes are used (see [143], [228]). Other time discretization can be considered, as ADER schemes developed by Toro and Dumbser (see [238],[92]).

Observe that there is an important difference between the conservative and the nonconservative case: while in the conservative case the numerical scheme is independent of the functions P_i chosen at the cells (only the property (2.2.45) is important), this is not the case for nonconservative systems. As a consequence, while the numerical scheme has order s for conservative systems, in the case of the scheme (2.2.46) the order is $\alpha = \min(s, s_1, s_2)$, where s_1 and s_2 are the order of accuracy of the reconstruction and its derivative inside the cell:

$$
\begin{aligned}
P_i(x) &= W(x) + O\left(\Delta x^{s_1}\right) \quad \forall\, x \in I_i, \\
P_i'(x) &= W'(x) + O\left(\Delta x^{s_2}\right) \quad \forall\, x \in I_i.
\end{aligned}
$$

For the usual reconstruction techniques one has $s_2 \le s_1 \le s$ and the order of (2.2.46) is thus s_2 for nonconservative systems and s for systems of conservation laws. Therefore a loss of accuracy may be observed when a technique of reconstruction is applied to a nonconservative problem. This effect has been detected and numerically verified for WENO-Roe methods in [29]. Nevertheless, the error estimate shown is rather pessimistic: in practice, the order of the observed error is usually $s_2 + 1$: see [24] or [29].

In [198] a very interesting technique has been introduced to avoid the explicit computation of $P_i'(x)$ so that the expected order of accuracy is increased to $\min(s, s_1)$. This technique is based on the use of the trapezoidal rule and Romberg extrapolation for the numerical approximation of the integrals in (2.2.46).

In [36] a high order finite volume central scheme on staggered grids for general hyperbolic systems, including those not admitting a conservation form, has been introduced. The method is based on a path-conservative method on staggered cells and central Runge–Kutta time discretization. In [31] a second order path-conservative Central-Upwind scheme for the two-mode shallow-water system was proposed.

ADER-FV and ADER-DG approaches proposed by Titarev and Toro [238] and Dumbser and Munz [97] are two other alternatives to construct high order schemes. In their original formulations, both approaches use the governing PDE itself in its strong differential form to achieve high order accuracy in time. This is done by means of the *Cauchy-Kovalewski* procedure that substitutes time derivatives with space derivatives via successive differentiation of the governing PDE with respect to space and time. This procedure may become cumbersome for general nonlinear hyperbolic PDE systems. In [99] and [93] an entirely numerical approach was presented that replaces the Cauchy-Kovalewski procedure by a local weak formulation of the governing PDE in space-time. The extension to nonconservative systems has been considered in [92] and the methodology will be briefly recalled in Subsection 2.4.

MUSCL reconstruction operator

In the literature, several reconstruction operators can be found, that usually are calculated by means of interpolation or approximation techniques. This is the case for ENO, WENO,

or hyperbolic reconstructions (see [153], [186], [62], [229], [93], [101], [102], among others.)

In this subsection we describe the MUSCL [169] reconstruction operator that will be used in this dissertation for rectangular meshes. Let us consider the second order reconstruction operator in one space dimension defined in a cell I_i by

$$W_i(x,t) = W_i(t) + (x - x_i)\left(\partial_x W(t)\right)_i, \tag{2.2.50}$$

where $W_i(t)$ is the averaged value of the solution at time t on the cell given by the numerical scheme and $\left(\partial_x W(t)\right)_i$ is an constant approximation of the partial derivative of the solution with respect to x. Here, we use the MUSCL reconstruction described in [169] where

$$\left(\partial_x W\right)_i = \text{minmod}\left(\theta\frac{W_i - W_{i-1}}{\Delta x}, \frac{W_{i+1} - W_{i-1}}{2\Delta x}, \theta\frac{W_{i+1} - W_i}{\Delta x}\right), \quad \theta \in [1,2], \tag{2.2.51}$$

where

$$\text{minmod}(z_1, z_2, \ldots) = \begin{cases} \min_j z_j & \text{si } z_j > 0 \,\forall\, j, \\ \max_j z_j & \text{si } z_j < 0 \,\forall\, j, \\ 0 & \text{en otro caso.} \end{cases} \tag{2.2.52}$$

The parameter θ is used to control the amount of numerical viscosity: higher values of θ corresponds with less dissipative numerical schemes but, in general, more oscillatory.

2.2.4   Well-balanced schemes

As it was said previously, when dealing with systems in the form (2.2.1), special care has to be taken when solving solutions that are close to a stationary solution. As it was mentioned in the introduction, the well-balanced property of the numerical method is crucial in these cases. In this section, first we state a precise definition of well-balanced method and next the well-balanced properties of the numerical methods introduced in the previous section are analyzed. Let us consider the following definitions:

Definition 4. *Consider a semi-discrete method to approximate* (2.1.1)

$$\begin{cases} U_i'(t) = \dfrac{1}{\Delta x}\, \mathcal{H}\left(U_j(t), j \in \mathcal{B}_i\right), \\ U(0) = U_0, \end{cases} \tag{2.2.53}$$

where $U(t) = \{U_i(t)\}_{i=1}^{N_T}$ represents the vector of the approximations to the averaged values of the exact solution; $U_0 = \{U_i^0\}$ is the vector of the all averages of the initial conditions; and $\mathcal{B}_i$ are the stencils. Given a smooth stationary solution U of the system, the numerical scheme is said to be exactly well-balanced for U if the vector of its cell averages is a critical point of (2.2.53), *i.e.*

$$\mathcal{H}(U_j, j \in \mathcal{B}_i) = 0. \tag{2.2.54}$$

Let us also introduce the concept of well-balanced reconstruction operator:

Definition 5. *Given a smooth stationary solution of* (2.1.1)*, a reconstruction operator is said to be well-balanced for* $U(x)$ *if the approximation functions* $P_i(x)$ *associated to the averaged values of* U *are also stationary solutions of the system* (2.1.1)*.*

Remark 2.2.5. *Here, as* $\sigma(x)$ *is a given function, we set that its reconstruction is* $P_i^\sigma(x) = \sigma(x), \ x \in V_i$.

In general, it is not easy to design a reconstruction operator which is well-balanced for every stationary solution. In [45] a strategy to construct such an operator has been introduced. The following results can be proved:

Theorem 2.2.1. *Let* U *be a stationary solution of* (2.1.1) *and let us assume that the family of paths* $\Phi(s, W_L, W_R) = (\Phi_U(s, W_L, W_R), \ \Phi_\sigma(s, W_L, W_R))^T$ *connecting two states* $W_L = (U(x_L), \sigma(x_L))^T$ *and* $W_R = (U(x_R), \sigma(x_R))^T$ *with* $x_L < x_R$ *is a reparametrization of* $x \in [x_L, x_R] \mapsto U(x)$, *then the first order PVM scheme* (2.2.37) *is exactly well-balanced for* U *whenever* $A_{i+1/2}$ *being a non-singular matrix.*

Remark 2.2.6. *Note that if the stationary solution is smooth, then* $U_{ij}^- = U_{ij}^+$ *and* $D_\Phi^\pm = 0$*, therefore, the well-balanced property of the high order method only depends on the well-balanced property of the reconstruction operator.*

Theorem 2.2.2. *Let* U *be a stationary solution of* (2.1.1)*. Let us suppose that the first order PVM path-conservative scheme* (2.2.37) *and the reconstruction operator chosen are exactly well-balanced for* U*. Then the numerical scheme* (2.2.49) *is also exactly well-balanced for* U *whenever* $A_{i+1/2}$ *being a non-singular matrix.*

Finally, let us remark that quadrature formulae also play an important role to preserve the well-balanced properties of the scheme. In fact, the previous results have been established assuming that the integrals are exactly computed. Thus, in order to preserve the well-balanced properties, quadrature formulae should be exact for the stationary solutions. For that purpose, the strategy developed in [34] can be used.

Well-balanced methods for a subset of stationary solutions of the system (SWE)

In many cases, depending on the characteristics of the phenomena, there is interest in preserving only a certain family of solutions. This is the case, for instance, in the one layer or the two-layer shallow water model with the stationary solutions corresponding to water at rest.

So, let us suppose that we are only interested in preserving stationary solutions related to a subset Γ_0 of Γ. In the particular case of the shallow water model (SWE), the family of stationary solution corresponding to water at rest are given by:

$$q = 0, \quad h - H = constant,$$

meaning that the velocity is zero and the free surface elevation is constant. The corresponding curves are straight lines in the space h, q, H and thus the family of straight segments

$$\Phi(s; W_L, W_R) = W_L + s(W_R - W_L),$$

satisfies the property (WB). Therefore, Roe and PVM methods based on this family of paths are well-balanced for water at rest.

Concerning high order schemes, let us consider the case of the shallow water system. In order to have a reconstruction operator which is well-balanced for water at rest solutions, the following strategy may be followed: given a sequence (q_i, h_i, H_i) of cell values and H being the bathymetry, consider the new sequence (q_i, h_i, η_i) with $\eta_i = h_i - H_i$ and apply the reconstruction operator to obtain polynomials

$$p_{i,q}, \quad p_{i,h}, \quad p_{i,\eta};$$

then, define

$$p_{i,H} = p_{i,h} - p_{i,\eta}.$$

This reconstruction is exactly well-balanced for stationary solutions corresponding to water at rest if the operator is exact for constant functions.

2.3   Finite volume path-conservative schemes in two space dimension

In this section the extension for two dimensional domains is introduced for the concepts presented in the previous sections. A family of high order finite volume methods combining a reconstruction operator and a first order path-conservative scheme is described. Then, the well-balanced property of the proposed methods is analysed. Let us recall the general system (2.1.2)

$$\partial_t U + \nabla \cdot \boldsymbol{F}(U) + \boldsymbol{B}(U) \cdot \nabla U = \boldsymbol{G}(U) \cdot \nabla \sigma,$$

where $\boldsymbol{F} = (F_1, F_2), \quad \boldsymbol{B} = (B_1, B_2), \quad \boldsymbol{G} = (G_1, G_2)$.

Thus, let us consider first order quasi-linear PDE systems:

$$\partial_t W + \boldsymbol{\mathcal{A}}(W) \cdot \nabla W = \boldsymbol{0}, \tag{2.3.1}$$

for $\boldsymbol{x} \in \Omega \subset \mathbb{R}^2, \ t > 0$, with initial condition

$$W(\boldsymbol{x}, 0) = W_0(\boldsymbol{x}), \quad \boldsymbol{x} = (x, y) \in D \subset \mathbb{R}^2,$$

in which the unknown $W(\boldsymbol{x}, t)$ is defined in $\Omega \times [0, T]$, Ω being a domain of $\mathbb{R}^2$, and takes values in an open convex set $\mathcal{O}$ of $\mathbb{R}^M$, and

$$\boldsymbol{\mathcal{A}} = (\mathcal{A}_1, \mathcal{A}_2), \quad W \in \mathcal{O} \mapsto \mathcal{A}_i(W) \in \mathcal{M}_{M \times M}(\mathbb{R}), \quad i = 1, 2$$

is a smooth locally bounded map. Note that any system (2.1.2) may be written in the quasi-linear form by considering σ as an unknown that satisfies $\partial_t \sigma = 0$, and

$$W = (U, \ \sigma)^T ,$$

$$\mathcal{A}_i(W) = \begin{pmatrix} A_i(U) & -G_i(U) \\ 0 & 0 \end{pmatrix} ,$$

where $A_i(U) = J_{F,i}(U) + B_i(U)$ and $J_{F,i}(U) = \dfrac{\partial F_i}{\partial U}(U)$ denotes the Jacobian of F_i. It is also assumed that (2.3.1) is strictly hyperbolic, i.e. for all $W \in \mathcal{O} = \mathcal{O} \times \mathbb{R}$ and $\forall \ \boldsymbol{n} = (n_1, n_2) \in \mathcal{S}^1$, where $\mathcal{S}^1 \subset \mathbb{R}^2$ denotes the unit sphere, the matrix

$$\mathcal{A}(W, \boldsymbol{n}) := \boldsymbol{\mathcal{A}}(W) \cdot \boldsymbol{n}$$

has $M = N + 1$ real and distinct eigenvalues

$$\lambda_1(W, \boldsymbol{n}) < \cdots < \lambda_M(W, \boldsymbol{n}),$$

and $\mathcal{A}(W, \boldsymbol{n})$ is thus diagonalizable.

As already mentioned in the one space dimension case (2.2.3), the nonconservative product $\mathcal{A}_1(W)\partial_x W + \mathcal{A}_2(W)\partial_y W$ does not make sense in the classical framework of distributions if W is discontinuous. However, the theory developed by Dal Maso, LeFloch and Murat in [72] allows to give a rigorous definition of nonconservative products as bounded measures provided that a family of Lipschitz continuous paths $\Phi\colon [0,1] \times \Omega \times \Omega \times \mathcal{S}^1 \to \Omega$ is prescribed. This family must satisfy certain natural regularity conditions, in particular:

C1: $\Phi(0; W_L, W_R, \boldsymbol{n}) = W_L$ and $\Phi(1; W_L, W_R, \boldsymbol{n}) = W_R$, for any $W_L, W_R \in \Omega$, $\boldsymbol{n} \in \mathcal{S}^1$.

C2: $\Phi(s; W_L, W_R, \boldsymbol{n}) = \Phi(1 - s; W_R, W_L, -\boldsymbol{n})$, for any $W_L, W_R \in \Omega$, $s \in [0,1]$, $\boldsymbol{n} \in \mathcal{S}^1$.

2.3.1   Path-conservative numerical schemes

The goal of this subsection is to present the general expression of a high order method for (2.3.1) based on the use of a first order path-conservative numerical scheme and a reconstruction operator.

To discretize (2.3.1) the computational domain Ω is covered with a set of non-overlapping Cartesian control volumes in space

$$V_i = \left[x_i - \frac{1}{2}\Delta x_i, x_i + \frac{1}{2}\Delta x_i \right] \times \left[y_i - \frac{1}{2}\Delta y_i, y_i + \frac{1}{2}\Delta y_i \right] ,$$

where the vector $\boldsymbol{x_i} = (x_i, y_i)$ describes the location of the barycentre of cell V_i, and the index i ranges from 1 to the total number of elements N_E. Furthermore, we denote the

vector of the mesh spacings in each direction by $\Delta \boldsymbol{x}_i = (\Delta x_i, \Delta y_i)$. Let us denote by $\overline{W}_i(t)$ the cell average of the solution W of (2.3.1) over the volume V_i at time t,

$$\overline{W}_i(t) = \int_{V_i} W(\boldsymbol{x}, t) \, d\boldsymbol{x}.$$

As usual, the computational domain or the *main grid* is the union of all spatial control volumes, hence

$$\Omega = \bigcup_{i=1}^{N_E} V_i.$$

Given a finite volume V_i, $|V_i|$ will represent its area; $N_i \in \mathbb{R}^2$ its center; $\mathcal{N}_i$ the set of indexes j such that V_j is a neighbour of V_i; E_{ij} the common edge of two neighbouring cells V_i and V_j, and $|E_{ij}|$ its length; $\boldsymbol{n}_{ij} = (n_{ij,1}, n_{ij,2})$ the normal unit vector at the edge E_{ij} pointing towards the cell V_j; and W_i^n the constant approximation to the average of the solution in the cell V_i at time t_n provided by the numerical scheme:

$$W_i^n \cong \frac{1}{|V_i|} \int_{V_i} W(\boldsymbol{x}, t_n) \, d\boldsymbol{x}.$$

According to Parés [207], a first order path-conservative scheme for the system (2.3.1) has the form:

Definition 6. *Given a family of Lipschitz continuous paths* $\Phi \colon [0,1] \times \Omega \times \Omega \times \mathcal{S}^1 \to \Omega$ *satisfying (C1-C2), a numerical scheme is said to be* Φ-*conservative if it can be written under the form:*

$$W_i^{n+1} = W_i^n - \frac{1}{|V_i|} \sum_{j \in \mathcal{N}_i} |E_{ij}| \mathcal{D}_\Phi^-(W_i^n, W_j^n, \boldsymbol{n}_{ij}), \qquad (2.3.2)$$

where $\mathcal{D}_\Phi^-(W_i^n(\gamma), W_j^n(\gamma), \boldsymbol{n}_{ij})$ is a path-conservative scheme for system (2.3.1), that is $\mathcal{D}_\Phi^-(W_L, W_R, \boldsymbol{n})$ is a regular function from $\Omega \times \Omega \times \mathcal{S}^1$ to $\mathbb{R}^M$, $M = N + 1$ satisfying

$$\mathcal{D}_\Phi^-(W, W, \boldsymbol{n}) = 0 \; \forall W \in \Omega, \; \forall \boldsymbol{n} \in \mathcal{S}^1 \qquad (2.3.3)$$

and

$$\mathcal{D}_\Phi^-(W_L, W_R, \boldsymbol{n}) + \mathcal{D}_\Phi^+(W_L, W_R, \boldsymbol{n}) = \int_0^1 \mathcal{A}(\Phi(s; W_L, W_R, \boldsymbol{n}), \boldsymbol{n})) \partial_s \Phi(s; W_L, W_R, \boldsymbol{n}) \, ds,$$
$$(2.3.4)$$

where $\mathcal{D}_\Phi^+(W_L, W_R, \boldsymbol{n}) = \mathcal{D}_\Phi^-(W_R, W_L, -\boldsymbol{n})$ and Φ is the chosen family of paths. Notice that an analogous to the Remark 2.2.1 can be extended in this case.

2.3.2 Some path-conservative schemes: PVM methods

The extension for two dimensional domains of the PVM methods presented in Subsection 2.2.2 is briefly introduced.

Definition 7. *Given a family of paths Φ, a Roe linearization of system (2.3.1) is a function*

$$\mathcal{A}_\Phi \colon \Omega \times \Omega \times \mathcal{S}^1 \to \mathcal{M}_M(\mathbb{R})$$

satisfying the following properties for each $W_L, W_R \in \Omega$ and $\boldsymbol{n} = (n_1, n_2) \in \mathcal{S}^1$:

1. $\mathcal{A}_\Phi(W_L, W_R, \boldsymbol{n})$ has M distinct real eigenvalues

$$\lambda_1(W_L, W_R, \boldsymbol{n}) < \lambda_2(W_L, W_R, \boldsymbol{n}) < \cdots < \lambda_M(W_L, W_R, \boldsymbol{n}).$$

2. $\mathcal{A}_\Phi(W, W, \boldsymbol{n}) = \mathcal{A}(W, \boldsymbol{n})$.

3. $\mathcal{A}_\Phi(W_L, W_R, \boldsymbol{n}) \cdot (W_R - W_L) =$

$$\int_0^1 \mathcal{A}(\Phi(s; W_L, W_R, \boldsymbol{n}), \boldsymbol{n}) \partial_s \Phi(s; W_L, W_R, \boldsymbol{n}) \, ds. \tag{2.3.5}$$

Note that in the particular case in which $\mathcal{A}_k(W)$, $k = 1, 2$, are the Jacobian matrices of smooth flux functions $F_k(W)$, property (2.3.5) does not depend on the family of paths and reduces to the usual Roe property:

$$\mathcal{A}_\Phi(W_L, W_R, \boldsymbol{n}) \cdot (W_R - W_L) = F_{\boldsymbol{n}}(U_R) - F_{\boldsymbol{n}}(U_L) \tag{2.3.6}$$

where

$$F_{\boldsymbol{n}}(U) = \boldsymbol{F}(U) \cdot \boldsymbol{n},$$

for any $\boldsymbol{n} = (n_1, n_2) \in \mathcal{S}^1$.

As in Subsection 2.2.2, one may consider the decomposition

$$\mathcal{A}_\Phi^\pm(W_L, W_R) = \frac{1}{2}\big(\mathcal{A}_\Phi(W_L, W_R) \pm |\mathcal{A}_\Phi(W_L, W_R)|\big),$$

and thus the numerical scheme introduced in 2.2.26 can be also generalized to the case of two space domains.

As it was warned in Subsection 2.2.2, in many situations, as in the case of the multilayer shallow-water system, it is not possible to obtain an easy analytical expression of the eigenvalues and eigenvectors. Similarly to what is done in Subsection 2.2.2, some other strategies can be used to construct path-conservative numerical schemes. The idea relies in to replace the absolute value of the intermediate matrix in 2.3.9, by an approximation Q_Φ easier to compute that plays the role of viscosity matrix.

Thus, in order to introduced PVM methods, given a Roe matrix $\mathcal{A}_\Phi(W_L, W_R, \boldsymbol{n})$, let us consider:

$$\widehat{\mathcal{A}}_\Phi^\pm(W_L, W_R, \boldsymbol{n}) = \frac{1}{2}\left(\mathcal{A}_\Phi(W_L, W_R, \boldsymbol{n}) \pm \mathcal{Q}_\Phi(W_L, W_R, \boldsymbol{n})\right),$$

where $\mathcal{Q}_\Phi(W_L, W_R, \boldsymbol{n})$ is a semi-definite positive matrix that can be seen as the viscosity matrix associated to the method.

Now, it is straightforward to define a path-conservative scheme in the sense defined in [207] based on the previous definition:

$$\mathcal{D}_\phi^\pm(W_L, W_R, \boldsymbol{n}) = \widehat{\mathcal{A}}_\Phi^\pm(W_L, W_R, \boldsymbol{n})(W_R - W_L). \tag{2.3.7}$$

Finally, we could also define a path-conservative scheme for the system (2.3.1) as follows:

$$U_i^{n+1} = U_i^n - \frac{1}{|V_i|}\sum_{j\in\mathcal{N}_i}|E_{ij}|\, D_\Phi^-(W_i^n, W_j^n, \boldsymbol{n}_{ij}), \tag{2.3.8}$$

$$\begin{aligned}
D_\Phi^\pm(W_L, W_R, \boldsymbol{n}) \;=\;& D_\Phi^\pm(U_L, \sigma_L, U_R, \sigma_R, \boldsymbol{n}) \\
& \frac{1}{2}\big(F_{\boldsymbol{n}}(U_R) - F_{\boldsymbol{n}}(U_L) + B_\Phi \cdot (U_R - U_L) \\
& -G_\Phi(\sigma_R - \sigma_L) \\
& \pm Q_\Phi \cdot (U_R - U_L - A_\Phi^{-1} \cdot G_\Phi(\sigma_R - \sigma_L)))
\end{aligned} \tag{2.3.9}$$

where the path is supposed to be given by $\Phi = (\Phi_U\ \Phi_\sigma)^T$ and

$$\begin{aligned}
B_\Phi \cdot (U_R - U_L) \;=\;& B_\Phi(U_L, U_R, \boldsymbol{n}) \cdot (U_R - U_L) \\
=\;& \int_0^1 B_{\boldsymbol{n}}(\Phi_U(s; W_L, W_R, \boldsymbol{n}))\partial_s\Phi(s; W_L, W_R, \boldsymbol{n})\,ds
\end{aligned}$$

with

$$B_{\boldsymbol{n}}(U) = \boldsymbol{B}(U) \cdot \boldsymbol{n};$$

$$\begin{aligned}
G_\Phi(\sigma_R - \sigma_L) \;=\;& G_\Phi(U_L, U_R, \boldsymbol{n})(\sigma_R - \sigma_L) \\
=\;& \int_0^1 G_{\boldsymbol{n}}(\Phi_U(s; W_L, W_R, \boldsymbol{n}))\partial_s\Phi(s; W_L, W_R, \boldsymbol{n})\,ds
\end{aligned}$$

with

$$G_{\boldsymbol{n}}(U) = \boldsymbol{G}(U) \cdot \boldsymbol{n}.$$

The matrix A_Φ is defined as follows

$$A_\Phi = A_\Phi(U_L, U_R, \boldsymbol{n}) = J(U_L, U_R, \boldsymbol{n}) + B_\Phi(U_L, U_R, \boldsymbol{n})$$

where $J(U_L, U_R, \boldsymbol{n})$ is a Roe matrix for the flux $F_{\boldsymbol{n}}(U)$, that is

$$J(U_L, U_R, \boldsymbol{n}) \cdot (U_R - U_L) = F_{\boldsymbol{n}}(U_R) - F_{\boldsymbol{n}}(U_L).$$

Remark 2.3.1. *Notice that the term $Q_\Phi \cdot (U_R - U_L - A_\Phi^{-1} \cdot G_\Phi(\sigma_R - \sigma_L))$ is not well defined and makes no sense if one of the eigenvalues of A_Φ vanishes. In this case, two eigenvalues of $\mathcal{A}_\Phi(W_L, W_R, \boldsymbol{n})$ vanish and the problem is said to be resonant. Resonant problems exhibit an additional difficulty, as weak solutions may not be uniquely determined by their initial data. The analysis of this difficulty depends on the considered problem and it is beyond of this dissertation. A general procedure, that formally avoids this difficulty is described in [35].*

A rough approximation is given by the local Lax-Friedrichs (or Rusanov) method, in which:

$$Q_\Phi(U_L, U_R, \boldsymbol{n}) = \max(|\lambda_i(U_L, U_R, \boldsymbol{n})|, i = 1, \ldots, N)I, \qquad (2.3.10)$$

I being the identity matrix. Note that this definition of $Q_\Phi(U_L, U_R, \boldsymbol{n})$ only requires an estimation of the largest wave speed in absolute value. However, this approach gives excessive numerical diffusion for the waves corresponding to the lower eigenvalues.

In general, one may consider viscosity matrices of the form

$$Q_\Phi(U_L, U_R) = f(A_\Phi(U_L, U_R, \boldsymbol{n})), \qquad (2.3.11)$$

where f satisfies the conditions (f_1)-(f_4) given in Subsection 2.2.2. Then, a similar stability property than for the 1D case, can be shown. In particular, if $\lambda_1(U_L, U_R, \boldsymbol{n}) < \cdots < \lambda_N(U_L, U_R, \boldsymbol{n})$ denote the eigenvalues of $A_\Phi(U_L, U_R, \boldsymbol{n})$ and the usual CFL condition is assumed

$$\Delta t \cdot \max\left\{ \frac{|\lambda_{ij,k}|}{d_{ij}}; \ i = 1, \ldots, N_\mathcal{T}, \ j \in \mathcal{N}_i, \ k = 1, \ldots, N \right\} = \delta, \qquad (2.3.12)$$

with $0 < \delta \le 1$, where d_{ij} is the distance from the center of cell V_i to the edge E_{ij}, then the resulting scheme is L^∞-stable if $f(x)$ satisfies the following condition (see [48]):

$$f(x) \ge |x|, \quad \forall\, x \in [\lambda_1(U_L, U_R, \boldsymbol{n}), \lambda_N(U_L, U_R, \boldsymbol{n})]. \qquad (2.3.13)$$

The approach presented in Subsection 2.2.2 , where the so-called PVM (Polynomial Viscosity Matrix) methods are defined in terms of viscosity matrices based on general polynomial evaluations of a Roe matrix can be easily extended to two dimensional domains. The idea is to consider viscosity matrices of the form:

$$Q_\Phi(U_L, U_R, \boldsymbol{n}) = P_r(A_\Phi(U_L, U_R, \boldsymbol{n})),$$

where $P_r(x)$ is a polynomial of degree r and then the expression (2.3.9) becomes:

$$
\begin{aligned}
D_\Phi^\pm(W_L, W_R, \boldsymbol{n}) \ &= D_\Phi^\pm(U_L, \sigma_L, U_R, \sigma_R, \boldsymbol{n}) \\
&= \frac{1}{2}\big(F_{\boldsymbol{n}}(U_R) - F_{\boldsymbol{n}}(U_L) + B_\Phi \cdot (U_R - U_L) \\
&\quad - G_\Phi(\sigma_R - \sigma_L) \\
&\quad \pm Q_\Phi \cdot (U_R - U_L - A_\Phi^{-1} \cdot G_\Phi(\sigma_R - \sigma_L))\big)
\end{aligned}
\qquad (2.3.14)
$$

Thus, for example the HLL scheme presented in (2.2.39) can be extended to bidimensional domains by considering an approximation of the minimum and maximum of the eigenvalues.

2.3.3 High order finite volume schemes based on reconstruction of states

Let us consider a reconstruction operator of order p. We will assume that the reconstructions are calculated as follows: given a family $\{W_i\}_{i=1}^{N_\mathcal{T}}$ of cell values, first an approximation function is constructed at every cell V_i, based on the values at some of the cells close to V_i:

$$P_i(\boldsymbol{x}) = P_i\left(\boldsymbol{x};\ \{W_j\}_{j\in\mathcal{B}_i}\right),$$

for some set of indexes $\mathcal{B}_i$ (the stencil). If, for instance, the reconstruction only depends on the neighbour cells of V_i, then $\mathcal{B}_i = \mathcal{N}_i \cup \{i\}$. These approximation functions are calculated usually by means of an interpolation or approximation procedure. Once these functions have been constructed, the reconstruction at $\gamma \in E_{ij}$ are defined as follows:

$$W_{ij}^-(\gamma) = \lim_{\boldsymbol{x}\to\gamma} P_i(\boldsymbol{x}), \quad W_{ij}^+(\gamma) = \lim_{\boldsymbol{x}\to\gamma} P_j(\boldsymbol{x}). \tag{2.3.15}$$

As usual, the reconstruction operator must satisfy the following properties:

(P1) It is conservative, i.e. the following equality holds for any cell V_i:

$$W_i = \frac{1}{|V_i|} \int_{V_i} P_i(\boldsymbol{x})d\boldsymbol{x}. \tag{2.3.16}$$

(P2) If the operator is applied to the cell averages $\{W_i\}$ for some smooth function $W(\boldsymbol{x})$, then
$$W_{ij}^\pm(\gamma) = W(\gamma) + O(\Delta\boldsymbol{x}^s), \quad \forall\gamma \in E_{ij},$$
and
$$W_{ij}^+(\gamma) - W_{ij}^-(\gamma) = O(\Delta\boldsymbol{x}^{s+1}), \quad \forall\gamma \in E_{ij}.$$

(P3) It is of order s_1 in the interior of the cells, i.e. if the operator is applied to a sequence $\{W_i\}$ for some smooth function $W(\boldsymbol{x})$, then:
$$P_i(\boldsymbol{x}) = W(\boldsymbol{x}) + O(\Delta\boldsymbol{x}^{s_1}), \ \forall\boldsymbol{x} \in int(V_i). \tag{2.3.17}$$

(P4) Under the assumption of the previous property, the gradient of P_i provides an approximation of order s_2 of the gradient of W:

$$\nabla P_i(\boldsymbol{x}) = \nabla W(\boldsymbol{x}) + O(\Delta\boldsymbol{x}^{s_2}), \ \forall\boldsymbol{x} \in int(V_i). \tag{2.3.18}$$

In the literature one can find many examples of reconstruction operators that satisfy (P1) and (P2): ENO, WENO, CWENO, hyperbolic reconstructions, among others (see [153], [186], [62], [229], [93],[101], [102], [131], [70]).

Remark 2.3.2. *Notice that, in general, $s_2 \leq s_1 \leq s$. If, for instance, the approximation functions are polynomials of degree s obtained by interpolating the cell values on a fixed stencil, then $s_2 = s - 1$ and $s_1 = s$. In the case of WENO-like reconstructions (see [228]), the approximation functions are obtained as a weighted combination of interpolation polynomials whose accuracy is greater on the boundary than at the interior of the cell: in this case $s_1 < s$. An interesting alternative of WENO reconstruction operator for which $s_1 = s$ is given by CWENO reconstruction (see [70]).*

Let us denote by P_i the approximation functions defined using the cell averages $W_i(t)$, i.e.

$$P_i(\boldsymbol{x}) = P_i\left(\boldsymbol{x};\ \{W_j(t)\}_{j \in \mathcal{B}_i}\right).$$

$W_{ij}^-(\gamma, t)$ (resp. $W_{ij}^+(\gamma, t)$) is then defined by

$$W_{ij}^-(\gamma, t) = \lim_{\boldsymbol{x} \to \gamma} P_i(\boldsymbol{x}), \quad W_{ij}^+(\gamma, t) = \lim_{\boldsymbol{x} \to \gamma} P_j(\boldsymbol{x}). \tag{2.3.19}$$

According to Parés [207], a high order path-conservative scheme for the nonconservative system (2.3.1) is given by:

$$
\begin{aligned}
W_i' = &-\frac{1}{|V_i|} \sum_{j \in \mathcal{N}_i} \int_{E_{ij}} \mathcal{D}_\Phi^-(W_{ij}^-(\gamma, t), W_{ij}^+(\gamma, t), \boldsymbol{n}_{ij})\, d\gamma \\
&-\frac{1}{|V_i|} \int_{V_i} \boldsymbol{\mathcal{A}}\left(P_i(\boldsymbol{x})\right) \cdot \nabla P_i(\boldsymbol{x})\, d\boldsymbol{x},
\end{aligned}
\tag{2.3.20}
$$

where $\mathcal{D}_\Phi^-$ are evaluated in $W_{ij}^\pm(\gamma, t)$ given by (2.3.19).

Theorem 2.3.1. *Let us assume that $\mathcal{A}_1$ and $\mathcal{A}_2$ are of class $\mathcal{C}^2$ with bounded derivatives and $\mathcal{D}_\Phi^-(\cdot, \cdot, \boldsymbol{n}_{ij})$ is bounded for all i, j. Let us also suppose that the reconstruction operator satisfies the hypothesis (P1)-(P4). Then (2.3.20) is an approximation of order at least $\alpha = \min(s, s_1, s_2)$ to the system (2.3.1) in the following sense:*

$$
\begin{aligned}
&\frac{1}{|V_i|} \sum_{j \in \mathcal{N}_i} \left[\int_{E_{ij}} \left(\mathcal{D}_\Phi^-(W_{ij}^-(\gamma, t), W_{ij}^+(\gamma, t), \boldsymbol{n}_{ij}) \right) d\gamma + \int_{V_i} \boldsymbol{\mathcal{A}}\left(P_i(\boldsymbol{x})\right) \cdot \nabla P_i(\boldsymbol{x})\, d\boldsymbol{x} \right] \\
&= \frac{1}{|V_i|} \sum_{j \in \mathcal{N}_i} \int_{V_i} \boldsymbol{\mathcal{A}}(W(\boldsymbol{x}, t)) \cdot \nabla W(\boldsymbol{x}, t)\, d\boldsymbol{x} + O(\Delta \boldsymbol{x}^\alpha),
\end{aligned}
$$

$$\tag{2.3.21}$$

for every solution W smooth enough, $W_{ij}^{\pm}(\gamma, t)$ being the associated reconstructions and P_i the approximation functions corresponding to the family

$$\overline{W}_i(t) = \frac{1}{|V_i|} \int_{V_i} W(\boldsymbol{x}, t)\, d\boldsymbol{x}.$$

Remark 2.3.3. *According to Remark 2.3.2 for the 1D case, the expected order of the numerical scheme is s_2. Nevertheless, this theoretical result is rather pessimistic: in practice order s_1 is often achieved.*

Now, taking into account the relation between systems (2.1.2) and (2.3.1), it is possible to rewrite (2.3.20) as follows:

$$U_i' = -\frac{1}{|V_i|} \sum_{j \in \mathcal{N}_i} \int_{E_{ij}} D_{\Phi}^-(W_{ij}^-(\gamma, t), W_{ij}^+(\gamma, t), \boldsymbol{n}_{ij})\, d\gamma$$

$$\text{(2.3.22)}$$

$$-\frac{1}{|V_i|} \int_{V_i} \nabla \cdot \boldsymbol{F}\left(P_{i,U}(\boldsymbol{x})\right) + \boldsymbol{B}\left(P_{i,U}(\boldsymbol{x})\right) \cdot \nabla P_{i,U}(\boldsymbol{x}) - \boldsymbol{G}\left(P_{i,U}(\boldsymbol{x})\right) \cdot \nabla P_{i,\sigma}(\boldsymbol{x})\, d\boldsymbol{x}$$

where $P_{i,U}$ is the reconstruction approximation function at time t of $U_i(t)$ at cell V_i defined using the stencil $\mathcal{B}_i$:

$$P_{i,U}(\boldsymbol{x}) = P_i\left(\boldsymbol{x}; \ \{U_j(t)\}_{j \in \mathcal{B}_i}\right),$$

and $P_{i,\sigma}$ is the reconstruction approximation function of σ. The functions $U_{ij}^{\pm}(\gamma, t)$ are given by

$$U_{ij}^-(\gamma, t) = \lim_{\boldsymbol{x} \to \gamma} P_{i,U}(\boldsymbol{x}), \quad U_{ij}^+(\gamma, t) = \lim_{\boldsymbol{x} \to \gamma} P_{j,U}(\boldsymbol{x}),$$

and $\sigma_{ij}^{\pm}(\gamma)$ are given by

$$\sigma_{ij}^-(\gamma) = \lim_{\boldsymbol{x} \to \gamma} P_{i,\sigma}(\boldsymbol{x}), \quad \sigma_{ij}^+(\gamma) = \lim_{\boldsymbol{x} \to \gamma} P_{j,\sigma}(\boldsymbol{x}).$$

Again, as in the 1D case, notice that (2.3.22) is a system of ordinary differential equations to be solved by using a high order numerical solver with good properties. In practice the TVD Runge-Kutta schemes are used (see [143], [228]). Other time discretization can be considered, as ADER schemes developed by Toro and Dumbser (see [92],[238]).

In practice, the integral terms in (2.3.22) are numerically approached using a high order quadrature formula, whose order is related to the one of the reconstruction operator (see [24] for more details). In this case, together with a 1D formula for the integrals on the edges, it can also be necessary to choose a quadrature formula for the integrals in the cells.

Concerning the well-balanced properties of the schemes, the 2D extensions of the 1D scheme do not inherit this property in general: this property is only preserved for

stationary solutions which are essentially 1D and for rectangular and properly oriented meshes. For the well-balanced properties, the aforementioned choice of the quadrature rule also plays a fundamental role. Nevertheless, in the case of the shallow-water and the two-layer systems, the 2D extension of all of the 1D numerical schemes presented here are well-balanced for water at rest solutions (see [24]).

2.4 Discontinuous Galerkin numerical schemes in two space dimension

In this section the ADER-DG scheme on rectangular grids with *a posteriori* subcell finite volume limiter (SCL) and applied to hyperbolic systems (2.1.2) including a source term vector $S(U)$,

$$\partial_t U + \nabla \cdot \boldsymbol{F}(U) + \boldsymbol{B}(U) \cdot \nabla U = \boldsymbol{G}(U) \cdot \nabla \sigma + S(U) \tag{2.1.2}$$

is briefly recalled. For more details, the reader is referred to [98],[261].

The PDE system (2.1.2) is solved by the aid of a high order one-step ADER-DG method, which provides at the same time high order of accuracy in both space and time in one single step, without the need of any intermediate Runge-Kutta stages. The construction of fully-discrete high order one-step schemes is typical of the ADER approach, which was introduced by Toro and Titarev in the finite volume context, see [237],[244],[238],[241].

The scheme is written under the form of a one-step predictor corrector method [132], where the predictor step solves (2.1.2) within each element in the small (see also [150]) by means of an element-local space-time discontinuous Galerkin scheme. The corrector step is obtained by directly integrating a weak form of the governing PDE in time by the aid of the predictor. In the following we only summarize the main steps, while for more details the reader is referred to [93],[155],[132],[12].

2.4.1 Data representation and spatial discretization

Similarly as in Subsection 2.3.1 we recall some of the nomenclature that will be used.

The computational domain Ω is covered with a set of non-overlapping Cartesian control volumes in space

$$V_i = \left[x_i - \frac{1}{2}\Delta x_i, x_i + \frac{1}{2}\Delta x_i \right] \times \left[y_i - \frac{1}{2}\Delta y_i, y_i + \frac{1}{2}\Delta y_i \right],$$

where the vector $\boldsymbol{x}_i = (x_i, y_i)$ describes the location of the barycentre of cell V_i, and the index i ranges from 1 to the total number of elements N_E. Furthermore, we denote the vector of the mesh spacings in each direction by $\Delta \boldsymbol{x}_i = (\Delta x_i, \Delta y_i)$. As usual, the

computational domain or the *main grid* is the union of all spatial control volumes, hence

$$\bar{\Omega} = \bigcup_{i=1}^{N_E} V_i.$$

Let us introduced the space $\mathbb{P}^{\mathcal{N}}$ of piecewise polynomials up to degree $\mathcal{N}$, spanned by the basis functions $\phi_l(\boldsymbol{x})$, $l = (l_1, l_2)$ being a multi-index.

In the following, the discrete solution of the PDE system (2.1.2) for the state vector U, as well as the known parameter function σ, are represented within each cell V_i of the main grid by piecewise polynomials of maximum degree $\mathcal{N} \geq 0$

$$U_h(\boldsymbol{x}, t) = U_{i,h}(\boldsymbol{x}, t) \in \mathbb{P}^{\mathcal{N}}, \quad i \text{ being such that } \boldsymbol{x} \in V_i,$$

$$\sigma_h(\boldsymbol{x}) = \sigma_{i,h}(\boldsymbol{x}) \in \mathbb{P}^{\mathcal{N}}, \quad i \text{ being such that } \boldsymbol{x} \in V_i,$$

where

$$U_{i,h}(\boldsymbol{x}, t_n) = \widehat{U}_{i,l}^n \phi_l(\boldsymbol{x}) := \sum_{l=1}^{\mathcal{N}+1} \widehat{U}_{i,l}^n \phi_l(\boldsymbol{x}), \quad \boldsymbol{x} \in V_i,$$

$$\sigma_{i,h}(\boldsymbol{x}) = \widehat{\sigma}_{i,l} \phi_l(\boldsymbol{x}) := \sum_{l=1}^{\mathcal{N}+1} \widehat{\sigma}_{i,l} \phi_l(\boldsymbol{x}), \quad \boldsymbol{x} \in V_i,$$

(2.4.1)

where U_h (and σ_h) is referred to as the discrete "representation" of the solution (known parameter function resp.) and the Einstein summation convention for repeated indexes is introduced.

In this thesis, we adopt a nodal basis for the spatial basis functions

$$\phi_l(\boldsymbol{x}) = \varphi_{l_1}(\xi)\varphi_{l_2}(\zeta).$$

The nodal basis is generated via tensor products of one-dimensional nodal basis functions $\varphi_k(\xi)$ on the reference interval $[0, 1]$, for which we have used the Lagrange interpolation polynomials of maximum degree $\mathcal{N}$ passing through the Gauss-Legendre quadrature nodes. The transformation from physical coordinates $\boldsymbol{x} \in V_i$ to reference coordinates $\boldsymbol{\xi} = (\xi, \zeta) \in [0, 1]^d$ is given by the linear mapping $\boldsymbol{x} = \boldsymbol{x}_i - \frac{1}{2}\Delta\boldsymbol{x}_i + (\xi\Delta x_i, \zeta\Delta y_i)^T$. With this choice, the nodal basis functions satisfy the interpolation property $\varphi_k(\xi_j) = \delta_{kj}$, where δ_{kj} is the usual Kronecker symbol, and the resulting basis is by construction *orthogonal*. Furthermore, due to this particular choice of a *nodal* tensor-product basis, the entire scheme can be written in a dimension-by-dimension fashion, where all integral operators can be decomposed into a sequence of one-dimensional operators acting only on the $\mathcal{N}+1$ degrees of freedom in the respective dimension.

2.4.2 ADER-DG space-time predictor

As already mentioned previously, the element-local space-time predictor is an important *key feature* of ADER-DG schemes and is briefly discussed in this subsection. The

computation of the predictor solution is based on a weak formulation of the governing PDE system in space-time and was first introduced in [93],[91]. Starting from the known solution $U_h(\boldsymbol{x}, t_n)$ at time t_n and following the terminology of Harten *et al.* [150], we solve a so-called Cauchy problem *in the small*, i.e. without considering the interaction with the neighbour elements. In the ENO scheme of Harten *et al.* [150] and in the original ADER approach of Toro and Titarev [244],[238],[241] the strong differential form of the PDE was used, together with a combination of Taylor series expansions and the so-called Cauchy-Kovalewskaya procedure. The latter is very cumbersome or gets even unfeasible, since it requires a lot of analytic manipulations of the governing PDE system, in order to replace time derivatives with known space derivatives at time t_n. This is achieved by successively differentiating the governing PDE system with respect to space and time and inserting the resulting terms into the Taylor series. Instead of, the local space-time discontinuous Galerkin predictor introduced in [93],[91], requires only point–wise evaluations of the fluxes, source terms and nonconservative products.

For each element V_i we denote the predictor solution q_h that is a solution of a weak formulation of the governing PDE system within each space-time control volume $V_i \times [t_n, t_{n+1}]$. The predictor is now expanded in terms of a local space-time basis

$$q_h(\boldsymbol{x}, t) = q_{i,h}(\boldsymbol{x}, t), i \text{ being such that } (\boldsymbol{x}, t) \in V_i \times [t_n, t_{n+1}],$$

where

$$q_{i,h}(\boldsymbol{x}, t) = \widehat{q}_{i,l}\theta_l(\boldsymbol{x}, t) := \sum_l \widehat{q}_{i,l}\theta_l(\boldsymbol{x}, t), \quad (\boldsymbol{x}, t) \in V_i \times [t_n, t_{n+1}] \tag{2.4.2}$$

with the multi-index $l = (l_0, l_1, l_2)$ and where the space-time basis functions

$$\theta_l(\boldsymbol{x}, t) = \varphi_{l_0}(\tau)\varphi_{l_1}(\xi)\varphi_{l_2}(\zeta)$$

are again generated from the same one-dimensional nodal basis functions $\varphi_k(\xi)$ as before, i.e. the Lagrange interpolation polynomials of maximum degree $\mathcal{N}$ passing through $\mathcal{N}+1$ Gauss-Legendre quadrature nodes. The spatial mapping $\boldsymbol{x} = \boldsymbol{x}(\boldsymbol{\xi})$ is also the same as before and the physical time is mapped to the reference time $\tau \in [0, 1]$ via $t = t_n + \tau\Delta t$. In the predictor step, and for each $(\boldsymbol{x}, t) \in V_i \times [t_n, t_{n+1}]$, we use the ansatz

$$\nabla \cdot \boldsymbol{F}(q_{i,h}(\boldsymbol{x}, t)) = \theta_l(\boldsymbol{x}, t)\widehat{\nabla \cdot \boldsymbol{F}}_{i,l},$$

$$\boldsymbol{B}(q_{i,h}(\boldsymbol{x}, t)) \cdot \nabla q_{i,h}(\boldsymbol{x}, t) = \theta_l(\boldsymbol{x}, t)\widehat{\boldsymbol{B} \cdot q}_{i,l},$$

$$\boldsymbol{G}(q_{i,h}(\boldsymbol{x}, t)) \cdot \nabla \sigma_{i,h}(\boldsymbol{x}) = \theta_l(\boldsymbol{x}, t)\widehat{\boldsymbol{G} \cdot \nabla \sigma}_{i,l},$$

$$\mathcal{S}(q_{i,h}(\boldsymbol{x}, t)) = \theta_l(\boldsymbol{x}, t)\widehat{\mathcal{S}}_{i,l},$$

where the gradient of fluxes the nonconservative products and the source terms are expressed in the space time basis. For example, $\widehat{\mathcal{S}}_{i,l}$ denote the degree of freedom of $\mathcal{S}(q_{i,h}(\boldsymbol{x}, t))$ when is represented in the space-time basis $\{\theta_l\}$.

Thus, if one employs a nodal basis, one simply has

$$\widehat{\nabla \cdot \boldsymbol{F}}_{i,l} = (\nabla \cdot \boldsymbol{F}(q))|_{q=\widehat{q}_{i,l}} , \tag{2.4.3}$$

$$\widehat{\boldsymbol{B} \cdot q}_{i,l} = (\boldsymbol{B}(q) \cdot \nabla q)|_{q=\widehat{q}_{i,l}} , \tag{2.4.4}$$

$$\widehat{\boldsymbol{G} \cdot \nabla}\sigma_{i,l} = \boldsymbol{G}(\widehat{q}_{i,l}) \cdot (\nabla \sigma)|_{\sigma=\widehat{\sigma}_{i,l}} \tag{2.4.5}$$

$$\widehat{\mathcal{S}}_{i,l} = \mathcal{S}(\widehat{q}_{i,l}), \tag{2.4.6}$$

which is computationally more efficient than L_2-projection via Gaussian quadrature formulae.

Multiplication of the PDE system (2.1.2) with a space-time test function θ_k and integration over the space-time control volume $V_i \times [t_n, t_{n+1}]$ yields the following weak form of the governing PDE:

$$
\int_{t_n}^{t_{n+1}} \int_{V_i} \theta_k(\boldsymbol{x},t) \Big(\partial_t q_{i,h}(\boldsymbol{x},t) + \nabla \cdot \boldsymbol{F}(q_{i,h}(\boldsymbol{x},t)) \Big) \, d\boldsymbol{x} \, dt
$$

$$
+ \int_{t_n}^{t_{n+1}} \int_{V_i} \theta_k(\boldsymbol{x},t) \Big(\boldsymbol{B}(q_{i,h}(\boldsymbol{x},t)) \cdot \nabla q_{i,h}(\boldsymbol{x},t) - \boldsymbol{G}(q_{i,h}(\boldsymbol{x},t)) \cdot \nabla \sigma_{i,h} \Big) \, d\boldsymbol{x} \, dt \tag{2.4.7}
$$

$$
= \int_{t_n}^{t_{n+1}} \int_{V_i} \theta_k(\boldsymbol{x},t) \Big(S(q_{i,h}(\boldsymbol{x},t)) \Big) \, d\boldsymbol{x} \, dt .
$$

Since we are only interested in an element local predictor solution, i.e. without considering interactions with the neighbour elements we do not yet take into account the jumps in q_h across the element interfaces, since this will be done in the final corrector step of the ADER-DG scheme. Instead, we introduce the known discrete solution $U_h(\boldsymbol{x}, t_n)$ at time t_n. For this purpose, the first term is integrated by parts in time. This leads to

$$
\int_{V_i} \theta_k(\boldsymbol{x},t_{n+1}) q_{i,h}(\boldsymbol{x},t_{n+1}) - \theta_k(\boldsymbol{x},t_n) U_{i,h}(\boldsymbol{x},t_n) \, d\boldsymbol{x} - \int_{t_n}^{t_{n+1}} \int_{V_i} q_{i,h}(\boldsymbol{x},t) \partial_t \theta_k(\boldsymbol{x},t) \, d\boldsymbol{x} \, dt
$$

$$
+ \int_{t_n}^{t_{n+1}} \int_{V_i} \theta_k(\boldsymbol{x},t) \Big(\nabla \cdot \boldsymbol{F}(q_{i,h}(\boldsymbol{x},t)) + \boldsymbol{B}(q_{i,h}(\boldsymbol{x},t)) \cdot \nabla q_{i,h}(\boldsymbol{x},t) \Big) \, d\boldsymbol{x} \, dt
$$

$$
= \int_{t_n}^{t_{n+1}} \int_{V_i} \theta_k(\boldsymbol{x},t) \Big(\boldsymbol{G}(q_{i,h}(\boldsymbol{x},t)) \cdot \nabla \sigma_{i,h} + S(q_{i,h}(\boldsymbol{x},t)) \Big) \, d\boldsymbol{x} \, dt
$$

$$\tag{2.4.8}$$

Using the local space-time ansatz (2.4.2)-(2.4.6) along with the Einstein summation convention, the equation (2.4.8) in a given element V_i becomes an element-local nonlinear system for the unknown degrees of freedom $\widehat{q}_{i,l}$ of the space-time polynomials q_h

$$
\left(\int\limits_{V_i} \theta_k(\boldsymbol{x}, t_{n+1})\theta_l(\boldsymbol{x}, t_{n+1})\, d\boldsymbol{x} - \int\limits_{t_n}^{t_{n+1}}\int\limits_{V_i} \theta_l(\boldsymbol{x}, t)\partial_t\theta_k(\boldsymbol{x}, t)\, d\boldsymbol{x}\, dt \right) \widehat{q}_{i,l}
$$
$$
= \left(\int\limits_{V_i} \theta_k(\boldsymbol{x}, t_n)\phi_l(\boldsymbol{x})\, d\boldsymbol{x} \right) \widehat{q}_{i,l}^{\,n} - \int\limits_{t_n}^{t_{n+1}}\int\limits_{V_i} \theta_k(\boldsymbol{x}, t)\left(\widehat{\nabla \cdot \boldsymbol{F}}_{i,l} + \widehat{\boldsymbol{B} \cdot q}_{i,l} - \widehat{\boldsymbol{G} \cdot \sigma}_{i,l} \right) d\boldsymbol{x}\, dt
$$
$$
+ \int\limits_{t_n}^{t_{n+1}}\int\limits_{V_i} \theta_k(\boldsymbol{x}, t)\widehat{\mathcal{S}}_{i,l}\, d\boldsymbol{x}\, dt
$$

$$(2.4.9)$$

The solution of (2.4.9) can be easily found via a simple and fast converging fixed point iteration detailed e.g. in [93],[155] for the degrees of freedom $\widehat{q}_{i,l}$.

For linear homogeneous systems, the iteration converges in a finite number of at most $\mathcal{N} + 1$ steps. We emphasize that the choice of an appropriate *initial guess* $q_h^0(\boldsymbol{x}, t)$ for $q_h(\boldsymbol{x}, t)$ is of fundamental importance to obtain a faster convergence and thus a computationally more efficient scheme. For this purpose, one can either use an extrapolation of q_h from the previous time interval $[t_{n-1}, t_n]$, as suggested e.g. in [260], or one can employ a second-order accurate MUSCL-Hancock-type approach, as forwarded in [155], which is based on discrete derivatives computed at time t_n. As alternative, one can also use a Taylor series expansion of the solution $q_h(\boldsymbol{x}, t)$ about time t_n and then use a continuous extension Runge-Kutta scheme (CERK) in order to generate the initial guess for the space-time predictor, as recently pointed out in [115]. For details, see [115] and [204],[132]. If an initial guess with polynomial degree $\mathcal{N} - 1$ in time is chosen, it is sufficient to use *one single* Picard iteration to solve (2.4.9) to the desired accuracy, see [91]. For an efficient task-based formalism of ADER-DG schemes, see [59].

2.4.3   Fully discrete one-step ADER-DG scheme

With the aid of the local space-time predictor q_h, a fully discrete one-step ADER-DG scheme can now be simply obtained by multiplication of the governing PDE system (2.1.2) by the space test functions ϕ_k, and subsequent integration over the space-time control volume $V_i \times [t_n, t_{n+1}]$. Due to the presence of nonconservative products, and that q_h, is allowed to jump across element interfaces, the resulting jump terms have to be taken properly into account. In this context, this is achieved via numerical flux functions (approximate Riemann solvers) and via the path-conservative approach previously presented (see [216],[92],[95]).

Let $\boldsymbol{n}_{ij} \in \mathcal{S}^1$ denote the normal unit vector at the edge E_{ij} pointing towards the cell V_j. According to the framework of path-conservative schemes, the path-conservative jump term in normal direction is defined as in (2.3.9). This jump term, denoted by D_Φ^- is a function of the boundary-extrapolated data:

$$D_\Phi^- \equiv D_\Phi^-(\underline{q_{i,h}}, \underline{q_{j,h}}, \boldsymbol{n}_{ij}),$$

where $\underline{q_{i,h}}$ and $\underline{q_{j,h}}$ are the extrapolated degree of freedoms of the space-time predictor $q_{i,h}$ and $\underline{q_{i,h}}$ to same edge E_{ij} respectively.

Thus, we obtain the following path-conservative one-step ADER Discontinuous Galerkin (ADER-DG) scheme for the unknown U, see [92]:

$$\left(\int\limits_{V_i} \phi_k \phi_l \, d\boldsymbol{x} \right) \left(\widehat{U}_{i,l}^{n+1} - \widehat{U}_{i,l}^n \right) + \sum_{j \in \mathcal{N}_i} \int\limits_{t^n}^{t^{n+1}} \int_{E_{ij}} D_\Phi^-(\underline{q_{i,h}}(\gamma, t), \underline{q_{j,h}}(\gamma, t), \boldsymbol{n}_{ij}) \, d\gamma \, dt$$

$$+ \int\limits_{t_n}^{t_{n+1}} \int\limits_{V_i^\circ} \phi_k \left(\nabla \cdot \boldsymbol{F}(q_{i,h}) + \boldsymbol{B}(q_{i,h}) \cdot \nabla q_{i,h} - \boldsymbol{G}(q_{i,h}) \cdot \nabla \sigma_{i,h} - S(q_{i,h}) \right) \, d\boldsymbol{x} \, dt = \boldsymbol{0},$$

(2.4.10)

where $q_{i,h}$ is the local space-time predictor computed at the previous space-time predictor. The first integral leads to the element mass matrix, which is diagonal since our basis is orthogonal. The boundary integral contains the approximate Riemann solver and accounts for the jumps across element interfaces. The last volume integral account for the smooth part of the flux, the nonconservative product, and the algebraic source terms.

We also recall that, having selected the nodal points in this way, we will compute the volume integrals through Gaussian quadrature rules, that is known to be exact for all polynomials up to degree $2\mathcal{N} + 1$.

Concerning the surface integral that appears in (2.4.10), it can be simply evaluated via some sufficiently accurate numerical quadrature formula. We typically use a the Gauss-Legendre quadrature rule. Here, the time integral is approximated by the rectangle rule, that is by using the information at the time level t_n. This will leads us to a simplification of the final numerical scheme. Since this integral contribution is a term of order $\mathcal{O}(\Delta x)^{\mathcal{N}}$ for smooth solutions, then the order of accuracy of the numerical scheme is maintained for regular solutions. Nevertheless, in [92] an alternative strategy to compute the time integral is discussed.

2.4.4 A posteriori subcell finite volume limiter

In regions where the discrete solution is smooth, there is indeed no need for using nonlinear limiters.

However, there are some situations where we have to supplement the high order unlimited ADER-DG method described above with a nonlinear limiter (e.g in the presence of shock waves, discontinuities or strong gradients).

In order to build a simple, robust and accurate limiter, we follow the ideas outlined in [98],[261],[96],[17], where a novel *a posteriori* limiting strategy for ADER-DG schemes was developed, based on the ideas of the MOOD paradigm introduced in [64],[88],[89],[173] in the finite volume context. In a first run, the unlimited ADER-DG scheme is used and produces a so-called *candidate solution*, denoted by $U_h^*(\boldsymbol{x}, t_{n+1})$ in the following. This candidate solution is then checked *a posteriori* against several physical and numerical detection criteria. For example, we require some relevant physical quantities of the solution to be positive (e.g. pressure and density or the total water depth in the case of shallow water flows), we require the absence of floating point errors (`NaN`) and we impose a relaxed discrete maximum principle (DMP) in the sense of polynomials, see [98]. As soon as one of these detection criteria are not satisfied, a cell is marked as troubled zone and is scheduled for limiting. The details of the MOOD detection criteria introduced in [173] will be described in the next subsection.

A cell V_i that has been marked for limiting is now split into $(2\mathcal{N}+1)^d$ finite volume subcells, which are denoted by $V_{i,s}$ and that satisfy

$$V_i = \bigcup_s V_{i,s}. \tag{2.4.11}$$

Note that this very fine division of a DG element into finite volume subcells does *not* reduce the time step of the overall ADER-DG scheme, since the CFL number of explicit DG schemes scales with $1/(2\mathcal{N}+1)$, while the CFL number of finite volume schemes (used on the subgrid) is of the order of unity. The discrete solution in the subcells $V_{i,s}$ is represented at time t_n in terms of *piecewise constant* subcell averages $\overline{U}_{i,s}^n$, i.e.

$$\overline{U}_{i,s}^n = \frac{1}{|\Omega_{i,s}|} \int\limits_{\Omega_{i,s}} U(\boldsymbol{x}, t^n) \, d\boldsymbol{x}. \tag{2.4.12}$$

These subcell averages are now evolved in time with a second or third order accurate finite volume scheme, where the ODE in time can be numerically solved via a standard TVD Runge-Kutta method (see [142]).

Once all subcell averages $\overline{U}_{i,s}^{n+1}$ inside a cell V_i have been computed according to the finite volume numerical scheme, the limited DG polynomial $U_h'(\boldsymbol{x}, t_{n+1})$ at the next time level is obtained again via a classical constrained least squares reconstruction procedure requiring

$$\frac{1}{|\Omega_{i,s}|} \int\limits_{\Omega_{i,s}} U_h'(\boldsymbol{x}, t_{n+1}) \, d\boldsymbol{x} = \overline{U}_{i,s}^{n+1} \qquad \forall \Omega_{i,s} \in \Omega_i, \tag{2.4.13}$$

and

$$\int\limits_{\Omega_i} U_h'(\boldsymbol{x}, t_{n+1}) \, d\boldsymbol{x} = \sum_{\Omega_{i,s} \in \Omega_i} |\Omega_{i,s}| \overline{U}_{i,s}^{n+1}. \tag{2.4.14}$$

Here, the second relation is a constraint and means conservation at the level of the control volume Ω_i.

Detection criteria

In this dissertation, we apply the following detection criteria at each volume cell V_i (see [64],[88],[89],[173]):

+ *Physical admissibility detection (PAD):* The detection criteria contains physic-based admissibility properties. In our case, we must ensured the positivity of the total water depth and hence, a candidate solution $\overline{U}_{i,s}^{*}$ is said to be physically valid inside the cell V_i for this system if

$$\overline{h}_{i,s}^{*} > 0, \quad \forall s \in \mathcal{S}_i, \tag{2.4.15}$$

where $\mathcal{S}_i$ accounts for the degree of freedom of the DG polynomial on the cell V_i, and h is a given total water depth variable. Furthermore, the candidate solution $\overline{U}_{i,s}^{*}$ is explicitly checked for the occurrence floating point errors, i.e. not-a- number (NaN) values that may have been produced by non-physical divisions by zero or by taking roots of negative numbers.

+ *Numerical admissibility detection (NAD):* In the past, the discrete maximum principle (DMP) was a very successful guideline for the construction of high resolution shock capturing schemes. In this dissertation, we therefore use the following relaxed discrete version of a discrete maximum principle, which takes into account the data representation of the DG method under the form of piecewise polynomials. The DMP is applied in an a posteriori manner as follows. A candidate solution $\overline{U}_{i,s}^{*}$ is said to fulfill the numerical admissibility detection criterion in cell V_i in cell V_i if the following relation is fulfilled component-wise for all conserved variables:

$$\min_{\bar{i}\in\mathcal{V}_i, \ \bar{s}\in\mathcal{S}_i} \overline{U}_{\bar{i},\bar{s}}^{n} - \delta \leq \overline{U}_{i,s}^{*} \leq \max_{\bar{i}\in\mathcal{V}_i, \ \bar{s}\in\mathcal{S}_i} \overline{U}_{\bar{i},\bar{s}}^{n} + \delta, \quad \forall s \in \mathcal{S}_i, \tag{2.4.16}$$

where $\mathcal{V}_i$ denote the Voronoi neighbourhood of cell V_i, i.e. the cells that share at least a common node with V_i. The small number δ is a parameter used to relax the discrete maximum principle thus allowing for very small undershoots and overshoots, which permits to maintain a good accuracy when dealing with smooth extrema. The value used in [98] and adopted in this thesis is

$$\delta = \max\left(\varepsilon_0, \varepsilon\left(\max_{\bar{i}\in\mathcal{V}_i, \ \bar{s}\in\mathcal{S}_i}\left(\overline{U}_{\bar{i},\bar{s}}^{n}\right) - \min_{\bar{i}\in\mathcal{V}_i, \ \bar{s}\in\mathcal{S}_i}\left(\overline{U}_{\bar{i},\bar{s}}^{n}\right)\right)\right), \tag{2.4.17}$$

where we set $\varepsilon = 10^{-3}$ and $\varepsilon_0 = 10^{-4}$. In other words, parameter δ defined allows the occurrence of new extrema. New extrema do not exceed one thousandth of the local jump at time t_n in the neighbourhood of the current cell. The value ε_0 is needed in the case where the jump is zero.

This completes the brief description of the subcell finite volume limiter used in this thesis.

Chapter 3

Numerical discretization of dispersive systems

Contents

In this chapter the numerical methods employed to solve the PDE systems presented in Chapter 1 are described.

First, in Section 3.1 the numerical scheme employed to discretize the one-layer non-hydrostatic pressure system (YAM) is described. The numerical scheme is based on a projection-correction technique, wherein a first step the underlying hydrostatic system (SWE) is solved by means of a finite volume scheme. Then, in a second step, the non-hydrostatic terms are included using a finite difference discretization. In this case, a staggered-grid is considered that contains the point values of the non-hydrostatic pressure and vertical velocity. The results of this section as well as the extension to bidimensional domains from Section 3.2, have been published by Escalante *et al.* in [112].

In Section 3.3 the numerical scheme employed to discretize the two-layer non-hydrostatic pressure system (NH-2L) is described. Similarly to the previous case, the scheme is based on a projection-correction technique, wherein a first step the underlying hydrostatic system (SWE-2L) is solved using a finite volume scheme. In a second step,

the non-hydrostatic terms are included employing a finite difference discretization. In this case, staggered-grids are not considered, and the non-hydrostatic pressure and vertical velocities variables are approximated as point values approximation in the centre of each finite volume cell. The results of this section have been recently submitted by Escalante *et al.* [118].

The system (NHyp) is discretized in Section 3.4. Note that, this non-hydrostatic pressure system is hyperbolic. Thus, it can be solved explicitly under a usual CFL restriction with a finite volume numerical scheme.

Finally, a Discontinuous Galerkin numerical scheme for the system (NHyp) will be described in Section 3.5. Since a non-linear limiter is needed, we will describe the a posteriori subcell finite volume limiter strategy adopted to limit numerical solution in presence of discontinuities, strong gradients or in the presence of wetting and drying fronts. To do that, we will use the previously described finite volume numerical scheme. The results of this section have been recently submitted by Escalante *et al.* [111] and are under a minor revision process.

In the subsequent Sections 3.1 to 3.5, for the sake of clarity, the corresponding numerical schemes are described for a fixed bed, that is:

$$\partial_t H = 0. \tag{3.0.1}$$

The extension of the proposed numerical schemes to the case of moving bottom is straightforward.

Furthermore, in Sections 3.1 to 3.4 the source term vector that contains friction, breaking and in the case of the system (NHyp), some non-hydrostatic terms, is set initially to zero:

$$S(U) = \mathbf{0}, \tag{3.0.2}$$

and later, it will be taken into account in a semi-implicit manner.

However, In Section 3.5 the source term is treated in a different way, that will be explained later.

3.1 An implicit projection-correction finite volume discretization of the system (YAM) on a staggered mesh

We describe now the numerical scheme used to discretize the system (YAM) with the assumptions made in (3.0.1) and (3.0.2). The numerical scheme employed is based on a two-step projection-correction method. First, we shall solve the underlying hyperbolic system (SWE) given by

$$\partial_t U + \partial_x F(U) = G(U)\partial_x H, \tag{SWE}$$

where U, F and G are defined in (SWE). Then, in a second step, non-hydrostatic terms will be taken into account. System (SWE) is discretized by a second order finite volume PVM positive-preserving well-balanced path-conservative method to be detailed in the next subsection. As usual, we consider a set of N_x finite volume cells $I_i = [x_{i-1/2}, x_{i+1/2}]$ with constant lengths Δx and define

$$U_i(t) = \frac{1}{\Delta x} \int_{I_i} U(x,t) \, dx,$$

the cell average of the function $U(x,t)$ on cell I_i at time t. Regarding non-hydrostatic terms, we consider a staggered-grid (see Figure 3.1) formed by the points $x_{i-1/2}$, $x_{i+1/2}$ of the interfaces for each cell I_i, and denote the point values of the functions p and w on point $x_{i+1/2}$ at time t by

$$p_{i+1/2}(t) = p(x_{i+1/2}, t), \ w_{i+1/2}(t) = w(x_{i+1/2}, t).$$

Non-hydrostatic terms will be approximated by second order compact finite differences.
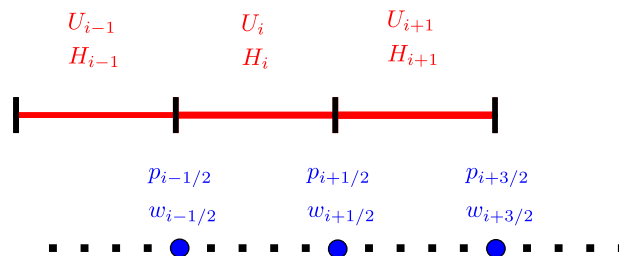
Figure 3.1: Numerical scheme stencil. Up: finite volume mesh. Down: staggered mesh for finite differences.

Time stepping

Assume given time steps Δt_n, and denote $t_n = \sum_{j \leq n} \Delta t_j$. To obtain second order accuracy in time, the two-stage second-order TVD Runge-Kutta scheme [142] is adopted. At the

kth stage, $k \in \{1, 2\}$, the two-step projection-correction method is given by

$$
\begin{cases}
\dfrac{U^{(\widetilde{k})} - U^{(k-1)}}{\Delta t} + \partial_x F(U^{(k-1)}) = G(U^{(k-1)}) \partial_x H, & \text{(3.1.1a)} \\[3ex]
\dfrac{U^{(k)} - U^{(\widetilde{k})}}{\Delta t} = \mathcal{T}(U^{(k)}, \partial_x U^{(k)}, P^{(k)}, \partial_x P^{(k)}, H, \partial_x H) & \text{(3.1.1b)} \\[3ex]
\dfrac{w^{(k)} - w^{(k-1)}}{\Delta t} = 2\dfrac{p^{(k)}}{h^{(k)}} & \text{(3.1.1c)} \\[3ex]
\mathcal{I}(U^{(k)}, \partial_x U^{(k)}, H, \partial_x H, w^{(k)}) = 0 & \text{(3.1.1d)}
\end{cases}
$$

where $U^{(0)}$ is U at the time level t_n, $U^{(\widetilde{k})}$ is an intermediate value in the two-step projection-correction method that contains the numerical solution of the hydrostatic system (SWE) (system (3.1.1a)) at the corresponding kth stage of the Runge-Kutta, and $U^{(k)}$, $w^{(k)}$ are the kth stage estimate. After that, a final value of the solution at the t_{n+1} time level is obtained:

$$
U^{n+1} = \frac{1}{2} U^n + \frac{1}{2} U^{(2)}. \tag{3.1.2}
$$

Note that, equations (3.1.1b)-(3.1.1d) require, at each stage of the calculation, to solve a Poisson-like equation on the non-hydrostatic pressure $p^{(k)}$. This will be described bellow.

For the computation of the time step the usual CFL restriction is considered given by

$$
\Delta t < CFL \frac{\Delta x}{|\lambda_{max}|}, \ 0 < CFL \le 1, \ |\lambda_{max}| = \max_{i \in \{1, \ldots, N_x\}} \left\{ |u_i| + \sqrt{gh_i} \right\}. \tag{3.1.3}
$$

Finite volume discretization for the underlying hyperbolic system

A second order path-conservative PVM scheme based on reconstruction operator for the discretization in space of the system (3.1.1a) is considered. To do so, we consider here a Roe linearization based on the simple straight-line segment path for the conserved variables. Following the high order numerical scheme in space (2.2.49) and approximating the ODE in time, we obtain the following numerical scheme that at the kth stage of the Runge-Kutta method reads:

$$
U_i^{(\widetilde{k})} = U_i^{(k-1)} - \frac{\Delta t}{\Delta x} \left(D_{i+1/2}^{(k-1),-} + D_{i-1/2}^{(k-1),+} + \mathcal{I}_i^{(k-1)} \right), \tag{3.1.4}
$$

where, skipping the time dependence in k to relax the notation, $D_{i+1/2}^{\pm}$ is given by a PVM path-conservative scheme (see (2.2.37))

$$D_{i+1/2}^{\pm} = D_{i+1/2}^{\pm}(U_{i+1/2}^{-}, H_{i+1/2}^{-}, U_{i+1/2}^{+}, H_{i+1/2}^{+}) =$$

$$= \frac{1}{2} \left(F(U_{i+1/2}^{+}) - F(U_{i+1/2}^{-}) - G_{i+1/2} \left(H_{i+1/2}^{+} - H_{i+1/2}^{-} \right) \right) \qquad (3.1.5)$$

$$\pm \frac{1}{2} Q_{i+1/2} \left(U_{i+1/2}^{+} - U_{i+1/2}^{-} - A_{i+1/2}^{-1} G_{i+1/2} \left(H_{i+1/2}^{+} - H_{i+1/2}^{-} \right) \right),$$

where

$$G_{i+1/2} \left(H_{i+1/2}^{+} - H_{i+1/2}^{-} \right) = \begin{pmatrix} 0 \\ g\widetilde{h}_{i+1/2} \left(H_{i+1/2}^{+} - H_{i+1/2}^{-} \right) \end{pmatrix},$$

is obtained from (2.2.30). $U_{i+1/2}^{\pm}$ is the vector defined by a reconstruction procedure on the variables to the left ($^-$) and right ($^+$) of the inter-cell $x_{i+1/2}$. This reconstruction procedure is done using a MUSCL reconstruction operator, combined with a minmod limiter as detailed in (2.2.50)-(2.2.52). The MUSCL reconstruction operator also takes into account the positivity of the water height. Finally, as explained in Subsection 2.2.4, the variable $H_{i+1/2}^{\pm}$ is recovered from $H_{i+1/2}^{\pm} = h_{i+1/2}^{\pm} - \eta_{i+1/2}^{\pm}$.

$Q_{i+1/2}$ is the viscosity matrix associated to PVM-1U(S_L, S_R) or HLL method. In this case, as in (2.2.39) $Q_{i+1/2}$ is obtained by a polynomial evaluation of the Roe Matrix

$$Q_{i+1/2} = \alpha_0 Id + \alpha_1 A_{i+1/2},$$

where

$$A_{i+1/2} = \begin{pmatrix} 0 & 1 \\ -\widetilde{u}_{i+1/2}^2 + g\widetilde{h}_{i+1/2} & 2\widetilde{u}_{i+1/2} \end{pmatrix}$$

is the Roe Matrix associated to the flux $F(U)$ of the SWE, $\widetilde{h}_{i+1/2}$ and $\widetilde{u}_{i+1/2}$ being the Roe averages

$$\widetilde{h}_{i+1/2} = \frac{h_{i+1/2}^{+} + h_{i+1/2}^{-}}{2}, \quad \widetilde{u}_{i+1/2} = \frac{u_{i+1/2}^{+}\sqrt{h_{i+1/2}^{+}} + u_{i+1/2}^{-}\sqrt{h_{i+1/2}^{-}}}{\sqrt{h_{i+1/2}^{+}} + \sqrt{h_{i+1/2}^{-}}},$$

α_0, α_1 are given by

$$\alpha_0 = \frac{S_R|S_L| - S_L|S_R|}{S_R - S_L}, \quad \alpha_1 = \frac{|S_R| - |S_L|}{S_R - S_L}.$$

where S_L, S_R are estimates of the smallest and biggest wave speeds respectively at the interface $x_{i+1/2}$, as it is usually considered for such methods:

$$S_L = \min \left(u_{i+1/2}^{-} - \sqrt{gh_{i+1/2}^{-}}, \ \widetilde{u}_{i+1/2} - \sqrt{g\widetilde{h}_{i+1/2}} \right),$$

$$S_R = \max\left(\widetilde{u}_{i+1/2} + \sqrt{g\widetilde{h}_{i+1/2}}, \ u^+_{i+1/2} + \sqrt{gh^+_{i+1/2}}\right).$$

Notice that the term

$$Q_{i+1/2}A^{-1}_{i+1/2}G_{i+1/2}\left(H^+_{i+1/2} - H^-_{i+1/2}\right)$$

in (3.1.5) can be interpreted as the up-winding part of the source term discretization and that the contribution

$$\alpha_0 A^{-1}_{i+1/2}G_{i+1/2}\left(H^+_{i+1/2} - H^-_{i+1/2}\right)$$

makes no sense if any of the eigenvalues of $A_{i+1/2}$ vanishes. In this case the problem is said to be resonant. Resonant problems exhibit an additional difficulty, as weak solutions may not be uniquely determined by their initial data. In this thesis we follow the strategy described in [46], where $A_{i+1/2}$ is replaced by an appropriate matrix $A^*_{i+1/2}$

$$A^*_{i+1/2} = \begin{pmatrix} 0 & 1 \\ g\widetilde{h}_{i+1/2} & 0 \end{pmatrix}.$$

After applying this technique, one has

$$\alpha_0\left(U^+_{i+1/2} - U^-_{i+1/2} - A^{-1}_{i+1/2}G_{i+1/2}\left(H^+_{i+1/2} - H^-_{i+1/2}\right)\right) = \alpha_0\begin{pmatrix} \eta^+_{i+1/2} - \eta^-_{i+1/2} \\ q^+_{i+1/2} - q^-_{i+1/2} \end{pmatrix}.$$

Let us introduce the following notation:

$$R_{i+1/2} = F_C(U^+_{i+1/2}) - F_C(U^-_{i+1/2}) + T_{p,i+1/2},$$

where F_C is the convective flux and $T_{p,i+1/2}$ contains the pressure terms:

$$F_C(U) = \begin{pmatrix} q \\ \dfrac{q^2}{h} \end{pmatrix}, \quad T_{p,i+1/2} = \begin{pmatrix} 0 \\ g\widetilde{h}_{i+1/2}\left(\eta^+_{i+1/2} - \eta^-_{i+1/2}\right) \end{pmatrix}.$$

Thus, one can rewrite $D^\pm_{i+1/2}$ as

$$D^\pm_{i+1/2} = \frac{1}{2}\left((1 \pm \alpha_1)\,R_{i+1/2} \pm \alpha_0\begin{pmatrix} \eta^+_{i+1/2} - \eta^-_{i+1/2} \\ q^+_{i+1/2} - q^-_{i+1/2} \end{pmatrix}\right).$$

Finally, the last term $\mathcal{I}_i$ in (3.1.4) comes from the volume integral that appears in (2.2.49). Notice that the integral in (2.2.49)

$$\int_{I_i} \partial_x F[P_{i,U}(x)] - G[P_{i,U}(x)]\frac{dP_{i,H}}{dx}(x)\,dx$$

can be written as

$$\int_{I_i} \partial_x F_C[P_{i,U}(x)] + \begin{pmatrix} 0 \\ gP_{i,h}(x)\dfrac{dP_{i,\eta}}{dx}(x) \end{pmatrix} dx.$$

Taking into account that $P_{i,h}(x)$ and $P_{i,\eta}(x)$ are lineal functions, $\mathcal{I}_i$ can be written as

$$\mathcal{I}_i = F_C(U^-_{i+1/2}) - F_C(U^+_{i-1/2}) + \begin{pmatrix} 0 \\ gh_i \left(\eta^-_{i+1/2} - \eta^+_{i-1/2} \right) \end{pmatrix},$$

where the integral of the pressure term has been exactly computed using a mid-point quadrature rule.

Remark 3.1.1. *The numerical scheme (3.1.4) considered for the underlying hyperbolic system is well-balanced for the steady state water at rest solutions*

$$\eta = h - H = cst, \ u = 0,$$

and linearly $L^\infty -$ stable under the usual CFL condition (3.1.3). Moreover the scheme is positive preserving for the water height for a smooth bathymetry under $\dfrac{1}{2}CFL$ condition.

Finite difference discretization for the non-hydrostatic terms

In this subsection we describe the discretization of the non-hydrostatic terms. From equations (3.1.1b)–(3.1.1d), for every $k \in \{1, 2\}$ of the Runge-Kutta stage, we get

$$\begin{cases} h_i^{(k)} = h_i^{(\widetilde{k})}, & \text{(3.1.6a)} \\[2ex] q_i^{(k)} = q_i^{(\widetilde{k})} - \Delta t \left(h_i^{(k)}\partial_x p_i^{(k)} + p_i^{(k)}\partial_x \left(2\eta_i^{(k)} - h_i^{(k)} \right) \right), & \text{(3.1.6b)} \\[2ex] w_{i+1/2}^{(k)} = w_{i+1/2}^{(k-1)} + \Delta t\dfrac{p_{i+1/2}^{(k)}}{h_{i+1/2}^{(k)}}, & \text{(3.1.6c)} \\[2ex] h_{i+1/2}^{(k)}\partial_x q_{i+1/2}^{(k)} - q_{i+1/2}^{(k)}\partial_x \left(2\eta_{i+1/2}^{(k)} - h_{i+1/2}^{(k)} \right) + 2h_{i+1/2}^{(k)}w_{i+1/2}^{(k)} = 0, & \text{(3.1.6d)} \end{cases}$$

where we will use a second order point value approximation in the center of the cell to compute $\partial_x h_i$, $\partial_x \eta_i$, p_i and $\partial_x p_i$ as follows:

$$\partial_x h_i = \frac{h_{i+1} - h_{i-1}}{2\Delta x}, \ \partial_x \eta_i = \frac{\eta_{i+1} - \eta_{i-1}}{2\Delta x},$$

$$p_i = \frac{p_{i+1/2} + p_{i-1/2}}{2}, \ \partial_x p_i = \frac{p_{i+1/2} - p_{i-1/2}}{\Delta x}. \tag{3.1.7}$$

In a similar way, second order point value approximations of $h_{i+1/2}$, $\partial_x h_{i+1/2}$, $\partial_x \eta_{i+1/2}$, $q_{i+1/2}$, $\partial_x q_{i+1/2}$, on the staggered-grid will be computed from the approximations of the average values on the cell I_i and I_{i+1} as follows:

$$h_{i+1/2} = \frac{h_{i+1} + h_i}{2}, \ \partial_x h_{i+1/2} = \frac{h_{i+1} - h_i}{\Delta x}, \ \partial_x \eta_{i+1/2} = \frac{\eta_{i+1} - \eta_i}{\Delta x},$$

$$q_{i+1/2} = \frac{q_{i+1} + q_i}{2}, \ \partial_x q_{i+1/2} = \frac{q_{i+1} - q_i}{\Delta x}. \tag{3.1.8}$$

Substituting equations (3.1.6b)-(3.1.6c) into (3.1.6d), we obtain a discrete Poisson-like linear system for the non-hydrostatic pressure:

$$\boldsymbol{A}\boldsymbol{\mathcal{P}} = \boldsymbol{\mathcal{RHS}}, \tag{3.1.9}$$

where $\boldsymbol{A}$ is a tridiagonal matrix. The matrix $\boldsymbol{A}$ as well as the *Right Hand Side* vector $\boldsymbol{\mathcal{RHS}}$ are given in Appendix B. We would also like to stress the dependency of $\boldsymbol{A}$ and $\boldsymbol{\mathcal{RHS}}$ on the variables $U \equiv U^{(\widetilde{k})}$ and $w \equiv w^{(\widetilde{k})}$. $\boldsymbol{\mathcal{P}}$ is a vector containing the non-hydrostatic pressure values $p_{i+1/2}^{(k)}$.

The linear system is efficiently solved using the Thomas algorithm [236]. Once the non-hydrostatic pressure terms $p_{i+1/2}^{(k)}$ have been computed, the discharges $q_i^{(k)}$ as well as the vertical velocities $w_{i+1/2}^{(k)}$ can be updated from equations (3.1.6b)-(3.1.6c), where in a similar way, a second order point value approximation in the centre of the cell will be used.

Final numerical scheme

For the sake of clarity, a guideline of the final numerical scheme will be highlighted in what follows. For every kth stage $k \in \{1, 2\}$ of the Runge-Kutta method, the problem (YAM) is split into two parts. A two-step projection-correction method on staggered grids is used:

- **Finite volume step** (solving the hydrostatic system): From (3.1.4), solve explicitly the System (SWE) at the kth stage of the Runge-Kutta:

$$U_i^{(\widetilde{k})} = U_i^{(k-1)} - \frac{\Delta t}{\Delta x}\left(D_{i+1/2}^{(k-1),-} + D_{i-1/2}^{(k-1),+} + \mathcal{I}_i^{(k-1)}\right),$$

by means of a PVM path-conservative finite volume scheme (3.1.4) combining a MUSCL reconstruction operator to obtain the intermediate value $U_i^{(\widetilde{k})}$ in the two-step projection-correction method that contains the numerical solution of the System (SWE).

- **Finite Difference step** (non-hydrostatic pressure correction):

  + Solve the discrete Poisson-like linear system (3.1.9) to obtain the non-hydrostatic pressures

  $$p_{i+1/2}^{(k)}.$$

  To do so, we use:

    * Second order point value approximations in the center of the cell of $\partial_x h_i$, $\partial_x \eta_i$, p_i and $\partial_x p_i$ computed from the averaged values to compute (3.1.6b).
    * Second order point value approximations of $h_{i+1/2}$, $\partial_x h_{i+1/2}$, $\partial_x \eta_{i+1/2}$, $q_{i+1/2}$, $\partial_x q_{i+1/2}$, on the staggered-grid that are computed from the approximations of the average values on the cell I_i and I_{i+1} to compute (3.1.6d).

  + With the computed non-hydrostatic pressure terms $p_{i+1/2}^{(k)}$, the horizontal discharge as well as the vertical velocity can be updated from (3.1.6b)–(3.1.6d). Notice that in order to update the horizontal discharge, a second order point value approximation in the centre of the cell will be used using (3.1.7).

Finally,

$$U^{n+1} = \frac{1}{2}U^n + \frac{1}{2}U^{(2)}.$$

Remark 3.1.2. *In order to include friction with the bottom and the breaking mechanism, the source term $S(U)$ is discretized in a semi-implicit way at the end of the second step of the proposed numerical scheme, at each Runge-Kutta stage.*

Remark 3.1.3. *Since non-hydrostatic, friction and breaking terms appear only in the momentum equations, the final numerical scheme is well-balanced for the water at rest solutions*

$$\eta = h - H = cst, \ u = w = p = 0,$$

and positive preserving for the water height for a smooth bathymetry under $\frac{1}{2}CFL$ condition.

3.2   An implicit projection-correction finite volume discretization of the system (YAM-2D) on a staggered mesh

We describe now the extension of the previously described numerical scheme in two space dimension used to discretize the system (YAM-2D) with the assumptions made in (3.0.1) and (3.0.2). The numerical scheme employed is based on a two-step projection-correction method. First, we shall solve the underlying hyperbolic system (SWE-2D) given by

$$\partial_t U + \nabla \cdot \boldsymbol{F}(U) = \boldsymbol{G}(U) \cdot \nabla H, \tag{SWE-2D}$$

where U, $\boldsymbol{F}$ and $\boldsymbol{G}$ are defined in (SWE-2D). Then, in a second step, non-hydrostatic terms will be taken into account. System (SWE-2D) is discretized by a second order finite volume PVM positive-preserving well-balanced segment path-conservative method to be detailed in the next subsection. As usual, let us consider a set of $N_E = N_x \times N_y$ non-overlapping Cartesian control volumes

$$V_{ij} = \left[x_i - \frac{1}{2}\Delta x, x_i + \frac{1}{2}\Delta x \right] \times \left[y_j - \frac{1}{2}\Delta y, y_j + \frac{1}{2}\Delta y \right],$$

i, j denote a multi-index

$$i = 1, \ldots, N_x, \ \ j = 1, \ldots, N_y.$$

Let us define $U_{ij}(t)$ the constant approximation to the average of the solution in the cell V_{ij} at time t :

$$U_{ij}(t) \cong \frac{1}{|V_{ij}|} \int_{V_{ij}} U(\boldsymbol{x}, t) \, d\boldsymbol{x}.$$

Regarding non-hydrostatic terms, we will use one common arrangement of the variables, known as the Arakawa C-grid (See Figure 3.2). This is an extension of the procedure used for the 1D case. Variables p and w will be computed at the intersection of the edges:

$$p_{i+1/2j+1/2}(t) = p\left(x_i + \frac{1}{2}\Delta x, y_j + \frac{1}{2}\Delta y, t \right), \ w_{i+1/2j+1/2}(t) = w\left(x_i + \frac{1}{2}\Delta x, y_j + \frac{1}{2}\Delta y, t \right).$$

We will also use second order point-value approximations of the non-hydrostatic pressure and vertical velocity at the center of the cell:

$$p_{ij}(t) = p(x_i, y_j, t), \ w_{ij}(t) = w(x_i, y_j, t).$$

Non-hydrostatic terms will be approximated by second order compact finite differences.

Figure 3.2: Numerical scheme stencil

Time stepping

Assume given time steps Δt_n, and denote $t_n = \sum_{j \leq n} \Delta t_j$. To obtain second order accuracy in time, the two-stage second-order TVD Runge-Kutta scheme [142] is adopted. At the kth stage, $k \in \{1, 2\}$, the two-step projection-correction method is given by

$$
\begin{cases}
\dfrac{U^{(\tilde{k})} - U^{(k-1)}}{\Delta t} + \nabla \cdot \boldsymbol{F}(U^{(k-1)}) = \boldsymbol{G}(U^{(k-1)}) \cdot \nabla H, & \text{(3.2.1a)} \\[3ex]
\dfrac{U^{(k)} - U^{(\tilde{k})}}{\Delta t} = \mathcal{T}(U^{(k)}, \nabla U^{(k)}, p^{(k)}, \nabla p^{(k)}, H, \nabla H) & \text{(3.2.1b)} \\[3ex]
\dfrac{w^{(k)} - w^{(k-1)}}{\Delta t} = 2\dfrac{p^{(k)}}{h^{(k)}} & \text{(3.2.1c)} \\[3ex]
\mathcal{I}(U^{(k)}, \nabla U^{(k)}, H, \nabla H, w^{(k)}) = 0 & \text{(3.2.1d)}
\end{cases}
$$

where $U^{(0)}$ is U at the time level t_n, $U^{(\tilde{k})}$ is an intermediate value in the two-step projection-correction method that contains the numerical solution of the hydrostatic system (SWE-2D) (system (3.2.1a)) at the corresponding kth stage of the Runge-Kutta, and $U^{(k)}$, $w^{(k)}$ are the kth stage estimate. After that, a final value of the solution at the t_{n+1} time level is obtained:

$$
U^{n+1} = \frac{1}{2}U^n + \frac{1}{2}U^{(2)}. \tag{3.2.2}
$$

Note that, equations (3.2.1b)-(3.2.1d) requires, at each stage of the calculation respectively, to solve a Poisson-like equation on the non-hydrostatic pressure $p^{(k)}$. This will be described bellow.

For the computation of the time step the usual CFL restriction is considered given by

$$\Delta t < CFL \frac{\max(\Delta x, \Delta y)}{2|\lambda_{max}|}, \ 0 < CFL \le 1,$$

$$|\lambda_{max}| = \max_{ij} \left\{ |u_{ij}| + \sqrt{gh_{ij}}, |v_{ij}| + \sqrt{gh_{ij}} \right\}.$$

(3.2.3)

Finite volume discretization for the underlying hyperbolic system

A second order path-conservative PVM scheme based on reconstruction operator for the discretization in space of the system (3.2.1a) is considered. To do so, we consider here a Roe linearization based on the simple straight-line segment path for the conserved variables. Following the high order numerical scheme in space (2.3.22) and approximating the ODE in time, we obtain the following numerical scheme that at the kth stage of the Runge-Kutta method reads:

$$U_{ij}^{(\widetilde{k})} = U_{ij}^{(k-1)} - \frac{\Delta t}{|V_{ij}|} \sum_{\overline{ij} \in \mathcal{N}_{ij}} \int_{E_{ij\overline{ij}}} D_{\Phi}^{(k-1),-}(W_{ij\overline{ij}}^{-}(\gamma), W_{ij\overline{ij}}^{+}(\gamma), \boldsymbol{n}_{ij\overline{ij}}) \, d\gamma$$

(3.2.4)

$$- \frac{\Delta t}{|V_{ij}|} \int_{V_{ij}} \nabla \cdot \boldsymbol{F}\left(P_{ij,U}(\boldsymbol{x})\right) - \boldsymbol{G}\left(P_{ij,U}(\boldsymbol{x})\right) \cdot \nabla P_{ij,H}(\boldsymbol{x}) \, d\boldsymbol{x}$$

where $D_{\Phi}^{(k-1),-}(W_{ij\overline{ij}}^{-}(\gamma), W_{ij\overline{ij}}^{+}(\gamma), \boldsymbol{n}_{ij\overline{ij}})$ is given by a HLL PVM path-conservative scheme (see (2.3.14)).

In order to compute the surface integral, a numerical quadrature mid-point rule is used. Thus, the reconstructed states $W_{ij\overline{ij}}^{\pm}(\gamma)$ are evaluated at the mid-point of each edge.

Concerning the volume integral, let us first rewrite it as in the 1D case as

$$\int_{V_{ij}} \nabla \cdot \boldsymbol{F}_C\left(P_{ij,U}(\boldsymbol{x})\right) - \boldsymbol{G}\left(P_{ij,U}(\boldsymbol{x})\right) \cdot \nabla P_{ij,\eta}(\boldsymbol{x}) \, d\boldsymbol{x}$$

$\boldsymbol{F}_C$ being the convective flux, defined as before. Then, notice that from the divergence theorem

$$\int_{V_{ij}} \nabla \cdot \boldsymbol{F}_C\left(P_{ij,U}(\boldsymbol{x})\right) \, d\boldsymbol{x} = \sum_{\overline{ij} \in \mathcal{N}_{ij}} \int_{E_{ij\overline{ij}}} F_{C,\boldsymbol{n}_{ij\overline{ij}}}(U_{ij\overline{ij}}^{-}(\gamma)),$$

which is also approximated numerically by a mid-point quadrature rule at each edge. Second, note that the term $\boldsymbol{G}\left(P_{ij,U}(\boldsymbol{x})\right) \cdot \nabla P_{ij,\eta}(\boldsymbol{x})$ is linear due to the use of the MUSCL operator reconstruction and that of the form of $\boldsymbol{G}$. Then, the volume integral can be exactly computed by using a mid-point quadrature rule.

Remark 3.2.1. *The numerical scheme (3.2.4) considered for the underlying hyperbolic system is well-balanced for the steady state water at rest solutions*

$$\eta = h - H = cst, \ u = v = 0,$$

and linearly $L^\infty - $ *stable under the usual CFL condition (3.2.3). Moreover the scheme is positive preserving for the water height for a smooth bathymetry under* $\dfrac{1}{2}CFL$ *condition.*

Finite difference discretization for the non-hydrostatic terms

In this subsection we give some guidelines for the discretization of the non-hydrostatic terms. The details of the scheme can be found in the Appendix C. From equations (3.2.1b)– (3.2.1d), for every $k \in \{1, 2\}$ of the Runge-Kutta stage, we get

$$
\begin{cases}
U_{ij}^{(k)} = U_{ij}^{(\widetilde{k})} + \Delta t \mathcal{T}(U^{(k)}, \nabla U^{(k)}, p^{(k)}, \nabla p^{(k)}, H, \nabla H)_{ij} & (3.2.5a) \\[3mm]
w_{i+1/2j+1/2}^{(k)} = w_{i+1/2j+1/2}^{(k-1)} + 2\Delta t \dfrac{p_{i+1/2j+1/2}^{(k)}}{h_{i+1/2j+1/2}^{(k)}} & (3.2.5b) \\[3mm]
\mathcal{I}(U^{(k)}, \nabla U^{(k)}, H, \nabla H, w^{(k)})_{i+1/2j+1/2} = 0. & (3.2.5c)
\end{cases}
$$

The term $\mathcal{T}(U^{(k)}, \nabla U^{(k)}, p^{(k)}, \nabla p^{(k)}, H, \nabla H)_{ij}$ appearing in equation (3.2.5a) denote the point value discretization in the center of the cell V_{ij} of the operator $\mathcal{T}$ that is approximated in space by second order finite differences (see (C.0.1) in the Appendix C).

In the same way, second order point value approximations of equations (3.2.5b) and (3.2.5c) on the staggered-grid points are computed from the approximations of the average values on the cell (see (C.0.2) and (C.0.3) in the Appendix C).

System (3.2.5a)–(3.2.5c) leads to solve a penta-diagonal linear system for the unknowns $p_{i+1/2}^{(k)}$. As for the 1D case, let us remark that the coefficients of the matrices depend on the variables $h^{(\widetilde{k})}$ and $\eta^{(\widetilde{k})}$. Since the resulting coefficients of the matrix are too tedious to be given here, we shall omit them. A rigorous analysis of the matrices in general is not an easy task. Nevertheless, in all the numerical computations, we have checked that the matrices are strictly diagonally dominant. Thus, due to the Gershgorin circle theorem, the matrices are non-singular for all the test cases shown in this dissertation.

The linear system is solved using an iterative Jacobi method combined with a scheduled relaxation method following [3].

Remark that the compactness of the numerical stencil and the easy parallelization of the Jacobi method adapts well to the implementation of the scheme on GPUs

architectures. Given $\boldsymbol{\mathcal{P}}$ a vector that contains the non-hydrostatic pressure unknowns, in order to define a convergence criteria, as in the 1D case we use

$$||\boldsymbol{\mathcal{P}}_{(s+1)} - \boldsymbol{\mathcal{P}}_{(s)}|| < \epsilon_{tol}, \qquad (3.2.6)$$

where $\boldsymbol{\mathcal{P}}_{(s+1)}$ denotes the k-th approximation of $\boldsymbol{P}^{n+1}$ given by the Jacobi algorithm. In the subsequent numerical test performed in this work, ϵ_{tol} is set to 10^{-8}. It is observed that the Jacobi method converges in a few iterations for the problems tested here.

Once the non-hydrostatic pressure terms $p_{i+1/2j+1/2}^{(k)}$ have been computed, the horizontal discharges can be updated from equation (3.2.5a), where in a similar way, a second order point value approximation in the centre of the cell will be used (see (C.0.1) in the Appendix C). Finally, the vertical velocities can be easily updated from (3.2.5b) and using (C.0.3) for the computation of $h_{i+1/2j+1/2}$ (See in Appendix C).

Final numerical scheme

For the sake of clarity, a guideline of the final numerical scheme will be highlighted in what follows. For every kth stage $k \in \{1, 2\}$ of the Runge-Kutta method, the problem (YAM-2D) is split into two parts. A two-step projection-correction method on staggered grids is used:

- **Finite volume step** (solving the hydrostatic system): From (3.2.4), solve explicitly the System (SWE-2D) at the kth stage of the Runge-Kutta:

$$U_{ij}^{(\widetilde{k})} = U_{ij}^{(k-1)} - \frac{\Delta t}{|V_{ij}|} \sum_{\overline{ij} \in \mathcal{N}_{ij}} \int_{E_{ij\overline{ij}}} D_{\Phi}^{(k-1),-}(W_{ij\overline{ij}}^{-}(\gamma), W_{ij\overline{ij}}^{+}(\gamma), \boldsymbol{n}_{ij\overline{ij}}) \, d\gamma$$

$$-\frac{\Delta t}{|V_{ij}|} \int_{V_{ij}} \nabla \cdot \boldsymbol{F}\left(P_{ij,U}(\boldsymbol{x})\right) - \boldsymbol{G}\left(P_{ij,U}(\boldsymbol{x})\right) \cdot \nabla P_{ij,H}(\boldsymbol{x}) \, d\boldsymbol{x}$$

  by means of a PVM path-conservative finite volume scheme (3.2.4) combining a MUSCL reconstruction operator to obtain the intermediate value $U_{ij}^{(\widetilde{k})}$ in the two-step projection-correction method that contains the numerical solution of the System (SWE-2D).

- **Finite Difference step** (non-hydrostatic pressure correction):

  + Solve the discrete Poisson-like linear system arising in (3.2.5a)–(3.2.5c) to obtain the non-hydrostatic pressures

$$p_{i+1/2}^{(k)}.$$

  To do so, we use:

∗ Second order point value approximations in the center of the cell of the variables h, η, p and its gradients, computed from the averaged values to compute (3.2.5a) (See (C.0.1) in the Appendix C).

∗ To compute (3.2.5c), second order point value approximations of h, η, q and its gradients on the staggered-grid are used (See (C.0.2) in the Appendix C).

+ With the computed non-hydrostatic pressure terms $p_{i+1/2}^{(k)}$, the horizontal discharges as well as the vertical velocity can be updated from (3.2.5a)–(3.2.5b). Notice that in order to update the horizontal discharge, a second order point value approximation in the centre of the cell will be used (See (C.0.1) in the Appendix C).

Finally,

$$U^{n+1} = \frac{1}{2}U^n + \frac{1}{2}U^{(2)}.$$

3.3 An implicit projection-correction finite volume discretization of the system (NH-2L)

We describe now the numerical scheme used to discretize the system (NH-2L) with the assumptions made in (3.0.1) and (3.0.2). The numerical scheme employed is based on a two-step projection-correction method. First, we shall solve the underlying non-conservative hyperbolic system (SWE-2L) given by

$$\partial_t U + \partial_x F(U) + B(U)\partial_x U = G(U)\partial_x H, \qquad \text{(SWE-2L)}$$

where U, F, B and G are defined in (NH-2L). Then, in a second step, non-hydrostatic terms will be taken into account. System (SWE-2L) is discretized by a second order finite volume PVM positive-preserving well-balanced segment path-conservative method to be detailed in the next subsection. As usual, we consider a set of N_x finite volume cells $I_i = [x_{i-1/2}, x_{i+1/2}]$ with constant lengths Δx and define

$$U_i(t) = \frac{1}{\Delta x}\int_{I_i} U(x,t)\ dx,$$

the cell average of the function $U(x,t)$ on cell I_i at time t. In this case, we do not consider a staggered grid as in Subsection 3.1 for the non-hydrostatic term vector defined in (NH-2L). Instead, we consider the mid-points x_i of each cell I_i and denote the point values of the function P at time t by

$$P_i(t) = P(x_i, t).$$

Non-hydrostatic terms will be approximated by second order compact finite differences.

Time stepping

Assume given time steps Δt_n, and denote $t_n = \sum_{j \leq n} \Delta t_j$. To obtain second order accuracy in time, the two-stage second-order TVD Runge-Kutta scheme [142] is adopted. At the kth stage, $k \in \{1, 2\}$, the two-step projection-correction method is given by

$$
\begin{cases}
\dfrac{U^{(\widetilde{k})} - U^{(k-1)}}{\Delta t} + \partial_x F(U^{(k-1)}) + B(U^{(k-1)})\partial_x U^{(k-1)} = G(U^{(k-1)})\partial_x H, & \text{(3.3.1a)} \\[2ex]
\dfrac{U^{(k)} - U^{(\widetilde{k})}}{\Delta t} = \mathcal{T}(U^{(k)}, \partial_x U^{(k)}, P^{(k)}, \partial_x P^{(k)}, H, \partial_x H) & \text{(3.3.1b)} \\[2ex]
\mathcal{I}(U^{(k)}, \partial_x U^{(k)}, H, \partial_x H) = \mathbf{0} & \text{(3.3.1c)}
\end{cases}
$$

where $U^{(0)}$ is U at the time level t_n, $U^{(\widetilde{k})}$ is an intermediate value in the two-step projection-correction method that contains the numerical solution of the hydrostatic system (SWE-2L) (system (3.3.1a)) at the corresponding kth stage of the Runge-Kutta, and $U^{(k)}$ is the kth stage estimate. After that, a final value of the solution at the t_{n+1} time level is obtained:

$$
U^{n+1} = \frac{1}{2}U^n + \frac{1}{2}U^{(2)}. \tag{3.3.2}
$$

Note that, equations (3.3.1b)-(3.3.1c) requires, at each stage of the calculation respectively, to solve a Poisson-like system for each one of the variables contained in $P^{(k)}$. This will be described bellow.

Considering the upper bound for the maximum wave speed estimated in Subsection (1.2.2)

$$
|\lambda_{max}| \leq \max\left(|u_1| + \sqrt{gh}, |u_2| + \sqrt{gh}\right),
$$

then the usual CFL condition considered for the computation of Δt is given by

$$
\Delta t < CFL\frac{\Delta x}{|\lambda_{max}|}, \ 0 < CFL \leq 1, \ |\lambda_{max}| = \max_{\substack{i \in \{1, \dots, N_x\} \\ \alpha \in \{1,2\}}} \left\{|u_{\alpha,i}| + \sqrt{gh_i}\right\}. \tag{3.3.3}
$$

Finite volume discretization for the underlying hyperbolic system

A second order path-conservative PVM scheme based on reconstruction operator for the discretization in space of the system (3.3.1a) is considered. To do so, we consider here a Roe linearization based on the simple straight-line segment path for the conserved variables. Following the high order numerical scheme in space (2.2.49) and approximating

the ODE in time, we obtain the following numerical scheme that at the kth stage of the Runge-Kutta method reads:

$$U_i^{(\widetilde{k})} = U_i^{(k-1)} - \frac{\Delta t}{\Delta x} \left(D_{i+1/2}^{(k-1),-} + D_{i-1/2}^{(k-1),+} + \mathcal{I}_i^{(k-1)} \right), \qquad (3.3.4)$$

where, skipping the time dependence in k to relax the notation, $D_{i+1/2}^{\pm}$ is given by a PVM path-conservative scheme (see (2.2.37))

$$D_{i+1/2}^{\pm} = D_{i+1/2}^{\pm}(U_{i+1/2}^-, H_{i+1/2}^-, U_{i+1/2}^+, H_{i+1/2}^+) =$$

$$= \frac{1}{2} \left(F(U_{i+1/2}^+) - F(U_{i+1/2}^-) + B_{i+1/2} \left(U_{i+1/2}^+ - U_{i+1/2}^- \right) - G_{i+1/2} \left(H_{i+1/2}^+ - H_{i+1/2}^- \right) \right)$$

$$\pm \frac{1}{2} Q_{i+1/2} \left(U_{i+1/2}^+ - U_{i+1/2}^- - A_{i+1/2}^{-1} G_{i+1/2} \left(H_{i+1/2}^+ - H_{i+1/2}^- \right) \right),$$

$$(3.3.5)$$

where

$$G_{i+1/2} \left(H_{i+1/2}^+ - H_{i+1/2}^- \right) = g \widetilde{h}_{i+1/2} \left(H_{i+1/2}^+ - H_{i+1/2}^- \right) (\vec{e}_2 + \vec{e}_3),$$

is obtained after compute the path-integral appearing in (2.2.30), $(\vec{e}_i)_j = \delta_{i,j}$ being the ith vector of the canonical basis on $\mathbb{R}^4$. Similarly, the path-integral (2.2.29) is approximated by

$$B_{i+1/2} \left(U_{i+1/2}^+ - U_{i+1/2}^- \right) = B(\widetilde{U}_{i+1/2}) \left(U_{i+1/2}^+ - U_{i+1/2}^- \right),$$

where

$$\widetilde{U}_{i+1/2} = \frac{U_{i+1/2}^+ + U_{i+1/2}^-}{2}, \; \widetilde{u}_{\alpha,i+1/2} = \frac{\widetilde{q}_{u,\alpha,i} + \widetilde{q}_{u,\alpha,i+1}}{\widetilde{h}_i + \widetilde{h}_{i+1}}.$$

$\widetilde{w}_{\alpha,i+1/2}$ is defined in the same way as $\widetilde{u}_{\alpha,i+1/2}$. $U_{i+1/2}^{\pm}$ is the vector defined by a reconstruction procedure on the variables to the to the left ($^-$) and right ($^+$) of the inter-cell $x_{i+1/2}$. This reconstruction procedure is done using a MUSCL reconstruction operator, combined with a minmod limiter as detailed in (2.2.50)-(2.2.52). The MUSCL reconstruction operator also takes into account the positivity of the water height.

$Q_{i+1/2}$ is the viscosity matrix associated to PVM-1U(S_L, S_R) or HLL method (2.2.39). Here S_L and S_R are estimated by using the bounds proposed in Subsection 1.2.2:

$$S_L = \min_{\alpha \in \{1,2\}} \left(u_{\alpha,i+1/2}^- - \sqrt{g h_{i+1/2}^-}, \; \widetilde{u}_{\alpha,i+1/2} - \sqrt{g \widetilde{h}_{i+1/2}} \right),$$

$$S_R = \max_{\alpha \in \{1,2\}} \left(\widetilde{u}_{\alpha,i+1/2} + \sqrt{g \widetilde{h}_{i+1/2}}, \; u_{\alpha,i+1/2}^+ + \sqrt{g \widetilde{h}_{i+1/2}} \right).$$

The matrix $A_{i+1/2}$ is the Roe matrix

$$A_{i+1/2} = J_F(\widetilde{U}_{i+1/2}) + B_{i+1/2},$$

J_F being the Jacobian matrix of the flux F.

Again,

$$\alpha_0 A_{i+1/2}^{-1} G_{i+1/2} \left(H_{i+1/2}^+ - H_{i+1/2}^- \right)$$

makes no sense if any of the eigenvalues of $A_{i+1/2}$ vanishes. Here we propose the following approximation

$$\alpha_0 \left(U_{i+1/2}^+ - U_{i+1/2}^- - A_{i+1/2}^{-1} G_{i+1/2} \left(H_{i+1/2}^+ - H_{i+1/2}^- \right) \right)$$
$$= \alpha_0 \left(U_{i+1/2}^+ - U_{i+1/2}^- - \left(H_{i+1/2}^+ - H_{i+1/2}^- \right) \vec{e}_1 \right).$$

Let us introduced the following notation:

$$R_{i+1/2} = F_C(U_{i+1/2}^+) - F_C(U_{i+1/2}^-) + T_{p,i+1/2} + B_{i+1/2},$$

where F_C is the convective flux, and is given by

$$F_C(U) = \left(l_1 q_{u,1} + l_2 q_{u,2}, \ \frac{q_{u,1}^2}{h}, \ \frac{q_{u,2}^2}{h}, \ \frac{q_{u,1} q_{w,1}}{h}, \ \frac{q_{u,2} q_{w,2}}{h} \right)^T,$$

and $T_{p,i+1/2}$ contains the pressure terms

$$T_{p,i+1/2} = g \widetilde{h}_{i+1/2} \left(\eta_{i+1/2}^+ - \eta_{i+1/2}^- \right) (\vec{e}_2 + \vec{e}_3).$$

Thus, one can rewrite $D_{i+1/2}^\pm$ as

$$D_{i+1/2}^\pm = \frac{1}{2} \left((1 \pm \alpha_1) R_{i+1/2} \pm \alpha_0 \left(U_{i+1/2}^+ - U_{i+1/2}^- - \left(H_{i+1/2}^+ - H_{i+1/2}^- \right) \vec{e}_1 \right) \right),$$

Finally, the last term $\mathcal{I}_i$ in (3.3.4) comes from the volume integral that appears in (2.2.49). Notice that the integral in (2.2.49)

$$\int_{I_i} \partial_x F[P_{i,U}(x)] + B[P_{i,U}(x)] \frac{dP_{i,U}}{dx}(x) - G[P_{i,U}(x)] \frac{dP_{i,H}}{dx}(x) \, dx$$

can be written as

$$\int_{I_i} \partial_x F_C[P_{i,U}(x)] + B[P_{i,U}(x)] \frac{dP_{i,U}}{dx}(x) + g P_{i,h}(x) \frac{dP_{i,\eta}}{dx}(x) (\vec{e}_2 + \vec{e}_3) \, dx.$$

Taking into account that $P_{i,U}(x)$ and $P_{i,\eta}(x)$ are lineal functions, then $\mathcal{VI}_i$ can be written as

$$\mathcal{I}_i = F_C(U_{i+1/2}^-) - F_C(U_{i-1/2}^+) + B(U_i) \left(U_{i+1/2}^- - U_{i-1/2}^+ \right) + g h_i \left(\eta_{i+1/2}^- - \eta_{i-1/2}^+ \right) (\vec{e}_2 + \vec{e}_3)$$

Remark 3.3.1. *The numerical scheme (3.3.4) considered for the underlying hyperbolic system is well-balanced for the steady state water at rest solutions*

$$\eta = h - H = cst, \ u_\alpha = w_\alpha = 0, \ \alpha \in \{1, 2\}$$

and linearly $L^\infty -$ stable under the usual CFL condition (3.3.3). Moreover the scheme is positive preserving for the water height for a smooth bathymetry under $\frac{1}{2} CFL$ condition.

Finite difference discretization for the non-hydrostatic terms

In this subsection we describe the discretization of the non-hydrostatic terms. From equation (3.3.1b), for every $k \in \{1, 2\}$ of the Runge-Kutta stage, we get

$$
\begin{cases}
h_i^{(k)} = h_i^{(\widetilde{k})}, & \text{(3.3.6a)} \\[2ex]
q_{u,1}^{(k)} = q_{u,1}^{(\widetilde{k})} - \Delta t \left(\partial_x(h^{(k)} p_1^{(k)}) - \dfrac{1}{l_1} \left(p_b^{(k)} \partial_x H + p_I^{(k)} \partial_x z I^{(k)} \right) \right), & \text{(3.3.6b)} \\[2ex]
q_{u,2}^{(k)} = q_{u,2}^{(\widetilde{k})} - \Delta t \left(\partial_x(h^{(k)} p_2^{(k)}) + \dfrac{1}{l_2} \left(\gamma_1 p_b^{(k)} + \gamma_2 p_I^{(k)} \right) \partial_x z I^{(k)} \right), & \text{(3.3.6c)} \\[2ex]
q_{w,1}^{(k)} = q_{w,1}^{(\widetilde{k})} - \dfrac{\Delta t}{l_1} \left(p_b^{(k)} - p_I^{(k)} \right), & \text{(3.3.6d)} \\[2ex]
q_{w,2}^{(k)} = q_{w,2}^{(\widetilde{k})} - \dfrac{\Delta t}{l_2} \left(\gamma_1 p_I^{(k)} + \gamma_2 p_b^{(k)} \right). & \text{(3.3.6e)}
\end{cases}
$$

Replacing equations (3.3.6b)-(3.3.6e) into (3.3.1c), we obtain the Poisson-like equations

$$
a_1 \partial_{xx} p_b^{(k)} + a_2 \partial_x p_b^{(k)} + a_3 p_b^{(k)} + a_4 \partial_{xx} p_I^{(k)} + a_5 \partial_x p_I^{(k)} + a_6 p_I^{(k)} = RHS_1, \qquad \text{(3.3.7)}
$$

$$
b_1 \partial_{xx} p_b^{(k)} + b_2 \partial_x p_b^{(k)} + b_3 p_b^{(k)} + b_4 \partial_{xx} p_I^{(k)} + b_5 \partial_x p_I^{(k)} + b_6 p_I^{(k)} = RHS_2, \qquad \text{(3.3.8)}
$$

where the coefficients a_j, b_j as well as the *Right-Hand-Sides* RHS_j, $j \in \{1, 2\}$, are given in Appendix D. We point out the dependency of the aforementioned coefficients

$$
a_j \equiv a_j(U^{(k)}), \ b_j \equiv b_j(U^{(k)}), \ RHS_j \equiv RHS_j(U^{(\widetilde{k})})
$$

and remark that, due to the form of the numerical scheme and that of the absence of non-hydrostatic terms on the mass equation, then one has equation (3.3.6a) and thus

$$
a_j \equiv a_j(U^{(\widetilde{k})}), \ b_j \equiv b_j(U^{(\widetilde{k})}), \ RHS_j \equiv RHS_j(U^{(\widetilde{k})}).
$$

Equations (3.3.7) and (3.3.8) are discretized using second order finite differences. In order to obtain point value approximations of the non-hydrostatic pressure variables, terms $p_{I,i}^{(k)}$, $p_{b,i}^{(k)}$ and $RHS_{j,i}$, $j \in \{1, 2\}$, $i \in \{1, \dots, N\}$ will be approximated at every mid point x_i of each cell I_i. In the same way, the corresponding space derivatives will be approximated using compact second order finite differences

$$
\partial_x P_i^{(k)} = \frac{P_{i+1}^{(k)} - P_{i-1}^{(k)}}{2\Delta x}, \ \partial_{xx} P_i^{(k)} = \frac{P_{i+1}^{(k)} - 2P_i^{(k)} + P_{i-1}^{(k)}}{\Delta x^2}. \qquad \text{(3.3.9)}
$$

To compute the coefficients a_j, b_j, RHS_j, that contain terms depending on $U^{(\widetilde{k})}$ as well as first derivatives $\partial_x U^{(\widetilde{k})}$, we will use the averaged values on the cell I_i of variables $U^{(\widetilde{k})}$ and H as second order point value approximations of $U_i^{(\widetilde{k})}$ and H_i at the centre of the cell I_i. The space derivatives are computed from the averaged values using compact second order finite differences

$$\partial_x U_i^{(\widetilde{k})} = \frac{U_{i+1}^{(\widetilde{k})} - U_{i-1}^{(\widetilde{k})}}{2\Delta x}, \ \partial_x H_i = \frac{H_{i+1} - H_{i-1}}{2\Delta x}. \tag{3.3.10}$$

After replacing (3.3.9) and (3.3.10) in (3.3.7) and (3.3.8), one has to solve a linear system

$$A\mathcal{P} = \mathcal{RHS}, \tag{3.3.11}$$

where

$$\mathcal{RHS} = \begin{pmatrix} \mathcal{RHS}_1 \\ \mathcal{RHS}_2 \end{pmatrix}, \ \mathcal{RHS}_j = \begin{pmatrix} RHSj, 1 \\ \vdots \\ RHSj, N \end{pmatrix}, \ \mathcal{P} = \begin{pmatrix} p_{b,1}^{(k)} \\ \vdots \\ p_{b,N}^{(k)} \\ p_{I,1}^{(k)} \\ \vdots \\ p_{I,N}^{(k)} \end{pmatrix},$$

and

$$A = D + M, \ D = \left(\begin{array}{c|c} T_{(1)} & 0 \\ \hline 0 & T_{(2)} \end{array}\right), \ M = \left(\begin{array}{c|c} 0 & C_{(1)} \\ \hline C_{(2)} & 0 \end{array}\right), \tag{3.3.12}$$

$T_{(j)}, C_{(j)}$ being tridiagonal and symmetrical matrices of dimension $N \times N$ (see details in Appendix D).

To solve the linear system (3.3.11), we propose an iterative linear solver based on a block version of the Jacobi method:

$$\begin{cases} \mathcal{P}_{(0)} = 0, \\ D\mathcal{P}_{(s)} = \mathcal{RHS} - M\mathcal{P}_{(s-1)}, \ s \in 1, 2, \ldots, \end{cases} \tag{3.3.13}$$

where at each iteration s, a tridiagonal linear system is efficiently solved by using the Thomas algorithm [236]. As stopping criteria for the iterative linear solver (3.3.13), we choose

$$||\mathcal{P}_{(s+1)} - \mathcal{P}_{(s)}|| < \epsilon_{tol}.$$

In the subsequent numerical test performed in this work, ϵ_{tol} is set to 10^{-8}.

Once the non-hydrostatic pressure terms $P^{(k)}$ have been computed, the discharges contained in $U^{(k)}$ can be updated from equations (3.3.6b)-(3.3.6e), where in a similar way, a second order point value approximation in the centre of the cell will be used.

Remark 3.3.2. *The proposed iterative linear solver has some advantages over other standard linear solvers such as Krylov gradient based methods (e.g., biconjugate gradient stabilized method) or LU factorization. A sort discussion is summarized:*

- *The proposed linear solver reaches the convergence in less than* 100 *iterations for the numerical tests showed in this work.*

- *It can be easily implemented, and it is matrix-free, since only tridiagonal systems have to be solved, which is done with the matrix-free Thomas algorithm [236]. This makes this algorithm extremely convenient for an implementation on GPU architectures, where memory is an important issue.*

- *A LU factorization method it is not feasible, since the matrix of the linear system* **A** *depends on time step. This will demand a considerable computational effort. Moreover, this choice is more memory consuming than the iterative method proposed in this dissertation in (3.3.13).*

- *Let us denote by* $\widetilde{\boldsymbol{\mathcal{P}}}$ *a convenient reorganization of the variable* $\boldsymbol{\mathcal{P}}$*, such that*

$$\widetilde{\boldsymbol{\mathcal{P}}} = \left(p_{b,1}^{(k)}, p_{I,1}^{(k)}, \ldots p_{b,N}^{(k)}, p_{I,N}^{(k)} \right)^t.$$

  Then the corresponding associated matrix $\widetilde{\boldsymbol{A}}$ *is symmetric and penta-diagonal. This organization is more convenient for an iterative Krylov space based method. Nevertheless, we have found that this methods are more memory consuming.*

- *Considering the extension of the scheme to bidimensional domains, this will lead to a Poisson-like equation in two dimensions. The proposed algorithm can be combined with a Jacobi or Jacobi relaxation method (see [3]) to take into account this extension.*

Final numerical scheme

For the sake of clarity, a guideline of the final numerical scheme will be highlighted in what follows. For every kth stage $k \in \{1, 2\}$ of the Runge-Kutta method, the problem (NH-2L) is split into two parts. A two-step projection-correction method is used:

- **Finite volume step** (solving the hydrostatic system): From (3.3.4), solve explicitly the System (SWE-2L) at the kth stage of the Runge-Kutta:

$$U_i^{(\widetilde{k})} = U_i^{(k-1)} - \frac{\Delta t}{\Delta x} \left(D_{i+1/2}^{(k-1),-} + D_{i-1/2}^{(k-1),+} + \mathcal{I}_i^{(k-1)} \right),$$

  by means of a PVM path-conservative finite volume scheme (3.3.4) combining a MUSCL reconstruction operator to obtain the intermediate value $U_i^{(\widetilde{k})}$ in the

two-step projection-correction method that contains the numerical solution of the System (SWE-2L).

- **Finite Difference step** (non-hydrostatic pressure correction):

  + Solve the Poisson-like equations (3.3.7) and (3.3.8) to obtain the non-hydrostatic pressures

  $$P^{(k)} = \begin{pmatrix} p_b^{(k)} \\ p_I^{(k)} \end{pmatrix}.$$

  To do so, compact centred second order finite differences are used for the discretization of the derivatives that appear in (3.3.7)-(3.3.8), and a linear system is solved to obtain $P^{(k)}$.

  + With the computed non-hydrostatic pressure terms $P^{(k)}$, the discharges can be updated from (3.3.6b)-(3.3.6e), where in a similar way, a second order point value approximation in the centre of the cell will be used to compute the non-hydrostatic contribution.

Finally,

$$U^{n+1} = \frac{1}{2}U^n + \frac{1}{2}U^{(2)}.$$

Remark 3.3.3. *In order to include friction with the bottom, the source term $S(U)$ is discretized in a semi-implicit way at the end of the second step of the proposed numerical scheme, at each Runge-Kutta stage.*

Remark 3.3.4. *In order to include the breaking mechanism, the breaking terms are discretized in a explicit manner using centred second order finite differences at the end of the second step of the proposed numerical scheme, at each Runge-Kutta stage.*

Remark 3.3.5. *Since non-hydrostatic, friction and breaking terms appear only in the momentum equations, the final numerical scheme is well-balanced for the water at rest solutions*

$$\eta = h - H = cst, \ u_\alpha = w_\alpha = p_\alpha = 0, \ \alpha \in \{1, 2\}$$

and positive preserving for the water height.

Remark 3.3.6. *The extension of the proposed numerical scheme to the case of two space dimension is straightforward. To do that, the same time stepping procedure is employed, and a second order finite volume PVM HLL solver as well. Non-hydrostatic terms are approximating using central second order finite differences. This will leads to solve a two space dimension Poisson-like equation, that can be solve in an efficient way using the linear solver employed for the 1D case.*

3.4 An explicit finite volume discretization of the system (NHyp)

We describe now the numerical scheme used to discretize the system (NHyp) with the assumptions made in (3.0.1) and (3.0.2). The system (NHyp) is discretized by means of a second order finite volume PVM positive-preserving well-balanced path-conservative method. As usual, we consider a set of N_x finite volume cells $I_i = [x_{i-1/2}, x_{i+1/2}]$ with constant lengths Δx and define

$$U_i(t) = \frac{1}{\Delta x} \int_{I_i} U(x,t) \, dx,$$

the cell average of the function $U(x,t)$ on cell I_i at time t.

Time stepping

Assume given time steps Δt_n, and denote $t_n = \sum_{j \le n} \Delta t_j$. To obtain second order accuracy in time, the two-stage second-order TVD Runge-Kutta scheme [142] is adopted. At the kth stage, $k \in \{1, 2\}$, numerical method is given by

$$\frac{U^{(k)} - U^{(k-1)}}{\Delta t} + \partial_x F(U^{(k-1)}) + B(U^{(k-1)})\partial_x U^{(k-1)} = G(U^{(k-1)})\partial_x H, \qquad (3.4.1)$$

where $U^{(0)}$ is U at the time level t_n, $U^{(k)}$ is an intermediate value that contains the numerical solution of the system (NHyp) at the corresponding kth stage of the Runge-Kutta, and $U^{(k)}$ is the kth stage estimate. After that, a final value of the solution at the t_{n+1} time level is obtained:

$$U^{n+1} = \frac{1}{2}U^n + \frac{1}{2}U^{(2)}. \qquad (3.4.2)$$

For the computation of the time step Δt the usual CFL condition is considered given by

$$\Delta t < CFL \frac{\Delta x}{|\lambda_{max}|}, \ 0 < CFL \le 1, \ |\lambda_{max}| = \max_{i \in \{1, ..., N_x\}} \left\{ |u_i| + \sqrt{gh_i + p_i + c^2} \right\}. \qquad (3.4.3)$$

Finite volume discretization

A second order path-conservative PVM scheme based on reconstruction operator for the discretization in space of the system (3.4.1) is considered. To do so, we consider in this case a Roe linearization based on the simple straight-line segment path for the variables h, u and p. Following the high order numerical scheme in space (2.2.49) and approximating

the ODE in time, we obtain the following numerical scheme that at the kth stage of the Runge-Kutta method reads:

$$U_i^{(\widetilde{k})} = U_i^{(k-1)} - \frac{\Delta t}{\Delta x}\left(D_{i+1/2}^{(k-1),-} + D_{i-1/2}^{(k-1),+} + \mathcal{I}_i^{(k-1)}\right), \qquad (3.4.4)$$

where, skipping the time dependence in k to relax the notation, $D_{i+1/2}^{\pm}$ is given by a PVM path-conservative scheme (see (2.2.37))

$$D_{i+1/2}^{\pm} = D_{i+1/2}^{\pm}(U_{i+1/2}^-, H_{i+1/2}^-, U_{i+1/2}^+, H_{i+1/2}^+)$$

$$= \frac{1}{2}\left(F(U_{i+1/2}^+) - F(U_{i+1/2}^-) + B_{i+1/2}\left(U_{i+1/2}^+ - U_{i+1/2}^-\right) - G_{i+1/2}\left(H_{i+1/2}^+ - H_{i+1/2}^-\right)\right)$$

$$\pm \frac{1}{2}Q_{i+1/2}\left(U_{i+1/2}^+ - U_{i+1/2}^- - A_{i+1/2}^{-1}G_{i+1/2}\left(H_{i+1/2}^+ - H_{i+1/2}^-\right)\right).$$

$$(3.4.5)$$

Note that in this case, due to the election of the family of paths, linear on h, u and p, the path-integrals can be exactly computed from the simple mid-point quadrature rule, and thus:

$$G_{i+1/2}\left(H_{i+1/2}^+ - H_{i+1/2}^-\right) = \left(\left(g\widetilde{h}_{i+1/2} + 2\widetilde{p}_{i+1/2}\right)\vec{e}_2 - 2c^2\widetilde{u}_{i+1/2}\vec{e}_4\right)\left(H_{i+1/2}^+ - H_{i+1/2}^-\right)$$

is obtained after integrating the path-integral (2.2.30), and similarly from (2.2.29) we obtain

$$B_{i+1/2}\left(U_{i+1/2}^+ - U_{i+1/2}^-\right) = -2c^2\widetilde{u}_{i+1/2}\left(h_{i+1/2}^+ - h_{i+1/2}^-\right)\vec{e}_4,$$

$\widetilde{h}_{i+1/2}$, $\widetilde{u}_{i+1/2}$ and $\widetilde{p}_{i+1/2}$ being the Roe averages computed as usually. $U_{i+1/2}^{\pm}$ is the vector defined by a reconstruction procedure on the variables to the to the left $(^-)$ and right $(^+)$ of the inter-cell $x_{i+1/2}$. This reconstruction procedure is done using a MUSCL reconstruction operator, combined with a minmod limiter as detailed in (2.2.50)-(2.2.52). The MUSCL reconstruction operator also takes into account the positivity of the water height. Finally, as explained in Subsection 2.2.4, the variable $H_{i+1/2}^{\pm}$ is recovered from $H_{i+1/2}^{\pm} = h_{i+1/2}^{\pm} - \eta_{i+1/2}^{\pm}$.

$Q_{i+1/2}$ is the viscosity matrix associated to PVM-1U(S_L, S_R) or HLL method (2.2.39). Here S_L and S_R are estimated as follows

$$S_L = \min\left(u_{i+1/2}^- - \sqrt{gh_{i+1/2}^- + p_{i+1/2}^- + c^2}, \; \widetilde{u}_{i+1/2} - \sqrt{g\widetilde{h}_{i+1/2} + \widetilde{p}_{i+1/2} + c^2}\right),$$

$$S_R = \max\left(\widetilde{u}_{i+1/2} + \sqrt{g\widetilde{h}_{i+1/2} + \widetilde{p}_{i+1/2} + c^2}, \; u_{i+1/2}^+ + \sqrt{gh_{i+1/2}^+ + p_{i+1/2}^+ + c^2}\right).$$

Again,

$$\alpha_0 A_{i+1/2}^{-1} G_{i+1/2} \left(H_{i+1/2}^+ - H_{i+1/2}^- \right)$$

makes no sense if any of the eigenvalues of $A_{i+1/2}$ vanishes. Here we propose the following approximation

$$\alpha_0 \left(U_{i+1/2}^+ - U_{i+1/2}^- - A_{i+1/2}^{-1} G_{i+1/2} \left(H_{i+1/2}^+ - H_{i+1/2}^- \right) \right)$$
$$= \alpha_0 \left(U_{i+1/2}^+ - U_{i+1/2}^- - \vec{e}_1 \left(H_{i+1/2}^+ - H_{i+1/2}^- \right) \right),$$

Let us introduced the following notation:

$$R_{i+1/2} = F_C(U_{i+1/2}^+) - F_C(U_{i+1/2}^-) + T_{p,i+1/2} + C_{i+1/2},$$

where F_C is the convective flux and $T_{p,i+1/2}$ contains the pressure terms:

$$F_C(U) = \left(q_u, \ \frac{q_u^2}{h} + q_p, \ \frac{q_u q_w}{h}, \ \frac{q_u q_p}{h} + c^2 q_u \right),$$

$$T_{p,i+1/2} = \left(\left(g\widetilde{h}_{i+1/2} - 2\widetilde{p}_{i+1/2} \right) \left(\eta_{i+1/2}^+ - \eta_{i+1/2}^- \right) + 2\widetilde{p}_{i+1/2} \left(h_{i+1/2}^+ - h_{i+1/2}^- \right) \right) \vec{e}_2,$$

$$C_{i+1/2} = -c^2 \widetilde{u}_{i+1/2} \left(2(\eta_{i+1/2}^+ - \eta_{i+1/2}^-) - (h_{i+1/2}^+ - h_{i+1/2}^-) \right) \vec{e}_4.$$

Thus, one can rewrite $D_{i+1/2}^{\pm}$ as

$$D_{i+1/2}^{\pm} = \frac{1}{2} \left((1 \pm \alpha_1) R_{i+1/2} \pm \alpha_0 \left(U_{i+1/2}^+ - U_{i+1/2}^- - \vec{e}_1 \left(H_{i+1/2}^+ - H_{i+1/2}^- \right) \right) \right). \quad (3.4.6)$$

Finally, the last term $\mathcal{I}_i$ in (3.4.4) comes from the volume integral that appears in (2.2.49). Notice that the integral in (2.2.49)

$$\int_{I_i} \partial_x F[P_{i,U}(x)] + B[P_{i,U}(x)] \frac{dP_{i,U}}{dx}(x) - G[P_{i,U}(x)] \frac{dP_{i,H}}{dx}(x) \, dx$$

can be written as

$$\int_{I_i} \partial_x F_C[P_{i,U}(x)] + \left((gP_{i,h}(x) - 2P_{i,p}(x)) \frac{dP_{i,\eta}}{dx}(x) + 2P_{i,p}(x) \frac{dP_{i,h}}{dx}(x) \right) \vec{e}_2 \, dx$$

$$- \int_{I_i} c^2 P_{i,u}(x) \left(2\frac{dP_{i,\eta}}{dx}(x) - \frac{dP_{i,h}}{dx}(x) \right) \vec{e}_4 \, dx$$

Taking into account that $P_{i,u}(x)$, $P_{i,p}(x)$, $P_{i,h}(x)$, $P_{i,\eta}(x)$ and $P_{i,H}(x) = P_{i,h}(x) - P_{i,\eta}(x)$ are lineal, then $\mathcal{VI}_i$ can be written as

$$\mathcal{I}_i = F_C(U_{i+1/2}^-) - F_C(U_{i-1/2}^+) + \left((gh_i - 2p_i) \left(\eta_{i+1/2}^- - \eta_{i-1/2}^+ \right) + 2p_i \left(h_{i+1/2}^- - h_{i-1/2}^+ \right) \right) \vec{e}_2$$

$$- c^2 u_i \left(2 \left(\eta_{i+1/2}^- - \eta_{i-1/2}^+ \right) - 2 \left(h_{i+1/2}^- - h_{i-1/2}^+ \right) \right) \vec{e}_4$$

Remark 3.4.1. *The numerical scheme considered (3.4.1) is well-balanced for the steady state water at rest solutions*

$$\eta = h - H = cst, \ u = w = p = 0,$$

and linearly L^∞ − stable under the usual CFL condition (3.4.3). Moreover the scheme is positive preserving for the water height for a smooth bathymetry under $\frac{1}{2}CFL$ condition.

Remark 3.4.2. *In order to include friction with the bottom, the breaking mechanism, and others geometrical non-hydrostatic source terms, $S(U)$ is discretized in a semi-implicit way at the end of the second step of the proposed numerical scheme, at each Runge-Kutta stage.*

3.5   An explicit ADER-DG discretization of the system (NHyp-2D)

In this section is proposed the use of an arbitrary high order accurate (ADER) discontinuous Galerkin (DG) finite element scheme with an a posteriori subcell finite volume limiter to solve numerically the PDE system (NHyp-2D).

The key idea of the employed limiter is to run first an unlimited ADER-DG scheme and then check the obtained solution for validity at the end of each time step. The discrete solution is recomputed in those elements (so-called troubled zones) where the positivity of the water depth is violated, where invalid floating point numbers have been produced due to divisions by zero or by taking roots of negative numbers, or in elements where the numerical solution produces spurious oscillations due to the presence of discontinuities and strong gradients.

In those troubled cells, a more robust finite volume scheme is employed, starting again from a valid solution at the previous time step, but using a finer subgrid to preserve the subcell resolution capability of the underlying DG scheme. The final scheme is highly accurate in smooth regions of the flow and very robust and positive preserving for emerging topographies and wet-dry fronts. It is well-balanced making use of a path-conservative formulation of HLL-type Riemann solvers based on the straight line segment path for the variables h, u, v and p. The resulting subcell finite volume limiter used in this section is the natural high order extension of the previously described numerical scheme presented in (3.4.4) in the framework of DG schemes.

Furthermore, the proposed ADER-DG scheme with a posteriori subcell finite volume limiter adapts very well to modern GPU architectures, resulting in a very accurate, robust and computationally efficient computational method for non-hydrostatic free surface flows.

For the sake of simplicity, let us rewrite the system in terms of convective fluxes and pressure terms. This allow us to easily mimic the procedure introduced in Section 3.4 (as well as for the other systems), where the numerical scheme is fully written in terms of the

free-surface, instead of the bathymetry. Thus, we propose to rewrite (NHyp-2D) as

$$\partial_t U + \partial_x \boldsymbol{F}_C(U) + \boldsymbol{B}(U) \cdot \nabla U = S(U), \tag{3.5.1}$$

where U is defined as in (NHyp-2D). The convective flux is given by

$$\boldsymbol{F}_C = (F_{C,1}, F_{C,2}), \quad F_{C,1}(U) = \begin{pmatrix} q_x \\ \dfrac{q_x^2}{h} + q_p \\ \dfrac{q_x q_y}{h} \\ \dfrac{q_x q_w}{h} \\ \dfrac{q_x q_p}{h} + c^2 q_x \end{pmatrix}, \quad F_{C,2}(U) = \begin{pmatrix} q_y \\ \dfrac{q_x q_y}{h} \\ \dfrac{q_y^2}{h} + q_p \\ \dfrac{q_y q_w}{h} \\ \dfrac{q_y q_p}{h} + c^2 q_y \end{pmatrix},$$

and the nonconservative product $\boldsymbol{B}(U) \cdot \nabla U$ is given by:

$$\boldsymbol{B}(U) \cdot \nabla U = \begin{pmatrix} 0 \\ (gh - 2p)\, \partial_x \eta + 2p\partial_x h \\ (gh - 2p)\, \partial_y \eta + 2p\partial_y h \\ 0 \\ -c^2 u\partial_x \left(2\eta - h\right) - c^2 v\partial_y \left(2\eta - h\right) \end{pmatrix}.$$

Finally the source term vector $S(U)$ contains the friction and breaking terms as well as the non-hydrostatic terms included in (NHyp-2D):

$$S(U) = - \begin{pmatrix} 0 \\ \tau_{b,x} \\ \tau_{b,y} \\ -2p + \boldsymbol{\mathcal{R}_{br}} \\ 2c^2 (\dfrac{q_w}{h} + \partial_t H) \end{pmatrix},$$

where $\boldsymbol{\mathcal{R}_{br}}$ contains the breaking terms defined in (1.5.8).

As usual, the computational domain Ω is covered with a set of non-overlapping Cartesian control volumes in space

$$V_i = \left[x_i - \frac{1}{2}\Delta x, x_i + \frac{1}{2}\Delta x \right] \times \left[y_i - \frac{1}{2}\Delta y, y_i + \frac{1}{2}\Delta y \right].$$

In the following, we give a summary of the ADER-DG scheme with an a posteriori subcell based MOOD limiting:

- **Space-time predictor.** Following (2.4.9), we solve the nonlinear problem *in the small* via a simple and fast converging fixed point iteration for the degrees of freedom $\widehat{q}_{i,l}$:

$$
\left(\int\limits_{V_i} \theta_k(\boldsymbol{x}, t_{n+1}) \theta_l(\boldsymbol{x}, t_{n+1}) \, d\boldsymbol{x} - \int\limits_{t_n}^{t_{n+1}} \int\limits_{V_i} \theta_l(\boldsymbol{x}, t) \partial_t \theta_k(\boldsymbol{x}, t) \, d\boldsymbol{x} \, dt \right) \widehat{q}_{i,l}
$$
$$
= \left(\int\limits_{V_i} \theta_k(\boldsymbol{x}, t_n) \phi_l(\boldsymbol{x}) \, d\boldsymbol{x} \right) \widehat{q}_{i,l}^n - \int\limits_{t_n}^{t_{n+1}} \int\limits_{V_i} \theta_k(\boldsymbol{x}, t) \left(\widehat{\nabla \cdot \boldsymbol{F}_{C i,l}} + \widehat{\boldsymbol{B} \cdot q}_{i,l} \right) d\boldsymbol{x} \, dt
$$
$$
+ \int\limits_{t_n}^{t_{n+1}} \int\limits_{V_i} \theta_k(\boldsymbol{x}, t) \widehat{\mathcal{S}}_{i,l} \, d\boldsymbol{x} \, dt.
$$

(3.5.2)

Here we just use the trivial initial guess given by the extrapolation of q_h from the previous time interval $[t_{n-1}, t_n]$. Another better initial guesses that can be employed have been commented in Subsection 2.4.2.

- **Fully discrete one-step ADER-DG scheme.** Once the space-time predictor $\widehat{q}_{i,h}$ has been computed, then we update $\widehat{U}_{i,l}^{n+1}$ with the path-conservative one-step ADER-DG scheme (2.4.10)

$$
\left(\int\limits_{V_i} \phi_k \phi_l \, d\boldsymbol{x} \right) \left(\widehat{U}_{i,l}^{n+1} - \widehat{U}_{i,l}^n \right) + \sum_{j \in \mathcal{N}_i} \int\limits_{t^n}^{t^{n+1}} \int_{E_{ij}} D_{\Phi}^- (\underline{q}_{i,h}(\gamma, t), \underline{q}_{j,h}(\gamma, t), \boldsymbol{n}_{ij}) \, d\gamma \, dt
$$
$$
+ \int\limits_{t_n}^{t_{n+1}} \int\limits_{V_i^\circ} \phi_k \left(\nabla \cdot \boldsymbol{F}_C(q_{i,h}) + \boldsymbol{B}(q_{i,h}) \cdot \nabla q_{i,h} - S(q_{i,h}) \right) d\boldsymbol{x} \, dt = \boldsymbol{0}.
$$

D_{Φ}^- represent the path-conservative jump term in the normal direction $\boldsymbol{n}_{ij} \in \mathcal{S}^1$. In this dissertation, D_{Φ}^- consists in the extension of the HLL PVM method (3.4.6) to bidimensional domains. In a similar way, the choice of the straight-line segment path for the variables h, u, v, and p has been considered.

We also recall that, having selected the nodal points in this way, we will compute the volume integrals through Gaussian quadrature rules, that is known to be exact for all polynomials up to degree $2\mathcal{N} + 1$.

Concerning the surface integral that appears in (2.4.10), it can be simply evaluated via some sufficiently accurate numerical quadrature formula. We typically use a the

Gauss-Legendre quadrature rule. Here, the time integral is approximated by the rectangle rule, that is by using the information at the time level t_n. This will leads us to a simplification of the final numerical scheme. Since this integral contribution is a term of order $\mathcal{O}(\Delta x)^{\mathcal{N}}$ for smooth solutions, then the order of accuracy of the numerical scheme is maintained for regular solutions. Nevertheless, in [92] an alternative strategy to compute the time integral is discussed.

- **A posteriori subcell finite volume limiter.** As described in (2.4.11) in Chapter 2, let us consider a set of subcells $V_{i,s}$ such that

$$V_i = \bigcup_{s=1}^{(2\mathcal{N}+1)^d} V_{i,s},$$

$\mathcal{N}$ being the order of the DG polynomials and $d = 2$ the dimension of the problem.

Cell-to-subcell scattering (projection):

Let us consider the discrete solution in the subcells $V_{i,s}$ is at time t_n in terms of *piecewise constant* subcell averages $\overline{U}_{i,s}^n$, i.e.

$$\overline{U}_{i,s}^n = \frac{1}{|\Omega_{i,s}|} \int_{\Omega_{i,s}} U(\boldsymbol{x}, t^n) \, d\boldsymbol{x} .$$

Then, let us compute the projection onto the *subcell grid* of the candidate solution computed at the previous step with the unlimited ADER-DG scheme:

$$\overline{U}_{i,s}^* = \frac{1}{|\Omega_{i,s}|} \int_{\Omega_{i,s}} U(\boldsymbol{x}, t^{n+1}) \, d\boldsymbol{x} .$$

A posteriori MOOD detection procedure:

An a posteriori Multi dimensional Optimal Order Detection (MOOD) described in Chapter 2 is applied:

+ The *Physical admissibility detection* (PAD) is applied to ensure the positivity of the water depth h (see (2.4.15)). The appearance of floating point errors is also checked.

+ The *Numerical admissibility detection (NAD)* described in (2.4.16)–(2.4.17) is applied.

Subcell-based TVD Runge-Kutta update:

Each subcell averages, contain in an invalid cell, are now evolved in time with the extension to two space domains of the second order accurate finite volume scheme described in Subsection 3.4.

Note that this very fine division of a DG element into finite volume subcells does *not* reduce the time step of the overall ADER-DG scheme, since the CFL number of explicit DG schemes scales with $1/(2\mathcal{N}+1)$, while the CFL number of finite volume schemes (used on the subgrid) is of the order of unity.

Subcell-to-cell gathering (reconstruction):

For any troubled cell gather the new subgrid information into a cell-centered DG polynomial of degree $\mathcal{N}$ on the main grid by applying the subcell reconstruction operator defined by (2.4.13)–(2.4.14).

Remark 3.5.1. *The numerical scheme considered is well-balanced for water at rest solutions, linearly L^∞-stable under the usual CFL condition and positive preserving for the water height.*

Remark 3.5.2. *In practice, on this dissertation, a cell is marked as troubled if the water depth h is bellow certain water depth value h_0, that has been fixed from the beginning. On this thesis, we set $h_0 = 10^{-3}H_0$, where H_0 is the typical water depth.*

In such a way, we will employ a second order accurate finite volume scheme that is robust and positive preserving for the water depth.

Remark 3.5.3. *Note that at wet-dry fronts the source term $S(U)$ may become stiff. Therefore, this term is discretized explicitly only in the unlimited ADER-DG solver, while $S(U)$ is discretized in a semi-implicit way inside the subcell finite volume limiter, in order to deal with the potential stiffness of, for example, the bottom friction source term. Due to the assumption made in Remark 3.5.2, we ensure the semi-implicit treatment of the source terms in regions where they may become stiff.*

3.6 Boundary conditions

In this dissertation, three types of Boundary Conditions (BC) have been considered: periodic, outflow and generating/absorbing BCs.

In the following, the imposition of the boundary conditions is described for the numerical schemes given in Sections 3.1–3.5 for one-dimensional domains. The techniques can be easily applied to the case of two space dimension.

1. Periodic BCs: Given the domain subdivided into a set of N_x cells, cell I_1 and I_{N_x}, which are the extremes of the domain, are considered as the same cell, surrounded by the neighbour cells I_{N_x} to the left and I_2 to the right.

2. Outflow BCs: homogeneous Neumann conditions are applied on the left and right boundaries. Since a second order MUSCL scheme is used, the usage of one ghost cell I_0, I_{N_x+1} in each boundary is required to determine the values of the closest nodes

to the boundary. The values of the variables at the ghost cells are extrapolated from the adjacent cells.

Nevertheless, reflections at the boundaries might modify the numerical solution at the interior of the domain. As in many other works (see [163], [217] among others), this condition is sometimes supplemented with an absorbing BC described below.

3. Generating/absorbing BCs: Periodic wave generation as well as absorbing BCs are achieved by using a generation/relaxation zone method similar to the one proposed in [183].

   Generation/absorption of waves is achieved by simply defining a relaxation coefficient $0 \leq m(x) \leq 1$, and a target solution (h^*, u^*, w^*, p^*). Given a width L_{Rel} of the relaxation zone on each boundary, k_{Rel} is defined as the first natural number that $k_{Rel} \Delta x \geq L_{Rel}$. The solution within the relaxation zone is then redefined to be, $\forall i \in \{1, \ldots, k_{Rel}, N_x - k_{rel}, \ldots N_x\}$:

   $$\widetilde{f}_i = m_i f_i + (1 - m_i) f_i^*, \quad f \text{ being one of the variables of the system } f = h, u, w, p.$$

   Note that in the case of the scheme (3.1) described for the system (YAM), due to the staggered grid it is applied:

   $$\widetilde{w}_{i\pm1/2} = m_{i\pm1/2} w_{i\pm1/2} + (1 - m_{i\pm1/2}) w_{i\pm1/2}^*,$$

   $$\widetilde{p}_{i\pm1/2} = m_{i\pm1/2} p_{i\pm1/2} + (1 - m_{i\pm1/2}) p_{i\pm1/2}^*,$$

   where m_i is defined as

   $$m_i = \sqrt{1 - \left(\frac{d_i}{L_{Rel}}\right)^2}, \quad m_{i\pm1/2} = \frac{m_i + m_{i\pm1}}{2},$$

   where d_i is the distance between the centre of the cells I_i and I_1 (respectively I_i and I_{N_x-k}), in the case of $i \in \{1, \ldots, k\}$ (respectively $i \in \{N_x - k, \ldots, N_x\}$).

   For the numerical experiments

   $$L \leq L_{Rel} \leq 1.5L,$$

   L being the typical wavelength of the outgoing wave.

   Absorbing BC is a particular case where $u^* = w^* = p^* = 0$. This will dump all the waves passing through the boundaries.

3.7   Wetting and drying treatment

In this subsection, some guidelines are given in order to make the numerical schemes described in Sections 3.1–3.5, able to deal with emerging topographies.

For the computation of $U^{(\widetilde{k})}$ in the finite volume discretization of the underlying hyperbolic systems (SWE) and (SWE-2L), as well as for the system (NHyp), a wet-dry treatment adapting the ideas described in [42] is applied. The key of the numerical treatment for wet-dry fronts with emerging bottom topographies relies in:

- First, notice that, one of the remarkable features of the described numerical schemes is that they have been entirely written in terms of the free-surface η instead of the bathymetry (see the implicit schemes described in (3.1) and (3.3) along with the corresponding coefficients of the matrices in Appendix (B), (D), as well as the explicit schemes described in (3.4) and (3.5)). This enables us to set the hydrostatic pressure terms $gh\partial_x\eta$ that appears, for instance at the horizontal velocity equations, to be modified for emerging bottoms to avoid spurious pressure forces (see similar techniques applied in [42]).

- To compute velocities appearing in the numerical schemes from the discharges, in general one has $u = q_u/h$, $w = q_w/h$. This may present difficulties close to dry areas due to small values of h, resulting in large round-off errors. The velocities are computed analogously as in [166], applying the desingularization formula, that for instance, for the horizontal velocity u reads:

$$u = \frac{hq_u\sqrt{2}}{\sqrt{h^4 + \max(h^4, \delta^4)}},$$

  which gives the exact value of u for $h \geq \delta$, and gives a smooth transition of u to zero when h tends to zero, with no truncation. In this work $\delta = 10^{-5}$ for the numerical tests. A more detailed discussion about the desingularization formula can be seen in [166]. In the numerical scheme (3.4), the variable p has to be computed from the conserved quantity hp, and thus, the same desingularization formula is applied in this case.

This is, so far, the end of the guidelines for the numerical treatment for wetting and drying fronts. Note that, in the second step of the numerical schemes (3.1) and (3.3), no special treatment is required due to the rewriting of the incompressibility equations, which have been multiplied by h^2, and they are expressed in terms of discharges. In presence of wet-dry fonts, the non-hydrostatic pressures vanish and no artificial truncation up to a threshold value is needed. This is shown in Appendix B and D, where an analysis is carried out for the case of an initial condition with zero speed, a planar bottom

$$\partial_x H = m$$

and a thin water layer

$$h = \epsilon.$$

In such a situation, the linear system that defines the non-hydrostatic pressures at each step is always invertible. Since the *Right Hand Side* vector of the linear systems vanishes, then the only solution for the homogeneous linear system is that the non-hydrostatic pressures vanish.

Remark 3.7.1. *It is worth to mention that, for the numerical scheme described in Section* 3.3*, for the studied case of planar bottom, zero velocities and* $h = \epsilon$*, the inverse of the matrix* $\boldsymbol{A}$ *can be computed:*

$$\boldsymbol{A}^{-1} = \frac{1}{4(\gamma_1 + \gamma_2)(m^2 + 1)} \left(\begin{array}{c|c} \gamma_1 \boldsymbol{I} & \boldsymbol{I} \\ \hline -\gamma_2 \boldsymbol{I} & \boldsymbol{I} \end{array} \right).$$

The resulting matrix is invertible due to the assumption in Remark 1.2.2 *that* $\gamma_1 + \gamma_2 \neq 0$.

Chapter 4

Numerical validation

Contents

In this chapter some numerical tests are shown for the described systems (YAM-2D), (NH-2L2D) and (NHyp-2D) presented in Chapter 1 and numerically solved in Chapter 3.

Furthermore, the breaking and friction terms introduced previously will be taken into account. Since the numerical schemes presented here exhibits a high potential for data parallelization, a parallel implementation of the numerical schemes has been carried out on GPU architectures. Some guidelines about the implementation are given in Appendix E.

The chosen tests have already been widely studied in the literature on dispersive water waves modelling (see [112], [39], [118], [182], [177], [53], [176], [163], [217], [108], [180] and references therein). Thus, this choice constitutes a proper way to validate the presented dispersive models and the numerical schemes with analytical solutions and real laboratory tests.

The first and fifth tests aim at validating the mathematical models and the numerical scheme with a comparison against exact or approximated analytical solutions for the original dispersive systems. The rest of the tests show that the proposed solved equations can simulate complex laboratory experiments, showing the comparison with real data.

The quantities of the parameters concerning the following numerical simulations are expressed in units of measure of the International System of Units.

Concerning the simulations carried out with the equations (NHyp-2D), are performed with a third order ADER-DG scheme ($\mathbb{P}_2$), except for the test where a systematic convergence analysis of the scheme is carried out, as well as for the computation of the GPU-performance tables. The limiting strategy presented in Chapters 2-3 is employed, with the parameters defined in (2.4.16), (2.4.17) and Remark (3.5.2) set to

$$\epsilon = 10^{-3}, \quad \epsilon_0 = 10^{-4}, \quad h_0 = 10^{-3} H_0,$$

being H_0 the typical depth. Similarly, as it was set in Section 3.7, the velocities are computed applying the desingularization formula where

$$\delta = 10^{-5},$$

as it was described in Subsection 3.7 where a general methodology to be applied in presence of wet-dry fronts for all the numerical schemes described within this thesis was given.

The small tolerance error defined for the linear solvers defined in (3.2.6) and (3.3.13) is set to

$$\epsilon_{tol} = 10^{-8}.$$

The proposed numerical tests also aim at validating the two-layer approach introduced in this thesis in Section 1.2 Chapter 1.

The proposed breaking mechanism for the systems (YAM-2D) and (NHyp-2D) given in (1.5.8) is used with the parameters $B_1 = 0.15$ and $B_2 = 0.5$ for all the test cases. Similarly, the proposed ad-hoc breaking mechanism for the system is also . The CFL number is set to 0.9. The artificial non-hydrostatic pressure wave speed c is set to $c = \alpha\sqrt{gH}$, $\alpha = 3$ for all test cases, except for the first test case where an analytical solution of the original system is studied, and thus $\alpha \in \{5, 10\}$. Concerning the parameters that improve the dispersion relation for the two layer approach, the parameters $l_1^{(5)}, \gamma_1^{(5)}, \gamma_2^{(5)}$ will be used, except for some numerical test that will be warned.

4.1 Solitary waves on a flat bottom

In this section, the simulation of solitary waves will be used to check the performance of the described models when dealing with this particular waves.

Moreover, the propagation of a solitary wave over a long distance is a standard test of the stability and conservative properties of numerical schemes for Boussinesq-type and non-hydrostatic pressure systems (see [21], [259], [219], [217], [231], [239], [112], [111], [118] among others). This also will be checked. The section is split into three parts:

- First, it is shown that the two layer system (NH-2L) with the proposed set of parameters $(l_1^{(5)}, \gamma_1^{(5)}, \gamma_2^{(5)})$, can propagate eulerian solitary waves of amplitude up to $A = 0.6$ in a more accurate way than the original two-layer system, which corresponds to the election of the parameters $(l_1^{(2L)}, \gamma_1^{(2L)}, \gamma_2^{(2L)})$.

  Moreover, it has been proved numerically the observation carried out in Subsection 1.6.3: the one-layer non-hydrostatic pressure systems can not correctly propagate eulerian solitary waves for bigger amplitudes.

- Secondly, the computed eulerian solitary waves (1.6.4) with $L = 2$ are used as the initial condition to check the numerical accuracy of the scheme for the two layer system (NH-2L).

  The numerical accuracy of the one-layer systems is also checked by using the analytical solitary wave described in Subsection 1.6.1.

- Finally, a solitary wave for the system (NHyp) is propagated in a very long integration of time for a coarse mesh with the third order ADER-DG scheme. This shows the abilities of ADER-DG schemes for the simulation of solitary waves in a very long integration times with coarser meshes. In other works (see [112], [117]) finer meshes were needed to maintain the correct amplitude. This especially occurs when flux limiters such as minmod ([112]) are present in the numerical scheme, resulting in an undesired clipping of local extrema.

In the subsequent test, periodic boundary conditions are considered and the minmod limiter for the SWE step of the numerical scheme is turned off to measure the order of accuracy of the numerical scheme.

Eulerian solitary gravity waves. Capabilities of the non-hydrostatic systems

When the amplitude of a solitary wave is small compared to the typical depth H, the characteristic length of the wave is relatively large. Thus, the solitary wave is a long wave and weakly-nonlinear weakly-dispersive models such as [21], or [259] can simulate the wave perfectly. However, as the amplitude increases, the wavelength decreases, and therefore

higher-order non-linear and dispersive effects become more important. This phenomenon will be investigated here with the two-layer model.

Let us consider the solitary wave computed in (1.6.4) with $L = 2$ that will be used as initial condition for the two layer system (NH-2L).

For the two solitary waves examined in this section, with amplitudes of $A_1 = 0.2$, $A_2 = 0.6$, a grid length $\Delta x = 0.01$ and a CFL number 0.4 is employed. The bathymetry is constant $H = 1.0$, the gravity acceleration is set to $g = 1$, and the simulations are carried out in a channel of 500 meters during 350 seconds.

The tests are performed with the two-layer with the improved parameters $(l_1^{(5)}, \gamma_1^{(5)}, \gamma_2^{(5)})$ and with the non-improved parameters $(l_1^{(2L)}, \gamma_1^{(2L)}, \gamma_2^{(2L)})$. The simulation with the one-layer system corresponding to the choice of the parameters $(1, \gamma_1^{(2L)}, \gamma_2^{(2L)})$ is also carried out. In the subsequent, only the results obtained with the parameters $(l_1^{(5)}, \gamma_1^{(5)}, \gamma_2^{(5)})$ will be commented.

As this wave solution is not an analytical solitary wave solution of the two layer model, when the numerical simulation is started the solitary wave drops some waves at the tail. Due to this initial fluctuation in wave form, the wave decreases in amplitude and so the celerity. Nevertheless, the solitary wave, which moves rapidly due to its large amplitude, eventually leaves this tail far behind and reaches a steady form. This initial mismatch effects also occurs when considering approximated solitary wave solutions for Boussinesq systems (see [176]).

Fig. 4.1 shows the evolution of the amplitude and speed of both solitary waves. The steady amplitudes and speeds reached for both cases are $\tilde{A}_1 = 0.197$, $\tilde{c}_{A_1} = 1.094$ and $\tilde{A}_2 = 0.588$, $\tilde{c}_{A_2} = 1.243$. Steady states are achieved not so far. This means that waves travel at constant speed even in the case of large amplitudes, which is one of the abilities of the two-layer model that is intended to show in this test.

It can be seen that celerities of the simulations $\tilde{c}_{A_1}$ and $\tilde{c}_{A_2}$ are both in agreement with the reference celerities that can be seen in [104].

Fig. 4.2 shows the numerical solutions obtained with the two-layer model at 350 seconds shifted by $(x - 350c_{A_i})$ meters and compared with the corresponding initial conditions. For all the cases, the two-layer model matches the initial conditions to a very high accuracy. It can be observed that a better fitted is obtained when considering the two-layer model with the improved parameters.

Fig. 4.3 shows the results obtained with the one-layer system corresponding to $l_1 = 1$ for the case of $A_2 = 0.6$. In this case, although a steady amplitude and celerity is also reached, it can be observed that the system can not maintain the initial amplitude. Thus the celerity decreases and the computed solitary wave is delayed in approximately 5 meters at 350 seconds.

It can be stated from these comparisons that the two-layer model presented here captures, to a highly accurate degree, the physics of a non-linear solitary wave.
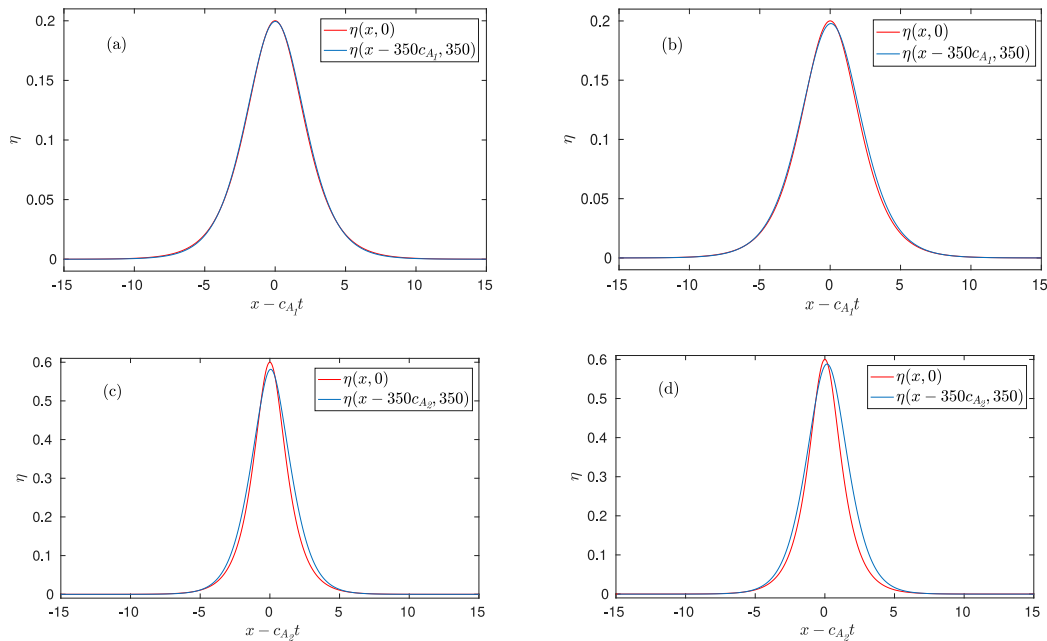
Figure 4.1: Comparison of surface at time $t = 350$ shifted by $(x - c_{A_i}t)$ m (blue) and initial condition (red). (a) and (c) show the comparison with the improved parameters $(l_1^{(5)}, \gamma_1^{(5)}, \gamma_2^{(5)})$ for the trial $A_1 = 0.2$ and $A_2 = 0.6$ respectively. (b) and (d) show the comparison with the non-improved parameters $(l_1^{(2L)}, \gamma_1^{(2L)}, \gamma_2^{(2L)})$ for the trial $A_1 = 0.2$ and $A_2 = 0.6$ respectively.

A convergence analysis with solitary waves

In this subsection we verify that the desired theoretical order of accuracy in both space and time of the proposed numerical schemes is achieved, as expected. Some numerical simulations for different grids have been computed up to time $t = 30$ s for the case of a solitary wave of amplitude $A = 0.2$ in a channel of 600 m. Periodic boundary conditions are used.

For the case of the system (YAM), the second order staggered numerical scheme introduced in Section 3.1 is used. As solitary wave for the initial condition, the approximated expression (1.6.1)-(1.6.2) is considered. Since the considered solitary wave is not an exact solution for the system, we take as reference solution a numerical simulation at time $t = 30$ s for a very fine grid with $N_x = 12000$ cells. Table 4.1 shows the L_2 errors and numerical orders of accuracy obtained.

The order of the numerical scheme proposed in Section 3.3 for the system (NH-2L) is numerically checked in Table 4.2. As solitary wave for the initial condition, we consider the eulerian solitary gravity wave computed in (1.6.4) with $L = 2$. Again, since the
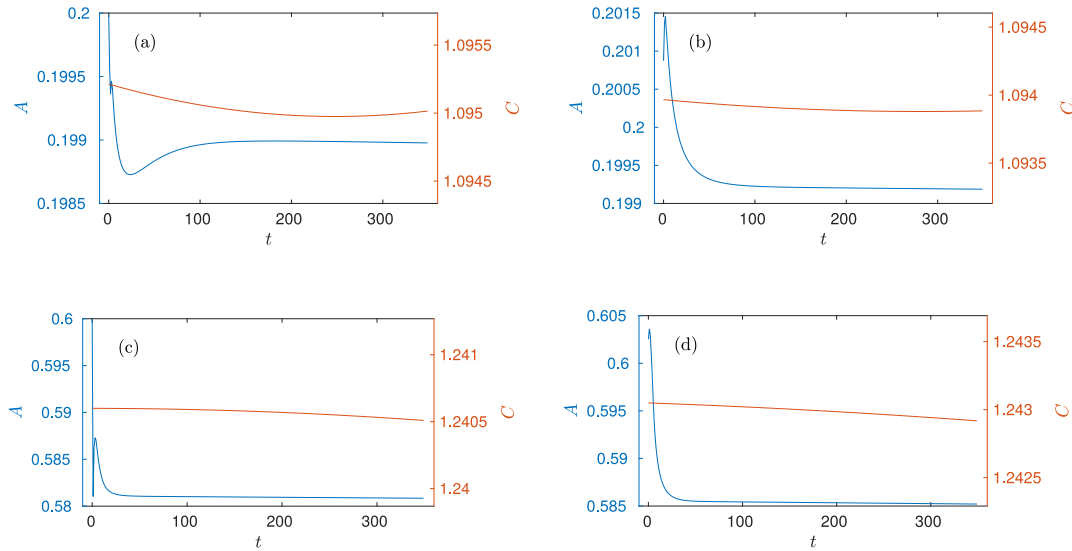
Figure 4.2: Variation through the time of the amplitude (blue) and celerity (red). (a) and (c) show the comparison with the improved parameters $(l_1^{(5)}, \gamma_1^{(5)}, \gamma_2^{(5)})$ for the trial $A_1 = 0.2$ and $A_2 = 0.6$ respectively. (b) and (d) show the comparison with the non-improved parameters $(l_1^{(2L)}, \gamma_1^{(2L)}, \gamma_2^{(2L)})$ for the trial $A_1 = 0.2$ and $A_2 = 0.6$ respectively.
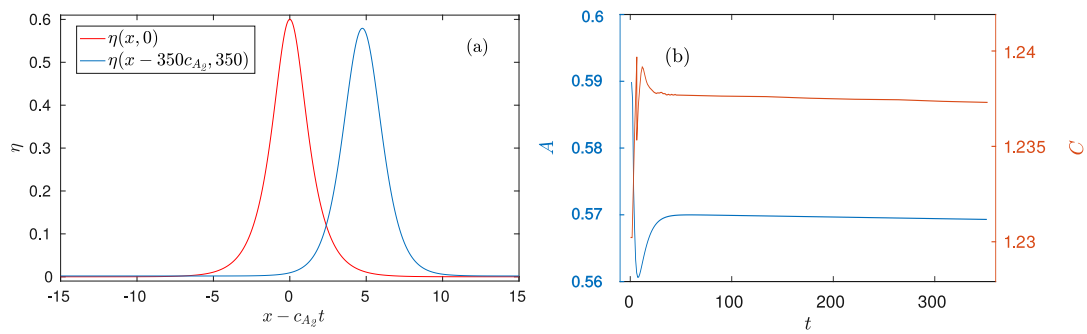

Figure 4.3: Comparison of surface at time $t = 350$ shifted by $(x - c_{A_2}t)$ m (blue) and initial condition (red) for the trial $A = 0.6$ with the one-layer system. (b) shows the variation through the time of the amplitude (blue) and celerity (red) for the trial $A_2 = 0.6$ with the one-layer system.

considered solitary wave is not an exact solution for the system, we take as reference solution a numerical simulation at time $t = 30$ s for a very fine grid with $N_x = 12000$ cells.

Finally, the order of the numerical scheme presented in Section 3.5 for the system (NHyp) is numerically checked in Table 4.3. We use the analytical solution for the system (NH-1L), given in (1.6.1)-(1.6.2), as an approximate solitary wave solution for the new hyperbolic system (NHyp) (see Subsection 1.6.2). The artificial non-hydrostatic pressure wave speed c is set to $c = \alpha\sqrt{gH}$, $\alpha = 5$. Although the *a posteriori* limiter strategy is implemented, it not detect any troubled elements, hence during the entire simulation of the solitary wave the pure unlimited ADER-DG scheme is used. Table 4.3 shows the L_2 errors and numerical convergence rates for general ADER-DG $\mathbb{P}_N$ schemes with $N = 2, 3, 4$. The error is computed with respect to the analytical solution of the original system (NH-1L). One can observe that the desired theoretical order of accuracy in both space and time is achieved, as expected. In the case of the scheme $\mathbb{P}_4$ and $\alpha = 5$, it can be seen that the desired theoretical order of the method is lost. This is due to the fact that the analytical solitary wave solution it is not the exact solution of the discretized system (NHyp), but it is the exact solution of the original dispersive system (NH-1L). Therefore, we cannot obtain errors below 1E-7 for $\alpha = 5$. This is a well-known issue in hyperbolic relaxation systems, see e.g. [243], as well as the discussion in [83]. Table 4.3 therefore also shows the results for the scheme $\mathbb{P}_4$ and $\alpha = 10$, where the above mentioned problem disappears, and the theoretical convergence order is again achieved.

One can observe that the desired theoretical order of accuracy in both space and time is achieved for all the test cases, as expected. We would like to remark that the proposed convergence analysis test is usually done for solitary waves of smaller amplitudes and integration times. Thus, this constitutes a standard test to check the order of accuracy of the numerical schemes for dispersive water waves models.

Solitary wave problem — System (YAM) — Staggered FV					
N_x	L_2 error h	L_2 error hu	L_2 order h	L_2 order hu	Theor.
$3 \cdot 10^3$	4.6979E-03	4.2391E-03	—	—	
$4 \cdot 10^3$	2.6308E-03	2.2622E-03	2.02	2.18	2
$5 \cdot 10^3$	1.5997E-03	1.4327E-03	2.23	2.05	
$6 \cdot 10^3$	1.1040E-03	9.4255E-04	2.03	2.30	

Table 4.1: L_2 errors and convergence rates for the Solitary wave problem for the finite volume staggered scheme. The errors have been computed for the variables h and hu.

A solitary wave over a long integration time

The propagation of a solitary wave over a long distance is a standard test of the stability and conservative properties of numerical schemes for weakly-nonlinear weakly-dispersive

Solitary wave problem — Two layer System (NH-2L) — **FV**					
N_x	L_2 error h	L_2 error hu	L_2 order h	L_2 order $h\boldsymbol{u}$	Theor.
$3 \cdot 10^3$	3.6000E-03	5.7000E-03	—	—	
$4 \cdot 10^3$	2.0460E-03	3.0471E-03	1.96	2.18	
$5 \cdot 10^3$	1.2805E-03	1.8396E-03	2.10	2.26	2
$6 \cdot 10^3$	8.9302E-04	1.2789E-03	1.98	1.99	

Table 4.2: L_2 errors and convergence rates for the Solitary wave problem for the finite volume scheme. The errors have been computed for the variables h and $h\boldsymbol{u} = l_1 q_{u,1} + l_2 q_{u,2}$.

Solitary wave problem — System (NHyp) — **ADER-DG-$\mathbb{P}_N$**						
	N_x	L_2 error h	L_2 error hu	L_2 order h	L_2 order hu	Theor.
DG-$\mathbb{P}_2$ $\alpha = 5$	50	1.4166E-3	4.9592E-3	—	—	
	100	3.0634E-4	8.3081E-4	2.21	2.58	
	150	1.2784E-4	1.7910E-4	2.15	3.78	3
	200	6.3940E-5	5.6724E-5	2.40	3.99	
DG-$\mathbb{P}_3$ $\alpha = 5$	50	6.2700E-4	1.5000E-3	—	—	
	100	5.9129E-5	7.6146E-5	3.41	4.30	
	150	1.0752E-5	9.6921E-6	4.20	5.08	4
	200	3.2610E-6	2.9417E-6	4.15	4.14	
DG-$\mathbb{P}_4$ $\alpha = 5$	50	1.6450E-4	3.4611E-4	—	—	
	100	6.0518E-6	5.2054E-6	4.76	6.06	
	150	1.0289E-6	1.8248E-6	4.37	2.59	5
	200	5.9428E-7	1.7494E-6	1.91	0.15	
DG-$\mathbb{P}_4$ $\alpha = 10$	50	2.1115E-4	4.0671E-4	—	—	
	100	8.4101E-6	8.6210E-6	4.65	5.56	
	150	1.3955E-6	8.4100E-7	4.43	5.74	5
	200	3.9809E-7	1.7584E-7	4.36	5.44	

Table 4.3: L_2 errors and convergence rates for the Solitary wave problem for the ADER-DG-$\mathbb{P}_N$ scheme. The errors have been computed for the variables h and hu.

models ([21], [259], [239], [217], [219], [231]). We use the analytical solution for the system (NH-1L), given by (1.6.1)-(1.6.2), as an approximate solitary wave solution for the new hyperbolic system (NHyp).

In this subsection we assess the abilities of the ADER-DG $\mathbb{P}_2$ scheme for the propagation of solitary waves of relatively big amplitudes with coarser meshes. In our test the solitary waves of amplitudes $A = 0.1, 0.3, 0.5, 0.7$ travels at a speed of $c_A = \sqrt{g(A + H)}$ over a constant still-water depth $H = 1$ in a channel of length 200 m along the x direction. The domain is divided just into 200 cells along the x axis. Periodic boundary conditions are used. The final simulation time is $t = 120$ s. The
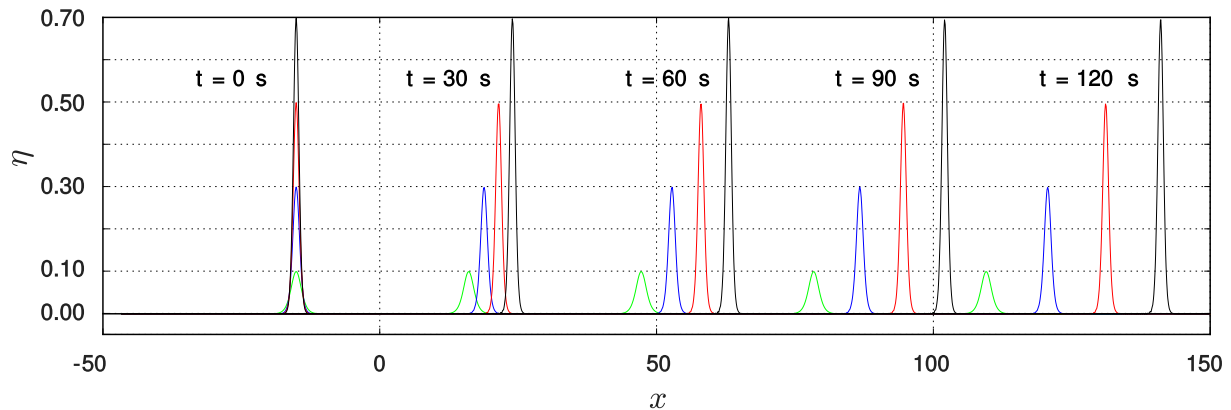
Figure 4.4: Solitary wave of amplitude $A = 0.2$ at $t = 0,\ 50,\ 100,\ 150$. ADER-DG $\mathbb{P}_2$ scheme

artificial non-hydrostatic pressure wave speed c is set to $c = \alpha\sqrt{gH}$, $\alpha = 5$. Although the *a posteriori* limiter strategy is implemented, it not detect any troubled elements, hence during the entire simulation of the solitary wave the pure unlimited ADER-DG scheme is used.

Figure 4.4 shows the evolution of the solitary waves at different times using the ADER-DG $\mathbb{P}_2$ scheme. Figures 4.5, 4.6, 4.7 and 4.8 show a perfect match between the numerical and the analytical solution after a large integration time for the free surface, the horizontal and vertical velocities as well as for the non-hydrostatic pressure.

It is worth mentioning that excellent results are obtained with a spatial discretization of only $\Delta x = 1\ m$. In other works (see [112], [117]) usually it was necessary to refine the grid substantially in order to maintain the correct amplitude of the solitary wave for large integration times. This especially occurs when flux limiters such as minmod ([112]) are present in the numerical scheme, resulting in an undesired clipping of local extrema. This makes the high order accurate DG schemes an appropriate framework for the propagation of dispersive water waves, and in particular, for solitary waves, see also the numerical results obtained in [109], [94].
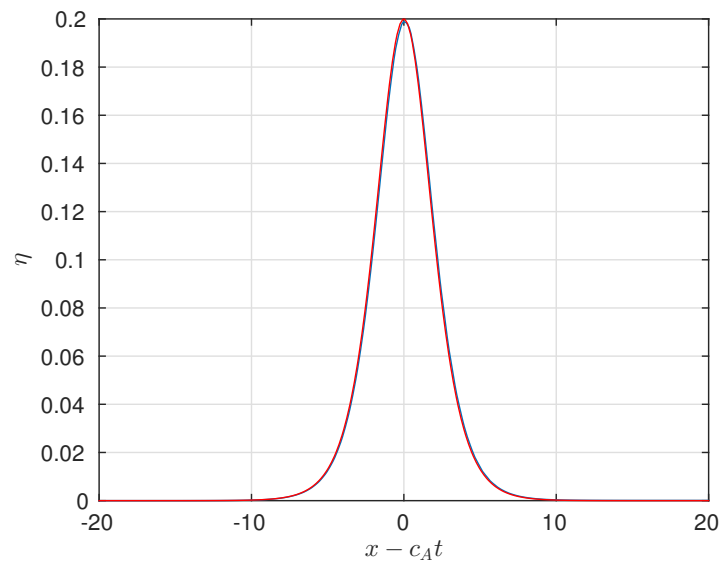
Figure 4.5: Comparison of surface η at time $t = 120$ shifted by $(x - C_A t)$ m (blue) and initial condition (red) for the solitary wave of amplitude $A = 0.2$. ADER-DG $\mathbb{P}_2$ scheme

Figure 4.6: Comparison of horizontal velocity u at time $t = 120$ shifted by $(x - C_A t)$ m (blue) and initial condition (red) for the solitary wave of amplitude $A = 0.2$. ADER-DG $\mathbb{P}_2$ scheme

Figure 4.7: Comparison of vertical velocity w at time $t = 120$ shifted by $(x - C_A t)$ m (blue) and initial condition (red) for the solitary wave of amplitude $A = 0.2$. ADER-DG $\mathbb{P}_2$ scheme
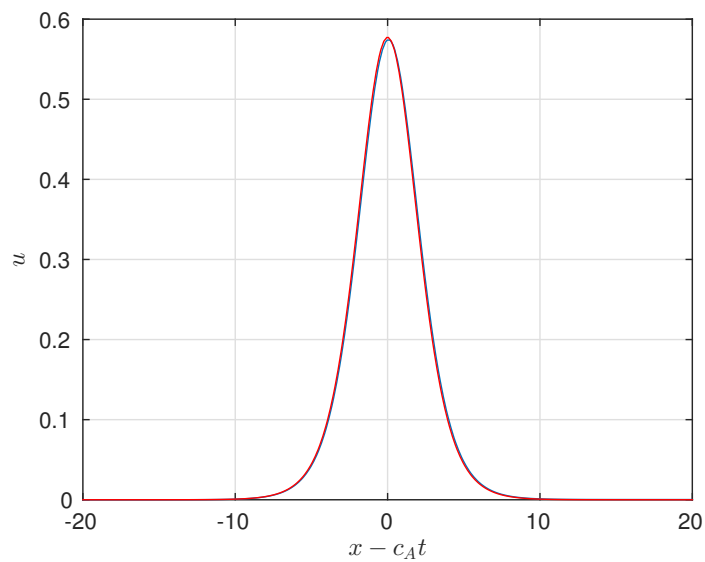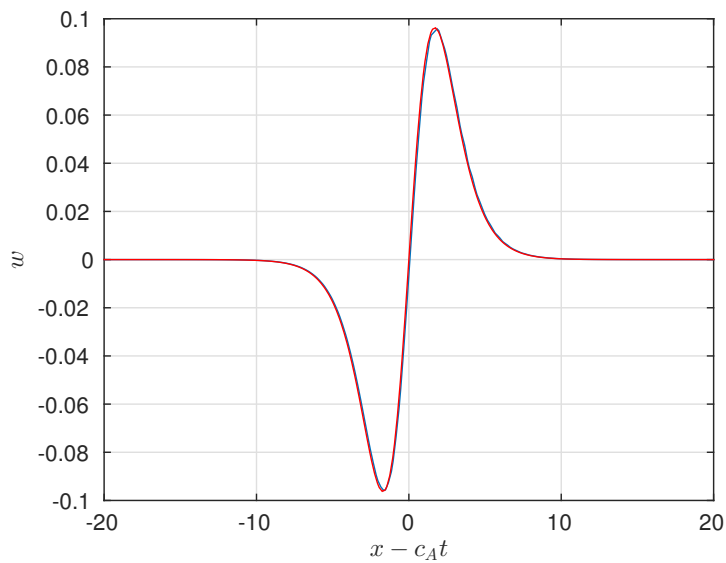

Figure 4.8: Comparison of non-hydrostatic pressure p at time $t = 120$ shifted by $(x - C_A t)$ m (blue) and initial condition (red) for the solitary wave of amplitude $A = 0.2$. ADER-DG $\mathbb{P}_2$ scheme
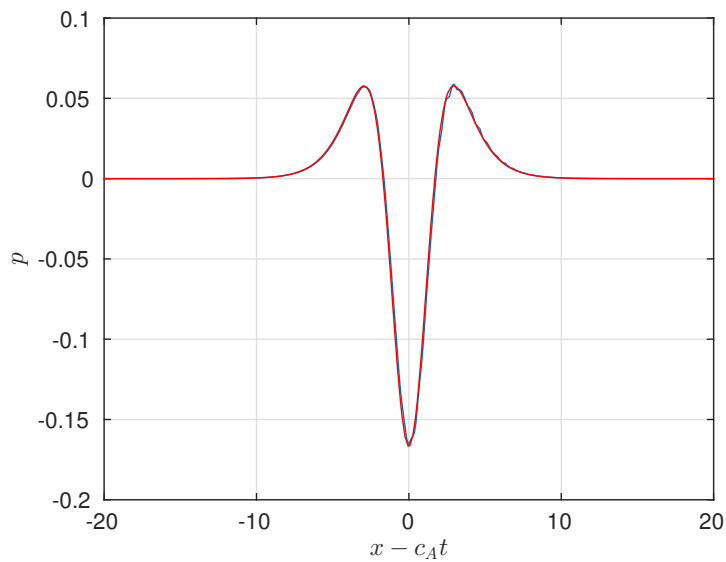
4.2   Solitary wave run-up on a plane beach

Synolakis [233] carried out laboratory experiments for incident solitary waves, to study propagation, breaking and run-up over a planar beach with a slope 1 : 19.85. Many researchers have used this data to validate numerical models. With this test case we assess the ability of the models to describe shoreline motions and wave breaking, when it occurs. Experimental data are available in [233] for surface elevation at different times. The bathymetry of the problem is described in Figure 4.9. A solitary wave of amplitude
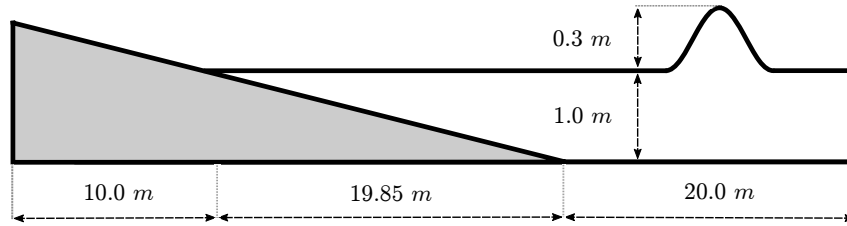

Figure 4.9: Sketch of the bathymetry used for the solitary wave run-up onto a beach test problem. .

$A = 0.3$, computed initially for each model following Section 4.1, is placed at the location $x = 20$. This serves as initial condition for the free-surface elevation and all other flow quantities. A Manning coefficient of $n_m = 0.01$ is used in order to define the glass surface roughness used in the experiments. The computational domain $\Omega = [-10, 40]$ is divided into 1000 equidistant cells. Free-outflow boundary conditions are considered.

Figure 4.10 and Figure 4.11 show snapshots, at different times, $t\sqrt{g/H} = t_0$ where $H = 1$, comparing experimental and simulated data. Figure 4.10 also shows where the breaking mechanism is active (region between the bars), for the system (NH-2L) and demonstrates the efficacy of its criteria. Similar region between bars can be shown for the rest of systems with their corresponding breaking mechanisms.

The breaking mechanism also works properly in terms of grid convergence. Figure 4.13 shows the snapshots at times $t\sqrt{g/H} = 15$ (run-up) and $t\sqrt{g/H} = 55$ (run-down) for different mesh sizes and systems.

Finally, Figure 4.12 represents the obtained numerical results when the breaking mechanism is not considered. In this case, a spurious overshoot of the wave amplitude appears, which underlines the importance to consider wave breaking in the context of dispersive non-linear shallow water models.

Due to the fact that the propagated wave in this test is weakly-nonlinear weakly-dispersive, the results obtained with the two-layer system are quite similar to the results obtained with the one-layer systems. Nevertheless, this test shows that the breaking mechanism introduced in this thesis, as well as friction terms, perform adequately for the two-layer system.
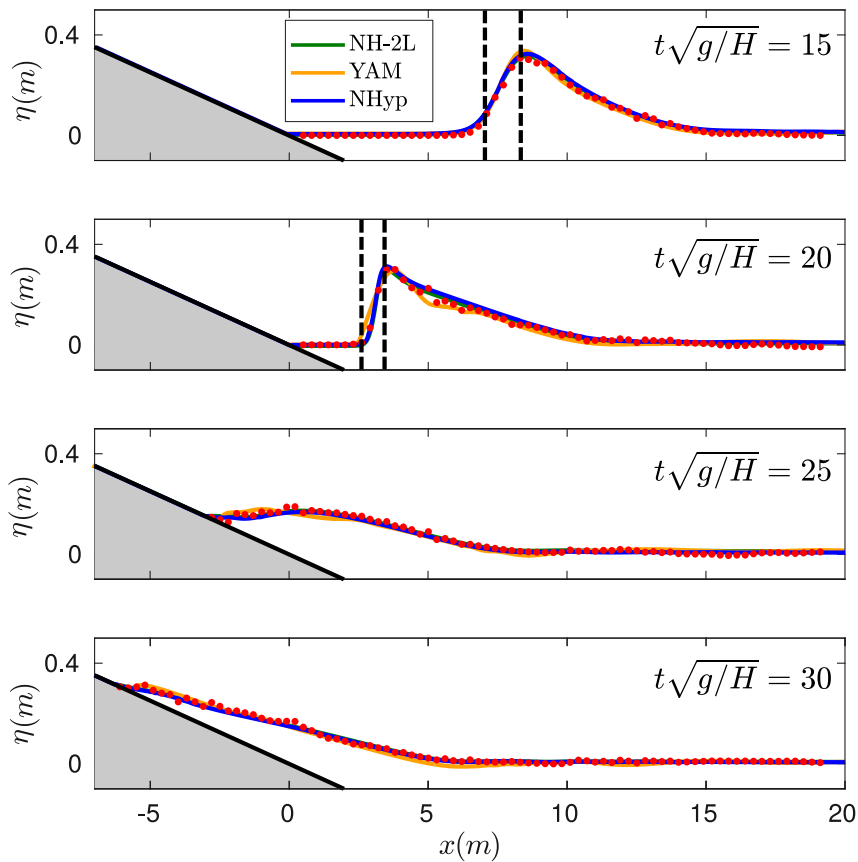
Figure 4.10: Comparison of experiments data (red) and simulated ones with the proposed non-hydrostatic systems including friction and wave breaking mechanism at different times during the run-up. Between bars, regions where breaking mechanism is active are shown for the case of the system (NH-2L2D).

In addition, good results are obtained for the maximum wave run-up, where the friction terms play an important role. Note that no additional wet-dry treatment for the non-hydrostatic pressure is needed. This test shows that the proposed *a posteriori* limiting strategy, the chosen breaking mechanism, as well as the standard SWE friction term perform adequately for the proposed hyperbolic system. Moreover, the corresponding discretization is robust and can deal with the presence of wet-dry fronts correctly.

Figure 4.11: Comparison of experiments data (red) and simulated ones with the proposed hyperbolic system including friction and wave breaking mechanism at different times during the run-down.

4.3   Solitary wave propagation over a reef

A test case on solitary wave over an idealized fringing reef examines the model's capability of handling nonlinear dispersive waves, breaking waves and bore propagation. The test configurations include a fore reef, a flat reef, and an optional reef crest to represent fringing reefs commonly found in tropical environment. Figure 4.14 shows a sketch of the laboratory experiments carried out at the O.H. Hinsdale Wave Research Laboratory of Oregon State University.
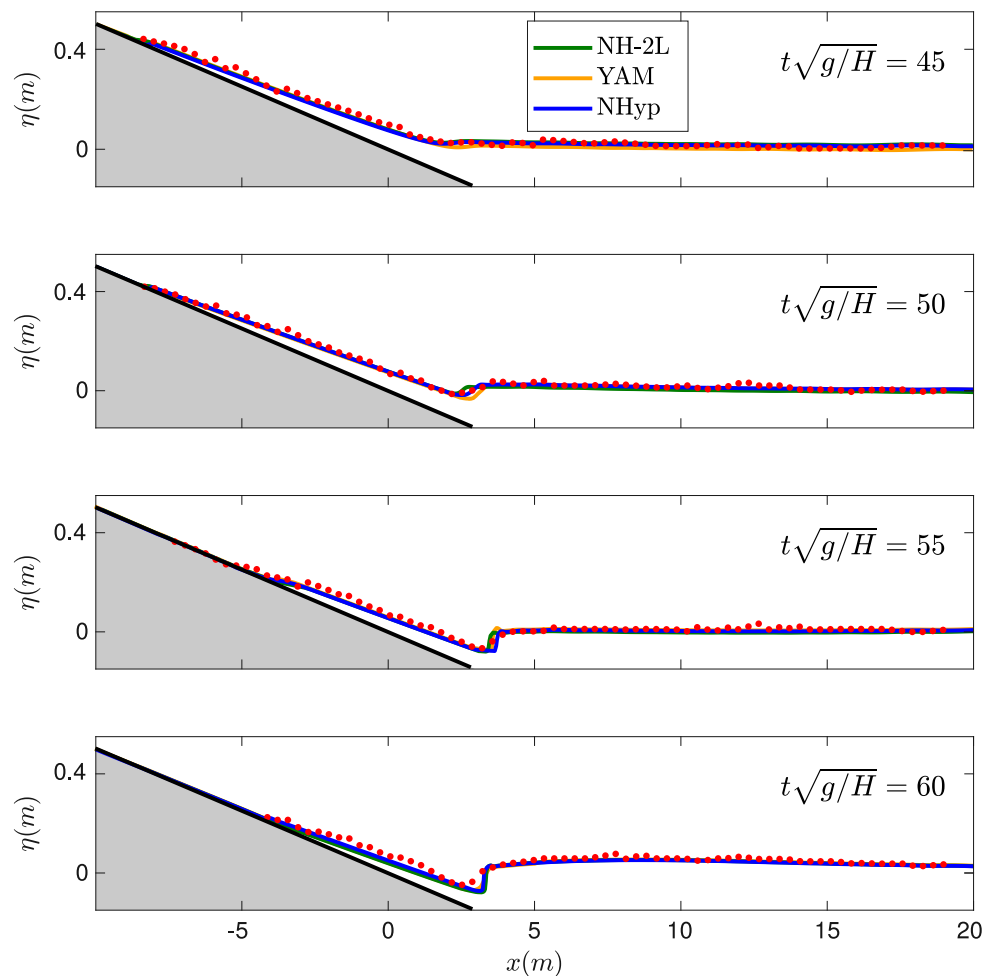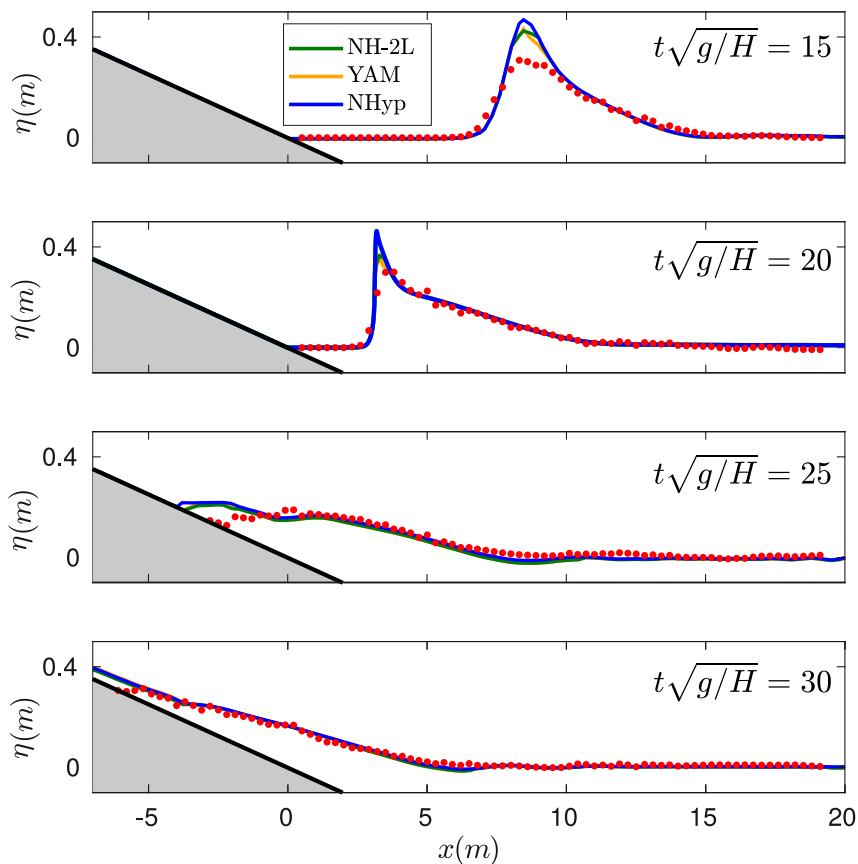
Figure 4.12: Comparison of experiments data (red) and simulated ones with the proposed hyperbolic system including friction at different times during the run-up without a breaking mechanism.
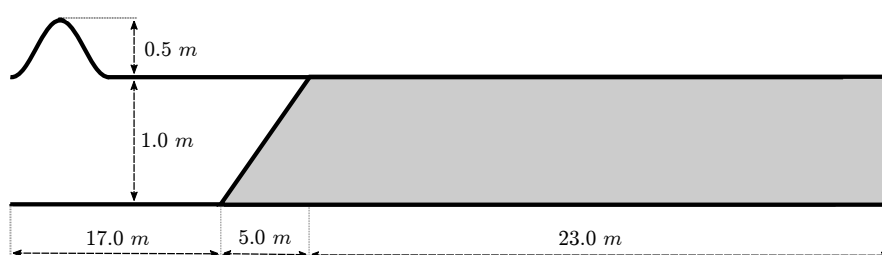
Figure 4.14: Sketch of the topography

A solitary wave of amplitude $A = 0.5$, computed initially for each model following Section 4.1, is placed at the location $x = 10$. This serves as initial condition for the free-surface elevation and all other flow quantities. A Manning coefficient of $n_m = 0.012$ is used in order to define the glass surface roughness used in the experiments. The computational
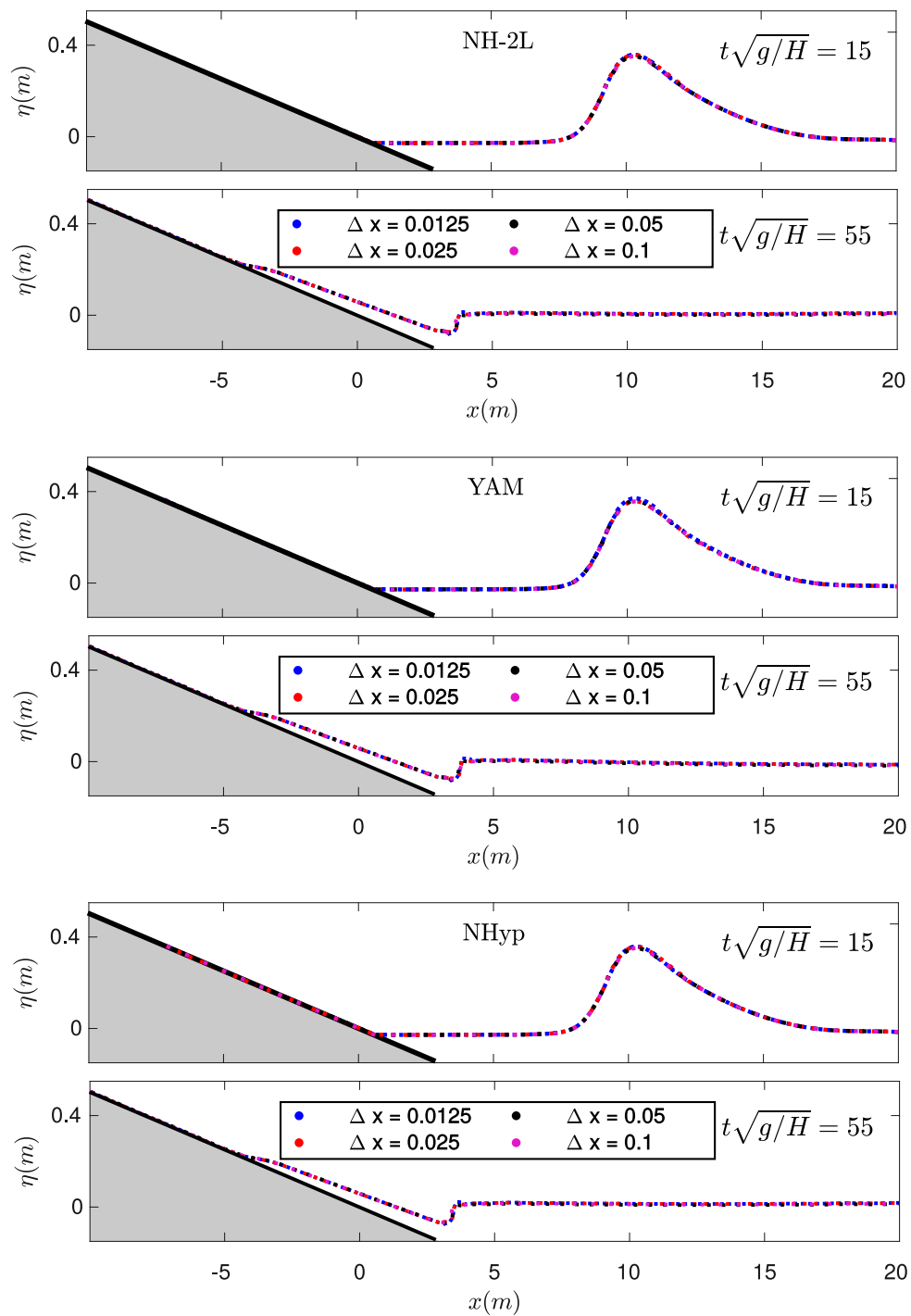
Figure 4.13: Comparison of free-surface simulation at times $t\sqrt{g/H} = 15$ and $t\sqrt{g/H} = 55$ for different mesh sizes and systems.

domain $\Omega = [0, 45]$ is divided into 900 equidistant cells. Free-outflow boundary conditions are considered.

Figure 4.15 shows snapshots at different times, $t\sqrt{g/H} = t_0$ where $H = 1$. Again, comparison between experimental and simulated data allows us to validate the numerical approach followed here. The water rushes over the flat reef without producing a pronounced bore-shape. The simulation also captures the offshore component of the rarefaction falls, exposing the reef edge, below the initial water level.

Again, as in the previous test case, due to the fact that the propagated wave in this test is weakly-nonlinear weakly-dispersive, the results obtained with the two-layer system are quite similar to the results obtained with the one-layer systems.

Figure 4.15: Comparison of experimental data (red points) and numerical at times $t\sqrt{g/H} = 0,\ 80,\ 100,\ 130,\ 170,\ 250\ s$

4.4   Favre waves

Here we consider an experiment where a fluid layer with a free surface is impacting against a vertical wall (see e.g. [117], [116], [249]). Due to dispersion, the reflected wave is a wave train of waves of different lengths and amplitudes (see Figure 4.16), rather than a simple shock wave as predicted by the shallow water equations (SWE).
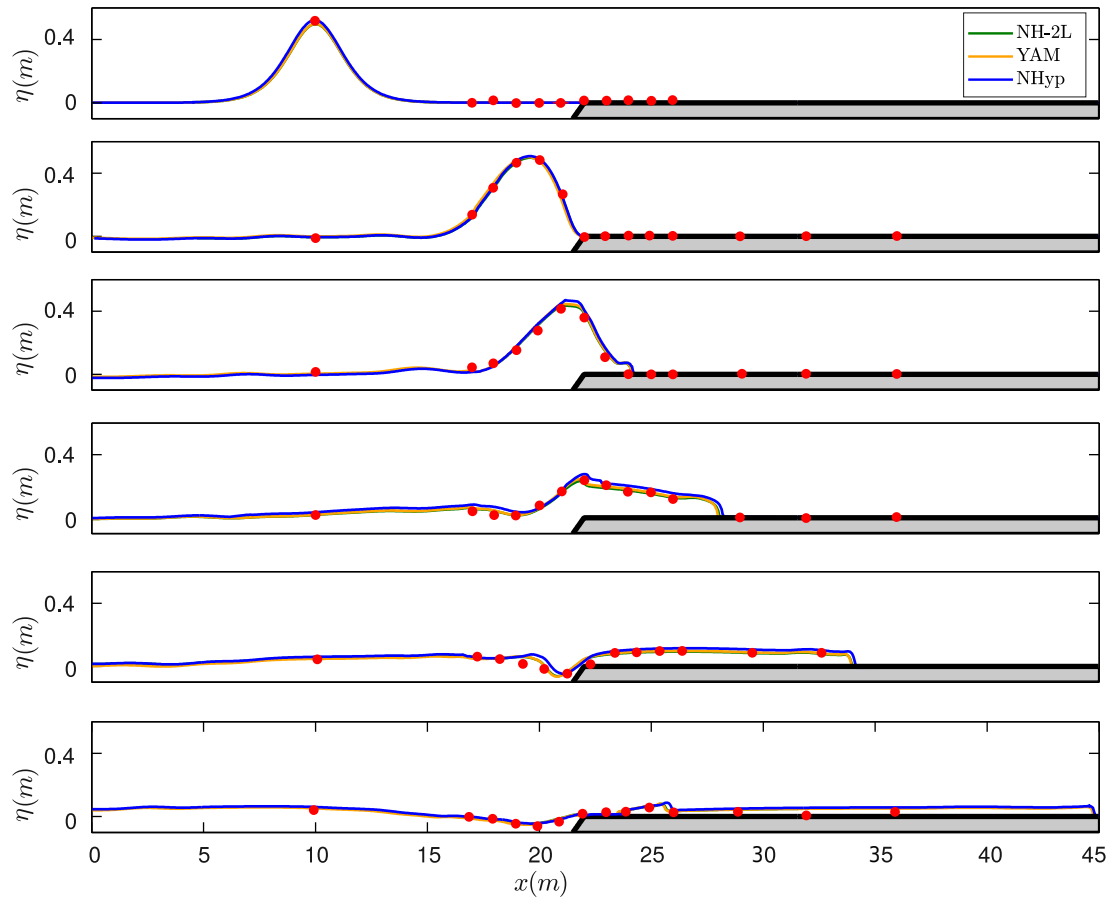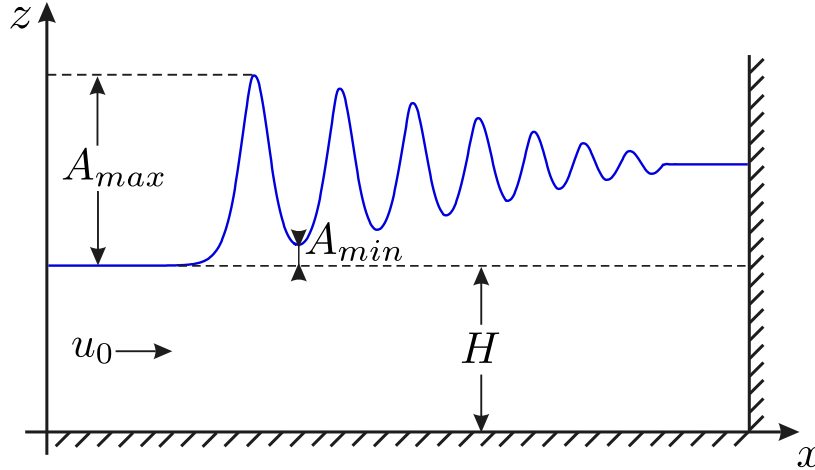

Figure 4.16: Sketch of Favre waves.

In this test we check again the performance of the proposed breaking mechanism for the systems (NH-2L), (YAM) and (NHyp).

The one-dimensional computational domain is $\Omega = [0, 180]$ and we set $H = 1$. The impact velocity u_0 is related to the relative Froude number F by the formula ([133])

$$u_0 = \left(F - \frac{1 + \sqrt{1 + 8F^2}}{4F} \right) \sqrt{gH}. \tag{4.4.1}$$

Hence, the initial condition for the horizontal velocity is given by (4.4.1) and $h = H$. The rest of the hydrodynamical variables are set to zero. The final simulation time was $t = 54$ s.

Figure 4.17 shows a comparison at time $t = 54$ for the Froude number $Fr = 1.35$ for different mesh sizes with the ADER-DG $\mathbb{P}_2$ scheme applied to the system (NHyp). One can observe that the results for 250 and 500 elements are quite similar, hence good numerical results can be obtained also on reasonably coarse meshes.

It is well-known that above the critical value $Fr = 1.35$, breaking waves arise (see [117], [133]) and the model is not valid without a breaking mechanism. Figure 4.18 shows
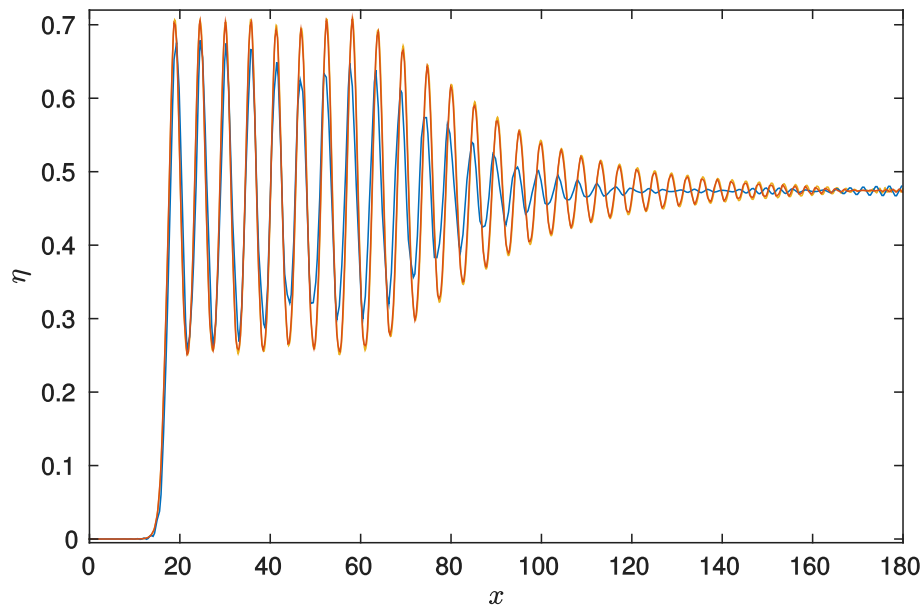
Figure 4.17: Comparison of the numerical results obtained at time $t = 54$ for the Froude number $Fr = 1.35$. The numerical simulations are shown for different mesh sizes: 125 (blue), 250 (red) and 500 (orange) elements.

the comparison between the experimental and the numerical results with a breaking mechanism included and without it. With wave breaking the obtained numerical results are in excellent agreement with the measured experimental data. Figure 4.18 also clearly shows that the breaking mechanism only acts when and where it is really needed, since similar results with respect to the simulations without the breaking mechanism are observed for $F < 1.35$, where no wave breaking occurs in the experiments.
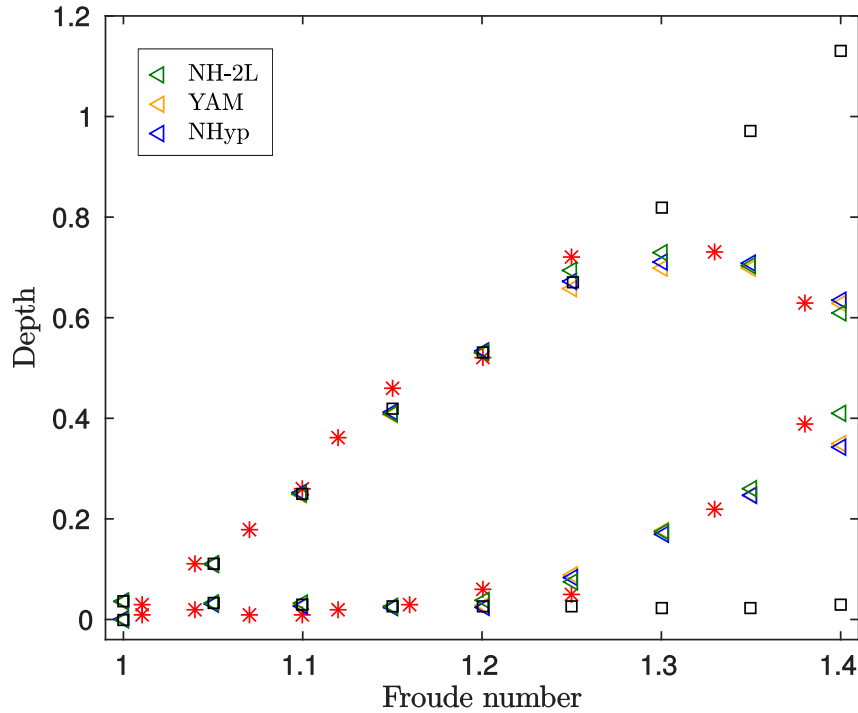
Figure 4.18: Comparison between the experimental data (red asterisks) and the numerical results with a breaking mechanism (triangles) and without (squares) with the systems (NH-2L), (YAM) and (NHyp). The upper markers indicate the amplitude of the first wave; the lower show the amplitude of the trough after the first wave.

4.5 Standing wave in closed basin

In this test case, we shall study the dispersive properties of the two layer system (NH-2L). To do so, we consider the analytical solution from the Stokes linear theory of a standing wave in closed basin with length L and flat bottom $H = 10$. The initial surface elevation is given by

$$\eta(x, 0) = A \cos \left(\frac{2\pi x}{L} \right),$$

where $A = 0.1$ is the amplitude of the standing wave. The wave length is the same than the length of the basin. This test case has been studied by various authors. For instance, Casulli and Stelling [51] use more than 20 vertical layers in order to correctly simulate wave dispersion. Using Keller-box scheme, Stelling and Zijlema [231] obtained good agreement with analytical solution by using two layers. Using a $\sigma-$coordinates discretization of the free-surface Euler equations, [180] shows excellent agreement with three layers.

To check the performance of the two proposed improved parameters, we will show two

cases: $L = 20/n$, $n = 1,3$. Since $kH = 20\pi/L = n\pi$, the waves are highly dispersive. From the dispersion relationship, we know that $2\pi/T = \sqrt{gk \tanh(kH)}$, and we can calculate the wave period T. The Stokes first order solution for this standing wave is

$$\eta(x,t) = \frac{A}{2} \cos(kx) \cos\left(\frac{2\pi}{T}t\right).$$

As in [181], a grid $\Delta x = 0.2/n$ that corresponds to 100 cells per wavelength for both cases of $n = 1,3$. A $CFL = 0.45$ is employed. Periodic boundary conditions are imposed. The simulation time is 40 seconds. The test is performed with the one-layer system that corresponds to $l_2 = 0$, and with the two-layer system proposed in this dissertation for some values of the optimization parameters that will be detailed.

Fig. 4.19 shows the comparison of the time series between the analytical solution for the case of $L = 20$ and the numerical solution, at $x = L/2$. In this case, $kH = \pi$, and the two-layer system with the non-optimized parameters $(l_1^{(2L)}, \gamma_1^{(2L)}, \gamma_2^{(2L)})$ gives good results. Nevertheless, the optimized parameters $(l_1^{(5)}, \gamma_1^{(5)}, \gamma_2^{(5)})$ improve the results and the solution matches perfectly with the analytical reference solution. This case highlights that the one-layer systems can not reproduce well these dispersive waves. This is due to the poor accuracy of the linear dispersion relation that the one-layer systems has for $kH \approx \pi$.

The case $L = 20/3$ gives $kH \approx 9.42$ and becomes more challenging. Fig. 4.20 shows comparisons of the time series at $x = L/2$. In this case, the two-layer model with the non-optimized parameters can not maintain the correct frequency, and it quickly loses the initial trim, which is also missed from the beginning in the case of the one-layer system. Fig. 4.20 also shows the results with the presenting improved parameters $(l_1^{(15)}, \gamma_1^{(15)}, \gamma_2^{(15)})$ with an excellent agreement. The numerical test shows the ability of the optimized two layer model presented here to deal with a wide range of waves.

Figure 4.19: Comparison of analytical (red) and numerical (blue) for the case $L = 20$. In (a) the numerical results for the one-layer ($l_2 = 0$); (b) the numerical results with the non-optimized parameter ($l_1^{(2L)}, \gamma_1^{(2L)}, \gamma_2^{(2L)}$); (c) the numerical results with the optimized parameters ($l_1^{(5)}, \gamma_1^{(5)}, \gamma_2^{(5)}$).
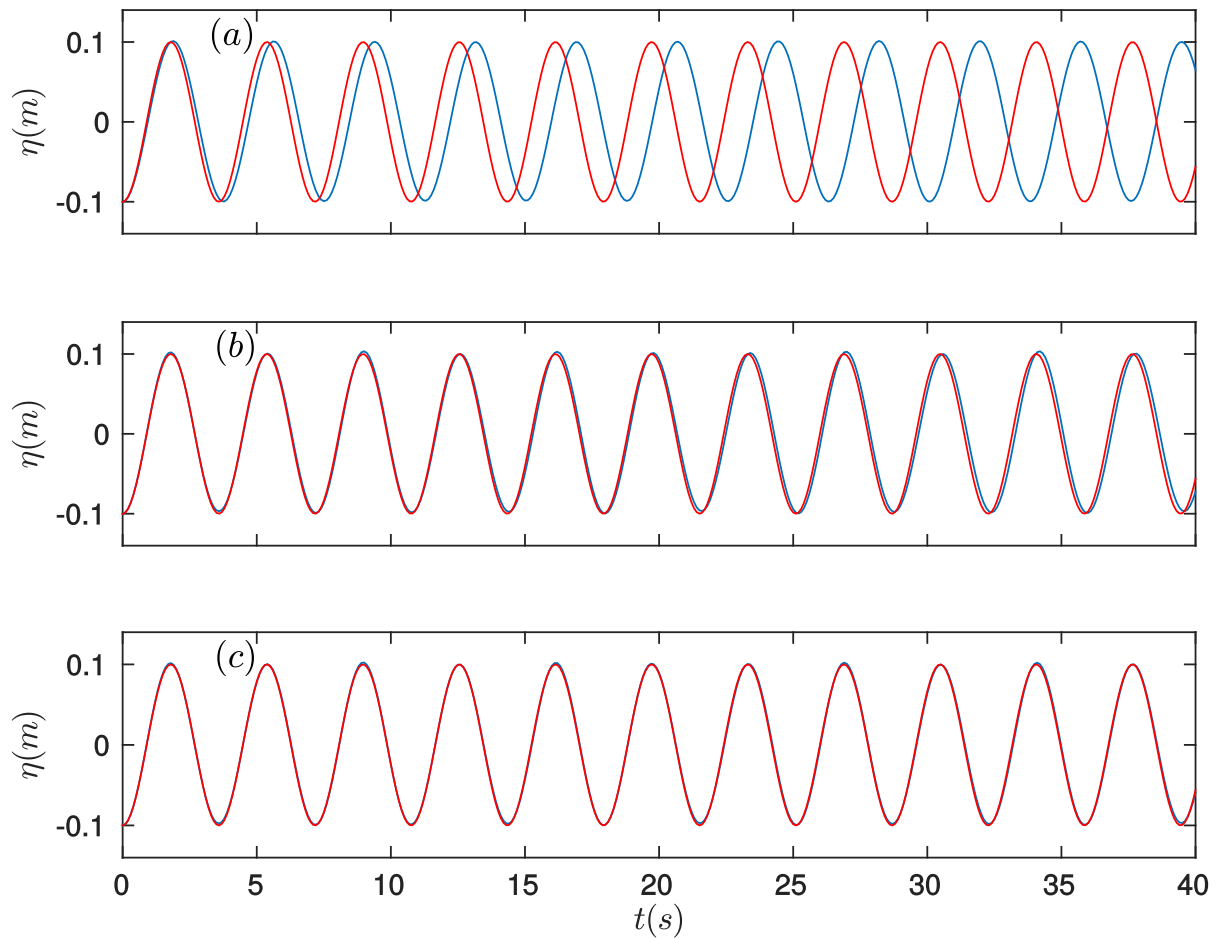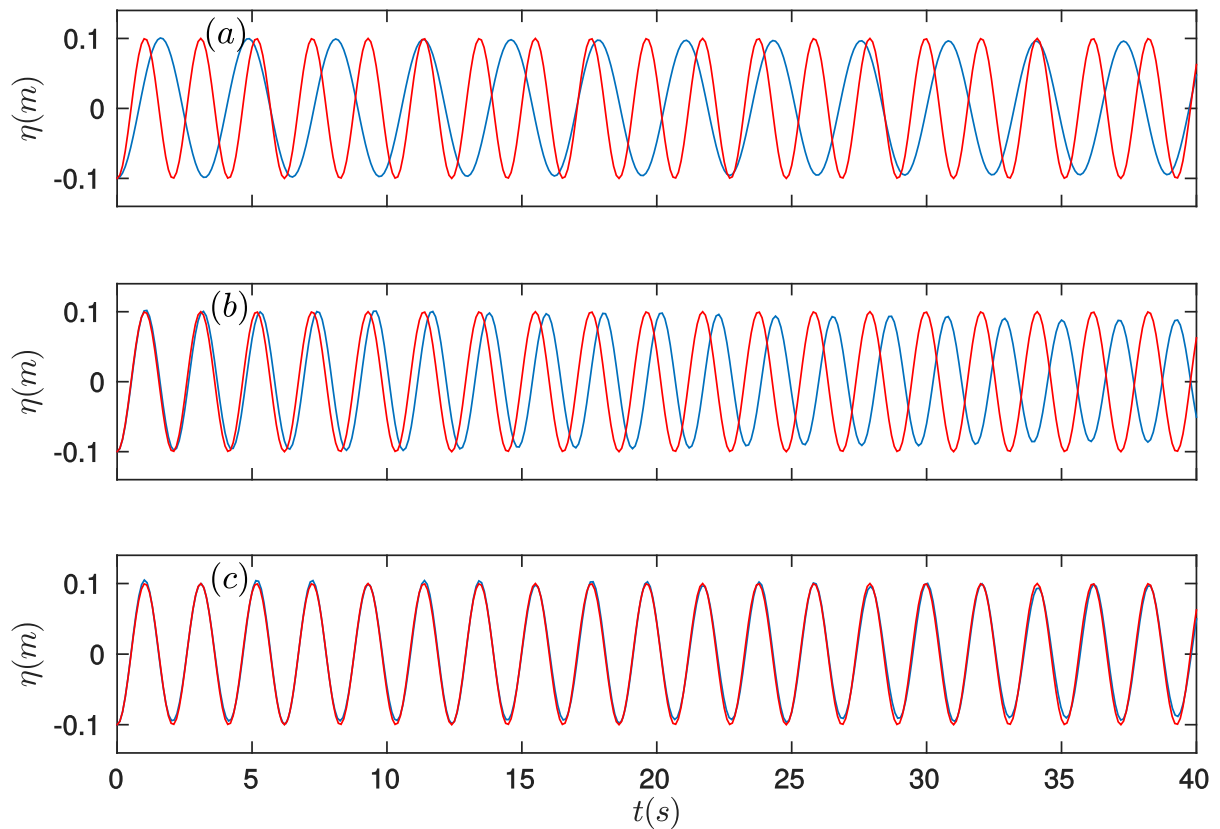
Figure 4.20: Comparison of analytical (red) and numerical (blue) for the case $L = 20/3$. In (a) the numerical results for the one-layer ($l_2 = 0$); (b) the numerical results with the non-optimized parameters ($l_1^{(2L)}, \gamma_1^{(2L)}, \gamma_2^{(2L)}$); (c) the numerical results with the optimized parameters ($l_1^{(15)}, \gamma_1^{(15)}, \gamma_2^{(15)}$).

4.6 Periodic waves over a submerged bar

The experiments of plunging breaking periodic waves over a submerged bar by Dingemans [87] and Beji and Battjes [13] are considered here. The experiments studies the frequency dispersion characteristics and non-linear interaction. As waves propagates over a submerged bar, multiple phenomena occurs, such as non-linear shoaling, amplification of higher harmonics and wave breaking.
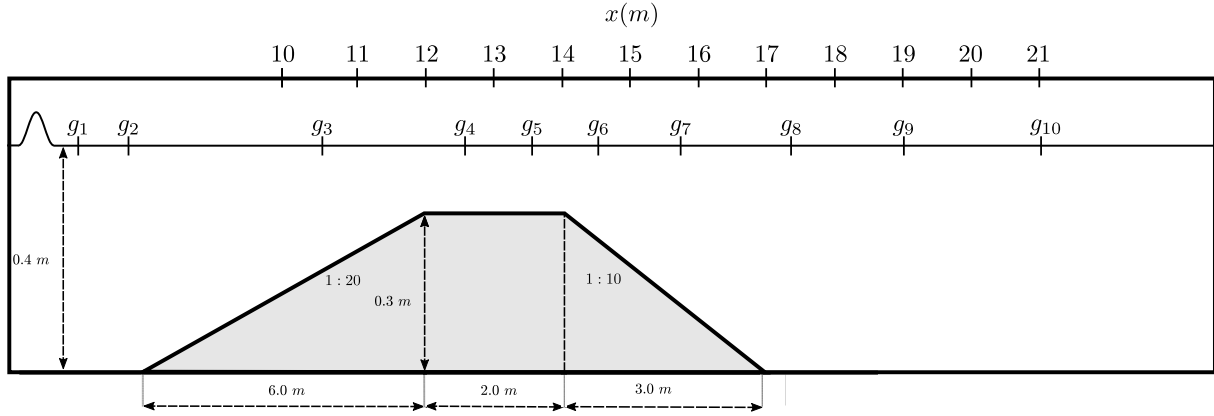
Figure 4.21: Periodic waves breaking over a submerged bar. Sketch of the bathymetry

The one-dimensional domain $[0, 30]$ is discretized with $\Delta x = 0.01$ and the bathymetry is defined in the Fig. 4.21 for all the experiment cases. The CFL is set to 0.5 and $g = 9.81$. Horizontal and vertical velocities and η are set initially to 0. Boundary conditions correspond to free-outflow at $x = 30$ and a sinusoidal wave train for η generated at $x = 0$. This is done using the target initial condition at the relaxation zone with $L_{Rel} = 2$:

$$\eta^*(t) = A \sin\left(\frac{2\pi}{T}t\right), u_\alpha^*(t) = \sqrt{gH_0}\eta^*(t),$$

where A and T denotes amplitude and period and $H_0 = 0.4$. The rest of hydrodynamical variables of the system are set to zero. We focus on test cases (a), (b), (c) and (d), that have been described in the table below along with the models used to its simulation

Case	A (m)	T (s)	Waves	Model used
(a)	0.01	2.02	non-breaking waves	(NH-2L)
(b)	0.0145	2.525	breaking waves	(NH-2L)
(c)	0.0205	1.01	non-breaking waves	(NH-2L)
(d)	0.01	1.25	non-breaking waves	(NH-2L), (YAM), (NHyp),

The test cases (a)-(c) corresponds to the experiment by Dingemans, whereas the case (d) corresponds to the experiment by Beji and Battjes.

Depth gauges, which measure the free surface elevation, are placed for cases along $x = g_i$, $g_1 = 4$, $g_2 = 5.7$, $g_3 = 10.5$, $g_4 = 12.5$, $g_5 = 13.5$, $g_6 = 14.5$, $g_7 = 15.7$, $g_8 = 17.3$, $g_9 = 19$, $g_{10} = 21$.

Test (a) and (c) produce, up to the front slope, waves with $kH \approx 0.63$ and $kH \approx 1.58$ respectively. Fig. 4.22 shows the time series of free surface for case (a). The numerical model maintains good agreement with the experimental data at each station. Minor discrepancies can be observed behind the bar at stations $g_5 - g_{10}$, where higher harmonics are released. The test case (a) coincides with one of the proposed in [13], and similar good agreement with other numerical models can be found in literature. Let us remark that in [180] $\sigma-$coordinate discretization of the free-surface Euler equations is used. While in that paper the authors need three layers for the test, we can achieve good results with the technique proposed here that only considers two layers. The results in [61] with a three-parameter Green-Naghdi model optimized for uneven bottoms, are also in good agreement. Comparing to that, let us remark that the Green-Naghdi system described there includes high order terms by means of third order derivatives. We would like to stress the ability of the proposed two-layer system to deal with a widely range of dispersive waves, which is achieved without including high order terms in the system of equations. Only first order derivatives are used here. In [9] the test is also studied with a depth-integrated free-surface two-layer non-hydrostatic system.

The results from case (c) are given in Fig. 4.24. In this situation, larger values of kH give short waves and make this case more challenging. Due to this fact, waves propagate and typical cnoidal profile can be observed over the top of the bar. This is well reproduced at gauges g_1, g_2, g_3, g_4. Behind the bar, at g_5, g_6, g_7, higher harmonics appear. As we see, a good fit for the amplitude is observed. This test case was studied in [176], where excellent results are obtained at g_5, g_6, g_8, g_{10}, with a two-layer system that it has been also optimized up to the a second-order nonlinear dispersive analysis.

Fig. 4.22 and Fig. 4.24 also show comparison with $(l_1^{(5)}, \gamma_1^{(5)}, \gamma_2^{(5)})$ and $(l_1^{(2L)}, \gamma_1^{(2L)}, \gamma_2^{(2L)})$ parameters. One can see a better matching in favour of the former. The next case presented is (b), where waves start to break on the top of the bar. Numerical time series of surface elevation are shown in Fig. 4.23 for $(l_1^{(5)}, \gamma_1^{(5)}, \gamma_2^{(5)})$. Here we use the proposed ς_α for the breaking mechanism described in Subsection 1.5. To evince that a breaking mechanism is needed, the corresponding numerical simulation without the breaking mechanism is also shown in Fig. 4.23. The test shows the need to consider a breaking mechanism. Before reaching the bar, both simulations coincide as expected, since the wave breaking starts around $x = 12$, revealing that the start/stopping criteria performs properly. In all gauges that follows, the wave shape, frequency and amplitude is well reproduced in favour of the simulations with the breaking mechanism. In [103], the test case (b) is performed with a Serre Green-Naghdi system and a different and well-validated breaking mechanism. The results obtained in this work, are in accordance with the ones presented in [103]. The experiment concerning to the case (d) is carried out with the one-layer systems. Figure 4.25 shows the time evolution of the free surface at

Figure 4.22: Comparison of experiment data (a) (red points) and simulated ones with improved dispersive parameters $(l_1^{(5)}, \gamma_1^{(5)}, \gamma_2^{(5)})$ (green) and $(l_1^{(2L)}, \gamma_1^{(2L)}, \gamma_2^{(2L)})$ (blue)

points $g_3, \ldots, g_8$. Both amplitude and frequency of the waves are captured on all wave gauges successfully, and all the models give similar results. In this test case, the resulting waves are weakly-nonlinear weakly-dispersive. These are in a range in which the one-layer systems has an accurate linear dispersion relation, and excellent results are obtained. For the test cases (a)-(c) studied here, high harmonic waves appear, as well as kH can increase up to 10. Thus, many dispersive models can not reproduce well the experiment. This is the case of the weakly-nonlinear weakly-dispersive one-layer models. The comparison with experimental data emphasizes the need to consider a dispersive model to faithfully
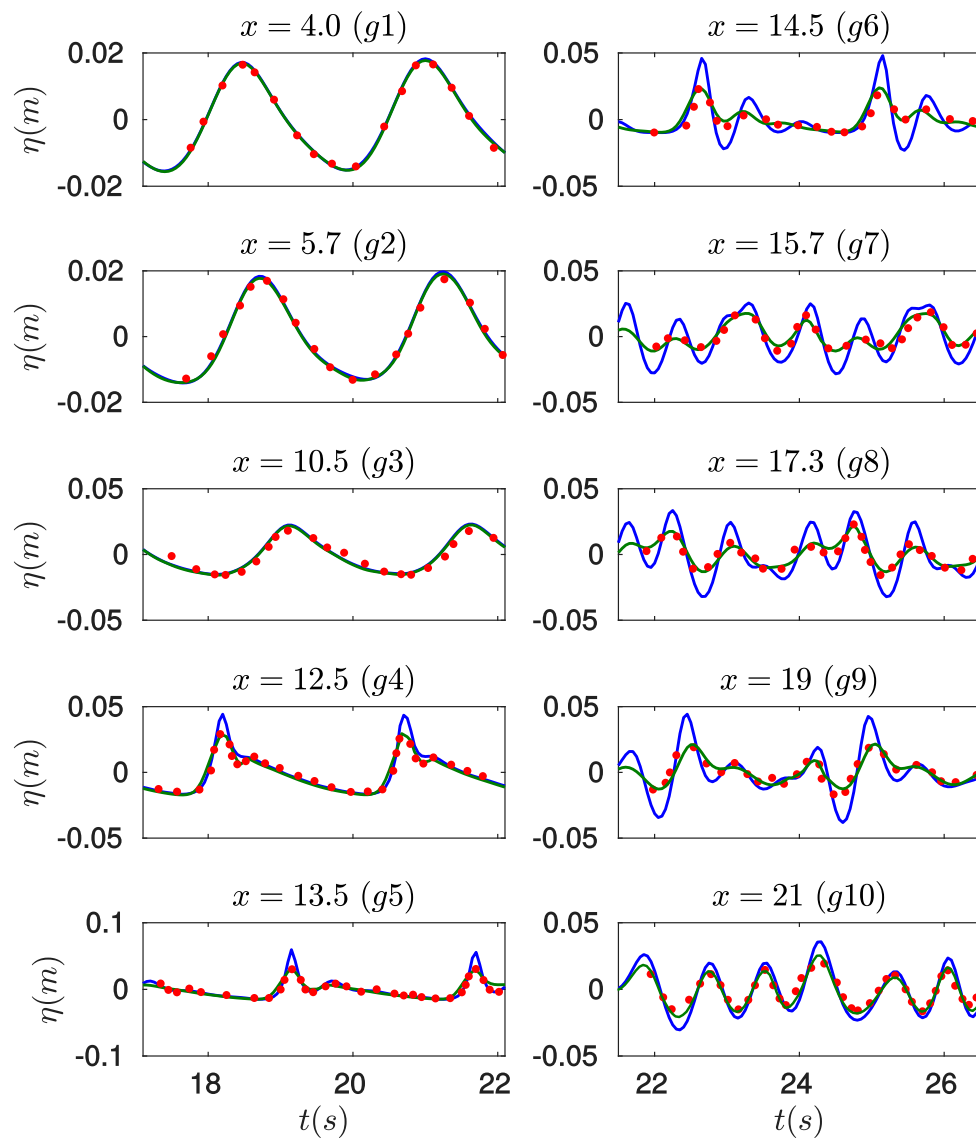
Figure 4.23: Comparison of experiment data (b) (red points) and simulated ones with breaking mechanism (green) and without (blue)

capture the shape of the waves near the continental shelf, where a wide range of dispersive waves can be released. Thus, the two-layer system presented in this work can simulate an extensive range of frequencies of dispersive waves, which typically arises in nature from intermediate to shallow waters.
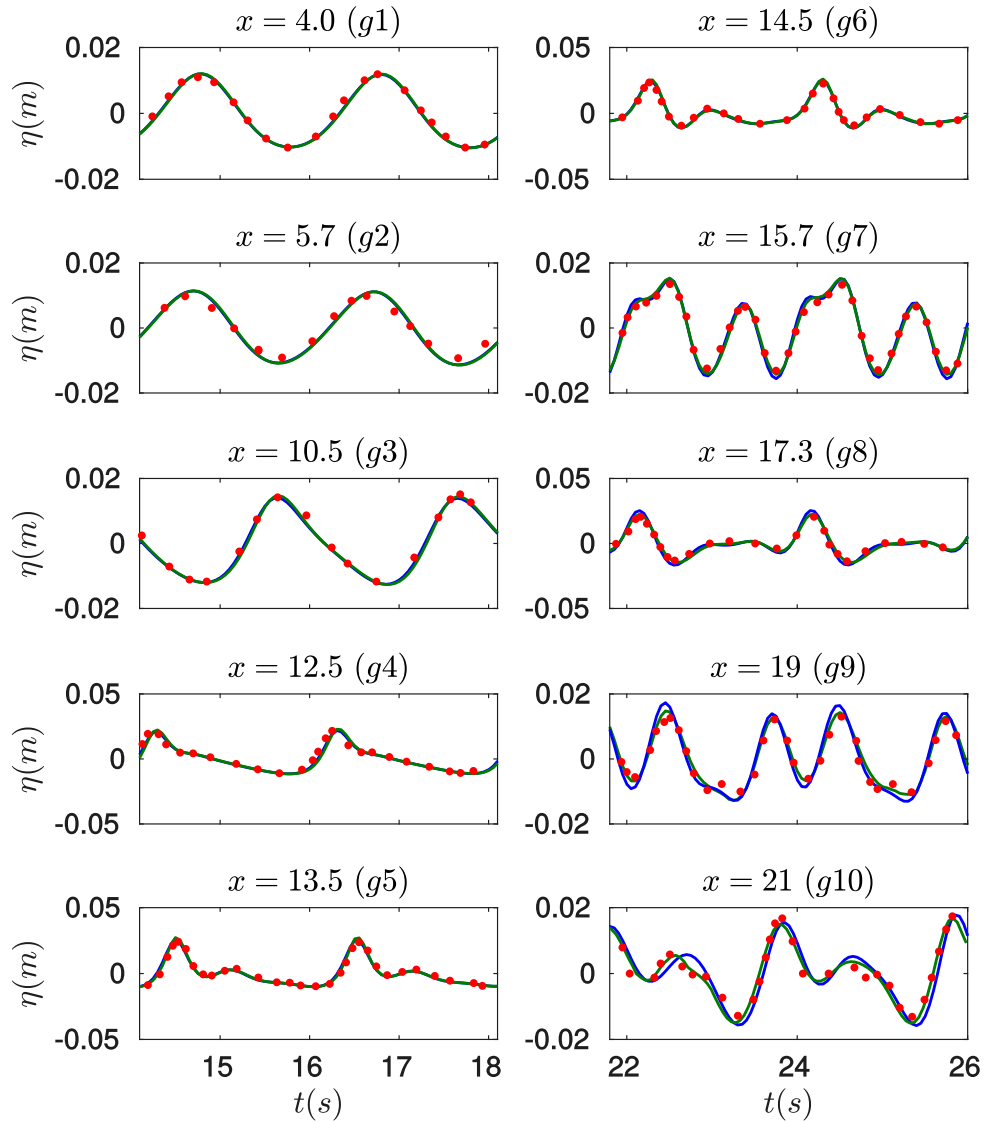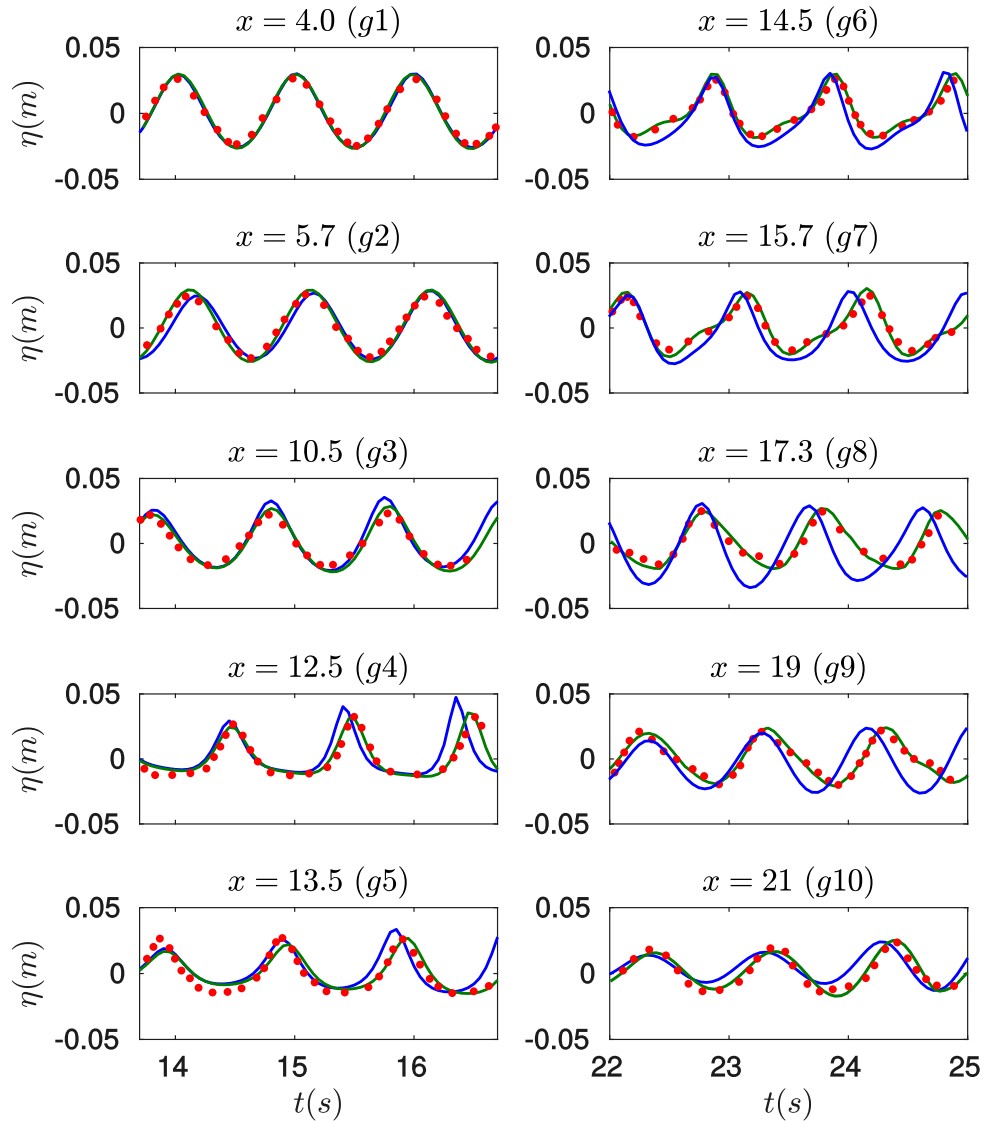
Figure 4.24: Comparison of experiment data (c) (red points) and simulated ones with improved dispersive parameters $(l_1^{(5)}, \gamma_1^{(5)}, \gamma_2^{(5)})$ (green) and $(l_1^{(2L)}, \gamma_1^{(2L)}, \gamma_2^{(2L)})$ (blue)

4.7   Solitary wave impinging on a conical island

The goal of this 2D numerical test is to compare the results of the mathematical models described in this dissertation with laboratory measurements for a two-dimensional problem. The experiment was carried out at the Coastal and Hydraulic Laboratory, Engineer Research and Development Center of the U.S. Army Corps of Engineers ([20]). The laboratory experiment consists in an idealized representation of Babi Island in the Flores Sea in Indonesia. The produced data sets have been frequently used to validate
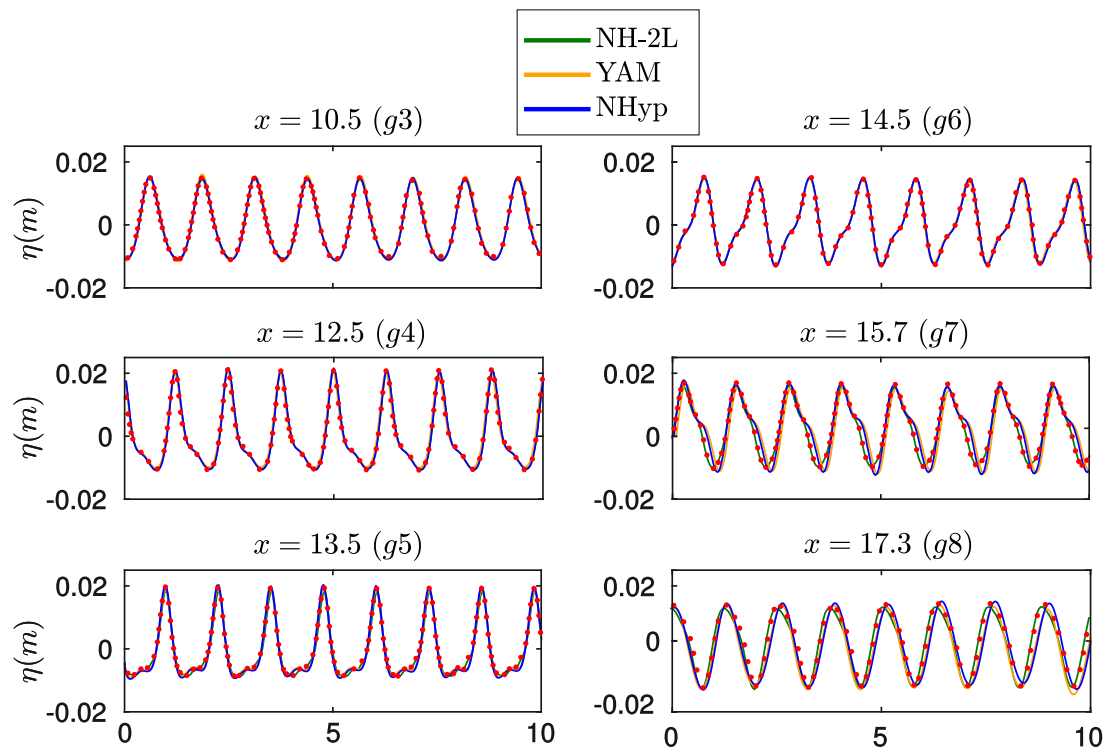
Figure 4.25: Comparison of experiment data (red line) and simulated ones

run-up models ([259], [179]).

A directional wave-maker is used to produce planar solitary waves of specified crest lengths and heights. The set–up consists in a 25×30 m^2 basin with a conical island situated near the centre. The still water level is $H = 0.32$ m. The island had a base diameter of 7.2 m, a top diameter of 2.2 m and it is 0.625 m high. Four wave gauges, $\{WG_1, \ WG_2, \ WG_3, \ WG_4\}$, are distributed around the island in order to measure the free surface elevation (see Figure 4.26).

For the numerical simulation we will use the systems (NH-2L2D),(YAM-2D) and (NHyp-2D).

The computational domain is chosen as $\Omega = [-5, 23] \times [0, 28]$ with $\Delta x = 0.02$ and $\Delta y = 0.02$. Free outflow boundary conditions are imposed. A solitary wave of amplitude $A = 0.06$, computed initially for each model following Section 4.1, is placed at the location $x = 0$. The wave propagates until $t = 30$ seconds and a Manning coefficient of $n_m = 0.015$ is used.

The numerical simulation shows two wave fronts splitting in front of the island and collide behind it (see Figures 4.31 and 4.32). Comparison between measured and computed water levels at gauges $WG_1, \ WG_2, \ WG_3, \ WG_4$ show good results (4.28) for the three systems. However, the simulation corresponding to (NHyp-2D) reveals a
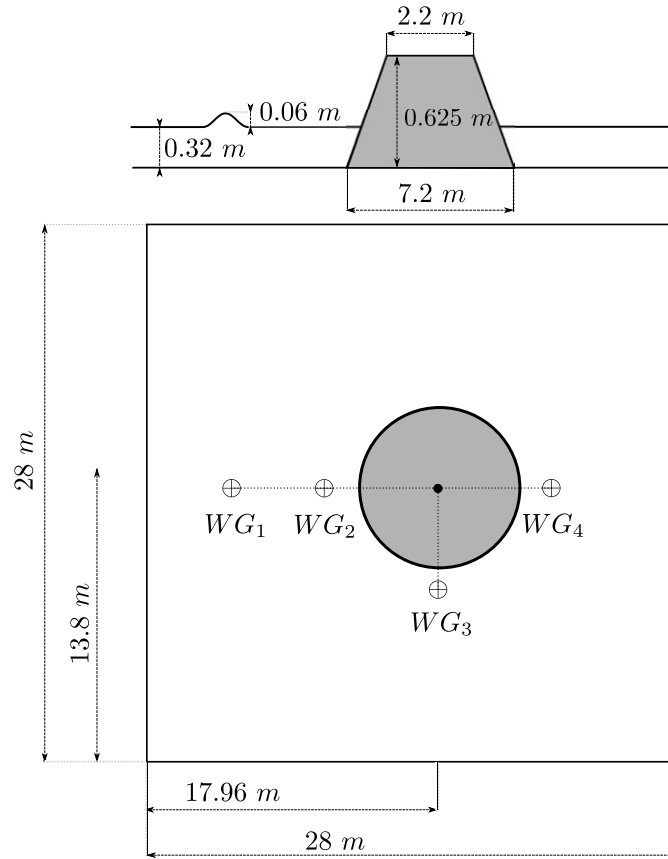
Figure 4.26: Sketch of the topography for the conical island test case.

better fit. This is due to the high order ADER-DG $\mathbb{P}_2$ scheme in opposition to the second order finite volume schemes used to discretize the systems (NH-2L2D) and (YAM-2D). A comparison between the computed run-up and the laboratory measurement, is shown in Figure 4.27. The results are in an excellent agreement with the laboratory measurement.

Table 4.4 shows the execution times on a NVIDIA Tesla P100 GPU for the system (NHyp-2D) with $\alpha = 0$ (SWE) and $\alpha = 3$. In view of the obtained results, we can conclude that the implementation of the DG scheme for the non-hydrostatic code can achieve a good computational performance with an additional computational cost that is only about 2.68 times the cost of a simple SWE simulation. This additional computational cost is similar to the one presented in [112], where the non-hydrostatic pressure system proposed in [259] was discretized with a second order hybrid finite volume–finite difference scheme, by solving a mix hyperbolic-elliptic problem. The real highlight in this work is that the same low additional computational cost is maintain for any order of accuracy in space and time of the numerical scheme.

Moreover, Figure 4.29 shows that the computational time required to evolve a degree

of freedom remains constant when the order of the DG scheme is increased.

As can be expected, almost all the execution time is spent in the space-time predictor *kernel*. Figure 4.30 shows graphically the GFLOPS/s obtained in the CUDA implementation for the space-time predictor *kernel*. The code achieves 700 GFLOPS/s for big enough meshes. Theoretical maximum peak performance for the Tesla P100 is 4.761 TFLOPS in double precision, and therefore the code can achieved around a 14% of this theoretical maximum peak performance value. Moreover, the GFLOP/s values obtained are independent on the order of the scheme.

It can thus be stated that the numerical scheme used here is computationally efficient and can correctly simulate dispersive water waves with only a moderate computational overhead compared to the classical SWE model.
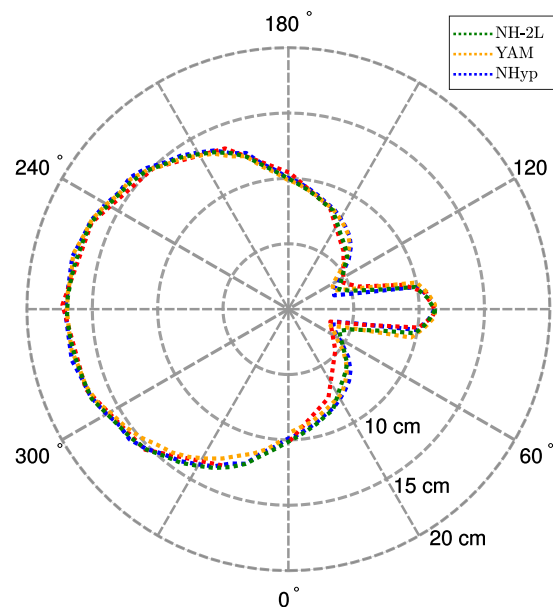
Figure 4.27: Maximum run-up measured (red) and simulated (legend) on a 200×200 cell mesh.
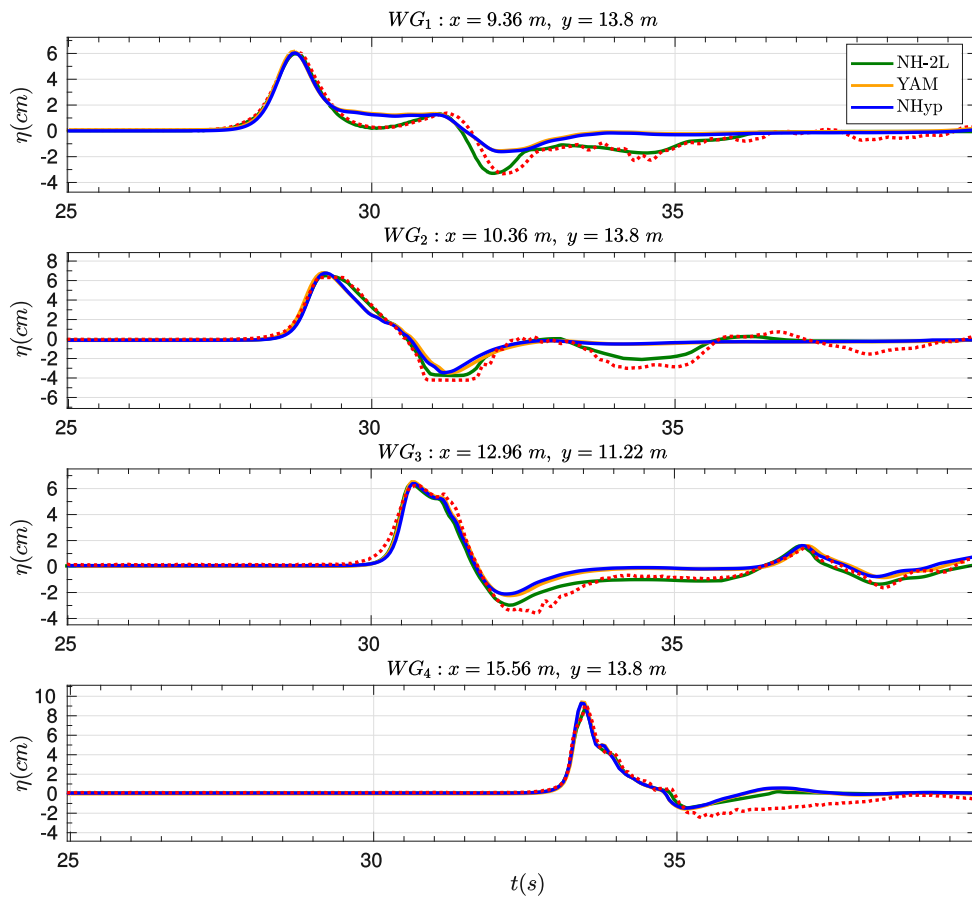
Figure 4.28: Comparison of data time series (red) and numerical (legend) at wave gauges WG_1, WG_2, WG_3, WG_4 on a mesh composed of 200×200 elements.
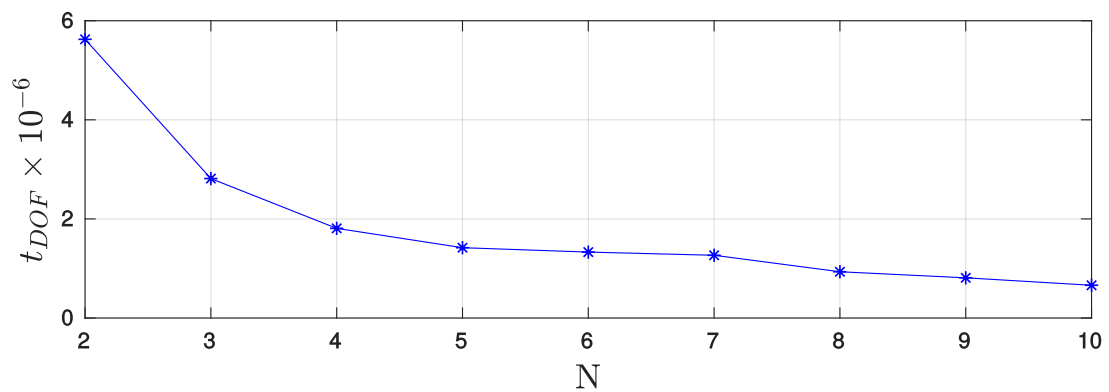
Figure 4.29: Computational time ($\times 10^{-6}$) to evolve a degree of freedom for a DG-$\mathbb{P}_N$ scheme for the system (NHyp-2D).

Runtime(s) GPU — ADER-DG-$\mathbb{P}_N$				
	$N_x \times N_y$	$\alpha = 3$	$\alpha = 0$	Ratio
DG-$\mathbb{P}_1$	100×100	7.29	4.85	1.50
	200×200	47.09	29.02	1.62
	300×300	147.88	70.04	2.11
	400×400	336.07	138.47	2.43
DG-$\mathbb{P}_2$	100×100	89.98	40.23	2.24
	200×200	705.90	296.10	2.38
	300×300	2323.79	932.51	2.49
	400×400	4953.49	1913.17	2.59
DG-$\mathbb{P}_3$	100×100	548.56	230.83	2.38
	200×200	4446.10	1803.18	2.47
	300×300	14496.71	5625.33	2.58
	400×400	40155.22	15009.88	2.68

Table 4.4: Execution times in sec for non-hydrostatic and SWE GPU implementations
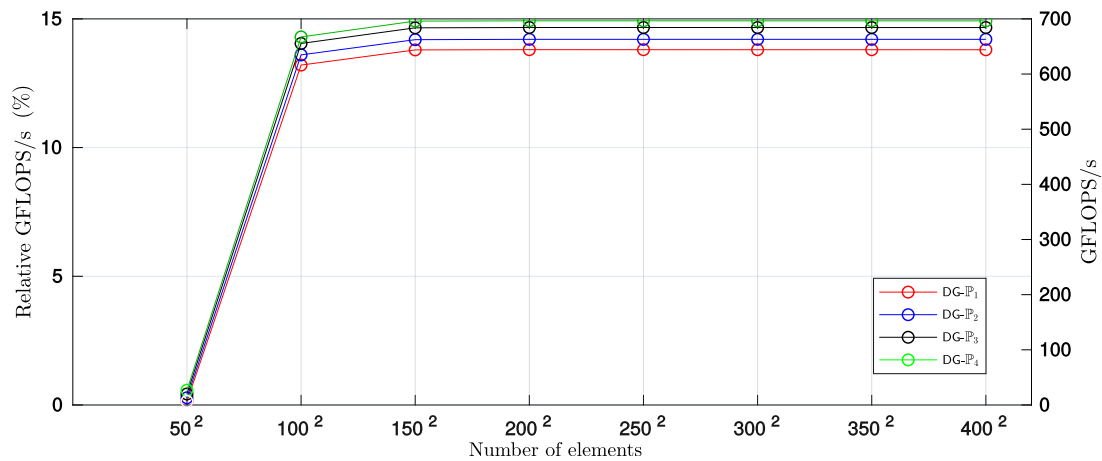
Figure 4.30: GFLOPS/s obtained for the space-time predictor *kernel* for several meshes and $DG - \mathbb{P}_N$ schemes.
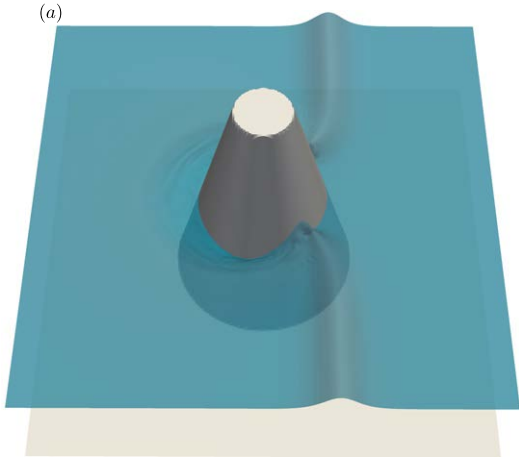
Figure 4.31: Snapshot of the free surface profile at time $t = 8$.
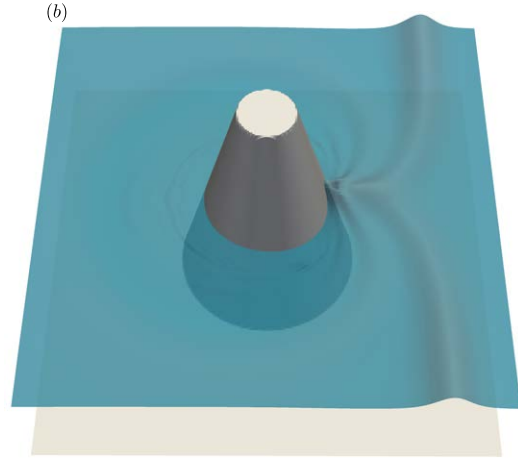
Figure 4.32: Snapshot of the free surface profile at time $t = 10$.

4.8 Dispersive water waves generated by rigid landslides

This benchmark problem is based on the 3D laboratory experiments of [108]. It was also used as a test problem in the International Workshop on Landslide Tsunami Model Benchmarking, that was held on Galveston in 2017, where all relevant data were also provided ([200]). A recent work has been submitted (see [158]), where the systems and numerical tools described in this thesis has been employed. In this subsection we will focus in one of the considered benchmarks.

This problem consists on the modelling of the water free surface perturbation due to a sliding mass down a plane slope. Experiments were performed in the University of Rhode Island (URI), in a wave tank of 3.6 m width, 30 m length and 1.8 m deep. The sliding mass down a plane slope built in the tank with an angle $\theta = 15°$. The vertical cross section of the landslide is shown in Figure 4.33. The geometry is defined using smoothed hyperbolic functions

$$\frac{T}{1 - \epsilon}(\text{sech}(k_b(x - x_g))\text{sech}(k_w y) - \epsilon),$$

$$k_b = 2C/b, \ k_w = 2C/w, \ C = \text{acosh}(1/\epsilon).$$

The slide has a length $b = 0.395$, width $w = 0.680$ and thickness $T = 0.081$. The smoothness parameter is $\epsilon = 0.717$. At time $t = 0$, the slide is initially located at given submergence depth d, and two cases for two different values of d will be shown: $d = 61 \ mm$ and $d = 120 \ mm$. $x_g \equiv x_g(d)$ is the x-abscissa point where the slide has d millimeters

depth. The movement of the landslide is prescribed as

$$S(t) = S_0 \ln \left(\cosh \frac{t}{t_0} \right), \ \ S_0 = \frac{u_t^2}{a_0}, \ t_0 = \frac{u_t}{a_0},$$

where u_t, a_0 are the slide terminal velocity and initial acceleration, respectively. $u_t = 1.7$ and $a_0 = 1.2$ for the case of $d = 61 \ mm$, and $u_t = 2.03$ and $a_0 = 1.17$ for the case of $d = 120 \ mm$. After t_0 seconds the slide is stopped. To measure the free-surface perturbation, four wave gauges, $g_0, \ldots, g_3$ are located at (x, y) meters

$$g_0 = (x_g, 0), \ g_1 = (1.469, 0.350), \ g_2 = (1.929, 0), \ g_3 = (1.929, 0.5),$$

where x denotes distance from the sill water shoreline and y denotes distances off the centre-line axis of the sliding mass.

To represent the experiment, the two-dimensional domain $[-1, 10] \times [-1.8, 1.8]$ is discretized with $\Delta x = \Delta y = 0.02$. The simulated time is 4 seconds. We set $g = 9.81$. Outflow boundary conditions are used at $x = -1$, $x = 10$ and wall boundary conditions at $y = -1.8$, $y = 1.8$.
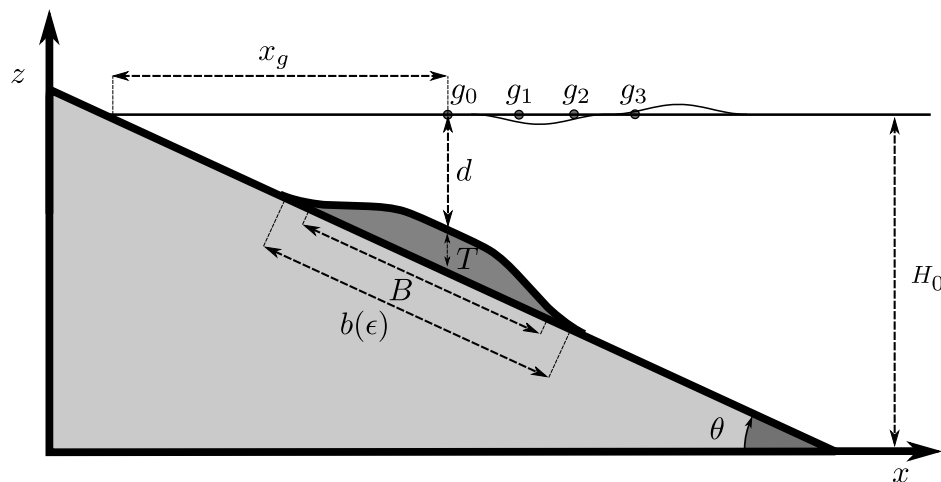
Figure 4.33: Sketch of the slide

Figure 4.35 shows the results for the first case, $d = 61 \ mm$, and Figure 4.36 the results for the second case, $d = 120 \ mm$. In this second case measured laboratory data for gauge g_2 are not available.

In this test case, the presence in the model of the term $\partial_t H$ plays an important role and is numerically computed from the displacement of the bottom H, which is prescribed in this experiment.

The one-layer systems (YAM-2D) and (NHyp-2D), fail when modelling such waves, as can be seen in Figure 4.34. Nevertheless, the two-layer model with the optimized parameters $(l_1^{(5)}, \gamma_1^{(5)}, \gamma_2^{(5)})$ represents the amplitude and frequency of generated waves correctly. As it can be seen, wave heights are highest at the gauge lying along the axis $y = 0$ and decreasing with the distance to the same. We note that the results presented in [180] showed comparable capabilities in predicting waves, using a Navier-Stokes equations written in surface and terrain using a three layer σ-coordinates.

Table 4.5 shows execution times using a GPU implementation on a GTX Titan Black for both codes. The improved two-layer non-hydrostatic code can achieve a good performance with an additional computation cost that is only between 4.55 and 5.89 times that of a SWE code. It can be stated thus that the scheme presented here is efficient and can model dispersive effects with a moderate computational cost. To our knowledge, similar models and/or numerical schemes that intend to simulate dispersive effects in such frameworks are much more expensive from the computational point of view.

The test shows the ability of the presented model to deal with dispersive water waves, that are not weakly-nonlinear weakly-dispersive, in bidimensional domains with varying bathymetries and with a moderate computational cost.

Number of Volumes	SWE	Runtime (s) Non-Hydrostatic	
		1 layer	2 layer
225×90	6.68	12.61	30.43
550×180	56.18	157.62	299.09
1100×360	225.25	557.98	1327.28

Table 4.5: Execution times in seconds for SWE and non-hydrostatic GPU implementations
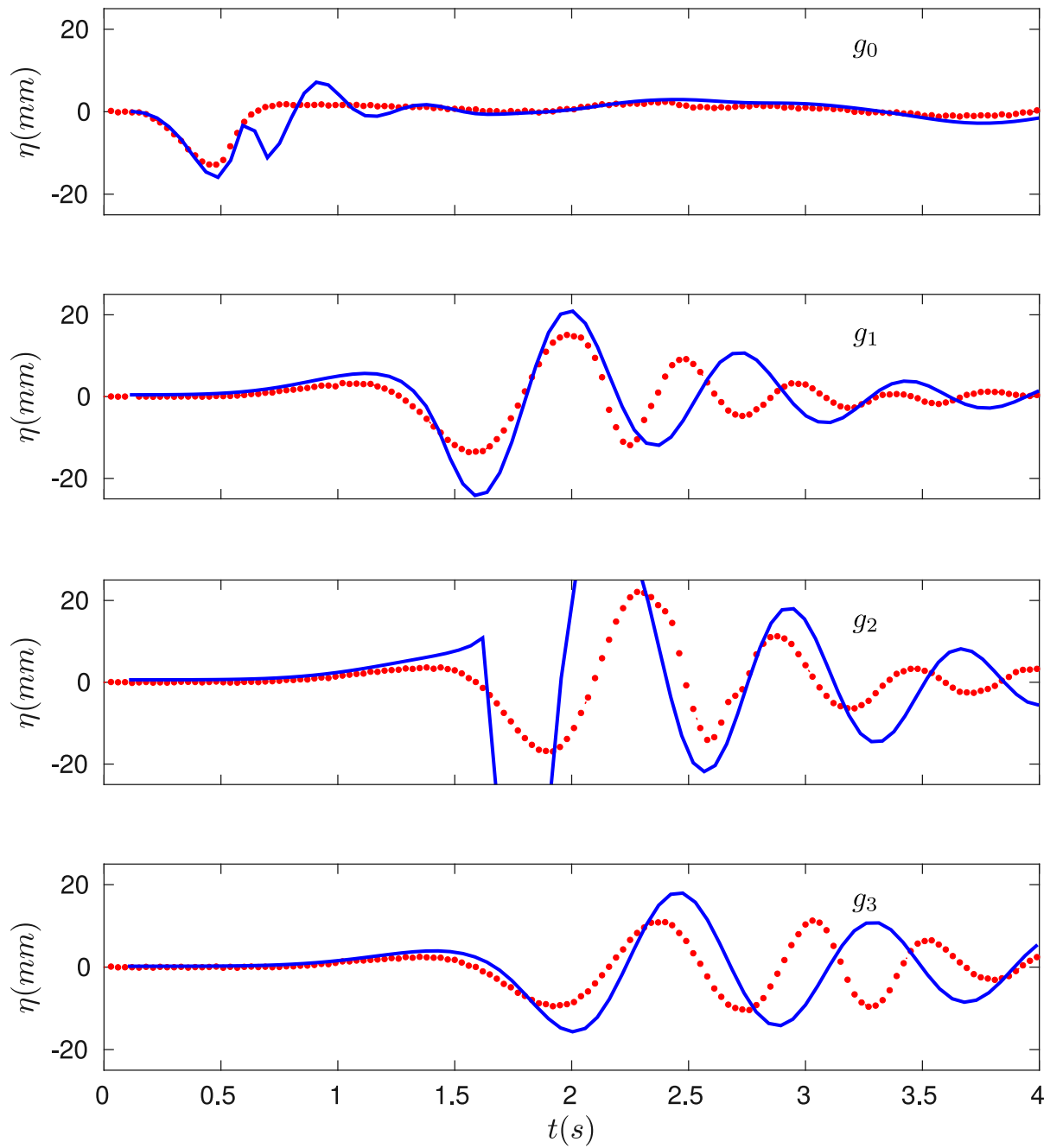
Figure 4.34: Comparison of data time series (red) and numerical (blue) with the one-layer system (YAM-2D) at wave gauges g_0, g_1, g_2, g_3 (up to the down) for the case $d = 61$ mm
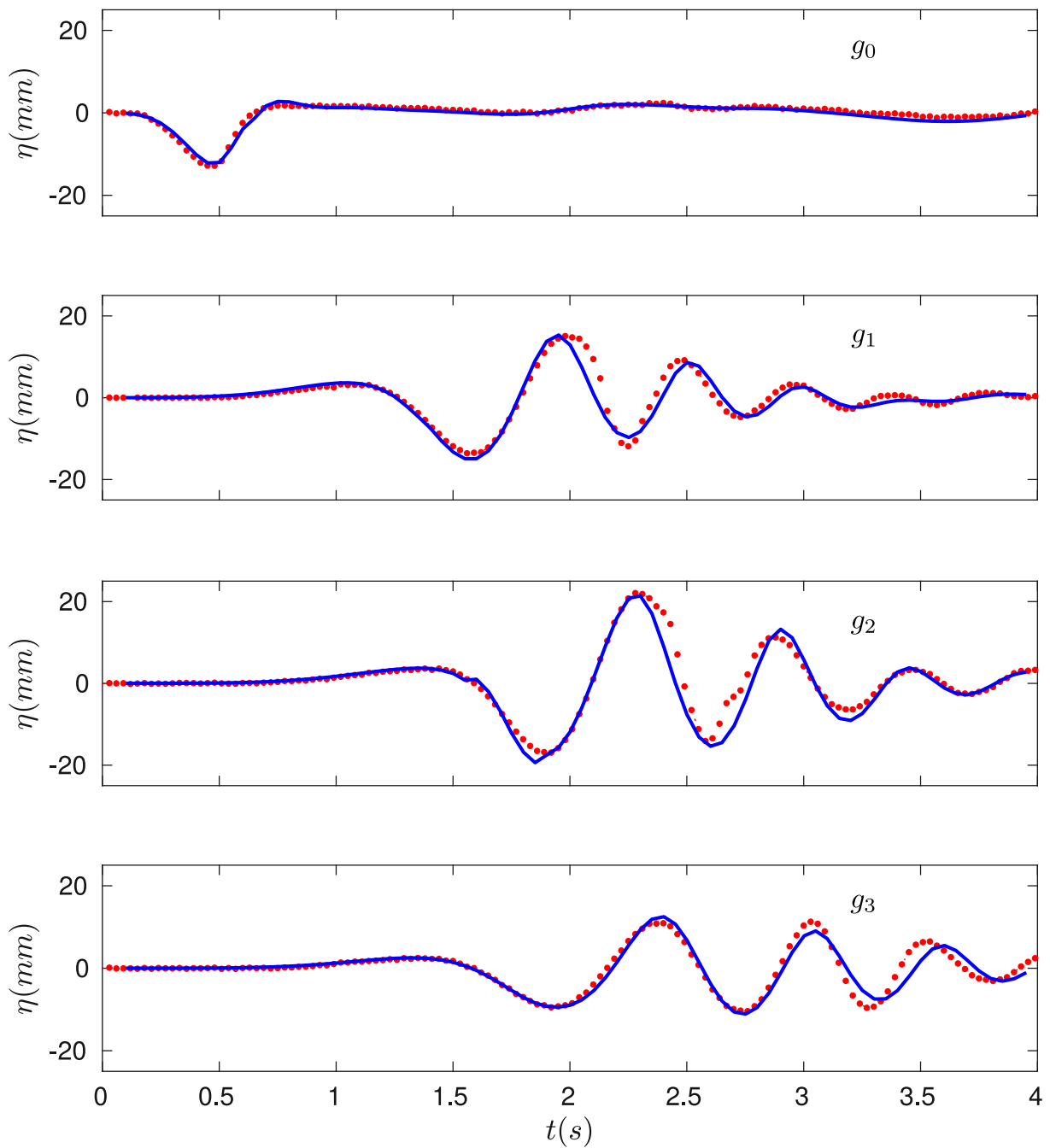
Figure 4.35: Comparison of data time series (red) and numerical (blue) with the two-layer system with the improved parameters $(l_1^{(5)}, \gamma_1^{(5)}, \gamma_2^{(5)})$ at wave gauges g_0, g_1, g_2, g_3 (up to the down) for the case $d = 61\ mm$
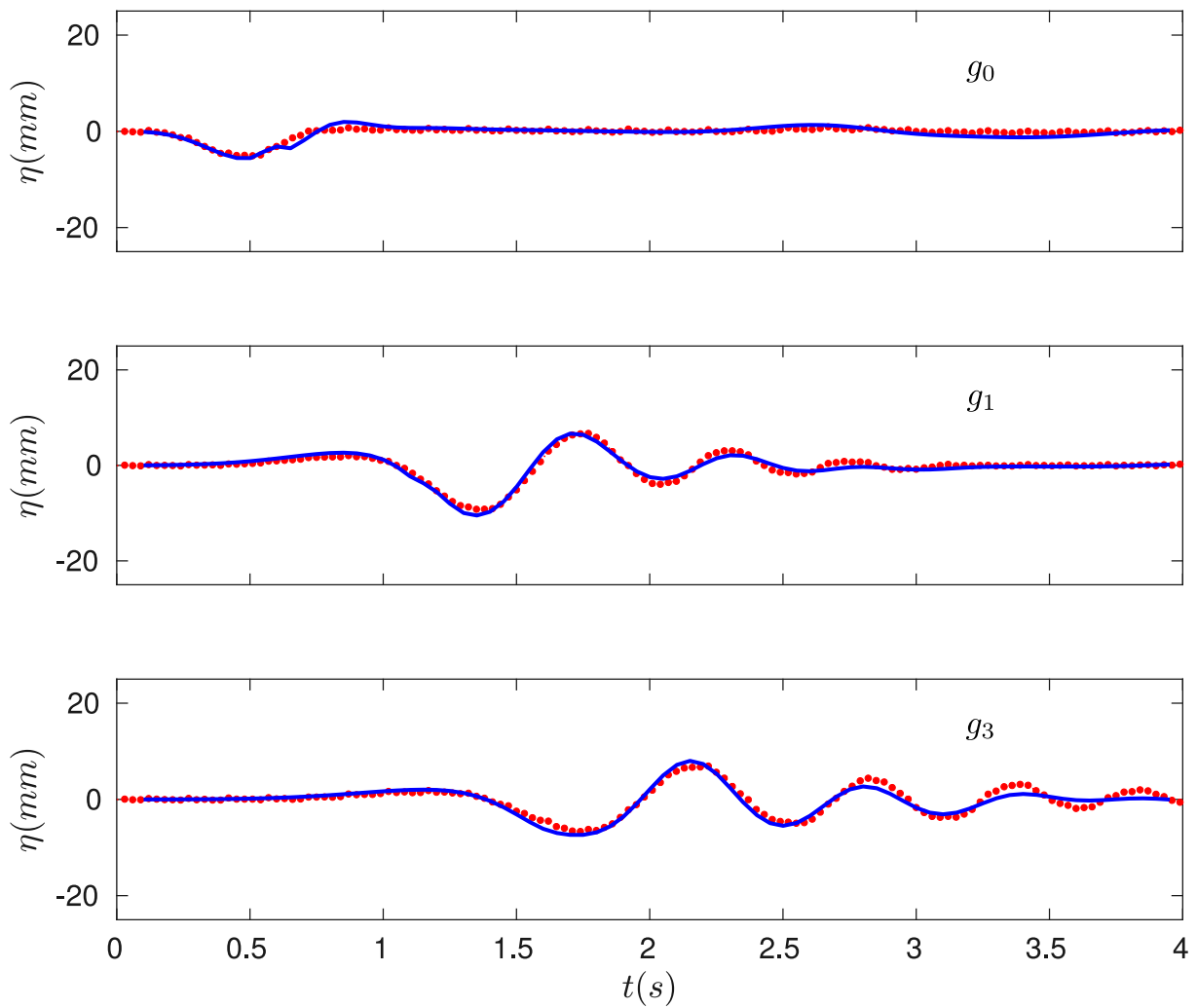
Figure 4.36: Comparison of data time series (red) and numerical (blue) with the two-layer system with the improved parameters $(l_1^{(5)}, \gamma_1^{(5)}, \gamma_2^{(5)})$ at wave gauges g_0, g_1, g_3 (up to the down) for the case $d = 120 \ mm$
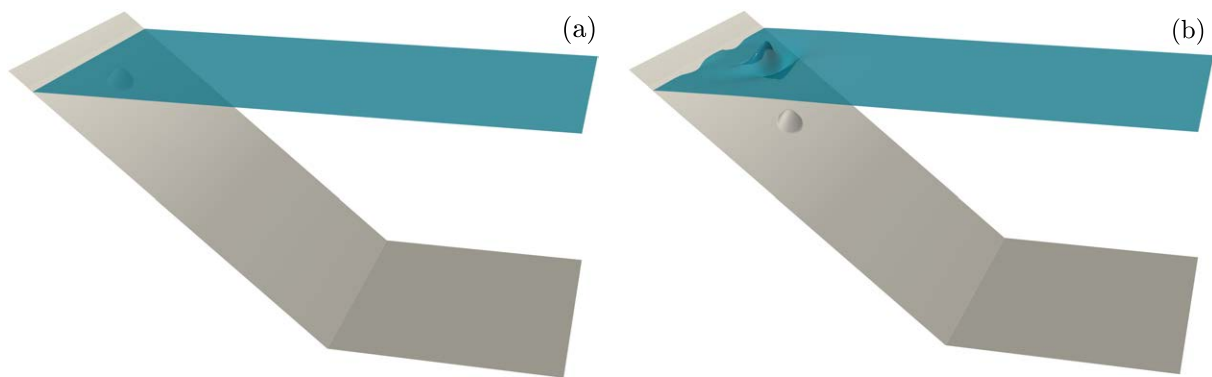
Figure 4.37: Snapshots at times (a) $t = 0$, (b) $t = 1.5$ for the case $d = 61$ mm. Free surface elevation is exaggerated 5 times.

Chapter 5

On the influence of dispersive water waves in bedload transport

Contents

In this chapter, it is presented an interesting, recent and new branch of the simulation of dispersive water waves applied to the simulation of bedload transport. In particular, we study the influence when considering non-hydrostatic or dispersive effects applied to the modelling of bedload transport processes. This chapter is based on a recent and ongoing work C. Escalante *et al.* [110]. In this work, a two-layer shallow water type model is proposed to describe bedload sediment transport for strong and weak interactions between

the fluid and the sediment. The critical point falls into the definition of the friction law between the two layers, which is a generalization of those introduced in Fernández-Nieto *et al.* [123]. This definition allows to properly apply the two-layer shallow water model for the case of intense and slow bedload sediment transport. Moreover, we prove formally that the two-layer model converges to a Saint-Venant-Exner system (SVE) including gravitational effects when the ratio between the hydrodynamic and morphodynamic time scales is small. The SVE with gravitational effects is a degenerated nonlinear parabolic system, whose numerical approximation can be very expensive from a computational point of view, see for example T. Morales de Luna *et al.* [81]. In this work, gravitational effects are introduced into the two-layer system without any parabolic term. Finally, we also consider a generalization of the model that includes a non-hydrostatic pressure correction for the fluid layer and the boundary condition at the sediment surface. Numerical simulations show that the model provides promising results and behave well in low transport rate regimes as well as in many other situations.

5.1   Introduction

Our goal is to obtain a general model for bedload sediment transport that is valid in any regime, for strong and weak interactions between the fluid and sediment.

In most models, a weak interaction between the sediment and the fluid is assumed. In this case, Saint-Venant-Exner models are usually considered (SVE in what follows, see [113]). For the case of high bedload transport rate, two-layer shallow water type model are considered instead, see for example [230], [232], [225]. In this work, we focus into the definition of a two-layer shallow water type model that can be applied in both situations.

In [123], a multi-scale analysis is performed taking into account that the velocity of the sediment layer is smaller than the one of the fluid layer. This leads to a shallow water type system for the fluid layer and a lubrication Reynolds equation for the sediment one.

For the case of uniform flows the thickness of the moving sediment layer can be predicted, because erosion and deposition rates are equal in those situations. This is a general hypothesis that is assumed when modelling weak bedload transport. The usual approach is to consider a coupled system consisting of a Shallow Water system for the hydrodynamical part combined with a morphodynamical part given by the so-called Exner equation. The whole system is known as Saint Venant Exner system [113]. Exner equation depends on the definition of the solid transport discharge. Different classical definitions can be found for the solid transport discharge, for instance the ones given by Meyer-Peter & Müller [190], Van Rijn's [218], Einstein [107], Nielsen [197], Fernández-Luque & Van Beek [175], Ashida & Michiue [5], Engelund & Fredsoe [114], Kalinske [161], Charru [60], etc. A generalization of these classical models was introduced in [123] where the morphodynamical component is deduced from a Reynolds equation and includes gravitational effects in the sediment layer. Classical models do not take into

account in general such gravitational effects because in their derivation the hypothesis of nearly horizontal sediment bed is used (see for example [165]).

In general, classical definitions for solid transport discharge can be written as follows,

$$\frac{q_b}{Q} = \text{sgn}(\tau) \, \frac{k_1}{(1 - \varphi)} \, \theta^{m_1} \, (\theta - k_2 \, \theta_c)_+^{m_2} \left(\sqrt{\theta} - k_3 \, \sqrt{\theta_c} \right)_+^{m_3}, \qquad (5.1.1)$$

where Q represents the characteristic discharge, $Q = d_s \sqrt{g(1/r - 1)d_s}$, $r = \rho_1/\rho_2$ is the density ratio, ρ_1 being the fluid density and ρ_2 the density of the sediment particles; d_s the mean diameter of the sediment particles, and φ is the averaged porosity. The coefficients k_l and m_l, $l = 1, 2, 3$, are positive constants that depend on the model. We usually find $m_2 = 0$ or $m_3 = 0$, for example, Meyer-Peter & Müller model takes $m_3 = 0$ and Ashida & Michiue's model uses $m_2 = 0$.

The Shields stress, θ, is defined as the ratio between the agitating and the stabilizing forces, $\theta = |\tau| d_s^2 / (g(\rho_2 - \rho_1) d_s^3)$, τ being the shear stress at the bottom. For example, for Manning's law, we have $\tau = \rho_1 g h_1 n^2 u_1 |u_1| / h_1^{4/3}$. Where h_1 and u_1 are the thickness and the velocity of the fluid layer, respectively, and n is the Manning coefficient.

Finally, θ_c is the critical Shields stress. The positive part, $(\cdot)_+$, in the definition implies that the solid transport discharge is null if $\theta \leq k\theta_c$ (with $k = k_2$ when $m_2 > 0$ and $k = \sqrt{k_3}$ when $m_3 > 0$). If the velocity of the fluid is zero, $u_1 = 0$, we have $\theta = 0 < k\theta_c$, and for any model that can be written under the structure (5.1.1) we obtain that $q_b = 0$, which means that there is no movement of the sediment layer. This is even true when the sediment layer interface is not horizontal which is a consequence of the fact that classical models do not take into account gravitational effects.

In order to introduce gravitational effects in classical models, Fowler *et al.* proposed in [126] a modification of the Meyer-Peter & Müller formula that consists in replacing θ by θ_{eff}, where:

$$\theta_{\text{eff}} = |\text{sgn}(u_1)\theta - \vartheta \partial_x (h_2 - H)|, \qquad (5.1.2)$$

with

$$\vartheta = \frac{\theta_c}{\tan \delta}, \qquad (5.1.3)$$

δ being the angle of repose of the sediment particles. The sediment surface is defined by $z = h_2 - H$, where h_2 is the thickness of the sediment layer and b the topography function or bedrock layer. Then, θ_{eff} is defined in terms of the gradient of sediment surface. This is a definition that can be also considered for 2D simulations, because in this case θ_{eff} is defined as the norm of the vector $\theta u_1 / \|u_1\| - \vartheta \partial_x (h_2 - H)$. Other alternatives have been proposed in the literature, namely consisting in the replacement of θ_c by a modified value $\widehat{\theta}_c$ depending on the angle α of the slope.

More explicitly, it is usually assumed that $(\theta_{\text{eff}} - \theta_c)_+ = (\theta - \widehat{\theta}_c)_+$. Nevertheless, remark that this is not true in general due to the absolute value (or the norm of the vectorial case) appearing in the definition of θ. Both approximations are equivalent in particular for the case of $u_1 > 0$ and $\partial_x b = -\tan \alpha < 0$ (see [123]).

In particular, in [175], it was proposed to modify the critical Shields parameter by

$$\widehat{\theta}_c = \theta_c \left(1 - \frac{\tan \alpha}{\tan \delta}\right), \tag{5.1.4}$$

where the gravitational effects are taken into account based on the angle of the slope α.

It is important to notice that in many situations it is assumed that the sediment transport follows the same direction as the flow. This is not always true as the sediment transport in rivers can deviate its direction from the depth-averaged flow direction due to the transverse slopping bed for instance (see [193]).

Moreover, the definition of $\widehat{\theta}_c$ for arbitrarily sloping bed for 2D problems is not an easy task (see [128], [129]).

As we mentioned previously, in [123] a SVE model is deduced from a multiscale analysis.

The model includes gravitational effects and the authors deduce that it can also be seen as a modification of classical models: θ is replaced by the proposed values $\theta_{\mathrm{eff}}^{(L)}$ or $\theta_{\mathrm{eff}}^{(Q)}$, depending on whether the friction law between the fluid and the sediment is linear or quadratic. In the case when h_m is of order of d_s/ϑ, for a linear friction law, the definition of the effective shear stress proposed in [123] can be written as follows:

$$\theta_{\mathrm{eff}}^{(L)} = \left| \mathrm{sgn}(u_1)\theta - \vartheta \partial_x (h_2 - H) - \vartheta \frac{\rho_1}{\rho_2 - \rho_1} \partial_x (h_1 + h_2 - H) \right|. \tag{5.1.5}$$

Let us remark that if the water free surface is horizontal, the definition of $\theta_{\mathrm{eff}}^{(L)}$ coincides with θ_{eff} (5.1.2), proposed by Fowler *et al.* in [126]. Otherwise, the main difference is that this definition for the effective shear stress takes into account not only the gradient of the sediment surface but also the gradient of the water free surface.

For the case of a quadratic friction law, although the definition is a combination of the same components, it is rather different. In this case we can write the effective Shields parameter proposed in [123] as follows:

$$\theta_{\mathrm{eff}}^{(Q)} = \left| \mathrm{sgn}(u_1)\sqrt{\theta} - \sqrt{\frac{\vartheta \rho_1}{\rho_2 - \rho_1} |\partial_x (\frac{\rho_1}{\rho_2} h_1 + h_2 - H)|} \; \mathrm{sgn}\left(\partial_x (\frac{\rho_1}{\rho_2} h_1 + h_2 - H)\right) \right|^2. \tag{5.1.6}$$

In the case of submerged bedload sediment transport, the drag term is defined by a quadratic friction law. Thus, we should consider an effective Shields stress given by $\theta_{\mathrm{eff}}^{(Q)}$. Nevertheless, in the bibliography it is θ_{eff} (5.1.2) which is usually considered, regardless the fact that θ_{eff} is an approximation of $\theta_{\mathrm{eff}}^{(L)}$ which is deduced from a linear friction law.

Although the quantities involved in the definitions of the effective Shields parameter associated to linear or quadratic friction are the same, their values may be very different.

They verify

$$|\theta_{\text{eff}}^{(L)} - \theta_{\text{eff}}^{(Q)}| = \mathcal{O}\left(|\partial_x(\frac{\rho_1}{\rho_2}h_1 + h_2 - H)|\left(\sqrt{\theta} - \sqrt{\frac{\vartheta\rho_1}{\rho_2 - \rho_1}|\partial_x(\frac{\rho_1}{\rho_2}h_1 + h_2 - H)|}\right)\right).$$

For instance, if we consider an initial condition with water at rest and a high gradient in the sediment surface, the difference between $\theta_{\text{eff}}^{(L)}$ and $\theta_{\text{eff}}^{(Q)}$ is of order of the gradient of the sediment surface. Thus, in the framework of SVE model, the definition $\theta_{\text{eff}}^{(Q)}$ should be considered in order to be consistent with the quadratic friction law usually considered for the drag force between the fluid and the sediment.

In any case, considering the definitions θ_{eff} (5.1.2), $\theta_{\text{eff}}^{(L)}$ (5.1.5), or $\theta_{\text{eff}}^{(Q)}$ (5.1.6), means that the corresponding SVE system with gravitational effects is a parabolic degenerated partial differential system with non linear diffusion. Moreover, the system cannot be written as combination of a hyperbolic part plus a diffusion term.

Let us remark that in the literature a linearized version can be found, where gravitational effects are included by considering a classical SVE model with an additional viscous term, see for example [235], [191] and references therein. The drawback of this approach is that the diffusive term should not be present in stationary situations, for instance when the velocity is not high enough and sediment slopes are under the one given by the repose angle. In such situations, it is necessary to include some external criterion that controls whether the diffusion term is applied or not. This is not the case in definitions (5.1.5) or (5.1.6) where the effective Shields stress is automatically limited by the effect of the Coulomb friction angle.

In this work, we propose a two-layer shallow water model for bedload transport. The model converges to a generalization of SVE model with gravitational effects for low transport regimes while being valid for higher transport regimes as well. Moreover, it has the advantage that the inclusion of gravitational effects does not imply to approximate any non-linear parabolic degenerated term, as for the case of SVE model with gravitational effects.

An additional advantage of the model introduced here is that it will take into account dispersive effects. When modelling and simulating geophysical shallow flows, the nonlinear shallow water equations are often a good choice as an approximation of the Navier-Stokes equations. Nevertheless, they are derived by assuming hydrostatic pressure and they do not take into account non-hydrostatic effects or dispersive waves. In coastal areas, close to the continental shelf, non-hydrostatic effects or equivalently, dispersive waves may become significant.

In recent years, an effort has been done in the derivation of relatively simple mathematical models for shallow water flows that include long nonlinear water waves. See for instance the works in [21], [184], [210], [259] among others. The hypothesis is that this dispersive effects will have an important impact on the sediment layer.

Following this idea, in this work, we will consider a non-hydrostatic pressure for the fluid layer. The non-hydrostatic pressure influences the sediment evolution in two ways.

First, the non-hydrostatic pressure acts on the sediment layer as a boundary condition on the interface between the fluid and the sediment. Second, it modifies the profile obtained of the water free-surface and the water velocity which will be reflected on the sediment pattern (see [250]). The model proposed in this work takes into account both influences.

The Chapter is organized as follows: We propose the new two-layer Shallow Water model for bedload transport in Section 5.2. Section 5.3 is devoted to showing the properties of the model: energy balance; the formal convergence to the SVE model; a simplified system in typical regimes; and hyperbolicity. In Section 5.4 we present the generalization of the proposed model by including non-hydrostatic pressure in the fluid layer and its influence on the sediment layer as a modification of the gradient pressure at the interface. A numerical method to approximate this model is described in Section 5.5. Finally, three numerical tests are shown in Section 5.6.

5.2   Proposed model

We consider a domain with two immiscible layers corresponding to water (upper layer) and sediment (lower layer). The sediment layer is in turn decomposed into a moving layer of thickness h_m and a sediment layer that does not move of thickness h_f, adjacent to the fixed bottom. These thicknesses are not fixed because there is an exchange of sediment material between the layers. Particles are eroded from the lower sediment layer and come into motion in the upper sediment layer. Conversely, particles from the upper layer are deposited into the lower sediment layer and stop moving.

We propose a one space dimension shallow water model that may be obtained by averaging on the vertical direction the Navier-Stokes equations and taking into account suitable boundary conditions. In particular, at the free surface we impose kinematic boundary conditions and vanishing pressure; at the bottom, a Coulomb friction law is considered. The friction between water and sediment is introduced through the term F at the water/sediment interface and T denotes the mass transference term in the internal sediment interface. The general notation for the water layer corresponds to the subindex 1 and for the sediment layer to the subindex 2. Thus, the water of layer has a thickness h_1 and moves with horizontal velocity u_1. The thickness of the total sediment layer is denoted by $h_2 = h_f + h_m$, and the moving sediment layer h_m flows with velocity u_m. $-H$ denotes the fixed bottom. See Figure 5.1 for a sketch of the domain.

Note that the velocity of the sediment layer is defined as $u_2 = u_m$ in the moving layer and $u_2 = 0$ in the static layer. We assume first a hydrostatic pressure regime.
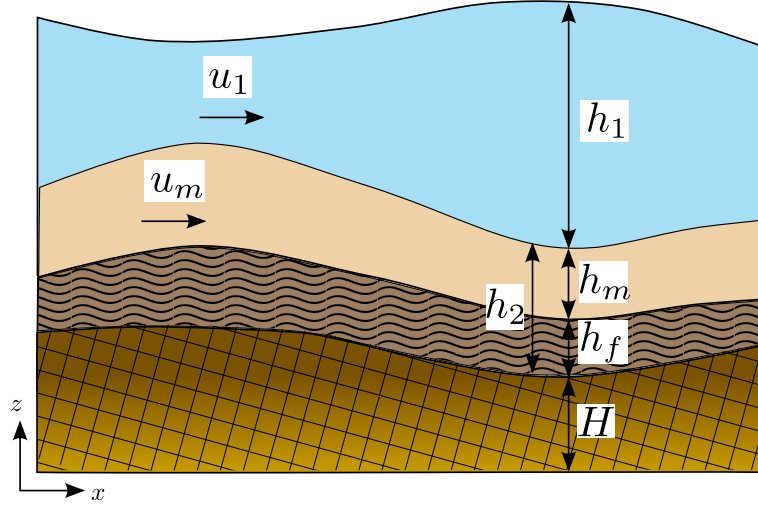
Figure 5.1: Sketch of the domain for the fluid-sediment problem

Then we propose the following two-layer shallow water model:

$$\partial_t h_1 + \partial_x (h_1 u_1) = 0, \tag{5.2.1a}$$

$$\partial_t (h_1 u_1) + \partial_x (h_1 u_1^2) + g h_1 \partial_x (h_1 + h_2 - H) = -F, \tag{5.2.1b}$$

$$\partial_t h_2 + \partial_x (h_m u_m) = 0, \tag{5.2.1c}$$

$$\partial_t (h_m u_m) + \partial_x (h_m u_m^2) + g h_m \partial_x (r h_1 + h_2 - H) = rF + \tag{5.2.1d}$$
$$+ \frac{1}{2} u_m T - (1 - r) g h_m \mathrm{sgn}(u_m) \tan \delta,$$

$$\partial_t h_f = -T, \tag{5.2.1e}$$

where $r = \rho_1/\rho_2$ is the ratio between the densities of the water, ρ_1, and the sediment particles, ρ_2. δ is the internal Coulomb friction angle. In the next lines we give the closures for the friction term F and the mass transference T.

Following [123] we consider two types of friction laws: linear and quadratic. The friction term for the linear friction law is defined as

$$F_L = C_L (u_1 - u_m) \quad \text{with} \quad C_L = g \left(\frac{1}{r} - 1 \right) \frac{h_1 h_m}{\vartheta (h_1 + h_m) \sqrt{(\frac{1}{r} - 1) g d_s}} \tag{5.2.2}$$

and for the quadratic friction law,

$$F_Q = C_Q(u_1 - u_m)|u_1 - u_m| \quad \text{with} \quad C_Q = \frac{1}{\beta} \frac{h_1 h_m}{\vartheta(h_1 + h_m)}, \tag{5.2.3}$$

d_s being the mean diameter of the sediment particles. ϑ is defined by equation (5.1.3). This definition of ϑ verifies the analysis of Seminara *et al.* [129], who concluded that the drag coefficient is proportional to $\tan(\delta)/\theta_c$.

Remark that the calibration coefficient β has units of length so that C_Q is non-dimensional. In [123], $\beta = d_s$ was assumed for the bedload in low transport situations. In our case, given that we deal with a complete bilayer system for any regime, this value is not always valid. In bedload framework, we can establish from experimental observations that the region of particles moving at this level is at most 10-20 particle-diameter in height [58].

So we may assume that the thickness of the bed load layer is $h_m = k\, d_s$ with $k \in [0, k_{\max}]$ ($k_{\max} = 10$ or 20). So that, when $h_m \leq k_{\max}d_s$ we are in a bedload low rate regime and it makes sense to consider the friction coefficient as in [123], that is, of the order of d_s. Conversely, when $h_m > k_{\max}d_s$ we are in an intense bedload regime and then we must turn to a more appropriate friction coefficient. Thus, to be consistent with our previous work, we propose to take:

$$\beta = \begin{cases} h_m & \text{if } h_m > k_{\max}d_s \\ d_s & \text{if } h_m \leq k_{\max}d_s \end{cases}$$

Another possibility for the second case would be to define $\beta = k_{\max}d_s$ when $h_m \leq k_{\max}d_s$. The coefficient $k_{\max}$ can be then considered as a calibration constant for the friction law.

The mass transference between the moving and the static sediment layers T is defined in terms of the difference between the erosion rate, $\dot{z}_e$, and the deposition rate $\dot{z}_d$. There exists in the literature different forms to close the definition of the erosion and deposition rates (see for example [60]). We consider in this work the following definitions (see [122]):

$$T = \dot{z}_e - \dot{z}_d \quad \text{with} \quad \dot{z}_e = K_e(\theta_e - \theta_c)_+ \frac{\sqrt{g(1/r - 1)d_s}}{1 - \varphi}, \quad \dot{z}_d = K_d h_m \frac{\sqrt{g(1/r - 1)d_s}}{d_s}.$$

The coefficients K_e and K_d are erosion and deposition constants, respectively, φ is the porosity. For the case of nearly flat sediment bed, $\theta_e = \theta$ is usually set. This corresponds to the Bagnold's relation (see [8]). Nevertheless, in order to take into account the gradient of the sediment bed θ_e must be defined in terms of the effective Shields stress (see [123]). Then we define θ_e in terms of the friction law between the fluid and the sediment layers:

$$\theta_e = \begin{cases} \theta_{\text{eff}}^{(L)}, \text{defined in equation (5.1.5), for a linear friction law,} \\ \\ \theta_{\text{eff}}^{(Q)}, \text{defined in equation (5.1.6), for a quadratic friction law.} \end{cases}$$

The system (5.2.1) can be written in the compact form

$$\partial_t U + \partial_x F(U) + B(U)\partial_x U = G(U)\partial_x \widetilde{H} + S(U), \tag{5.2.4}$$

defining

$$U = \begin{pmatrix} h_1 \\ h_1 u_1 \\ h_m \\ h_m u_m \\ h_f \end{pmatrix}, \quad F(U) = \begin{pmatrix} h_1 u_1 \\ h_1 u_1^2 + \frac{1}{2}gh_1^2 \\ h_m u_m \\ h_m u_m^2 + \frac{1}{2}gh_m^2 \\ 0 \end{pmatrix}, \quad B(U) = \begin{pmatrix} 0 & 0 & 0 & 0 & 0 \\ 0 & 0 & gh_1 & 0 & 0 \\ 0 & 0 & 0 & 0 & 0 \\ rgh_m & 0 & 0 & 0 & 0 \\ 0 & 0 & 0 & 0 & 0 \end{pmatrix},$$

$$G(U) = \begin{pmatrix} 0 \\ gh_1 \\ 0 \\ gh_m \\ 0 \end{pmatrix}, \quad \widetilde{H} = h_f - H, \quad S(U) = \begin{pmatrix} 0 \\ -F \\ T \\ rF + \frac{1}{2}u_m T - (1-r)gh_m\mathrm{sgn}(u_m)\tan\delta \\ -T \end{pmatrix}.$$

5.3 Properties of the model

In this section the energy balance, the convergence of the proposed model to SVE system and several possible simplifications are presented. Some comments on the hyperbolicity of the model are also given.

5.3.1 Energy balance

The proposed model has an exact dissipative energy balance, which is an easy consequence of two-layer shallow water systems, opposed to classical SVE models which have not, and we obtain the following result.

The system (5.2.4) admits a dissipative energy balance that reads:

$$\partial_t \left(rh_1 \frac{|u_1|^2}{2} + h_m \frac{|u_m|^2}{2} + \frac{1}{2}g(rh_1^2 + h_2^2) + g\,rh_1h_2 - g(rh_1 + h_2)H \right)$$

$$+\partial_x \left(rh_1 u_1 \frac{|u_1|^2}{2} + h_m u_m \frac{|u_m|^2}{2} + g\,rh_1 u_1(h_1 + h_2 - H) + gh_m u_m(rh_1 + h_2 - H) \right)$$

$$\leq -r(u_1 - u_m)F - (1-r)gh_m|u_m|\tan\delta,$$

where the friction term F is given by (5.2.2) or (5.2.3).

The proof of the previous result is straightforward and for the sake of brevity we omit it. Notice that classical SVE model does not verify in general a dissipative energy balance. In [123] a modification of a classical SVE models and a generalization, by including gravitational effects, has been proposed that allows to verify a dissipative energy balance. In the following subsection we see that the proposed two-layer model converges to the SVE model proposed in [123].

5.3.2 Convergence to the classical SVE system for large morphodynamic time scale

In this subsection we show formally the convergence of system (5.2.4) to the Saint-Venant-Exner model presented in [123]. This model is obtained from an asymptotic approximation of the Navier-Stokes equations. In particular, it has the following advantages: it preserves the mass conservation, the velocity (and hence, the discharge) of the bedload layer is explicitly deduced, and it has a dissipative energy balance.

The model introduced in [123] reads as follows:

$$\begin{cases} d\partial_t h_1 + \partial_x(h_1 u_1) = 0, \\[2mm] d\partial_t(h_1 u_1) + \partial_x(h_1 u_1^2) + gh_1\partial_x(b + h_2 + h_1) = -\frac{gh_m}{r}\mathcal{P}, \\[2mm] d\partial_t h_2 + \partial_x\left(h_m\, v_b\, \sqrt{(1/r - 1)gd_s} \right) = 0, \\[2mm] \partial_t h_f = -T. \end{cases} \tag{5.3.1}$$

with

$$\mathcal{P} = \partial_x(rh_1 + h_2 - H) + (1-r)\mathrm{sgn}(u_2)\tan\delta. \tag{5.3.2}$$

The definition of the non-dimensional sediment velocity v_b depends on the friction law. When a linear friction law is considered, it reads:

$$v_b^{(LF)} = \frac{u_1}{\sqrt{(1/r - 1)gd_s}} - \frac{\vartheta}{1-r}\mathcal{P}, \tag{5.3.3}$$

where

$$\text{sgn}(u_2) = \text{sgn}\left(\frac{u_1}{\sqrt{(1/r - 1)gd_s}} - \frac{\vartheta}{1 - r}\partial_x(rh_1 + h_2 + b)\right).$$

For a quadratic friction law:

$$v_b^{(QF)} = \frac{u_1}{\sqrt{(1/r - 1)gd_s}} - \left(\frac{\vartheta}{1 - r}\right)^{1/2}|\mathcal{P}|^{1/2}\text{sgn}(\mathcal{P}), \tag{5.3.4}$$

where $\text{sgn}(u_2) = \text{sgn}(\Psi)$ and

$$\Psi = \frac{u_1}{\sqrt{(1/r - 1)gd_s}} - \left|\frac{\vartheta}{1 - r}\partial_x(rh_1 + h_2 + b)\right|^{1/2}\text{sgn}\left(\frac{\vartheta}{1 - r}\partial_x(rh_1 + h_2 + b)\right).$$

The convergence is obtained when we assume the adequate asymptotic regime in terms of the time scales. As it is well known, for the weak bedload transport problem, the morphodynamic time is much larger than the hydrodynamic time, which makes the pressure effects much more important than the convective ones. As a consequence, the behavior of the sediment layer is just defined by the solid mass equation (Exner equation), omitting a momentum equation. This large morphodynamic time turns into an assumption of a smaller velocity for the lower layer. In order to fall into the low bedload transport regime we must also assume that the thickness of the bottom layer is smaller, because it represents the layer of moving sediment. Thus, we suppose:

$$u_m = \varepsilon_u\tilde{u}_m; \quad h_m = \varepsilon_h\tilde{h}_m; \quad T = \varepsilon_u\tilde{T}. \tag{5.3.5}$$

Now we take these values into the momentum conservation equation for the lower layer in (5.2.4):

$$d\partial_t(\varepsilon_h\varepsilon_u\tilde{h}_m\tilde{u}_m) + \partial_x(\varepsilon_h\varepsilon_u^2\tilde{h}_m\tilde{u}_m^2) + g\varepsilon_h\tilde{h}_m\partial_x(rh_1 + h_2 - H)$$
$$d = r\tilde{F} + \varepsilon_u^2\tfrac{1}{2}\tilde{u}_m\tilde{T} - (1 - r)g\varepsilon_h\tilde{h}_m\text{sgn}(\tilde{u}_m)\tan\delta$$

Then, if we neglect second order terms, we get

$$g\varepsilon_h\tilde{h}_m\partial_x(rh_1 + h_2 - H) = r\tilde{F} - (1 - r)g\varepsilon_h\tilde{h}_m\text{sgn}(\tilde{u}_m)\tan\delta.$$

In dimension variables, this equation reads:

$$rF = gh_m\partial_x(rh_1 + h_2 - H) + (1 - r)gh_m\text{sgn}(u_m)\tan\delta = gh_m\mathcal{P},$$

where the last equality follows from the definition of $\mathcal{P}$. Thus the expression of the friction term is

$$rF = gh_m\mathcal{P}; \tag{5.3.6}$$

which coincides with the friction term in the momentum equation of layer 1, r.h.s. of (5.3.1).

Now, from this equation and using the expressions of F, for linear (5.2.2) and quadratic (5.2.3) laws, we have to compute the value of u_m to check that it fits with (5.3.3) and (5.3.4) respectively.

○ Linear friction law:

$$
\begin{aligned}
\tilde{F} &= g\Big(\frac{1}{r} - 1\Big)\frac{\varepsilon_h h_1 \tilde{h}_m}{\vartheta(h_1 + \varepsilon_h \tilde{h}_m)\sqrt{(\frac{1}{r}-1)g d_s}}(u_1 - \varepsilon_u \tilde{u}_m) \\
&= g\Big(\frac{1}{r} - 1\Big)\frac{1}{\vartheta\sqrt{(\frac{1}{r}-1)g d_s}}\frac{\varepsilon_h \tilde{h}_m}{1 + \varepsilon_h \frac{\tilde{h}_m}{h_1}}(u_1 - \varepsilon_u \tilde{u}_m) \\
&= g\Big(\frac{1}{r} - 1\Big)\frac{\varepsilon_h \tilde{h}_m}{\vartheta\sqrt{(\frac{1}{r}-1)g d_s}}(u_1 - \varepsilon_u \tilde{u}_m) + \mathcal{O}(\varepsilon_h^2) \qquad (5.3.7)
\end{aligned}
$$

where in the last equality we have used that $d\frac{1}{1+\varepsilon_h \frac{\tilde{h}_m}{h_1}} = 1 - \varepsilon_h \frac{\tilde{h}_m}{h_1} + \mathcal{O}(\varepsilon_h^2)$.

So turning to the dimension variables and neglecting second order terms, the equation (5.3.6) reads:

$$
rg\Big(\frac{1}{r} - 1\Big)\frac{h_m}{\vartheta\sqrt{(\frac{1}{r}-1)g d_s}}(u_1 - u_m) = g h_m \mathcal{P}.
$$

From where we directly obtain that $u_m = v_b^{(LF)}\sqrt{(\frac{1}{r}-1)g d_s}$.

○ Quadratic friction law:

Note that in this case β reduces to d_s and then

$$
\begin{aligned}
\tilde{F} &= \frac{\varepsilon_h h_1 \tilde{h}_m}{\vartheta d_s(h_1 + \varepsilon_h \tilde{h}_m)}(u_1 - \varepsilon_u \tilde{u}_m)|u_1 - \varepsilon_u \tilde{u}_m| \\
&= \frac{\varepsilon_h \tilde{h}_m}{\vartheta d_s}(u_1 - \varepsilon_u \tilde{u}_m)|u_1 - \varepsilon_u \tilde{u}_m| + \mathcal{O}(\varepsilon_h^2). \qquad (5.3.8)
\end{aligned}
$$

Following the same reasoning as above, the equation (5.3.6) reads:

$$
r\frac{h_m}{\vartheta d_s}(u_1 - u_m)|u_1 - u_m| = g h_m \mathcal{P}.
$$

From where we obtain that

$$
r\frac{1}{\vartheta d_s}(u_1 - u_m)^2 = g\,\mathcal{P}\,\mathrm{sgn}(\mathcal{P}) \quad \text{and then} \quad u_m = v_b^{(QF)}\sqrt{\Big(\frac{1}{r}-1\Big)g d_s}.
$$

5.3.3   Simplifications in typical regimes

In this subsection we consider two possible simplifications of the proposed model:

i) Nearly constant water free surface ($h_2 + h_1 - H = \text{cst}$).

ii) Uniform flows where the water thickness h_1 and the sediment layer h_2 are nearly constant.

Remark that both cases imply the following condition,

$$\gamma h_2 + h_1 - H = \text{cst}, \quad \gamma = 0, 1. \tag{5.3.9}$$

For a constant free surface we set $\gamma = 1$ and for the case of a uniform flow we set $\gamma = 0$. Using this hypothesis we can simplify the momentum equation of the sediment layer. Then, the model is described by system (5.2.4) replacing equation (5.2.1d) by

$$\partial_t(h_m u_m) + \partial_x(h_m u_m^2) + g h_m \partial_x((r\gamma - 1)H + (1 - r)h_2)$$
$$= rF + \frac{1}{2}u_m T - (1 - r)g h_m \text{sgn}(u_m)\tan\delta \tag{5.3.10}$$

By another way, it is related to the simplifications considered in the deduction of classical SVE models.

For case i), following the same arguments as in previous subsection and using this momentum equation, we obtain that the model converges formally to a SVE model where the effective Shields parameter coincides, for the case of a linear friction law, with (5.1.2). Then, for the case of a constant bed slope $\partial_x H = \tan\alpha$, with $u_1 > 0$ and $\tan\alpha > 0$ we obtain

$$\theta_{\text{eff}}^{(L)} - \theta_c = \theta - \theta_c\left(1 - \frac{\tan\alpha - \partial_x h_2}{\tan\delta}\right).$$

Notice that for the case where the height of sediment layer is constant this coincides with the modification proposed in [175] (see equation (5.1.4)).

For case ii), we obtain from (5.1.5)

$$\theta_{\text{eff}}^{(L)} = \left|\text{sgn}(u_1)\theta + \vartheta\frac{\partial_x H}{1 - r}\right|.$$

Notice that, for a constant bed slope $\partial_x H = \tan\alpha$, with $u_1 > 0$ and $\tan\alpha > 0$, then we get

$$\theta_{\text{eff}}^{(L)} - \theta_c = \theta - \theta_c\left(1 - \frac{\tan\alpha}{\tan\delta}\frac{1}{1 - r}\right).$$

This implies a modification of (5.1.4) that takes into account the influence of density ratio in gravitational effects (see [187]).

We conclude that the model proposed in this Chapter can be seen as a generalization that recovers these particular cases and agrees with existing studies concerning bedload transport.

5.3.4 Hyperbolicity of the model

The eigenvalues of the system are the roots of the following characteristic polynomial,

$$P(\lambda) = \lambda \bigg((\lambda^2 - 2u_1\lambda + u_1^2 - gh_1)(\lambda^2 - 2u_m\lambda + u_m^2 - gh_2) - g^2 h_1 h_2 r \bigg).$$

In general we cannot state that the model is always hyperbolic. However, we have not found complex eigenvalues in any of the performed numerical tests.

Nevertheless, considering the simplified model described in previous subsection, defined by equations (5.2.1a)-(5.2.1b)-(5.2.1c)-(5.3.10)-(5.2.1e), we get that the system is always hyperbolic. Indeed, in such case the eigenvalues of the system are

$$u_1 \pm \sqrt{gh_1}, \quad 0, \quad u_m \pm \sqrt{gh_m(1-r)}.$$

5.4 Non-hydrostatic pressure model

The hydrostatic hypothesis may be inaccurate and fails when non-hydrostatic pressure can affect the mobility of sediment and hence the bedload transport. We present in this section the two-layer shallow water model described in (5.2.4) with a correction in the total pressure applying a similar approach to the one proposed by Yamazaki *et al.* in [259], where the non-hydrostatic effects are taken into account for the SWE.

The challenge is thus to improve nonlinear dispersive properties of the model by including information on the vertical structure of the flow while designing fast and efficient algorithms for its simulation. First, we resume the development introduced by Yamazaki *et al.* in [259] to later apply it to our system. The idea is that in the depth averaging process, the vertical velocity average is not neglected and the total pressure is decomposed into a sum of hydrostatic and non-hydrostatic components.

Besides, during the process of depth averaging, vertical velocity is assumed to have a linear vertical profile as well as the non-hydrostatic pressure. Moreover, in the vertical momentum equation, the vertical advective and dissipative terms, which are small compared with their horizontal counterparts, are neglected. At the free surface, we assume that the non-hydrostatic pressure vanishes as a boundary condition.

Now, using a similar procedure as in [259], the proposed model with non-hydrostatic effects reads:

- Water layer:

$$
\begin{cases}
\partial_t h_1 + \partial_x(h_1 u_1) = 0, \\[2mm]
\partial_t(h_1 u_1) + \partial_x(h_1 u_1^2 + h_1 \widetilde{p}_{1_{h_2+h_1/2-H}}) \\[2mm]
\qquad\qquad\qquad + g h_1 \partial_x(b + h_1 + h_2) = -\widetilde{p}_{1_{h_2-H}} \partial_x(h_2 - H) - F, \\[2mm]
\partial_t w = \dfrac{\widetilde{p}_{1_{h_2-H}}}{h}, \\[2mm]
\partial_x u_1 + \dfrac{w_1 - w_{1_{h_2-H}}^+}{h_1/2} = 0.
\end{cases}
\tag{5.4.1}
$$

The sediment layer will also be affected by the non-hydrostatic terms. This influence comes from the boundary condition at the interface. Therefore we obtain:

- Sediment layer:

$$
\begin{cases}
\partial_t h_2 + \partial_x(h_m u_m) = 0, \\[2mm]
\partial_t(h_m u_m) + \partial_x(h_m u_m \otimes u_m) + g h_m \partial_x(r h_1 + h_2 - H) \\[2mm]
\qquad\qquad + r h_m \partial_x(\widetilde{p}_{1_{h_2-H}}) = rF + \dfrac{1}{2} u_m T - (1-r) g h_m \mathrm{sgn}(u_m) \tan \delta, \\[2mm]
\partial_t h_f = -T,
\end{cases}
\tag{5.4.2}
$$

The system is completed with closures relations on the pressure and vertical velocity of the water layer:

$$
\widetilde{p}_{1_{h_2+h_1/2-H}} = \frac{1}{2}\widetilde{p}_{1_{h_2-H}}, \qquad w_{1_{h_2-H}}^+ = \partial_t h_2 + u_1 \partial_x(h_2 - H).
$$

For more details see [124]. Note that system (5.4.1)-(5.4.2) reduces to (5.2.4) when the non-hydrostatic pressure is set to zero.

In Section 5.6 we will present a numerical test to show the importance of taking into account the non-hydrostatic effects in suitable cases.

Similarly to what is done in (5.2.4) and in (YAM), let us denote $p := \widetilde{p}_{1_{h_2+h_1/2-H}}$. Then the resulting non-hydrostatic pressure system can be written in the compact form

$$
\begin{cases}
\partial_t U + \partial_x F(U) + B(U)\partial_x U = G(U)\partial_x \widetilde{H} \\[2em]
\qquad\qquad + \mathcal{T}(U, \partial_x U, p, \partial_x p, \widetilde{H}, \partial_x \widetilde{H}) + S(U), \\[1em]
\partial_t w = 2\dfrac{p}{h_1}, \\[1em]
\mathcal{I}(U, \partial_x U, p, \partial_x p, \widetilde{H}, \partial_x \widetilde{H}, w) = 0,
\end{cases}
\qquad \text{(2L-NHBED)}
$$

U, F, B, G and $\widetilde{H}$ are defined as in (5.2.4). Finally,

$$
\mathcal{T}(U, \partial_x U, p, \partial_x p, \widetilde{H}, \partial_x \widetilde{H}) = -
\begin{pmatrix}
0 \\[0.5em]
h_1 \partial_x p + p \partial_x \left(h_1 + 2(\widetilde{H} + h_m) \right) \\[0.5em]
0 \\[0.5em]
2r h_m \partial_x p \\[0.5em]
0
\end{pmatrix},
\qquad (5.4.3)
$$

and

$$
\mathcal{I}(U, \partial_x U, \widetilde{H}, \partial_x \widetilde{H}, w) = h_1 \partial_x q_1 - q_1 \partial_x \left(h_1 + 2(\widetilde{H} + h_m) \right) + 2 h_1 w + 2 h_1 \partial_x q_m. \qquad (5.4.4)
$$

Note that last equation in (5.4.1), corresponding to free-divergence equation, has been multiplied by h_1, giving equation (5.4.4).

5.5 Numerical scheme

The system (2L-NHBED) is solved numerically using a two-step algorithm following ideas described by Escalante *et al.* in [112]. As in Chapter 3, the source term vector that contains friction terms, is set initially to zero:

$$
S(U) = \mathbf{0},
$$

and later, it will be taken into account in a semi-implicit manner. As in Section 3.1, the numerical scheme employed is based on a two-step projection-correction method. First, we shall solve the underlying hydrostatic system:

$$
\partial_t U + \partial_x F(U) + B(U)\partial_x U = G(U)\partial_x \widetilde{H}, \qquad (5.5.1)
$$

where U, F, B and G are defined in (5.2.4). System (5.5.1) is discretized by a second order finite volume PVM positive-preserving well-balanced path-conservative method to be detailed in the next subsection. As usual, we consider a set of N_x finite volume cells $I_i = [x_{i-1/2}, x_{i+1/2}]$ with constant lengths Δx and define

$$U_i(t) = \frac{1}{\Delta x} \int_{I_i} U(x,t) \, dx,$$

the cell average of the function $U(x,t)$ on cell I_i at time t. Regarding non-hydrostatic terms, we consider a staggered-grid (see Figure 5.2) formed by the points $x_{i-1/2}$, $x_{i+1/2}$ of the interfaces for each cell I_i, and denote the point values of the functions p and w on point $x_{i+1/2}$ at time t by

$$p_{i+1/2}(t) = p(x_{i+1/2}, t), \ \ w_{i+1/2}(t) = w(x_{i+1/2}, t).$$

Non-hydrostatic terms will be approximated by second order compact finite differences.

Figure 5.2: Numerical scheme stencil. Up: finite volume mesh. Down: staggered mesh for finite differences.

Time stepping

Assume given time steps Δt_n, and denote $t_n = \sum_{j \leq n} \Delta t_j$. To obtain second order accuracy in time, the two-stage second-order TVD Runge-Kutta scheme [142] is adopted. At the

kth stage, $k \in \{1, 2\}$, the two-step projection-correction method is given by

$$
\begin{cases}
\dfrac{U^{(\widetilde{k})} - U^{(k-1)}}{\Delta t} + \partial_x F(U^{(k-1)}) + B(U^{(k-1)})\partial_x U^{(k-1)} = G(U^{(k-1)})\partial_x \widetilde{H}, & \text{(5.5.2a)} \\[2.5em]
\dfrac{U^{(k)} - U^{(\widetilde{k})}}{\Delta t} = \mathcal{T}(U^{(k)}, \partial_x U^{(k)}, p^{(k)}, \partial_x p^{(k)}, \widetilde{H}, \partial_x \widetilde{H}) & \text{(5.5.2b)} \\[2.5em]
\dfrac{w^{(k)} - w^{(k-1)}}{\Delta t} = 2\dfrac{p^{(k)}}{h_1^{(k)}} & \text{(5.5.2c)} \\[2.5em]
\mathcal{I}(U^{(k)}, \partial_x U^{(k)}, \widetilde{H}, \partial_x \widetilde{H}, w^{(k)}) = 0, & \text{(5.5.2d)}
\end{cases}
$$

where $U^{(0)}$ is U at the time level t_n, $U^{(\widetilde{k})}$ is an intermediate value in the two-step projection-correction method that contains the numerical solution of the hydrostatic system (5.5.1) (system (5.5.2a)) at the corresponding kth stage of the Runge-Kutta, and $U^{(k)}$, $w^{(k)}$ are the kth stage estimate. After that, a final value of the solution at the t_{n+1} time level is obtained:

$$
U^{n+1} = \frac{1}{2}U^n + \frac{1}{2}U^{(2)}. \tag{5.5.3}
$$

Note that, equations (5.5.2b)-(5.5.2d) require, at each stage of the calculation, to solve a Poisson-like equation on the non-hydrostatic pressure $p^{(k)}$. This will be described bellow. For the computation of the time step the usual CFL restriction is considered.

5.5.1   Finite volume discretization for the underlying hydrostatic system

The system (5.5.1)

$$
\partial_t U + \partial_x F(U) + B(U)\partial_x U = G(U)\partial_x \widetilde{H}.
$$

is solved numerically by using a finite volume method. In this Section, we will describe a formally first order in space numerical scheme for the underlying hydrostatic system for the sake of simplicity. The higher order extension can be obtained following ideas described in Chapters 2-3.

As usual, we subdivide the horizontal spatial domain into standard computational cells $I_i = [x_{i-1/2}, x_{i+1/2}]$ with length Δx_i and define

$$
U_i(t) = \frac{1}{\Delta x_i} \int_{I_i} U(x,t)dx,
$$

the cell average of the function $U(x,t)$ on cell I_i at time t. We shall also denote by x_i the centre of the cell I_i. For the sake of simplicity, let us assume that all cells have the same length Δx.

In [105] authors introduce a first order path-conservative numerical scheme, named IFCP, which is constructed by using a suitable decomposition of a Roe matrix of system (5.5.1) by means of a parabolic viscosity matrix, that captures information of the intermediate fields. IFCP is a path-conservative scheme in the sense defined in (2.2.13). We remind the written of the IFCP numerical scheme previously described in Subsection 2.2.2:

$$U_i^{(\widetilde{k})} = U_i^{(k-1)} - \frac{\Delta t}{\Delta x}\left(D_{i+1/2}^{(k-1),-} + D_{i-1/2}^{(k-1),+}\right), \tag{5.5.4}$$

being $D_{i-1/2}^{\pm} = D_{i-1/2}^{\pm}(U_i, U_{i+1}, \widetilde{H}_i, \widetilde{H}_{i+1})$ defined by

$$\begin{aligned} D_{i+1/2}^{\pm} = \ & \frac{1}{2}\left(F(U_{i+1}^n) - F(U_i^n) + B_{i+1/2}(U_{i+1}^n - U_i^n)\right. \\ & -G_{i+1/2}(\widetilde{H}_{i+1} - \widetilde{H}_i) \\ & \left. \pm Q_{i+1/2}\left(U_{i+1}^n - U_i^n - A_{i+1/2}^{-1}G_{i+1/2}(\widetilde{H}_{i+1} - \widetilde{H}_i)\right)\right), \end{aligned} \tag{5.5.5}$$

where

$$B_{i+1/2} = \begin{pmatrix} 0 & 0 & 0 & 0 \\ 0 & 0 & gh_{1,i+1/2} & 0 \\ 0 & 0 & 0 & 0 \\ rgh_{m,i+1/2} & 0 & 0 & 0 \end{pmatrix}, \quad G_{i+1/2} = \begin{pmatrix} 0 \\ -gh_{1,i+1/2} \\ 0 \\ -gh_{m,i+1/2} \end{pmatrix},$$

$$A_{i+1/2} = J_{F,i+1/2} + B_{i+1/2},$$

being $J_{F,i+1/2}$ a Roe linearisation of the Jacobian of the flux F in the usual sense:

$$A_{i+1/2} = \begin{pmatrix} 0 & 1 & 0 & 0 \\ -u_{1,i+1/2}^2 + gh_{1,i+1/2} & 2u_{1,i+1/2} & gh_{1,i+1/2} & 0 \\ 0 & 0 & 0 & 1 \\ rgh_{m,i+1/2} & 0 & -u_{m,i+1/2}^2 + gh_{m,i+1/2} & 2u_{m,i+1/2} \end{pmatrix},$$

and

$$h_{*,i+1/2} = \frac{h_{*,i} + h_{*,i+1}}{2}, \quad u_{*,i+1/2} = \frac{u_{*,i}\sqrt{h_{*,i}} + u_{*,i+1}\sqrt{h_{*,i+1}}}{\sqrt{h_{*,i}} + \sqrt{h_{*,i+1}}}, \quad * \in \{1,2\}.$$

The key point is the definition of the matrix $Q_{i+1/2}$, that in the case of the IFCP is defined by:

$$Q_{i+1/2} = \alpha_0 Id + \alpha_1 A_{i+1/2} + \alpha_2 A_{i+1/2}^2,$$

where α_j, $j = 0,1,2$ are given by (2.2.43). It can be proved that the numerical scheme is linearly L^∞–stable under the usual CFL condition.

In the eventual case that eigenvalues become complex we can always apply this method. Because, it depends only on the norm of the internal eigenvalues λ_2 and λ_3 in the definition of χ_{int}. In the numerical simulations that we have performed we do not found any spurious oscillations.

5.5.2   Finite difference discretization for the non-hydrostatic terms

In this subsection we describe the discretization of the non-hydrostatic terms. As in Section 3.1, we consider a staggered-grid (see Figure 5.2) formed by the points $x_{i-1/2}$, $x_{i+1/2}$ of the interfaces for each cell I_i, and denote the point values of the functions $\widetilde{p}_{1|h_2-H}$ and w_1 on point $x_{i+1/2}$ at time t by

$$p_{i+1/2}(t) = \widetilde{p}_{1|h_2-H}(x_{i+1/2}, t), \ \ w_{i+1/2}(t) = w_1(x_{i+1/2}, t).$$

Following [112] and ideas applied in Section 3.1, $\widetilde{p}_{1|h_2-H}$ and w_1 will be discretized using second order compact finite differences. In order to obtain point value approximations for the non-hydrostatic variables $p_{i+1/2}$ and $w_{i+1/2}$, operator $\mathcal{I}(U, \partial_x U, \widetilde{H}, \partial_x \widetilde{H}, w)$ will be approximated for every point $x_{i+1/2}$ of the staggered-grid (Figure 5.2). Then, a second order compact finite difference scheme is applied to

$$
\begin{cases}
\partial_t U = \mathcal{T}(U, \partial_x U, p, \partial_x p, \widetilde{H}, \partial_x \widetilde{H}), \\[2mm]
\partial_t w = 2\dfrac{p}{h}, \\[2mm]
\mathcal{I}(U, \partial_x U, \widetilde{H}, \partial_x \widetilde{H}, w_1) = 0,
\end{cases}
\tag{5.5.6}
$$

where the values obtained in previous step are used as initial condition for the system. The resulting tridiagonal linear system is solved using an efficient Thomas algorithm [236].

Final numerical scheme

For the sake of clarity, a guideline of the final numerical scheme will be highlighted in what follows. For every kth stage $k \in \{1, 2\}$ of the Runge-Kutta method, the problem (2L-NHBED) is split into two parts. A two-step projection-correction method on staggered grids is used:

- **Finite volume step** (solving the hydrostatic system): From (5.5.4), solve explicitly the hydrostatic System (5.5.1) at the kth stage of the Runge-Kutta:

$$U_i^{(\widetilde{k})} = U_i^{(k-1)} - \frac{\Delta t}{\Delta x}\left(D_{i+1/2}^{(k-1),-} + D_{i-1/2}^{(k-1),+}\right),$$

by means of a PVM path-conservative finite volume scheme (5.5.4) to obtain the intermediate value $U_i^{(\widetilde{k})}$ in the two-step projection-correction method that contains the numerical solution of the System (SWE). The method can be combined with a MUSCL reconstruction operator to obtain second order in space.

- **Finite Difference step** (non-hydrostatic pressure correction):

  + Consider the discrete Poisson-like linear system that arises in (5.5.6) when applied a second order finite difference scheme in the spirit of Section 3.1. Then the non-hydrostatic pressures are obtained:

  $$p_{i+1/2}^{(k)}.$$

  + With the computed non-hydrostatic pressure terms $p_{i+1/2}^{(k)}$, the horizontal discharges as well as the vertical velocity can be updated from (5.5.2b)-(5.5.2c). Notice that in order to update the horizontal discharge, a second order point value approximation in the centre of the cell will be used using a similar approach that the one used in (3.1.7).

Finally,

$$U^{n+1} = \frac{1}{2}U^n + \frac{1}{2}U^{(2)}.$$

5.6 Numerical simulations

In this section, we present three numerical simulations, for the model proposed in Section 5.4 with the quadratic friction law proposed in (5.2.3). The first one corresponds to the evolution of a dune, where the computed velocity of the two-layer model and the one deduced for the SVE model are compared. The second test is a dam break problem over an erodible sediment layer where laboratory data is used to validate the model. The test proves as well its validity for regions where the interaction between the fluid and the sediment is strong. In those situations, the velocities computed by the two-layer model and the SVE one are not close. The last test shows the difference between the hydrostatic and the non-hydrostatic model on the shape of the bed surface.

The numerical results follow from a combination of the scheme described in Section 5.5 with a discrete approximation of bottom and surface derivatives. The numerical simulations are done with a CFL number equal to 0.9.

5.6.1 Test 1: weak bedload transport

In this test, we would like to show the ability of the proposed model to reproduce the low bedload transport regime. Two cases are presented. First, in Test 1.a we study
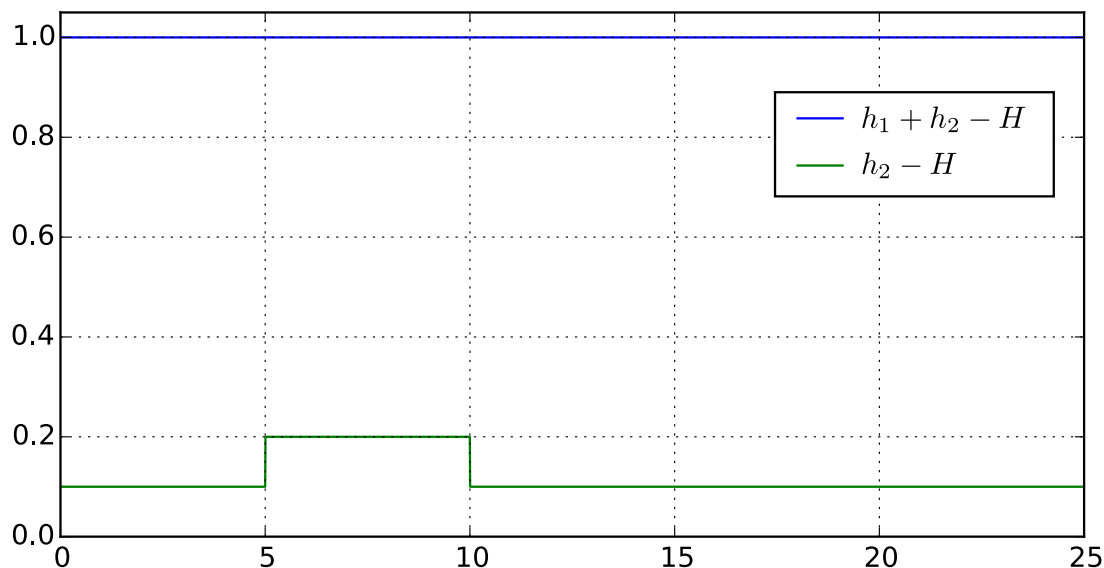
Figure 5.3: Test 1.a: Initial condition

the formation and evolution of a dune. Secondly, in Test 1.b we compare the numerical solution of the two-layer proposed model with the numerical solution of a system verified by a semi-analytical solution of the SVE model (5.3.1).

Test 1.a: formation and evolution of a dune

In particular we study the formation and evolution of a dune. To do so, let us consider the following initial condition over a domain of 25m, (see Figure 5.3):

$$h_2(0,x) = \begin{cases} 0.2 \text{ m}, & \text{if } x \in [5, 10], \\ 0.1 \text{ m}, & \text{otherwise}. \end{cases} \qquad h_1(0,x) + h_2(0,x) = 1 \text{ m}, \qquad h_1 u_1(0,x) = 1 \text{ m}^2/\text{s}^2.$$

The fixed bottom is set to $H(x) = 0$. We set left boundary condition $h_1 u_1(t, 0) = 1\text{m}^2/\text{s}^2$, and open boundary condition on the right hand side. The parameters for the model in this academic test have been set as follows: $r = 0.34$, $d_s = 0.01\text{m}$, $\theta_c = 0.047$, $\delta = 25^o$. Additionally for the transference term we introduce: $K_e = 0.1$, $K_d = 0.01$, $\varphi = 0.4$, $n = 0.01$. We use a discretization of 5000 points for the computational domain.

In Figure 5.4 we show the free surface and the sediment bottom surface at different times. We can see the dune profile that is transported by the flow.
In Figure 5.5 we show the difference between the velocities u_m obtained by the model and $v_b^{(QF)}$, the velocity deduced in [123] for the Saint Venant Exner model given in equation
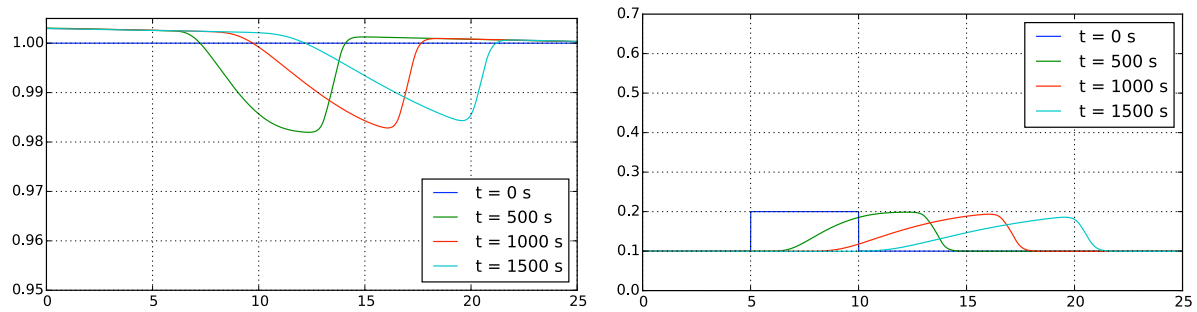
Figure 5.4: Test 1.a: (a) Surface and (b) bottom, at times $t = 0,\ 500,\ 1000,\ 1500\ s$
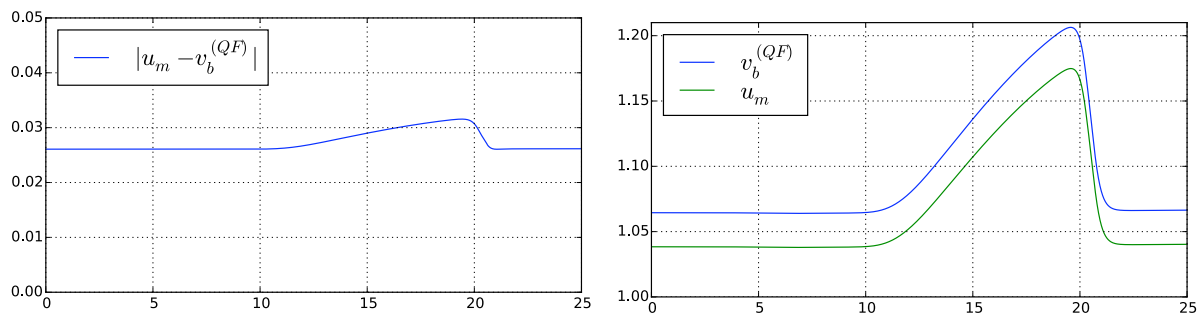
Figure 5.5: Test 1.a: Comparison between u_m and $v_b^{(QF)}$ at time $t = 1500\ s$

(5.3.4). The difference is of order 10^{-2} at last computed time $t = 1500$s. In Figure 5.6 we show the evolution in time of the relative error between $v_b^{(QF)}$ and u_m. We remark that it remains constant in time and the difference is small. The results show that the model behaves well in low bedload transport regimes and behaves in a similar way as a SVE.

Test 1.b: comparison with a semi-analytical solution of the SVE model

In this test we compare the solution computed with the proposed two-layer model with a semi-analytical solution of the SVE model (5.3.1). Let us remember that in Section 5.3.2 we showed that the proposed model converges formally to the SVE model when the morphodynamic time is much larger than the hydrodynamic time. In this section we present a system of partial differential equations verified by a semi-analytical solution of the SVE model (5.3.1) to which the two-layer model converges. A comparison between the numerical solutions of the two-layer model and the one associated to the system that verifies the semi-analical solution of the SVE model is presented.

A semi-analytical solution of classical SVE models (see [156]) is deduced by assuming a weak interaction between the fluid and the sediment layer, what implies that the
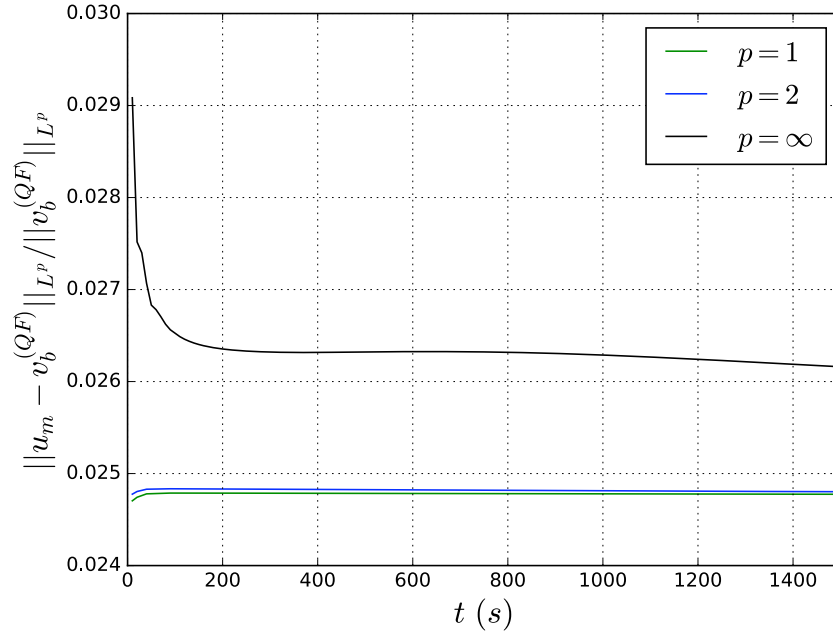
Figure 5.6: Test 1.a: Evolution in time of the relative error between u_m and $v_b^{(QF)}$ in L^1, L^2 and L^∞ norm.

morphodynamic time is much larger than the hydrodynamic time. The second assumption is that the water free surface and the water discharge are nearly constant. Let us denote by A_r the constant that defines the reference level of the water surface and q_1 the constant value of the water discharge. Under these assumptions we can deduce that the evolution of the sediment layer of the SVE model (5.3.1) is done by the solution of the following partial differential sytem with unknowns h_2 and h_f,

$$\begin{cases} d\partial_t h_2 + \partial_x \left((h_2 - h_f)\, v_b\, \sqrt{(1/r - 1)g d_s} \right) = 0, \\ \\ \partial_t h_f = -T; \end{cases} \qquad (5.6.1)$$

where the definition of the non-dimensional sediment velocity v_b depends on the friction law. In this test we only consider the quadratic friction law, from which we deduce

$$v_b = \frac{h_1 u_1}{(A_r + H - h_2)\sqrt{(1/r - 1)g d_s}}$$

$$-\vartheta^{1/2} \left| \partial_x(h_2 - H) + \mathrm{sgn}(u_2)\tan\delta \right|^{1/2} \mathrm{sgn}(\partial_x(h_2 - H) + \mathrm{sgn}(\Psi)\tan\delta),$$

where,

$$\Psi = \frac{h_1 u_1}{(A_r + H - h_2)\sqrt{(1/r - 1)g d_s}} - \left| \vartheta \partial_x(h_2 - H) \right|^{1/2} \mathrm{sgn}\left(\partial_x(h_2 - H) \right).$$

The transference term is defined in this case as follows:

$$T = \dot{z}_e - \dot{z}_d \quad \text{with} \quad \dot{z}_e = K_e(\theta_e - \theta_c)_+ \frac{\sqrt{g(1/r - 1)d_s}}{1 - \varphi}, \quad \dot{z}_d = K_d(h_2 - h_f)\frac{\sqrt{g(1/r - 1)d_s}}{d_s},$$

with $\theta_e = \left| \text{sgn}(q_1)\sqrt{\theta} - \sqrt{|\partial_x(h_2 - H)|} \, \text{sgn}\left(\partial_x(h_2 - H)\right) \right|^2$ and

$$\theta = \frac{g(A_r + H - h_2)n^2 q_1^2}{g(1/r - 1)d_s(A_r + H - h_2)^{4/3}}.$$

The Manning coefficient, n, erosion and deposition parameters, K_e, K_d and the initial condition for h_2 are set as in previous test. Nevertheless, we consider the following initial condition for the free surface and the fluid discharge, following the assumptions that consider the semi-analytical solution,

$$h_1(0, x) + h_2(0, x) = 10 \text{ m}, \quad h_1 u_1(0, x) = 20 \text{ m}^2/\text{s}^2.$$

To compare the solution of the two-layer model with the analytical solution of the SVE system, we consider a numerical approximation for both systems with the same number of points. We have set 2500 points in the domain. To approximate the semi-analytical solution a finite volume method is also considered, the one corresponding to the method considered for the two-layer system applied to system (5.6.1). In Figure 5.7 we can see that the numerical solution reached with the two-layer system and the one verified by the semi-analytical solution of the SVE model are indeed very close.

5.6.2 Test 2: Comparison with experimental data for strong bedload transport

The purpose of this second test is to validate the ability of the proposed model to reproduce sheet-flow transport by a comparison with experimental data. In particular, erosional dam break problems are simulated for three different cases. The first two cases have been presented in Fraccarollo and Capart [127] and carried out in two laboratories: Taipei (Case A) and Louvain-la-Neuve (Case B). The third one (Case C) has been also performed in the laboratory Louvain-la-Neuve and presented in Spinewine and Zech [7]. All of them occur for a layer of water confined behind a removable gate over an erodible saturated sediment layer of beads with mean diameter d_s and density ρ_s. The sediment is disposed all along the flume with a height h_{s0} and the water level has a depth h_{w0} above the top of the granular bed. Table below summarizes these characteristics for each case:

Case	d_s (mm)	ρ_s (kg/m^3)	h_{s0} (m)	h_{w0} (m)
A	6.1	1048	0.05	0.10
B	3.5	1540	0.05	0.10
C	3.9	1580	0.05	0.35
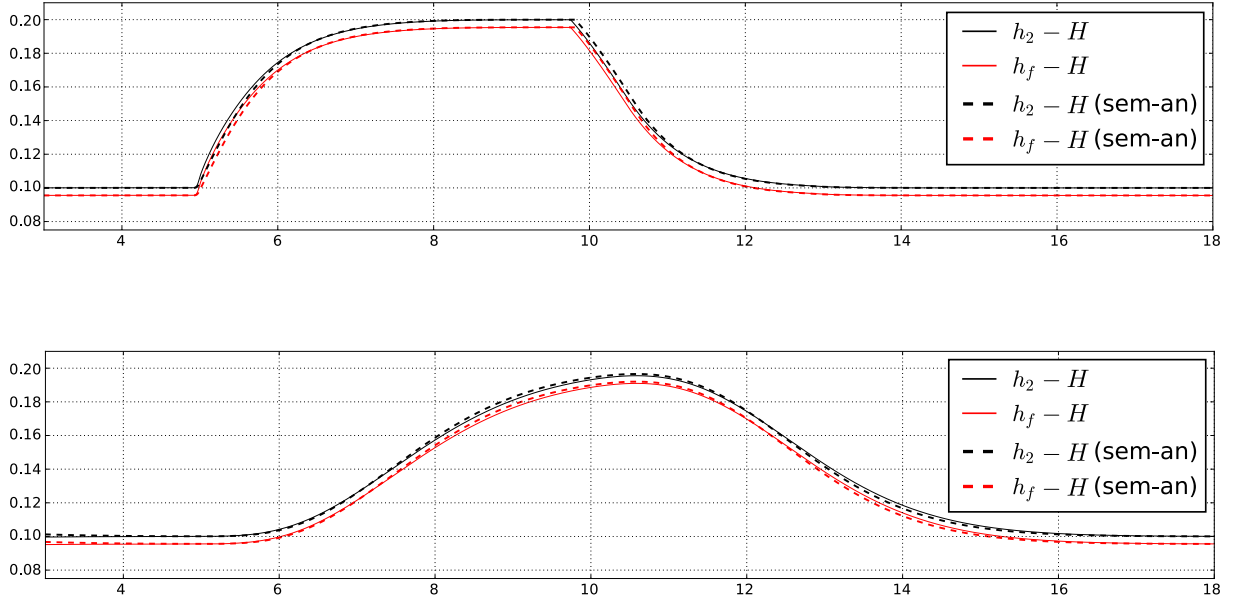
Figure 5.7: Test 1.b: Comparison with a semi-analytical solution of the SVE model at times $t = 100\ s$ and $t = 1800\ s$.

The morphological characteristics of the sediment are similar in Cases B and C, being more dense than in Case A where the material is not much heavier than water.

The same numerical test has been performed in [213] for the Cases A, B and in [252] for Case C, using classical models. Nevertheless we remark again that classical models make an assumption of low transport regime so that this test is not in the range of their validity.

The experimental test takes place in a rectangular flume, the river bed is flat and, at the initial state, the retained water mass is released. To do so, let us consider the following initial condition at the domain $[-1\ \text{m}, 1\ \text{m}]$ for the Cases A, B:

$$h_1(0, x) = \begin{cases} 10^{-12}\ \text{m}, & \text{if } x > 0, \\ 0.10\ \text{m}, & \text{if } x \leq 0, \end{cases} \quad h_2(0, x) = 0.05\ \text{m}, \quad h_1 u_1(0, x) = h_2 u_2(0, x) = 0\ \text{m}^2/\text{s}^2.$$

For the Case C the domain is $[-3\ \text{m}, 3\ \text{m}]$ and the following initial condition is considered

$$h_1(0, x) = \begin{cases} 10^{-12}\ \text{m}, & \text{if } x > 0, \\ 0.35\ \text{m}, & \text{if } x \leq 0, \end{cases} \quad h_2(0, x) = 0.05\ \text{m}, \quad h_1 u_1(0, x) = h_2 u_2(0, x) = 0\ \text{m}^2/\text{s}^2.$$

Finally, the fixed bottom is set to zero and open boundary conditions are imposed. The table below sums up the parameters used in the model. Notice that since the sediment layer is saturated, we use the bulk density to calculate the density ratio r, that is, $r = \frac{\rho_1}{\rho_2}$

with $\rho_2 = \varphi\rho_1 + (1 - \varphi)\rho_s$ for φ the porosity.

Case	r	d_s (mm)	θ_c	δ (^{o})	K_e	K_d	φ	n
A	0.972	6.1	0.047	35	0.1	0.1	0.4	0.045
B	0.755	3.5	0.047	35	0.1	0.15	0.4	0.012
C	0.741	3.9	0.047	35	0.15	0.15	0.4	0.085

The Manning coefficient n as well as the erosion and deposition parameters K_e, K_d are calibrated in terms of the laboratory data, the focus being on accurately describing the front position at the final time.

The computational domain used is discretized with $\Delta x = 0.0075$ for the three cases. In Figures 5.8-5.10 we show the results obtained with the model proposed here compared to the experimental data for several times. In particular, three interfaces are depicted: free surface ($h_1 + h_2 - H$), upper limit transport layer ($h_2 - H$) dividing the flow into water and sediment regions and the seabed level ($h_f - H$) for the motionless sediment bed. Since the curves for experiments are obtained from the digital images [127, 7] we focus on a qualitative comparison. These interfaces lines help to know quite precisely the behaviour of the flow and we can see that the model qualitative agree with experimental data.

Given the results, the front position is well captured for the three cases at the final time. We can also see that the front of the flow is filled with sediment material as in real data, only in Case C this point is not captured. As a typical behaviour in the results, the water thickness is overestimated and the sediment layer is underestimated, but in general, both free surface and sediment bottom are captured successfully. Notice that the calculated interface between water and sediment ($h_2 - H$) fits always between the lines of experimental data for the sediment interfaces (black and red lines in figures) so the position of the sediment interface is qualitative well captured by the model. For initial times the erosion is underestimated but at final times the position of the seabed level is not so far from the experimental data except in Case A. Note that in that case, the ratio between the densities is close to 1. The use of classical models in this type of situations, where the interaction between the sediment and the fluid is strong, does not allow to accurately capture the sediment layer (see [213], [252]). Here we see a better fit to the data for the advancing front of the sediment thanks to the proposed bilayer model.

As expected, in this test the difference between the velocities u_m and $v_b^{(QF)}$ is not so small (see Figure 5.11). Thus, the hypothesis of sediment transport in a large morphodynamic time scale is not fulfilled for this test. The difference is specially relevant at the advancing front, where the hypothesis of low transport rate is no longer valid. The new model introduced here does not requires such an assumption and it adjusts automatically to the physical situation. Figure **??** shows the evolution in time of the relative error between $v_b^{(QF)}$ and u_m. We can observe that the error in norm L^∞ remains constant until the simulated time, where the error in norms L^1 and L^2 decrease.

Nevertheless, during all the simulation these errors are of a degree of magnitude bigger than for the case of a dune evolution presented in the previous test.

Figure 5.8: Test 2. Case A. Comparison of the obtained flow interfaces (solid lines) with experimental data (symbol lines) for times $t = 0.1$ s, 0.2 s, 0.3 s, 0.4 s, 0.5 s.

5.6.3   Test 3: non-hydrostatic effects

The focus now is to study the influence of the non-hydrostatic effects on the sediment layer, solving the model proposed in Section 5.4. The computational domain is $[0 \text{ m}, 15 \text{ m}]$. Let us consider the following initial condition

$$h_1(0, x) = 0.8 \text{ m} \quad h_2(0, x) = 0.2 \text{ m}, \quad q_1(0, x) = q_2(0, x) = 0 \text{ m}^2/\text{s}^2.$$

Figure 5.9: Test 2. Case B. Comparison of the obtained flow interfaces (solid lines) with experimental data (symbol lines) for times $t = 0.25$ s, 0.5 s, 0.75 s, 1.00 s.

An incoming wave train is simulated through the left boundary condition $h_1(t,0) = 0.8 + 0.1\sin(5t)$, and open boundary condition on the right hand side is considered. The parameters for the model have been set as follows $r = 0.63$, $d_s = 0.1$, $\theta_c = 0.047$, $\delta = 35^o$, $K_e = 0.001$, $K_d = 0.01$, $\varphi = 0.4$, $n = 0.1$. We take 1200 points to discretize the domain.

In Figure **??** we show the evolution of the sediment bottom surface at times $t = 500,\ 750,\ 1000\ s$ for the model with and without non-hydrostatic effects. A zoom by comparing the final bottom and free surface can be seen in Figure **??**. Two main differences can be observed in these figures. First, the form of the water waves are very different for the hydrostatic and the non-hydrostatic models, see Figure **??**. The profile closer to real life pattern is the one given by the non-hydrostatic model (see [13]). Indeed, the hydrostatic model generates a shock in the water surface that should not be present in the configuration of this test. Second, it is clear that the wave pattern on the surface has a deep impact on the profile of the bed form, as can be seen in Figure **??**. Remark that here the bedload model is the same for both configurations so that the differences in the bedform are due to the non-hydrostatic effect in the water layer.

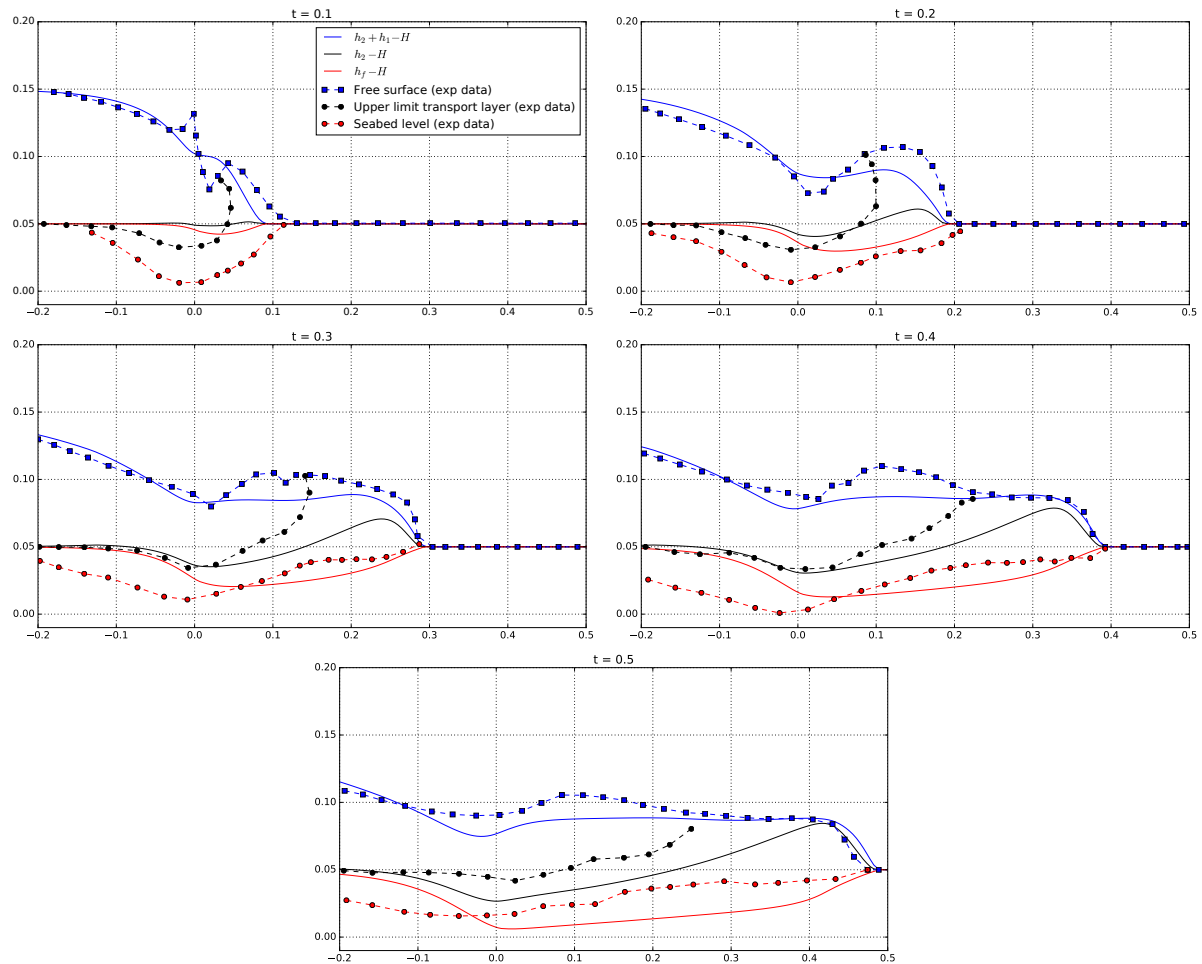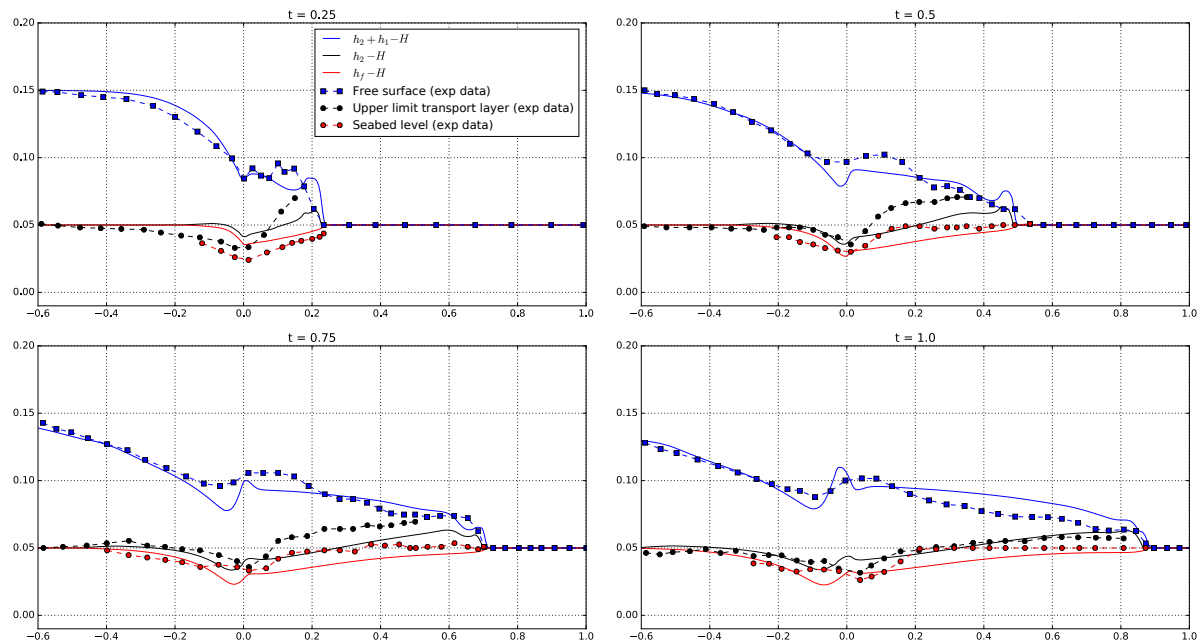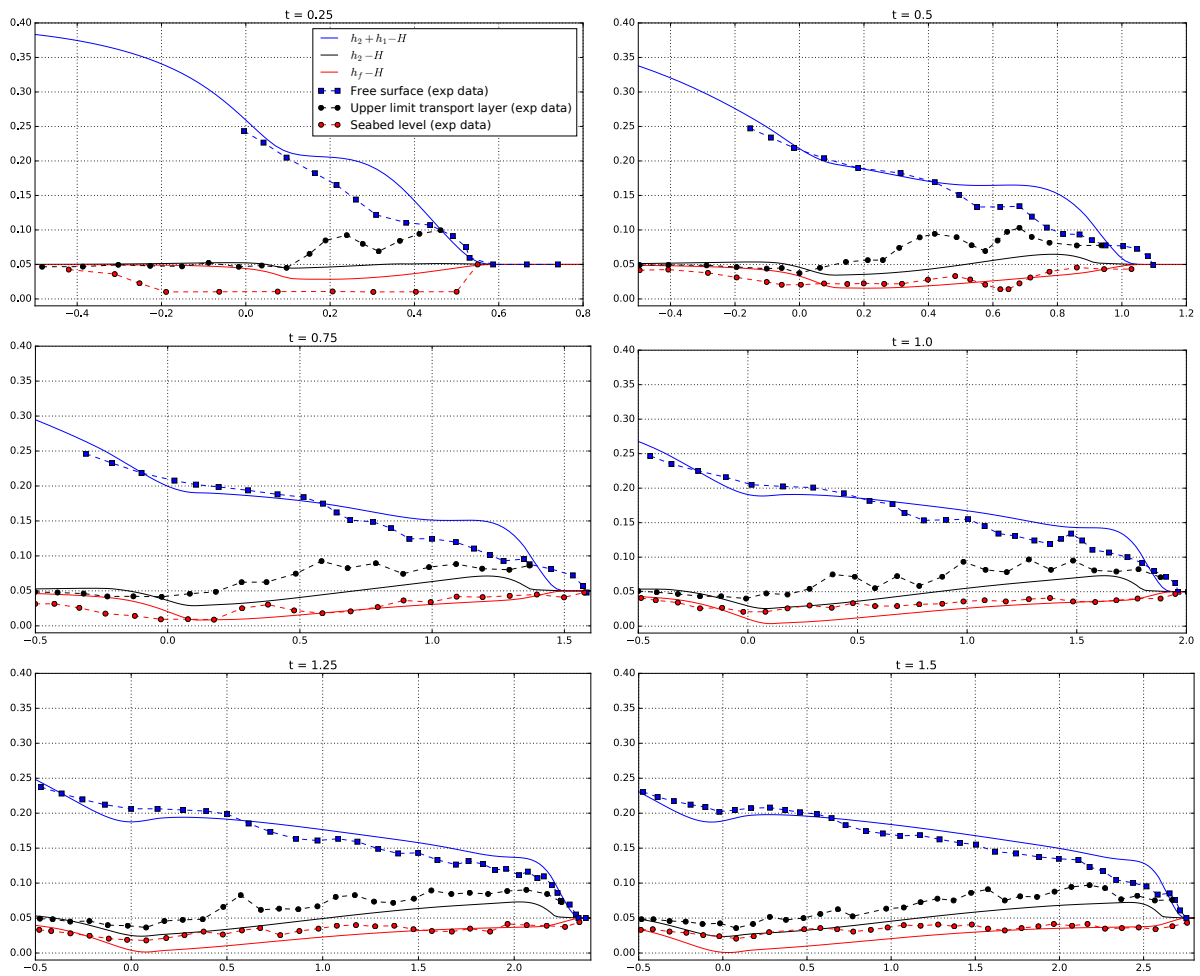Figure 5.10: Test 2. Case C. Comparison of the obtained flow interfaces (solid lines) with experimental data (symbol lines) for times $t = 0.25$ s, 0.5 s, 0.75 s, 1.00 s, 1.25 s, 1.5 s.
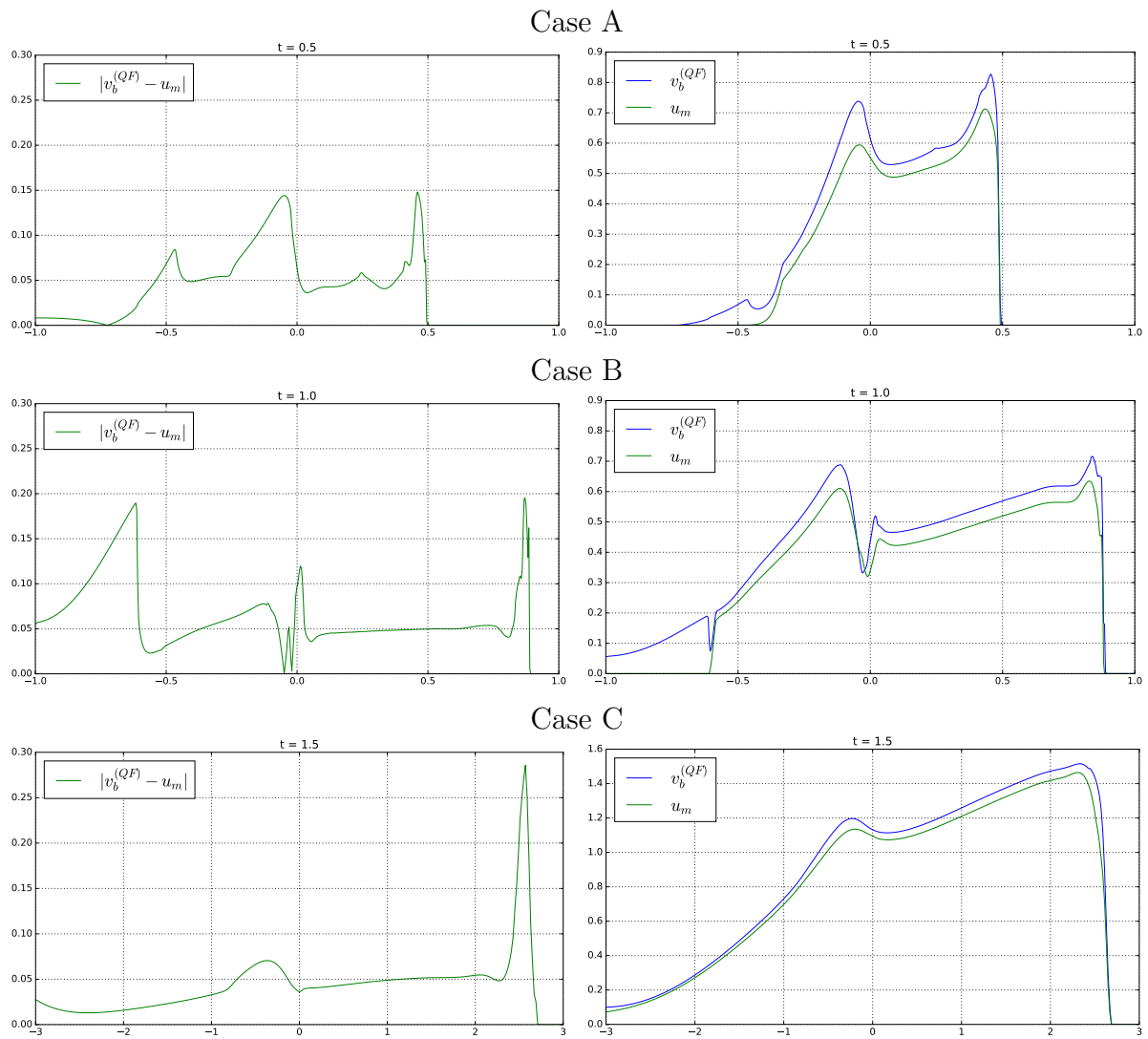
Figure 5.11: Test 2: Difference between u_m and $v_b^{(QF)}$ at times $t = 0.5$ s (case A), $t = 1.0$ s (case B) and $t = 1.5$ s (case C).

Chapter 6

Conclusions and future work

Here we present a summary of the results achieved in this dissertation. Then, some possible and auspicious future research trends are given.

6.1 Conclusion

Given that a wide number of topics have been considered here, the conclusions obtained from this thesis are many. This thesis adds some relevant and novel contributions to areas such as *mathematical modelling* and *numerical analysis*, as well as some good results concerning validation throughout *laboratory or field experiments* and efficient and *parallel computation* of geophysical flows. Thus, we split the conclusions into those three topics:

- **Mathematical modelling:**

  We highlight the main contributions in the field of *mathematical modelling* of dispersive water waves: The introduction of two novel non-hydrostatic pressure systems for free surface flows has been proposed in order to incorporate dispersive effects in the propagation of waves in a homogeneous, inviscid and incompressible fluid: the system (NH-2L) with enhanced dispersive properties and the hyperbolic system (NHyp).

  - System (NH-2L), recently submitted by C. Escalante, E.D. Fernández-Nieto, T. Morales de Luna and M.J. Castro [118] and under review with minor revision. In this work, a non-hydrostatic two-layer model has been proposed to incorporate dispersive effects in the propagation of dispersive water waves. The presented model corresponds to the system derived by E.D.Fernández Nieto *et al.* in [124] for the two-layer case, with a slight difference in the definition of the non-hydrostatic pressure at the interface. This allows us to derive a two-layer non-hydrostatic model with improved dispersive properties. This improvement on the dispersive properties expands the range of validity of the system for kH

values up to 15, while reducing the relative error of the phase velocity in a factor of 8.6 concerning the original two layer system derived in [124] (see Table 1.2). The advantage is that this is done while keeping the computational cost of the model low.

- System (NHyp), recently submitted by C. Escalante, M. Dumbser and M.J. Castro [111]. The presented model corresponds to a hyperbolic approximation of the dispersive system derived by Sainte-Marie *et* al in [21]. The dispersion properties of our new hyperbolic system are close to those of the aforementioned original model. Moreover, the new system satisfies an extra energy conservation law and the full eigenstructure of the system can be easily computed. However, the big advantage of our new hyperbolic reformulation is that it can be easily discretized with explicit and high order accurate numerical schemes for hyperbolic conservation laws, without requiring the solution of an elliptic problem in each time step, in contrast to the original PDE system proposed in [21] (see [4], [112]).

- System (2L-NHBED). A two-layer shallow water model that can deal with intense and slow bedload sediment transport has been introduced, as an ongoing work by C. Escalante, G.Narbona–Reina, E.D. Fernández–Nieto and T. Morales [110]. The system leads to measure the influence of a non-hydrostatic pressure in the fluid layer and its influence on the gradient pressure of the sediment layer as well. In the case that the interaction between the fluid and the sediment is weak, we are in a regime where SVE models can be considered. In this case, we show that the proposed two-layer model converges formally to the SVE with gravitational effects. The proposed model has the advantage that the inclusion of gravitational effects does not imply to approximate any non-linear parabolic degenerated term, as for the case of SVE model with gravitational effects.

Some other contributions are highlighted. As it is well known, Boussinesq-type and non-hydrostatic pressure systems described need some dissipative mechanism for breaking waves to accurately model waves near the coastal areas (see [112]). Breaking mechanisms are based on a diffusive term that must be discretized implicitly due to the high order derivatives from the diffusion. Thus, an extra discrete Poisson-like operator must be solved, losing efficiency. This challenge is overcome by C. Escalante *et al.* [112] for the systems (YAM), (NH-2L) and (NHyp) in [112], [118] and [111] respectively. There, we have proposed a new, simple and efficient breaking mechanism that performs properly in the tests shown.

Finally, in the spirit of Sainte-Marie *et al.* in [21] where Serre-Green-Naghdi system is written as a first order hyperbolic-elliptic non-hydrostatic pressure system for a flat bottom, we have proposed, up to our knowledge, a novel rewriting of system (PER) for a given arbitrary bathymetry in a similar way. Similar techniques

can also be applied in a future for some of the most used Boussinesq-type systems (e.g. Madsen *et al.* systems [184]).

- **Numerical analysis:**

  We highlight the main contributions from Chapter 3 in the field of *numerical analysis* for the discretization of the described systems: the hyperbolic systems (SWE-2D) and (NHyp-2D), and the hyperbolic-elliptic systems (YAM-2D) and (NH-2L2D), for one and two space dimensions.

  In this thesis, the systems (YAM-2D) and (NH-2L2D) have been approximated by using a hybrid finite volume finite difference numerical schemes, based on an implicit projection-correction technique. The system (YAM-2D) has been discretized by using a staggered Arakawa C-grid. However, the hyperbolic system (NHyp-2D) is discretized using an explicit finite volume numerical scheme. The aforementioned numerical schemes are second order accurate in both space and time, by using the polynomial reconstruction of states, second order finite differences and a second order Runge-Kutta TVD discretization in time.

  As an alternative to getting arbitrary high order numerical schemes in space and time, we have considered finite element Discontinuous Galerkin schemes, with an a posteriori subcell finite volume limiter. Since hyperbolic systems are amenable to be discretized using ADER-DG schemes, we have considered an arbitrarily high order numerical scheme for the hyperbolic system (NHyp-2D). Up to our knowledge, this is the first time that this strategy of using a DG scheme combined with a finite volume subcell limiter based is employed for the simulation of dispersive/non-hydrostatic water waves.

  To sum up, the proposed numerical schemes satisfy the following properties:

  - The proposed numerical schemes can deal with conservative and nonconservative systems by means of path-conservative schemes. In particular, a robust and efficient HLL written as a PVM scheme is used for both finite volume and ADER-DG solvers.

  - The numerical schemes are linearly L^∞-stable under the usual CFL condition.

  - The numerical schemes are well-balanced for water at rest solutions.

  - The numerical schemes can deal with a variety of challenging domains that involves wetting and drying areas. Moreover, the schemes are positive preserving for smooth bathymetries and under $\dfrac{1}{2}$ of usual CFL condition. In the particular case of hybrid finite volume finite difference numerical schemes for systems (NH-2L) and (YAM), we have shown that non-hydrostatic pressure vanishes in areas where the water height is small or identically zero (dry area). Thus, no numerical truncation for the non-hydrostatic pressure is needed at

wet-dry areas, as it is usually done (see [259]). This is due to the writing of the incompressibility condition, written in terms of discharges. To the best of our knowledge, this is an improvement in non-hydrostatic numerical schemes, where usually non-hydrostatic pressure is truncated to zero up to a threshold value.

- The numerical schemes exhibit a high degree of parallelism. Although implicit schemes need to solve a linear system at each time step, it can be done efficiently on GPU architectures.

- **Numerical validation and parallel computing:**

Concerning the numerical validation, system (YAM-2D) has been widely validated by Y.Yamazaki *et al.* Moreover, this system and its corresponding discretization given in [259] corresponds to the well-known tsunami code NEOWAVE. Moreover, this system with our corresponding discretization proposed in this thesis has been validated in a series of papers ([157], [182], [177]). Similarly, system (NH-2L2D) and its corresponding discretization are benchmarked using laboratory experiment data for rigid slides. The experimental data used have been proposed by the US National Tsunami Hazard and Mitigation Program (NTHMP) and established for the NTHMP Landslide Benchmark Workshop, held in January 2017 at Galveston.

As a general concluding remark, the comparison with experimental data requires to incorporate dispersive effects to capture faithfully wave propagation in the vicinity of the continental shelf, in particular involving complex processes such as wave run-up, shoaling, the appearance of higher harmonics and wet-dry areas. A simple shallow water model would not be able to capture all these physical effects simultaneously, hence more sophisticated non-hydrostatic models are needed.

The described numerical schemes for the systems mentioned above can simulate properly the run-up and run-down process in wet-dry areas on the shore, as well as shoaling processes and breaking waves. The numerical experiments show that the new approaches presented here correctly describes the propagation of solitary waves and can accurately preserve their shape even for very long integration times. In particular for solitary waves, high order DG type schemes are ideal due to their little numerical dissipation and dispersion error, and since the undesired clipping of local extrema that is typical for second order TVD finite volume schemes can be completely avoided. This is achieved with the hyperbolic non-hydrostatic pressure system (NHyp-2D) for smaller values of the relaxation parameter $C = \alpha\sqrt{gH}$, with α typically equals to 3.

Moreover, numerical simulations show that the described system (NH-2L) correctly solves the propagation of eulerian solitary waves of high amplitude, preserving their shape for large integration times accurately. Moreover, complicated processes such as run-up or shoaling can be simulated with the two layer system. Furthermore,

the appearance of higher harmonics that can not be well reproduced with a one-layer non-hydrostatic pressure system, are simulated successfully for the proposed tests with the novel two-layer system (NH-2L). We would like to stress the good performance when dealing with a wide range of non-linear dispersive waves, as it was said in Section 4.6, where usually a Green-Naghdi type model or multilayer non-hydrostatic model is needed to correctly simulate the tests. Numerical tests also evince that the proposed model introduced in this work with the jump of the non-hydrostatic pressure at the interface (1.2.15), improves the results with respect to the two-layer system derived in [124]. This has been shown by comparing with analytical solutions from the Stokes first order theory. This improvement is achieved without the need for increasing the order of the derivatives or adding more layers which would increase the complexity of the model and its computational cost. Instead, the two layer performs perfectly with the same computational cost than the original two-layer system derived in [124],

The GPU implementations of the described 2D numerical schemes are carried out and some guidelines are given in Appendix E. From a computational point of view, the non-hydrostatic GPU implementation for the two layer system (NH-2L2D) presents good computational times concerning the SWE GPU times. A numerical test was carried out to illustrate such claim and reveals that the wall-clock times for the two layer non-hydrostatic code are no higher than 5.89 times than the SWE code for refined meshes (see table 4.5). Concerning the GPU implementation of the finite volume scheme described for the system (YAM-2D), the wall-clock times for the non-hydrostatic code are no higher than 2.8 times than the SWE code for refined meshes (see table 4.5). It is worth mentioning that a similar ratio is also maintained for the GPU implementation of the DG numerical scheme for the system (NHyp-2D) (see Table 4.4). The real highlight, in this case, is that the same low additional computational cost is maintained for any order of accuracy in space and time of the DG numerical scheme. This point is underlined in Figure 4.29, that reveals the computational time needed to evolve a degree of freedom, which is independent on the order of the DG scheme.

The considered numerical schemes for the different systems presented in this work provides thus an efficient and accurate approach to model dispersive effects in the propagation of waves near coastal areas.

Moreover, the multi-layer non-hydrostatic pressure system (NH-L) has been implemented on GPU architectures, following the same ideas for its numerical approximation than the ones described in this thesis for the two layer system, and has been integrated on the high-performance software package HySEA (Hyperbolic Systems and Efficient Algorithms) that consists of a family of geophysical codes based on either single layer, two-layer stratified systems or multilayer shallow water models developed by the EDANYA group at the University of Málaga (see [254]).

6.2   Future work

We conjecture that the present hyperbolic approach applied to the original system (0.0.8), can be applied in general to the multi layer non-hydrostatic pressure system (NH-L), and thus, a straightforward generalization of the finite volume as well as ADER-DG schemes could be easily applied.

Moreover, given the apparent connexion between some Boussinesq-type systems and first order non-hydrostatic pressure PDE systems, a future line of work follows this idea. In that way, Boussinesq-type systems written as a first order PDE non-hydrostatic system will be amenable to be approximated by a first order hyperbolic PDE system, and thus again, arbitrary high order ADER-DG schemes could be also considered to numerically solve them.

Further research will concern a direct comparison of the new mathematical model proposed in this thesis (NHyp-2D) with the hyperbolic reformulation of the Serre-Green-Naghdi (SGN) equations recently forwarded by S.Gavrilyuk *et al.* in [117].

An extension of the work proposed in [34] is being considered for non-hydrostatic flows and its integration on the software package HySEA. In that paper, the shallow water equations in spherical coordinates are efficiently solved by means of a path-conservative finite volume scheme, resulting in a robust, efficient and well balanced numerical method.

We would like to point out that the techniques that have been employed in this dissertation also fit other problems. In particular, the design of numerical schemes well-balanced for the resolution of PDEs on manifolds that is a topic in demand on

computational astrophysics.

Appendix A

Breaking waves parameters for the two layer system (NH-2L)

By taking into account the two vertical velocities equations and the incompressibility equations, which relates w_α with u_α, lead us to write P in terms of the derivatives of U

$$
A_{(xx)}\partial_{xx}\boldsymbol{U} + A_{(xt)}\partial_{xt}\boldsymbol{U} + A_{(x)}\partial_x\boldsymbol{U} + A_{(t)}\partial_t\boldsymbol{U} + A\boldsymbol{U} + B = \begin{pmatrix} p_b - p_I \\ \\ \gamma_1 p_b + \gamma_2 p_I \end{pmatrix} + I_{(\varsigma)}\partial_x\boldsymbol{U},
$$

where

$$
I_{(\varsigma)} = \begin{pmatrix} -\varsigma_1 l_1 h & 0 \\ \\ 0 & -\varsigma_2 l_2 h \end{pmatrix}, \quad A_{(\cdot)} \in \mathcal{M}_2(\mathbb{R}).
$$

We propose define ς_α such that

$$
I_{(\varsigma)} := Diag(A_{(x)}).
$$

We then proceed to compute $A_{(x)}$. The two continuity equations can be written as

$$
\begin{cases} w_1 = u_1 \partial_x H - \dfrac{1}{2} l_1 h \partial_x u_1 - \partial_t H, \\ \\ w_2 = -u_1 \partial_x l_1 h + u_2 \partial_x z_I - l_1 h \partial_x u_1 - \dfrac{1}{2} l_2 h \partial_x u_2 - \partial_t H. \end{cases}
$$

Neglecting mass transfer terms due to Γ_I, the vertical equations can be written as

$$
\begin{cases} \partial_t (l_1 h w_1) + \partial_x (l_1 h u_1 w_1) = p_b - p_I + \varsigma_1 l_1 h \partial_x u_1, \\ \\ \partial_t (l_2 h w_2) + \partial_x (l_2 h u_2 w_2) = \gamma_1 p_b + \gamma_2 p_I + \varsigma_2 l_2 h \partial_x u_2. \end{cases} \tag{A.0.2}
$$

Then, retaining at the left hand side of equation (A.0.2) only the terms multiplied by $\partial_x u_\alpha$ at the equation concerning to the layer α, leads to

$$I_{(\varsigma)} = \begin{pmatrix} l_1 h\left(-\partial_t l_1 h + w_1 - u_1 \partial_x\left(l_1 h + H\right)\right) & 0 \\ \\ 0 & l_2 h\left(-\partial_t l_2 h + w_2 + u_2 \partial_x\left(z_I - l_2 h\right)\right) \end{pmatrix},$$

Again, using that $\Gamma_I = 0$, $I_{(\varsigma)}$ can be rewritten as

$$I_{(\varsigma)} = \begin{pmatrix} l_1 h\left(-w_1 + 3u_1\partial_x H - 2\partial_t H\right) & 0 \\ \\ 0 & l_2 h\left(-w_2 - 2\partial_t H - 3u_2\partial_x z_I\right) \end{pmatrix},$$

and finally we propose

$$\begin{cases} \varsigma_1 = \left(w_1 - 3u_1\partial_x H + 2\partial_t H\right), \\ \\ \varsigma_2 = \left(w_2 + 3u_2\partial_x z_I + 2\partial_t H\right). \end{cases} \tag{A.0.3}$$

Appendix B

Coefficients and matrix of the linear system for the one layer system (YAM)

Coefficients for the one-dimensional case

The linear system defined in (3.1.9)

$$\boldsymbol{A}^{n+1/2}\boldsymbol{\mathcal{P}}^{n+1} = \boldsymbol{\mathcal{RHS}}^{n+1/2},$$

where

$$\boldsymbol{\mathcal{P}}^{n+1} = \begin{pmatrix} p_{1/2}^{n+1} \\ p_{1+1/2}^{n+1} \\ \vdots \\ p_{N+1/2}^{n+1} \end{pmatrix}$$

is given by:

$$\boldsymbol{A}^{n+1/2} = \begin{pmatrix} b_0^{n+1/2} & c_0^{n+1/2} & & \cdots & & 0 \\ a_1^{n+1/2} & b_1^{n+1/2} & c_1^{n+1/2} & & & \\ & \ddots & \ddots & \ddots & & \vdots \\ & & a_i^{n+1/2} & b_i^{n+1/2} & c_i^{n+1/2} & \\ \vdots & & & \ddots & \ddots & \ddots \\ & & & & a_{N-1}^{n+1/2} & b_{N-1}^{n+1/2} & c_{N-1}^{n+1/2} \\ 0 & & \cdots & & & a_N^{n+1/2} & b_N^{n+1/2} \end{pmatrix}, \qquad \text{(B.0.1)}$$

where for $k \in \{0, \dots, N\}$, neglecting the dependence on time in the notation:

$$\begin{cases} a_i = (\xi_{\Delta x, i} - 2h_i)(\xi_{\Delta x, i+1/2} + 2h_{i+1/2}), \\[2mm] b_i = 16\Delta x^2 + \xi_{\Delta x, i+1/2}(\xi_{\Delta x, i} + \xi_{\Delta x, i+1} + 2h_i - 2h_{i+1}) + 2h_{i+1/2}(\xi_{\Delta x, i} - \xi_{\Delta x, i+1} + 4h_{i+1/2}), \\[2mm] c_i = (\xi_{\Delta x, i+1} + 2h_{i+1})(\xi_{\Delta x, i+1/2} - 2h_{i+1/2}). \end{cases}$$

$$\text{(B.0.2)}$$

The coefficients described above are conveniently modified depending on the choice of the boundary conditions.

$h_{i+1/2}$ is given by (3.1.8) and

$$\xi_{\Delta x, i} = \Delta x \left(2\eta_{x,i} - h_{x,i} \right), \ \xi_{\Delta x, i+1/2} = \Delta x \left(2\eta_{x,i+1/2} - h_{x,i+1/2} \right),$$

being $\eta_{x,i}$ and $h_{x,i}$ given by (3.1.7) and $\eta_{x,i+1/2}$ and $h_{x,i+1/2}$ given by (3.1.8).

Finally, the *Right Hand Side* is given by

$$(\boldsymbol{\mathcal{RHS}})_i = \frac{8\Delta x^2}{\Delta t} \left(h_{i+1/2} q_{x,i+1/2} - q_{i+1/2} \left(2\eta_{x,i+1/2} - h_{x,i+1/2} \right) + 2h_{i+1/2} w_{i+1/2} \right),$$

where $q_{i+1/2}$ and $q_{x,i+1/2}$ are given by (3.1.8).

Analysis of the linear system for small water heights

If we assume

$$h = \epsilon, \ q = w = 0, \ H = mx$$

then the coefficients (B.0.2) reduce to

$$
\begin{cases}
a_i = 4(m - \epsilon)(m + \epsilon), \\[2mm]
b_i = 8(2\Delta x^2 + m^2 + \epsilon^2), \\[2mm]
c_i = 4(m - \epsilon)(m + \epsilon),
\end{cases}
$$

and the *Right Hand Side* vector vanishes

$$
\mathcal{RHS} = \mathbf{0}
$$

Moreover, since the linear system is strictly diagonal dominant, the matrix $\boldsymbol{A}$ is invertible.

Appendix C

Finite difference approximations. 2D numerical scheme for the system (YAM-2D)

Le us denote the non-hydrostatic terms appearing in the horizontal momentum equations as

$$
\mathcal{T}(U, \nabla U, p, \nabla p, H, \nabla H) = \begin{pmatrix} 0 \\ \mathcal{T}^{Hor}(h, h_x, p, p_x, H, H_x) \\ \mathcal{T}^{Ver}(h, h_y, p, p_y, H, H_y) \end{pmatrix},
$$

$\mathcal{T}^{Hor}$, $\mathcal{T}^{Ver}$ being the horizontal and vertical non-hydrostatic contributions respectively:

$$
\mathcal{T}^{Hor}(h, h_x, p, p_x, H, H_x) = -\frac{1}{2}(hp_x + p((2\eta - h)_x)),
$$

$$
\mathcal{T}^{Ver}(h, h_y, p, p_y, H, H_y) = -\frac{1}{2}(hp_y + p((2\eta - h)_y)).
$$

Let us also define the North and South approximations in the middle of the horizontal edges for the volume V_{ij} of $\mathcal{T}^{Hor}$ by

$$
\mathcal{T}^{Hor}_{N(ij)}(h, h_x, p, p_x, H, H_x) = -\frac{1}{2}h_{ij}\frac{p_{i+1/2j+1/2} - p_{i-1/2,j+1/2}}{\Delta x}
$$
$$
-\frac{1}{2}\frac{p_{i+1/2j+1/2} + p_{i-1/2j+1/2}}{2}\cdot\frac{2\eta_{i+1j} - h_{i+1j} - (2\eta_{i-1j} - h_{i-1j})}{2\Delta x},
$$

$$
\mathcal{T}^{Hor}_{S(ij)}(h, h_x, p, p_x, H, H_x) = -\frac{1}{2}h_{ij}\frac{p_{i+1/2j-1/2} - p_{i-1/2j-1/2}}{\Delta x}
$$
$$
-\frac{1}{2}\frac{p_{i+1/2j-1/2} + p_{i-1/2j-1/2}}{2}\cdot\frac{2\eta_{i+1j} - h_{i+1j} - (2\eta_{i-1j} - h_{i-1j})}{2\Delta x},
$$

respectively. Same ideas for the East and West approximations in the middle of the vertical edges for the volume V_{ij} of $\mathcal{T}^{Ver}$:

$$
\mathcal{T}^{Ver}_{E(i,j)}(h, h_y, p, p_y, H, H_y) = -\frac{1}{2}h_{i,j}\frac{p_{i+1/2j+1/2} - p_{i+1/2j-1/2}}{\Delta y}
$$
$$
-\frac{1}{2}\frac{p_{i+1/2j+1/2} + p_{i+1/2j-1/2}}{2}\cdot\frac{2\eta_{ij+1} - h_{ij+1} - (2\eta_{ij-1} - h_{ij-1})}{2\Delta y},
$$

$$
\mathcal{T}^{Ver}_{W(ij)}(h, h_y, p, p_y, H, H_y) = -\frac{1}{2}h_{ij}\frac{p_{i-1/2j+1/2} - p_{i-1/2j-1/2}}{\Delta y}
$$
$$
-\frac{1}{2}\frac{p_{i-1/2j+1/2} + p_{i-1/2j-1/2}}{2}\cdot\frac{2\eta_{ij+1} - h_{ij+1} - (2\eta_{ij-1} - h_{ij-1})}{2\Delta y}.
$$

Note that, if we approximate

$$
\mathcal{T}(U, \nabla U, p, \nabla p, H, \nabla H)_{ij} \approx \begin{pmatrix} 0 \\ \frac{1}{2}\left(\mathcal{T}^{Hor}_{N(ij)} + \mathcal{T}^{Hor}_{S(ij)}\right) \\ \frac{1}{2}\left(\mathcal{T}^{Ver}_{E(ij)} + \mathcal{T}^{Ver}_{W(ij)}\right) \end{pmatrix}, \tag{C.0.1}
$$

then we have a second order approximation of $\mathcal{T}(U^{(k)}, \nabla U^{(k)}, p^{(k)}, \nabla p^{(k)}, H, \nabla H)$ at the center of the volume V_{ij}.

Likewise, $\mathcal{I}(U, \nabla U, H, \nabla H, w)_{i+1/2j+1/2}$ will be discretized for every point $(x_{i+1/2}y_{j+1/2})$ of the staggered mesh by

$$
\mathcal{I}(U, \nabla U, H, \nabla H, w)_{i+1/2j+1/2} \approx h_{i+1/2j+1/2}(\nabla\cdot\boldsymbol{q})_{i+1/2j+1/2}
$$
$$
\tag{C.0.2}
$$
$$
-\boldsymbol{q}_{i+1/2j+1/2}\cdot\nabla(2\eta - h)_{i+1/2j+1/2} + 2h_{i+1/2j+1/2}w_{i+1/2j+1/2},
$$

where $\boldsymbol{q} = (q_x, q_y)$, and

$$
h_{i+1/2j+1/2} = \frac{1}{4}\left(h_{ij} + h_{i+1j} + h_{i+1j+1} + h_{ij+1}\right), \tag{C.0.3}
$$

$$(\nabla \cdot \boldsymbol{q})_{i+1/2j+1/2} = \frac{q_{x,E} - q_{x,W}}{\Delta x} + \frac{q_{y,N} - q_{y,S}}{\Delta y},$$

$$\boldsymbol{q}_{i+1/2j+1/2} = \begin{pmatrix} \dfrac{q_{x,E} + q_{x,W}}{2} \\ \dfrac{q_{y,N} + q_{y,S}}{2} \end{pmatrix}, \quad \nabla(2\eta - h)_{i+1/2j+1/2} = \begin{pmatrix} \dfrac{(2\eta - h)_E - (2\eta - h)_W}{2} \\ \dfrac{(2\eta - h)_N - (2\eta - h)_S}{2} \end{pmatrix},$$

where $q_{x,E}, \ q_{x,W}, \ q_{y,N}, \ q_{y,S}$ and $(2\eta - h)_E, \ (2\eta - h)_W, \ (2\eta - h)_N, \ (2\eta - h)_S$ are second order approximations of $q_x, \ q_y$ and $(2\eta - h)$ respectively in the middle of the edges (see Figure 3.2) given by:

$$q_{x,E} = \frac{1}{2} \left(q_{x,i+1j+1} + q_{x,i+1j} \right)$$

$$+ \frac{1}{2} \Delta t \mathcal{T}_{S(i+1j+1)}^{Hor}(h, h_x, p, p_x, H, H_x) + \frac{1}{2} \Delta t \mathcal{T}_{N(i+1j)}^{Hor}(h, h_x, p, p_x, H, H_x),$$

$$q_{x,W} = \frac{1}{2} \left(q_{x,ij+1} + q_{x,ij} \right)$$

$$+ \frac{1}{2} \Delta t \mathcal{T}_{S(ij+1)}^{Hor}(h, h_x, p, p_x, H, H_x) + \frac{1}{2} \Delta t \mathcal{T}_{N(ij)}^{Hor}(h, h_x, p, p_x, H, H_x),$$

$$q_{y,N} = \frac{1}{2} \left(q_{y,i+1j+1} + q_{y,ij+1} \right)$$

$$+ \frac{1}{2} \Delta t \mathcal{T}_{W(i+1j+1)}^{Ver}(h, h_y, p, p_y, H, H_y) + \frac{1}{2} \Delta t \mathcal{T}_{E(ij+1)}^{Ver}(h, h_y, p, p_y, H, H_y),$$

$$q_{y,S} = \frac{1}{2} \left(q_{y,i+1j} + q_{y,ij} \right)$$

$$+ \frac{1}{2} \Delta t \mathcal{T}_{W(i+1j)}^{Ver}(h, h_y, p, p_y, H, H_y) + \frac{1}{2} \Delta t \mathcal{T}_{E(ij)}^{Ver}(h, h_y, p, p_y, H, H_y),$$

$$(2\eta - h)_E = \frac{2\eta_{i+1j+1} - h_{i+1j+1} + (2\eta_{i+1j} - h_{i+1j})}{2},$$

$$(2\eta - h)_W = \frac{2\eta_{i,j+1} - h_{ij+1} + (2\eta_{ij} - h_{ij})}{2},$$

$$(2\eta - h)_N = \frac{2\eta_{i+1j+1} - h_{i+1j+1} + (2\eta_{ij+1} - h_{ij+1})}{2},$$

$$(2\eta - h)_S = \frac{2\eta_{i+1j} - h_{i+1j} + (2\eta_{ij} - h_{ij})}{2}.$$

Appendix D

Coefficients and matrix of the linear system for the two layer system (NH-2L)

Coefficients of the Poisson-like equations

The coefficients appearing in (3.3.7) and (3.3.8) are:

$$\begin{cases} a_1 = -(l_1 h)^2, \\[2mm] a_2 = -l_1^2 h \partial_x h, \\[2mm] a_3 = l_1 h \partial_{xx} (l_1 h + 2l_2 h - 2\eta) + \partial_x (h_1 + 2l_2 h - 2\eta)^2 + 4, \\[2mm] a_4 = -(l_1 h)^2, \\[2mm] a_5 = -l_1 h \partial_x (3l_1 h + 4l_2 h - 4\eta), \\[2mm] a_6 = -l_1 h \partial_{xx} (l_1 h + 2l_2 h - 2\eta) - \partial_x (l_1 h + 2l_2 h - 2\eta)^2 - 4, \end{cases} \qquad \text{(D.0.1)}$$

$$\begin{cases} b_1 = -(l_2 h)^2 \left(\gamma_1 + 2\frac{l_1}{l_2} \right), \\[2mm] b_2 = l_2 h \partial_x \left((4 - \gamma_1) l_2 h - 4\eta \right), \\[2mm] b_3 = l_2 h \partial_{xx} \left(2l_1 h + (2\gamma_1 + 3) l_2 h - 2(\gamma_1 + 2)\eta \right) + \gamma_1 \partial_x \left(l_2 h - 2\eta \right) + 4\gamma_1, \\[2mm] b_4 = -(l_2 h)^2 \left(\gamma_2 + 2\frac{l_1}{l_2} \right), \\[2mm] b_5 = l_2 h \partial_x \left(4l_1 h + (4 - \gamma_2) l_2 h - 4\eta \right), \\[2mm] b_6 = l_2 h \partial_{xx} \left(-2l_1 h + (2\gamma_2 - 5) l_2 h - 2(\gamma_2 - 2)\eta \right) + \gamma_2 \partial_x \left(l_2 h - 2\eta \right) + 4\gamma_2, \end{cases} \tag{D.0.2}$$

$$RHS_1 = l_1 h^{(\widetilde{k})} \partial_x q_{u,1}^{(\widetilde{k})} - 2 q_{u,1}^{(\widetilde{k})} \partial_x z_1^{(\widetilde{k})} + 2 q_{w,1}^{(\widetilde{k})} + 2 h^{(\widetilde{k})} \partial_t H,$$

$$RHS_2 = 2 l_1 h^{(\widetilde{k})} \partial_x q_{u,1}^{(\widetilde{k})} + l_2 h^{(\widetilde{k})} \partial_x q_{u,2}^{(\widetilde{k})} - 2 q_{u,2}^{(\widetilde{k})} \partial_x z_2^{(\widetilde{k})} + 2 q_{w,2}^{(\widetilde{k})} + 2 h^{(\widetilde{k})} \partial_t H.$$

Matrices of the linear systems

After replace (3.3.9) and (3.3.10) in (3.3.7) and (3.3.8), one has to solve a linear system

$$\boldsymbol{A} \mathcal{P} = \mathcal{RHS},$$

$$\boldsymbol{A} = \boldsymbol{D} + \boldsymbol{M}, \ \boldsymbol{D} = \left(\begin{array}{c|c} T_{(1)} & \mathbf{0} \\ \hline \mathbf{0} & T_{(2)} \end{array} \right), \ \boldsymbol{M} = \left(\begin{array}{c|c} \mathbf{0} & C_{(1)} \\ \hline C_{(2)} & \mathbf{0} \end{array} \right),$$

being $T_{(j)}, C_{(j)}$ tridiagonal matrices of dimension $N \times N$ given by:

$$T_{(1)} = \frac{A_{(1)}}{\Delta x^2} T_{(1,-2,1)} + \frac{A_{(2)}}{2\Delta x} T_{(-1,0,1)} + A_{(3)} I,$$

$$C_{(1)} = \frac{A_{(4)}}{\Delta x^2} T_{(1,-2,1)} + \frac{A_{(5)}}{2\Delta x} T_{(-1,0,1)} + A_{(6)} I,$$

$$T_{(2)} = \frac{B_{(1)}}{\Delta x^2} T_{(1,-2,1)} + \frac{B_{(2)}}{2\Delta x} T_{(-1,0,1)} + B_{(3)} I,$$

$$C_{(2)} = \frac{B_{(4)}}{\Delta x^2} T_{(1,-2,1)} + \frac{B_{(5)}}{2\Delta x} T_{(-1,0,1)} + B_{(6)} I,$$

where

$$T_{(a,b,c)} = \begin{pmatrix} b & c & & & 0 \\ a & b & c & & \\ & \ddots & \ddots & \ddots & \\ & & a & b & c \\ 0 & & & a & b \end{pmatrix},$$

gather the centred finite difference matrix of second $(T_{(1,-2,1)})$ and first $(T_{(-1,0,1)})$ order, and I the identity matrix of dimension $2N \times 2N$.

The matrices $A_{(j)}$ and $B_{(j)}$, $j \in \{1, \ldots, 6\}$ are diagonal matrices of dimension $N \times N$

$$A_{(j)} = \begin{pmatrix} a_{j,1} & & & & 0 \\ & a_{j,2} & & & \\ & & \ddots & & \\ & & & a_{j,N-1} & \\ 0 & & & & a_{j,N} \end{pmatrix}, \ B_{(j)} = \begin{pmatrix} b_{j,1} & & & & 0 \\ & b_{j,2} & & & \\ & & \ddots & & \\ & & & b_{j,N-1} & \\ 0 & & & & b_{j,N} \end{pmatrix},$$

where the coefficients $a_{j,i}$ (and $b_{j,i}$) are the point value approximations of a_j (and b_j) by using compact centred second order finite differences.

Analysis of the linear system for small water heights

If we assume

$$h = \epsilon, \ u_\alpha = w_\alpha = 0,$$

then the coefficients (D.0.1) and (D.0.2) reduce to

$$\begin{cases} a_1 = -l_1^2 \epsilon^2, \\[2mm] a_2 = 0, \\[2mm] a_3 = 4(1 + (\partial_x H)^2) + 2l_1 \epsilon \partial_{xx} H, \\[2mm] a_4 = -l_1^2 \epsilon^2, \\[2mm] a_5 = -4l_1 \epsilon \partial_x H, \\[2mm] a_6 = -4(1 + (\partial_x H)^2) - 2l_1 \epsilon \partial_{xx} H, \end{cases}$$

$$\begin{cases} b_1 = -l_2((\gamma_1 - 2)l_2 + 2)\epsilon^2, \\[2mm] b_2 = 4l_2 \epsilon \partial_x H, \\[2mm] b_3 = 4\gamma_1(1 + (\partial_x H)^2) + 2l_2(\gamma_1 + 2)\epsilon \partial_{xx} H, \\[2mm] b_4 = -l_2((\gamma_2 - 2)l_2 + 2)\epsilon^2, \\[2mm] b_5 = -4l_2 \epsilon \partial_x H, \\[2mm] b_6 = 4\gamma_2(1 + (\partial_x H)^2) + 2l_2(\gamma_2 - 2)\epsilon \partial_{xx} H, \end{cases}$$

and the Right Hand Side vectors reduce to

$$\mathcal{RHS} = \begin{pmatrix} \mathcal{RHS}_1 \\ \mathcal{RHS}_2 \end{pmatrix} = \begin{pmatrix} 0 \\ 0 \end{pmatrix}.$$

In the following analysis we will assume:

$$\epsilon^2 \approx 0, \ \epsilon\partial_x H \approx 0, \ \epsilon\partial_{xx}H \approx 0, \tag{D.0.3}$$

and for the sake of simplicity we assume that $\partial_x H = m$. Then the linear system becomes

$$\boldsymbol{A} = 4(1 + m^2)\left(\begin{array}{c|c} \boldsymbol{I} & -\boldsymbol{I} \\ \hline \gamma_2\boldsymbol{I} & \gamma_1\boldsymbol{I} \end{array}\right).$$

The matrix $\boldsymbol{A}$ is invertible

$$\boldsymbol{A}^{-1} = \frac{1}{4(\gamma_1 + \gamma_2)(m^2 + 1)}\left(\begin{array}{c|c} \gamma_1\boldsymbol{I} & \boldsymbol{I} \\ \hline -\gamma_2\boldsymbol{I} & \boldsymbol{I} \end{array}\right),$$

since we assume in Remark 1.2.2 that $\gamma_1 + \gamma_2 \neq 0$.

We note that (D.0.3) collects the particular case of a slowly varying bathymetry $\partial_x H \approx 0$, and in particular some of the cases under study within this dissertation, when $\partial_x H = m$ with $\epsilon \cdot m \approx 0$.

Appendix E

GPU implementation

We are mainly interested in the application to real-life problems: simulation in channels, dambreak problems, ocean currents, tsunami propagation, etc. Simulating those phenomena gives place to long time simulations in big computational domains. Thus, extremely efficient implementations are needed to be able to analyze those problems in low computational time.

The numerical schemes presented here exhibits a high potential for data parallelization. This fact suggests the design of parallel implementation of the numerical scheme. NVIDIA has developed the CUDA programming toolkit [201] for modern Graphics Processor Units (GPUs). CUDA includes an extension of the C language and facilitates the programming on GPUs for general purpose applications by preventing the programmer to deal with low level language programming on GPU.

In this appendix, guidelines for the implementation of the numerical schemes presented in the previous Section 3.2 for the system (YAM-2D) and in Section 3.5 for the system (NHyp-2D) are given.

GPU implementation for the system (YAM-2D)

The general steps of the parallel implementation for the scheme described in Section 3.2 are shown in Figure E.1. Each step executed on the GPU is assigned to a CUDA *kernel*, which is a function executed on the GPU. Let us describe the main loop of the program. To do so, let us assume that we have at time t^n the values U_{ij}^n for each volume V_{ij} and a precomputed estimation Δt^n. We will also describe the numerical algorithm for the first order in time case.

At the beginning of the algorithm we build the finite volume mesh and the main data structure to be used in GPU. For each volume V_{ij} we store the state variables in one array of type `double4`[1]. This array contains h, q_x, q_y and H, given by U_{ij}^n. A series of CUDA *kernels* will do the following tasks:

1. **Process fluxes on edges:** In this step, each thread computes the contribution at every edge of two adjacent volumes. This thread will also compute the volume integral appearing in (3.2.4) using the mid-point rule. This implementation follows a similar approach to the one applied in [75] and [76]. The edge processing is succesively done in the horizontal and vertical direction, computing even and odd edges separetly. This avoids simultaneous access to the same memory values by two different threads. The computed contributions are stored in an array accumulator of type `double4` with size equal to the number of volumes (see [75] for further details).

   Note that previous computations require the use of the reconstructed values, $U_{ij}^{n,-}, U_{ij}^{n,+}$, as well as the reconstructed topography values, H_{ij}^-, H_{ij}^+.

2. **Update $U_{ij}^{n+1/2}$ for each volume**: In this step, each thread will compute the next state $U_{ij}^{n+1/2}$ for each volume V_{ij} by using the values stored in accumulator and the precomputed estimation of Δt^n. Moreover, a local Δt_{ij}^{n+1} is computed for each volume from the CFL condition.

3. **Solve the linear system for non-hydrostatic pressure**: In order to solve the linear system arising in Subsection 3.2, we use a Jacobi iterative method. This implementation is matrix-free, as the the coefficients of the matrix are not pre-computed and stored. Instead, the coefficients are computed on the fly, which means less memory usage. For each point of the staggered mesh $(x_{i+1/2}, y_{j+1/2})$, we

---

[1]The `double4` data type represent structures with four double precision real components

store the last two iterations of the non-hydrostatic pressure of the Jacobi algorithm, the local error, and the vertical velocity using an array of type `double4`.

This step is splitted into two parts: first, given $\boldsymbol{\mathcal{P}}_{(s)}$, a *kernel* will perform an iteration of the Jacobi method, obtaining $\boldsymbol{\mathcal{P}}_{(s+1)}$ and $\boldsymbol{E}^{(k+1)} = |\boldsymbol{\mathcal{P}}_{(s+1)} - \boldsymbol{\mathcal{P}}_{(s)}|$. Second, another CUDA *kernel* will compute the minimum of all local errors by applying a reduction algorithm in GPU.

4. **Compute the values U_{ij}^{n+1} for each volume**: In this step, each thread has access to a given volume and it computes the next state U_{ij}^{n+1} by using the values of the non-hydrostatic pressure obtained previously.

5. **Get estimation of Δt^{n+1}**: Similarly to what is done in [75] and [76], the minimum of all the local Δt_{ij}^{n+1} values is obtained by applying a reduction algorithm in GPU. This value shall be used as precomputed Δt^{n+1} for the next step of the loop.

When considering a second order discretization in time, the steps 1-4 are repeated twice, for each step of the Runge-Kutta method. Finally, the step 5 is done at the end of the temporal evolution for every time step.
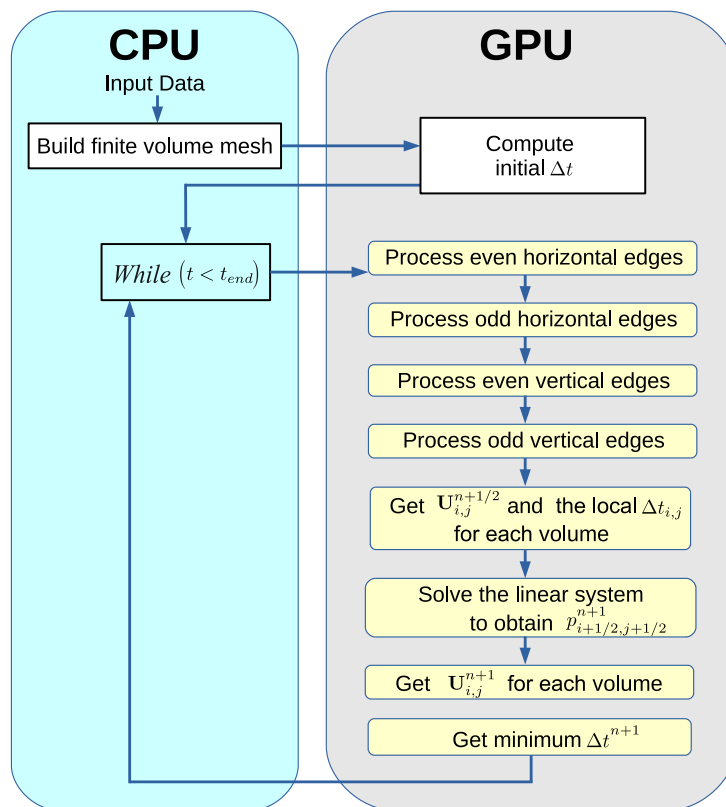

Figure E.1: Parallel CUDA implementation.

GPU implementation for the system (NHyp-2D)

The general steps of the parallel implementation for the scheme described in Section 3.5 are shown in Figure E.2. As before, each step executed on the GPU is assigned to a CUDA *kernel*.

At the beginning of the algorithm we build the *main grid*, that corresponds to the Cartesian finite element mesh $\{V_i\}$ as well as the finite-volume subcell $\{V_{i,S}\}$, that we will call the *subcell grid*. For each element V_i on the *main grid* we store the degree of freedom of the variables h, hu, hv, hw and hp, in one array $\boldsymbol{u}$ of type `double5`[2]. The bathymetry H is stored in another array of type `double`.

Once the data structure is created, the grids are initialized. To do so, we first compute the mean values from a given initial condition on the *subcell grid* and they are stored in a vector $\boldsymbol{v}_0$ of type `double5`. In a second place, the *main grid* is initialized by computing the degree of freedom of the DG polynomial by the reconstruction procedure described in 2.4.13 from the computed mean values. Now the initial time step Δt is computed and the main loop in time of the algorithm starts, where the numerical scheme is iterated until the final simulation time is reached. A series of CUDA *kernels* will do the following tasks:

1. **Space-time predictor and sum regular contributions:** Each thread computes for each element on the *main grid*, the degree of freedom of the predictor solution q_h. This *kernel* also computes the local regular contribution to each element following (2.4.10), avoiding the computation of the double integral over $[t_n, t_{n+1}] \times E_{ij}$. This regular contribution is stored in $\boldsymbol{u}$. Note that the *kernel* acts over each element V_i of the *main grid* and is one of the most intensive but parallelizable part of the proposed numerical scheme.

2. **Solve the Riemann-problems and sum jump contributions:** In this step, the boundary extrapolated states at a given interface E_{ij} are computed

$$\underline{q_{i,h}}(\gamma_k, t_n) \text{ and } \underline{q_{j,h}}(\gamma_k, t_n),$$

γ_k being the Gaussian quadrature points. This boundary extrapolated states are computed from the degree of freedom q_h, obtained at the previous predictor *kernel* for each interface of a given element V_i. After that, it is computed the aforementioned integral. Then, the value of the variable $\boldsymbol{u_1}$ is upgrade to include the jump contribution:

$$\boldsymbol{u} \leftarrow \boldsymbol{u} + \sum_{j \in \mathcal{N}_i} \int_{t^n}^{t^{n+1}} \int_{E_{ij}} D_\Phi^-(\underline{q_{i,h}}(\gamma, t), \underline{q_{j,h}}(\gamma, t), \boldsymbol{n}_{ij}) \, d\gamma \, dt,$$

where the integral is approximated as it was indicated in Section 3.5.

---

[2]The `double5` data type represent structures with five double precision real components

3. **A posteriori subcell finite volume limiter:**

Let us give some brief ideas employed in the implementation of the subcell finite volume solver. It is clear that a *kernel* to project the DG polynomial onto the *subcell grid* must be implemented. The same applies for the reconstruction procedure. Also a third *kernel* to check the validity of the candidate solution computed with the unlimited ADER-DG is also needed. Note that, the third *kernel* can be launched whenever the projected values onto the *subcell grid* are already computed. Additionally, this third *kernel* can not be combined with the first one, since to check the validity of the numerical solution, the corresponding Voronoi neighbours are needed. Therefore, it is justified to split this procedure into at least three parts.

Another *kernel* to evolve the numerical solution with the finite volume solver is needed. In this case, the *kernel* will compute a numerical solution for a given marked $V_{i,S}$ of the *subcell grid* at the previous step, stored in $\boldsymbol{v_0}$. We would like to remark that this procedure applied to two different elements $V_{i,S}$, $V'_{i,S}$ are completely independent. Thus each thread acts over differents marked subcells independently.

Note that the finite-volume *kernel* only acts on a subset contained in the *subcell grid*, in particular the *kernel* acts over those subcells that are marked with the MOOD detector. The number of elements of the subgrid is changing along the simulation, since the number of troubled cells changes. Due to that, it has been implemented a *kernel* that take advantage of such situation. Let us described now the following *kernels* that define the steps during the a posteriori subcell finite volume limiter procedure:

- Projection: In this *kernel*, $\boldsymbol{u}$ that contains $U_h(\mathbf{x}, t^{n+1})$ is projected onto the subcells and stored in an array of type `double5` $\boldsymbol{v_1}$.

- A posteriori MOOD detection procedure: Each thread checks the relaxed discrete maximum principle, the positivity of the water height and the presence of floating point errors (`NaN`) within each cell V_i. This kernel also uses $\boldsymbol{v_0}$.
  To do so, an array of type `int2` is defined on the *main grid* as (fl_i, pos_i), being

$$fl_i = \begin{cases} 1, & \text{if } V_i \text{ is detected as a troubled cell} \\ 0, & \text{Otherwise} \end{cases}, \ pos_i = \begin{cases} i, & \text{if } fl_i = 1 \\ -1, & \text{if } fl_i = 0 \end{cases}$$

- Counting troubled cells: In this step, a *kernel* is used to count the number of troubled cells, and it is stored in a `integer` variable $M_{troubled}$. To do so, we remark that:

$$M_{troubled} = \sum_i fl_i,$$

that is computed by applying a reduction algorithm in GPU, similarly to what is done in [75] and [76].

- Sorting troubled cells: A sorting algorithm is applied to the vector pos_i. The algorithm separates positive from negative values. In that way, we can separate the marked index cells from the rest (see Figure **??** to better clarify). To do so, we use the `Thrust` c++ library for CUDA.

- Finite volume solver: This *kernel* contains a finite volume solver that computes a numerical solution on the time-dependent cluster formed by the marked subcells, whose indexes are ordered and stored in pos_i. Thanks to that, the *kernel* it is configured on the small grid that contains the troubled cells and acts in parallel over a smaller set of data. Note that with this procedure, no communication is needed for the computation of two different marked subcells. The results are stored in v_1.

- Reconstruction: In this *kernel*, the degree of freedom of the DG polynomial, are reconstructed from the news computed mean values v_1 that contains the solution given by the finite-volume method at the previous step. This *kernel*, as the previous one, only acts on those subcells that are marked as troubled.

4. **Element update and computing the local Δt_i^{n+1}:** In this *kernel* the mean values are updated, $v_1 \leftarrow v_0$, and a local Δt_i^{n+1} is computed for each element of the *main grid*.

5. **Computing the minimum of all local Δ_i^{n+1}:** Similarly to what is done in [75] and [76], the minimum of all the local Δt_i^{n+1} values is obtained by applying a reduction algorithm in GPU. This value shall be used as precomputed Δt^{n+1} for the next step of the loop.
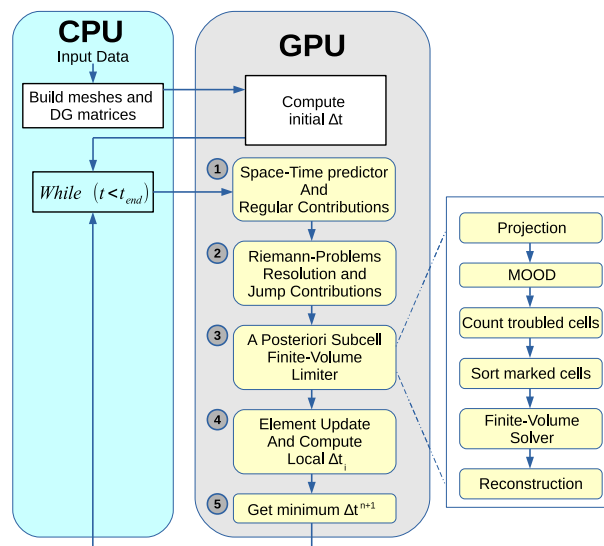

Figure E.2: Parallel CUDA implementation.

a)

Ω_1 $fl=1$ $pos=1$	Ω_2 $fl=1$ $pos=2$	Ω_3 $fl=0$ $pos=-1$	Ω_4 $fl=0$ $pos=-1$
Ω_5 $fl=1$ $pos=3$	Ω_6 $fl=1$ $pos=4$	Ω_7 $fl=0$ $pos=-1$	Ω_8 $fl=0$ $pos=-1$
Ω_9 $fl=0$ $pos=-1$	Ω_{10} $fl=0$ $pos=-1$	Ω_{11} $fl=0$ $pos=-1$	Ω_{12} $fl=1$ $pos=5$
Ω_{13} $fl=0$ $pos=-1$	Ω_{14} $fl=1$ $pos=6$	Ω_{15} $fl=1$ $pos=7$	Ω_{16} $fl=1$ $pos=8$

b)

| 1 | 2 | -1 | -1 | 3 | 4 | -1 | -1 | -1 | -1 | 5 | -1 | 6 | 7 | 8 |

c)

| 1 | 2 | 5 | 6 | 12 | 14 | 15 | 16 | -1 | -1 | -1 | -1 | -1 | -1 | -1 | -1 |

Figure E.3: Troubled cells marking process. In $a)$, an example of tagging. In $b)$ and $c)$ the array of integers pos_i before and after the *Sorting troubled cells kernel*.

Bibliography

[1] M.B. Abbott, A.D. McCowan, and I.R. Warren. Accuracy of short wave numerical models. *Journal of Hydraulic Engineering*, 110(10):1287–1301, 1984.

[2] Rémi Abgrall and Smadar Karni. A comment on the computation of non–conservative products. *Journal of Computational Physics*, 229(8):2759–2763, April 2010.

[3] J.E. Adsuara, I. Cordero-Carrión, P. Cerdá-Durán, and M.A. Aloy. Scheduled relaxation jacobi method: Improvements and applications. *Journal of Computational Physics*, 321:369–413, sep 2016.

[4] N. Aïssiouene, M.-O. Bristeau, E. Godlewski, A. Mangeney, C. Parés, and J. Sainte-Marie. Application of a combined finite element—finite volume method to a 2d non–hydrostatic shallow water problem. In Clément Cancès and Pascal Omnes, editors, *Finite Volumes for Complex Applications VIII–Hyperbolic, Elliptic and Parabolic Problems*, pages 219–226, Cham, 2017. Springer International Publishing.

[5] Kazuo Ashida and Masanori Michiue. Study on hydraulic resistance and bed–load transport rate in alluvial streams. *Proceedings of the Japan Society of Civil Engineers*, 206:59–69, 1972.

[6] Emmanuel Audusse, François Bouchut, Marie-Odile Bristeau, Rupert Klein, and Benoit Perthame. A fast and stable well–balanced scheme with hydrostatic reconstruction for shallow water flows. *SIAM Journal on Scientific Computing*, 25:2050–2065, 2004.

[7] Y. Zech B. Spinewine. Small–scale laboratory dam–break waves on movable beds. *J. Hydraulic Res.*, 1(45), 2007.

[8] R.A. Bagnold. The flow of cohesionless grains in fluids. *Philosophical Transactions of the Royal Society of London A: Mathematical, Physical and Engineering Sciences*, 249(964):235–297, 1956.

[9] Yefei Bai and Kwok Fai Cheung. Depth integrated free surface flow with parameterized non hydrostatic pressure. *International Journal for Numerical Methods in Fluids*, 71(4):403–421, 2012.

[10] Yefei Bai and Kwok Fai Cheung. Linear shoaling of free–surface waves in multi–layer non–hydrostatic models. *Ocean Modelling*, 121:90 – 104, 2018.

[11] D. Baldwin, Ü. Göktaş, W. Hereman, L. Hong, R.S. Martino, and J.C. Miller. Symbolic computation of exact solutions expressible in hyperbolic and elliptic functions for nonlinear pdes. *Journal of Symbolic Computation*, 37(6):669–705, 2004.

[12] Dinshaw S. Balsara. A two-dimensional hllc riemann solver for conservation laws: Application to euler and magnetohydrodynamic flows. *Journal of Computational Physics*, 231(22):7476 – 7503, 2012.

[13] S. Beji and J.A. Battjes. Experimental investigation of wave propagation over a bar. *Coastal Engineering*, 19:151–162, 1993.

[14] A. Bermúdez and M.E. Vázquez. Upwind methods for hyperbolic conservation laws with source terms. *Computers & Fluids*, 23(8):1049–1071, November 1994.

[15] C. Berthon, F. Coquel, and P.G. LeFloch. Why many theories of shock waves are necessary: Kinetic functions, equivalent equations, and fourth–order models. *J. Comput. Phys.*, pages 4162–4189, 2008.

[16] Christophe Berthon and Frédéric Coquel. Nonlinear Projection Methods for Multi–Entropies Navier–Stokes Systems. *Mathematics of Computation*, 76(259):1163–1194, 2007.

[17] W. Boscheri and M. Dumbser. Arbitrary–Lagrangian–Eulerian Discontinuous Galerkin schemes with a posteriori subcell finite volume limiting on moving unstructured meshes. *Journal of Computational Physics*, 346:449–479, 2017.

[18] François Bouchut. *Nonlinear stability of finite volume methods for hyperbolic conservation laws and well–balanced schemes for sources.* Frontiers in Mathematics. Birkhäuser Verlag, Basel, 2004.

[19] J. Boussinesq. Théorie des ondes et des remous qui se propagent le long dun canal rectangulaire horizontal, en communiquant au liquide contenu dans ce canal des vitesses sensiblement pareilles de la surface au fond. *Journal de Mathématiques Pures et Appliquèes*, 17:55–108, 1872.

[20] M.J. Briggs., C.E. Synolakis, G.S. Harkins, and D.R. Green. Laboratory experiments of tsunami runup on a circular island. *pure and applied geophysics*, 144(3):569–593, 1995.

[21] M.-O. Bristeau, A. Mangeney, J. Sainte-Marie, and N. Seguin. An energy–consistent depth–averaged euler system: Derivation and properties. *Discrete and Continuous Dynamical Systems Series B*, 20(4):961–988, 2015.

[22] A.R. Brodtkorb, T.R. Hagen, and M.L. Sætra. Graphics processing unit (GPU) programming strategies and trends in GPU computing. *J. Parallel Distrib. Comput.*, 73(1):43–13, 2013.

[23] R. K. Bullough. "the wave" "par excellence", the solitary progressive great wave of equilibrium of the fluid: An early history of the solitary wave. In Muthusamy Lakshmanan, editor, *Solitons*, pages 7–42, Berlin, Heidelberg, 1988. Springer Berlin Heidelberg.

[24] M. Castro, E. Fernández-Nieto, A. Ferreiro, J. García-Rodríguez, and C. Parés. High order extensions of Roe schemes for two–dimensional nonconservative hyperbolic systems. *Journal of Scientific Computing*, 39(1):67–114, 2008.

[25] M. J. Castro, J. M. Gallardo, and C. Parés. High–order finite volume schemes based on reconstruction of states for solving hyperbolic systems with nonconservative

products. applications to shallow–water systems. *Mathematics of Computation*, 75:1103–1134, 2006.

[26] M. J. Castro, J. A. García, J. M. González, and C. Parés. A parallel 2D finite volume scheme for solving systems of balance laws with nonconservative products: Application to shallow flows. *Computer Methods in Applied Mechanics and Engineering*, 195(19–22):2788–2815, 2006.

[27] M. J. Castro, J. A. García-Rodríguez, J. M. González-Vida, and C. Parés. A parallel 2d finite volume scheme for solving systems of balance laws with nonconservative products: application to shallow flows. *Comput. Methods Appl. Mech. Engrg.*, 195(19–22):2788–2815, 2006.

[28] M. J. Castro, S. Ortega, M. de la Asunción, J. M. Mantas, and J. M. Gallardo. GPU computing for shallow water flow simulation based on finite volume schemes. *Comptes Rendus Mécanique*, 339(2–3):165–184, 2011.

[29] Manuel Castro, José Gallardo, and Carlos Parés. High order finite volume schemes based on reconstruction of states for solving hyperbolic systems with nonconservative products. Applications to shallow–water systems. *Mathematics of computation*, 75(255):1103–1134, 2006.

[30] Manuel Castro, Jorge Macías, and Carlos Parés. A Q–scheme for a class of systems of coupled conservation laws with source term. Application to a two–layer 1–D shallow water system. *M2AN Math. Model. Numer. Anal.*, 35(1):107–127, 2001.

[31] Manuel J. Castro, Yuanzhen Cheng, Alina Chertock, and Alexander Kurganov. Solving two–mode shallow water equations using finite volume methods. *Commun. Comput. Phys.*, 15(5):1323–1354, 2014.

[32] Manuel J. Castro, José M. Gallardo, and Antonio Marquina. Approximate Osher–Solomon schemes for hyperbolic systems. *Applied Mathematics and Computation*, 272, Part 2:347–368, January 2016.

[33] Manuel J. Castro, Philippe G. LeFloch, María Luz Muñoz–Ruiz, and Carlos Parés. Why many theories of shock waves are necessary: Convergence error in formally path–consistent schemes. *Journal of Computational Physics*, 227(17):8107–8129, September 2008.

[34] Manuel J. Castro, Sergio Ortega, and Carlos Parés. Well–balanced methods for the shallow water equations in spherical coordinates. *Computers & Fluids*, 157:196–207, 2017.

[35] Manuel J. Castro, Alberto Pardo, Carlos Parés, and E. F. Toro. On some fast well–balanced first order solvers for nonconservative systems. *Math. Comp.*, 79(271):1427–1472, 2010.

[36] Manuel J. Castro, Carlos Parés, Gabriella Puppo, and Giovanni Russo. Central schemes for nonconservative hyperbolic systems. *SIAM J. Sci. Comput.*, 34(5):523–558, 2012.

[37] M.J. Castro, T. Chacón, E.D. Fernández, and C. Parés. On well–balanced finite volume methods for non–conservative non–homogeneous hyperbolic systems. *SIAM J. Sci. Comput.*, 29:1093–1126, 2007.

[38] M.J. Castro, T. Morales de Luna, and C. Parés. Chapter 6–well–balanced schemes and path–conservative numerical methods. In Rémi Abgrall and Chi-Wang Shu, editors, *Handbook of Numerical Methods for Hyperbolic Problems*, volume 18 of *Handbook of Numerical Analysis*, pages 131–175. Elsevier, 2017.

[39] M.J. Castro, C. Escalante, and R. Morales de Luna. Modelling and simulation of non–hydrostatic shallow flows. In Clément Cancès and Pascal Omnes, editors, *Finite Volumes for Complex Applications VIII–Hyperbolic, Elliptic and Parabolic Problems*, pages 119–126, Cham, 2017. Springer International Publishing.

[40] M.J. Castro and E.D. Fernández-Nieto. A class of computationally fast first order finite volume solvers: PVM methods. *SIAM Journal on Scientific Computing*, 34(4):173–196, 2012.

[41] M.J. Castro, E.D. Fernández-Nieto, A. M. Ferreiro, J. A. García-Rodríguez, and C. Parés. High order extensions of Roe schemes for two–dimensional nonconservative hyperbolic systems. *J. Sci. Comput.*, 39(1):67–114, 2009.

[42] M.J. Castro, A.M. Ferreiro Ferreiro, J.A. García-Rodríguez, J.M. González-Vida, J. Macías, C. Parés, and M. Elena Vázquez-Cendón. The numerical treatment of wet/dry fronts in shallow flows: application to one–layer and two–layer systems. *Mathematical and Computer Modelling*, 42(3):419 – 439, 2005.

[43] M.J. Castro, J.M. Gallardo, and A. Marquina. A class of incomplete Riemann solvers based on uniform rational approximations to the absolute value function. *Journal of Scientific Computing*, 60(2):363–389, 2014.

[44] M.J. Castro, J.M. Gallardo, and C. Parés. High order finite volume schemes based on reconstruction of states for solving hyperbolic systems with nonconservative products. applications to shallow water systems. *Mathematics of Computation*, 75:1103–1134, 2006.

[45] M.J. Castro, J.A. López, and C. Parés. Well–balanced high order extensions of godunov method for linear balance laws. *SIAM J. Num. Anal.*, 46:1012–1039, 2008.

[46] M.J. Castro, A. Pardo, C. Parés, and E.F. Toro. On some fast well–balanced first order solvers for nonconservative systems. *Mathematics of computation*, 79(271):1427–1472, 2010.

[47] M.J. Castro, A. Pardo, C. Parés, and E.F. Toro. On some fast well–balanced first order solvers for nonconservative systems. *Mathematics of Computation*, 79(271):1427–1472, 2010.

[48] M. J. Castro Díaz and E. Fernández-Nieto. A class of computationally fast first order finite volume solvers: PVM methods. *SIAM Journal on Scientific Computing*, 34(4):2173–2196, January 2012.

[49] Manuel Jesús Castro Díaz, Enrique Domingo Fernández-Nieto, Tomás Morales de Luna, Gladys Narbona-Reina, and Carlos Parés Madroñal. A HLLC scheme for nonconservative hyperbolic problems. Application to turbidity currents with sediment transport. *ESAIM: Mathematical Modelling and Numerical Analysis*, 47(1):1–32, July 2013.

[50] M.J. Castro Díaz, E.D. Fernández-Nieto, and A.M. Ferreiro. Sediment transport models in shallow water equations and numerical approach by high order finite volume methods. *Computers & Fluids*, 37(3):299–316, March 2008.

[51] V. Casulli. A semi–implicit finite difference method for non–hydrostatic free–surface flows. *International Journal for Numerical Methods in Fluids*, 30:425–440, 1999.

[52] V. Casulli. A semi–implicit finite difference method for non–hydrostatic free surface flows. *Numerical Methods in Fluids*, 30(4):425–440, 1999.

[53] V. Casulli. A semi–implicit finite difference method for non–hydrostatic free surface flows. *Numerical Methods in Fluids*, 30(4):425–440, 1999.

[54] J. J Cauret, J. F Colombeau, and A. Y Le Roux. Discontinuous generalized solutions of nonlinear nonconservative hyperbolic equations. *Journal of Mathematical Analysis and Applications*, 139(2):552–573, May 1989.

[55] Tomás Chacón Rebollo, Antonio Domínguez Delgado, and Enrique D. Fernández Nieto. A family of stable numerical solvers for the shallow water equations with source terms. *Computer Methods in Applied Mechanics and Engineering*, 192(1–2):203–225, January 2003.

[56] Tomás Chacón Rebollo, Antonio Domínguez Delgado, and Enrique D. Fernández Nieto. Asymptotically balanced schemes for non–homogeneous hyperbolic systems. Application to the Shallow Water equations. *Comptes Rendus Mathematique*, 338(1):85–90, January 2004.

[57] N. Chalmers and E. Lorin. On the numerical approximation of one–dimensional nonconservative hyperbolic systems. *Journal of Computational Science*, 4(1–2):111–124, January 2013.

[58] H. Chanson. The hydraulics of open channel flow: an introduction. *Elsevier Butterworth–Heinemann Oxford*, 2004.

[59] D.E. Charrier and T. Weinzierl. Stop talking to me–a communication–avoiding ADER–DG realisation. *SIAM Journal on Scientific Computing*, 2018. submitted to. https://arxiv.org/abs/1801.08682.

[60] F. Charru. Selection of the ripple length on a granular bed sheared by a liquid flow. *Physics of Fluids*, 18(12):121508, 2006.

[61] F. Chazel, D. Lannes, and F. F. Marche. Numerical simulation of strongly nonlinear and dispersive waves using a green–naghdi model. *Journal of Scientific Computing*, 48(1):105–116, Jul 2011.

[62] Wang Chi-Shu. Essentially non-oscillatory and weighted essentially non–oscillatory schemes for hyperbolic conservation laws. Technical report, Institute for Computer Applications in Science and Engineering (ICASE), 1997.

[63] J. Chorin. Numerical solution of the navier–stokes equations. *Mathematics of computation*, 22:745–762, 1968.

[64] S. Clain, S. Diot, and R. Loubère. A high–order finite volume method for systems of conservation laws–multi–dimensional optimal order detection (MOOD). *Journal of Computational Physics*, 230(10):4028 – 4050, 2011.

[65] D. Clamond and D. Dutykh. https://es.mathworks.com/matlabcentral/fileexchange/39189--solitary--water--wave, 2012.

[66] B. Cockburn, S. Hou, and C.W. Shu. The Runge–Kutta local projection discontinuous Galerkin finite element method for conservation laws IV: the multidimensional case. *Mathematics of Computation*, 54(190):545–581, 1990.

[67] B. Cockburn, S.Y. Lin, and C.W. Shu. TVB Runge–Kutta local projection discontinuous Galerkin finite element method for conservation laws III: one–dimensional systems. *Journal of Computational Physics*, 84(1):90–113, 1989.

[68] B. Cockburn and C.W. Shu. TVB Runge–Kutta local projection discontinuous Galerkin finite element method for conservation laws II: general framework. *Mathematics of Computation*, 52(186):411–435, 1989.

[69] B. Cockburn and C.W. Shu. The Runge–Kutta discontinuous Galerkin method for conservation laws V: multidimensional systems . *Journal of Computational Physics*, 141(2):199–224, 1998.

[70] I. Cravero and M. Semplice. On the accuracy of weno and cweno reconstructions of third order on nonuniform meshes. *Journal of Scientific Computing*, 67(3):1219–1246, Jun 2016.

[71] H. Cui, J.D. Pietrzak, and G.S. Stelling. Optimal dispersion with minimized poisson equations for non–hydrostatic free surface flows. *Ocean Modelling*, 81:1 – 12, 2014.

[72] Gianni Dal Maso, Philippe G. LeFloch, and François Murat. Definition and weak stability of nonconservative products. *Journal de Mathématiques Pures et Appliqués*, 74, 01 1995.

[73] S. Davis. Simplified second–order godunov–type methods. *SIAM Journal on Scientific and Statistical Computing*, 9(3):445–473, 1988.

[74] M. de la Asunción. *Desarrollo de Software Numérico de Simulación de Flujos Geofísicos Basado en Volúmenes Finitos usando Hardware Gráfico*. PhD thesis, Universidad de Granada, 2012.

[75] M. de la Asunción, J.M. Mantas, and M.J. Castro. *Programming CUDA–Based GPUs to Simulate Two–Layer Shallow Water Flows*, volume 6272 of *Lecture Notes in Computer Science*, pages 353–364. Springer Berlin / Heidelberg, 2010.

[76] M. de la Asunción, J.M. Mantas, and M.J. Castro. Simulation of one–layer shallow water systems on multicore and CUDA architecture. *The Journal of Supercomputing*, 58(2):206–214, 2011.

[77] M. de la Asunción, J.M. Mantas, M.J. Castro, and E.D. Fernández-Nieto. Two-layer shallow water simulation on clusters of CUDA enabled GPUs. *Parallel CFD*, 2011.

[78] M. de la Asunción, J.M. Mantas, M.J. Castro, and E.D. Fernández-Nieto. An mpi-cuda implementation of an improved roe method for two-layer shallow water systems. *Journal of Parallel and Distributed Computing, Special Issue on Accelerators for High-Performance Computing*, 72(9):1065–1072, 2012.

[79] M. de la Asunción, J.M. Mantas, M.J. Castro, and E.D. Fernández-Nieto. Two-layer shallow water simulation on clusters of CUDA enabled GPUs. *Advances in Engineering Software*, 99:59–72, 2016.

[80] Marc de la Asunción, Manuel J. Castro Díaz, E. D. Fernández-Nieto, José M. Mantas, Sergio Ortega Acosta, and J. M. González-Vida. Efficient GPU implementation of a two waves TVD–WAF method for the two–dimensional one layer shallow water system on structured meshes. *Computers & Fluids*, 80:441–452, 2013.

[81] T. Morales de Luna and C. Parés M.J. Castro. A duality method for sediment transport based on a modified meyer–peter & müller model. *Journal of Scientific Computing*, 1(48):258–273, 2011.

[82] Florian De Vuyst and Y. Maday. *Schémas nonconservatifs et schémas cinétiques pour la simulation numérique d'écoulements hypersoniques non visqueux en déséquilibre thermochimique*. Text, Thése de Doctorat de l'Université Paris VI, 1994.

[83] A. Dedner, F. Kemm, D. Kröner, C.D Munz, T. Schnitzer, and M. Wesenberg. Hyperbolic Divergence Cleaning for the MHD Equations. *Journal of Computational Physics*, 175:645–673, January 2002.

[84] Pierre Degond, Pierre-François Peyrard, Giovanni Russo, and Philippe Villedieu. Polynomial upwind schemes for hyperbolic systems. *Comptes Rendus de l'Académie des Sciences–Series I–Mathematics*, 328(6):479–483, March 1999.

[85] Vivien Desveaux, Markus Zenk, Christophe Berthon, and Christian Klingenberg. A well–balanced scheme to capture non–explicit steady states in the Euler equations with gravity. *International Journal for Numerical Methods in Fluids*, 81(2):104–127, May 2016.

[86] Vivien Desveaux, Markus Zenk, Christophe Berthon, and Christian Klingenberg. Well–balanced schemes to capture non–explicit steady states: Ripa model. *Mathematics of Computation*, 85(300):1571–1602, 2016.

[87] M.W. Dingemans. Comparison of computations with boussinesq–like models and laboratory measurements. *Report H–1684.12, 32, Delft Hydraulics*, 1994.

[88] S. Diot, S. Clain, and R. Loubère. Improved detection criteria for the multi–dimensional optimal order detection (MOOD) on unstructured meshes with very high–order polynomials. *Computers and Fluids*, 64:43–63, 2012.

[89] S. Diot, R. Loubère, and S. Clain. The MOOD method in the three–dimensional case: Very–high–order finite volume method for hyperbolic systems. *International Journal of Numerical Methods in Fluids*, 73:362–392, 2013.

[90] M. Dumbser and D.S. Balsara. A new, efficient formulation of the HLLEM Riemann solver for general conservative and non–conservative hyperbolic systems. *Journal of Computational Physics*, 304:275–319, 2016.

[91] M. Dumbser, D.S. Balsara, E.F. Toro, and C.D. Munz. A unified framework for the construction of one–step finite volume and discontinuous Galerkin schemes on unstructured meshes. *Journal of Computational Physics*, 227(18):8209–8253, 2008.

[92] M. Dumbser, M. Castro, C. Parés, and E.F. Toro. ADER schemes on unstructured meshes for non–conservative hyperbolic systems: Applications to geophysical flows. *Computers and Fluids*, 38:1731–1748, 2009.

[93] M. Dumbser, C. Enaux, and E.F. Toro. Finite Volume schemes of very high order of accuracy for stiff hyperbolic balance laws. *Journal of Computational Physics*, 227(8):3971–4001, 2008.

[94] M. Dumbser and M. Facchini. A local space–time discontinuous Galerkin method for Boussinesq–type equations. *Applied Mathematics and Computation*, 272:336–346, 2016.

[95] M. Dumbser, A. Hidalgo, M. Castro, C. Parés, and E.F. Toro. FORCE schemes on unstructured meshes II: Non–conservative hyperbolic systems. *Computer Methods in Applied Mechanics and Engineering*, 199:625–647, 2010.

[96] M. Dumbser and R. Loubère. A simple robust and accurate a posteriori sub–cell finite volume limiter for the discontinuous Galerkin method on unstructured meshes. *Journal of Computational Physics*, 319:163–199, 2016.

[97] M. Dumbser and C.D. Munz. Building blocks for arbitrary high order discontinuous Galerkin schemes. *Journal of Scientific Computing*, 27:215–230, 2006.

[98] M. Dumbser, O. Zanotti, R. Loubère, and S. Diot. A posteriori subcell limiting of the discontinuous Galerkin finite element method for hyperbolic conservation laws. *Journal of Computational Physics*, 278:47–75, 2014.

[99] Michael Dumbser, Cedric Enaux, and Eleuterio F. Toro. Finite volume schemes of very high order of accuracy for stiff hyperbolic balance laws. *Journal of Computational Physics*, 227(8):3971–4001, April 2008.

[100] Michael Dumbser, A. Hidalgo, Manuel J. Castro Díaz, Carlos Parés, and E.F. Toro. FORCE schemes on unstructured meshes II: Nonconservative hyperbolicsystems. *Comput. Methods Appl. Mech. Engrg.*, 199(9–12):625–647, 2010.

[101] Michael Dumbser and Martin Käser. Arbitrary high order non–oscillatory finite volume schemes on unstructured meshes for linear hyperbolic systems. *Journal of Computational Physics*, 221(2):693–723, February 2007.

[102] Michael Dumbser, Martin Käser, Vladimir A. Titarev, and Eleuterio F. Toro. Quadrature–free non–oscillatory finite volume schemes on unstructured meshes for nonlinear hyperbolic systems. *Journal of Computational Physics*, 226(1):204–243, September 2007.

[103] A. Duran and F. Marche. A discontinuous galerkin method for a new class of green–naghdi equations on simplicial unstructured meshes. *Applied Mathematical Modelling*, 45:840 – 864, 2017.

[104] D. Dutykh and D. Clamond. Efficient computation of steady solitary gravity waves. *Wave Motion*, 51(1):86–99, 2014.

[105] M.J. Castro. C. Parés E. D. Fernández-Nieto. On an intermediate field capturing riemann solver based on a parabolic viscosity matrix for the two–layer shallow water system. *Journal Scientific Computing*, 1–3(48):117–140, 2011.

[106] B. Einfeldt, P.L Roe, C.D. Munz, and B. Sjogreen. On Godunov–type methods near low densities. *Journal of Computational Physics*, 92:273–295, February 1991.

[107] H. A. Einstein. Formulas for the transportation of bed load. *ASCE*, 107:561–575, 1942.

[108] F. Enet and S.T. Grilli. Experimental study of tsunami generation by three–dimensional rigid underwater landslides. *Journal of Waterway, Port, Coastal, and Ocean Engineering*, 133(6):442–454, 2007.

[109] A.P. Engsig-Karup, J.S. Hesthaven, H.B. Bingham, and T. Warburton. DG–FEM solution for nonlinear wave–structure interaction using Boussinesq–type equations. *Coastal Engineering*, 55:197–208, 2008.

[110] C. Escalante, G.Narbona-Reina, E.D. Fernández-Nieto, and T. Morales. A non–hydrostatic bilayer model for bed–load sediment transport that tends to classical sve models for small morphodynamic time. *Ongoing work*, 2018.

[111] C. Escalante, M.Dumbser, and M.J. Castro. An efficient hyperbolic relaxation system for dispersive non–hydrostatic water waves and its solution with high order discontinuous galerkin schemes. *Journal of Computational Physics*, 2018.

[112] C. Escalante, T. Morales, and M.J. Castro. Non–hydrostatic pressure shallow flows: Gpu implementation using finite volume and finite difference scheme. *Applied Mathematics and Computation*, 338:631–659, 2018.

[113] F. Exner. Uber die wechselwirkung zwischen wasser und geschiebe in flüssen. *itzungsber., Akad. Wissenschaften*, 134, 1925.

[114] J. Dresoe F. Engelund. A sediment transport model for straight alluvial channels. *Nordic Hydrol.*, 7:293–306, 1976.

[115] F. Fambri, M. Dumbser, S. Köppel, L. Rezzolla, and O. Zanotti. ADER discontinuous Galerkin schemes for general–relativistic ideal magnetohydrodynamics. *Monthly Notices of the Royal Astronomical Society*, 477:4543–4564, 2018.

[116] H. Favre. Ondes de translation dans les canaux découverts. *Paris: Dunod*, 1935.

[117] N. Favrie and S. Gavrilyuk. A rapid numerical method for solving serre–green–naghdi equations describing long free surface gravity waves. *Nonlinearity*, 30(7):2718, 2017.

[118] C. Escalante E.D. Fernández-Nieto, T. Morales, and M.J. Castro. An efficient two–layer non–hydrostatic approach for dispersive water waves. *Journal of Scientific Computing*, doi.org/10.1007/s10915-018-0849-9, 2018.

[119] E. D. Fernández-Nieto, F. Bouchut, D. Bresch, M. J. Castro Díaz, and A. Mangeney. A new Savage–Hutter type model for submarine avalanches and generated tsunami. *Journal of Computational Physics*, 227(16):7720–7754, August 2008.

[120] E. D. Fernández-Nieto, José M. Gallardo, and Paul Vigneaux. Efficient numerical schemes for viscoplastic avalanches. Part 1: The 1D case. *Journal of Computational Physics*, 264(1):55–90, May 2014.

[121] E. D. Fernández-Nieto, E. H. Koné, and T. Chacón Rebollo. A multilayer method for the hydrostatic navier–stokes equations: A particular weak solution. *J. Sci. Comput.*, 60(2):408–437, August 2014.

[122] E. D. Fernández-Nieto, C. Lucas, T. Morales de Luna, and S. Cordier. On the influence of the thickness of the sediment moving layer in the definition of the bedload trasport formula in exner systems. *Computer & Fluids*, 91:87–106, 2014.

[123] E.D. Fernández-Nieto, T. Morales de Luna, G. Narbona-Reina, and J.D. Zabsonré. Formal deduction of the saint–venant–exner model including arbitrarily sloping sediment beds and associated energy. *ESAIM: Mathematical Modelling and Numerical Analysis*, 51:115–145, 2017.

[124] E.D. Fernández-Nieto, M. Parisot, Y. Penel, and J. Sainte-Marie. Layer–averaged approximation of euler equations for free surface flows with a non–hydrostatic pressure. *Accepted in Communications in Mathematical Sciences. (hal–01324012v3)*, 2018.

[125] Enrique D. Fernández-Nieto, Manuel J. Castro, and Carlos Parés. On an intermediate field capturing riemann solver based on a parabolic viscosity matrix for the two–layer shallow water system. *J. Sci. Comput*, 48(1–3):117–140, 2011.

[126] A. C. Fowler, N. Kopteva, and C. Oakley. The formation of river channel. *SIAM J. Appl. Math*, 67:1016–1040, 2007.

[127] L. Fraccarollo and H. Capart. Riemann wave description of erosional dam–break flows. *Journal of Fluid Mechanics*, 461:183–228, 2002.

[128] L. Solari G. Parker, G. Seminara. Bed load at low shields stress on arbitrarily sloping beds: Alternative entrainment formulation. *Water Resources Res.*, 7(29), 2003.

[129] G. Parker G. Seminara, L. Solari. Bed load at low shields stress on arbitrarily sloping beds: Failure of the bagnold hypothesis. *Water Resources Res*, Vol, 2002.

[130] G. N. Galica, N. Heuer, R. Rodríguez, and E. F. Toro. MUSTA: A multi–stage numerical flux. *Applied Numerical Mathematics*, 56(10):1464–1479, October 2006.

[131] José M. Gallardo, Sergio Ortega, Marc de la Asunción, and José Miguel Mantas. Two–dimensional compact third–order polynomial reconstructions. solving nonconservative hyperbolic systems using gpus. *Journal of Scientific Computing*, 48(1):141–163, Jul 2011.

[132] G. Gassner, M. Dumbser, F. Hindenlang, and C.D. Munz. Explicit one–step time discretizations for discontinuous Galerkin and finite volume schemes based on local predictors. *Journal of Computational Physics*, 230(11):4232–4247, 2011.

[133] S. Gavrilyuk, V.Y. Liapidevskii, and A.A. Chesnokov. Spilling breakers in shallow water: applications to Favre waves and to the shoaling and breaking of solitary waves. *Journal of Fluid Mechanics*, 808:441–468, December 2016.

[134] Paola Goatin and Philippe G. LeFloch. The Riemann problem for a class of resonant hyperbolic systems of balance laws. *Annales de l'Institut Henri Poincare (C) Non Linear Analysis*, 21(6):881–902, November 2004.

[135] M.F. Gobbi, J.T. Kirby, and W. Ge. A fully nonlinear boussinesq model for surface waves. part 2. extension to o(kh)4. *Journal of Fluid Mechanics*, 405:181–210, 2000.

[136] S.K. Godunov. An interesting class of quasilinear systems. *Dokl. Akad. Nauk SSSR*, 139(3):521–523, 1961.

[137] S.K. Godunov and E.I. Romenski. Nonstationary equations of nonlinear elasticity theory in eulerian coordinates. *Journal of Applied Mechanics and Technical Physics*, 13(6):868–884, 1972.

[138] S.K. Godunov and E.I. Romenski. *Elements of continuum mechanics and conservation laws.* Kluwer Academic/Plenum Publishers, 2003.

[139] L. Gosse. A well–balanced flux–vector splitting scheme designed for hyperbolic systems of conservation laws with source terms. *Comput. Math. Appl.*, 39(9–10):135–159, 2000.

[140] Laurent Gosse. A well–balanced scheme using non–conservative products designed for hyperbolic systems of conservation laws with source terms. *Math. Models Methods Appl. Sci.*, 11(2):339–365, 2001.

[141] Laurent Gosse. Localization effects and measure source terms in numerical schemes for balance laws. *Math. Comp.*, 71(238):553–582 (electronic), 2002.

[142] S. Gottlieb and C.W. Shu. Total variation diminishing runge–kutta schemes. *Mathematics of Computation*, 67(221):73–85, 1998.

[143] Sigal Gottlieb and Chi-Wang Shu. Total variation diminishing Runge–Kutta schemes. *Mathematics of Computation of the American Mathematical Society*, 67(221):73–85, 1998.

[144] A. Green and P. Naghdi. A derivation of equations for wave propagation in water of variable depth. *Fluid Mechanics*, 78:237–246, 1976.

[145] J. M. Greenberg and A. Y. Leroux. A well–balanced scheme for the numerical processing of source terms in hyperbolic equations. *SIAM J. Numer. Anal.*, 33(1):1–16, 1996.

[146] J. M. Greenberg, A. Y. LeRoux, R. Baraille, and A. Noussair. Analysis and approximation of conservation laws with source terms. *SIAM J. Numer. Anal.*, 34(5):1980–2007, 1997.

[147] G. Grosso, M. Antuono, and M. Brocchini. Dispersive nonlinear shallow–water equations: some preliminary numerical results. *Journal of Engineering Mathematics*, 67(1):71–84, Jun 2010.

[148] G.Wei, J.T. Kirby, S.T. Grilli, and R. Subramanya. A fully nonlinear boussinesq model for surface waves. part 1. highly nonlinear unsteady waves. *Journal of Fluid Mechanics*, 294(-1):71, 1995.

[149] Steudel H, P. G. Drazin, and R. S. Johnson. Solitons: An introduction. *ZAMM - Journal of Applied Mathematics and Mechanics / Zeitschrift für Angewandte Mathematik und Mechanik*, 70(8):340–340, 1989.

[150] A. Harten, B. Engquist, S. Osher, and S. Chakravarthy. Uniformly high order essentially non–oscillatory schemes, III. *Journal of Computational Physics*, 71:231–303, 1987.

[151] A. Harten, P. Lax, and B. Leer. On Upstream Differencing and Godunov–Type Schemes for Hyperbolic Conservation Laws. *SIAM Review*, 25(1):35–61, January 1983.

[152] A. Harten, P. D. Lax, and B. van Leer. On upstream differencing and Godunov–type schemes for hyperbolic conservation laws. *SIAM Review*, 25(1):35–61, January 1983.

[153] Ami Harten, Bjorn Engquist, Stanley Osher, and Sukumar R. Chakravarthy. Uniformly High Order Accurate Essentially Non–oscillatory Schemes, III. *Journal of Computational Physics*, 131(1):3–47, February 1997.

[154] Ami Harten and James M Hyman. Self adjusting grid methods for one–dimensional hyperbolic conservation laws. *Journal of Computational Physics*, 50(2):235–269, May 1983.

[155] A. Hidalgo and M. Dumbser. ADER schemes for nonlinear systems of stiff advection–diffusion–reaction equations. *Journal of Scientific Computing*, 48:173–189, 2011.

[156] J. Hudson. *Numerical technics for morphodynamic modelling.* PhD dissertation, University of Whiteknights, 2001.

[157] C. Escalante J. Macías, M. J. Castro. Performance assessment of tsunami–hysea model for nthmp tsunami currents benchmarking. part i lab data. *Submitted to Coastal Engineering*, 2017.

[158] M J. Castro J. Macías, C. Escalante. Multilayer-hysea model validation for landslide generated tsunamis for rigid slides. *Submitted to Ocean Modelling*, 2018.

[159] Owens JD, Houston M, Luebke D, Green S, Stone JE, and Phillips JC. Gpu computing. *Proceedings of the IEEE*, 96(5):879–899, 2008.

[160] A. Jeschke, G. Pedersen, K. Geir, S. Vater, and J. Behrens. Depth–averaged non–hydrostatic extension for shallow water equations with quadratic vertical pressure profile: equivalence to boussinesq–type equations. *International Journal for Numerical Methods in Fluids*, 2017.

[161] A. A. Kalinske. Criteria for determining sand transport by surface creep and saltation,. *Trans. AGU.*, 2(23):639–643, 1942.

[162] R Käppeli and S Mishra. Well–balanced schemes for gravitationally stratified media. *ASTRONUM 2014 proceedings*, 2014.

[163] M. Kazolea, A.I. Delis, and C.E. Synolakis. Numerical treatment of wave breaking on unstructured finite volume approximations for extended boussinesq–type equations. *Journal of Computational Physics*, 271:281–305, aug 2014.

[164] J. Kim. *Finite volume methods for tsunamis generated by submarine landslides.* PhD dissertation, University of Washington, 2014.

[165] A. Kovacs and G. Parker. A new vectorial bedload formulation and its application to the time evolution of straight river channels. *J. Fluid Mech.*, 267:153–183, 1994.

[166] A. Kurganov and G. Petrova. A second–order well–balanced positivity preserving central–upwind scheme for the saint–venant system. *Commun. Math. Sci.*, 5(1):133–160, 03 2007.

[167] D. Lannes. *The Water Waves Problem: Mathematical Analysis and Asymptotics.* Mathematical Surveys and Monographs. American Mathematical Society, 2013.

[168] D. Lannes and F. Marche. A new class of fully nonlinear and weakly dispersive green–naghdi models for efficient 2d simulations. *Journal of Computational Physics*, 282:238 – 268, 2015.

[169] B. Van Leer. Towards the ultimate conservative difference scheme. v. a second order sequel to godunov's method. *Computational Physics*, 32:101–136, 1979.

[170] Philippe G. LeFloch. Shock waves for nonlinear hyperbolic systems in nonconservative form. *Institute for Math. and its Appl.*, Minneapolis, Preprint 593, 1989.

[171] Philippe G. LeFloch and Siddhartha Mishra. Numerical methods with controlled dissipation for small–scale dependent shocks. *Acta Numerica*, 23:743–816, May 2014.

[172] Randall J. LeVeque. Balancing source terms and flux gradients in high–resolution Godunov methods: the quasi–steady wave–propagation algorithm. *J. Comput. Phys.*, 146(1):346–365, 1998.

[173] R. Loubère, M. Dumbser, and S. Diot. A new family of high order unstructured mood and ader finite volume schemes for multidimensional systems of hyperbolic conservation laws. *Communication in Computational Physics*, 16:718–763, 2014.

[174] M. Lukáčová-Medvid'ová, S. Noelle, and M. Kraft. Well–balanced finite volume evolution Galerkin methods for the shallow water equations. *Journal of Computational Physics*, 221(1):122–147, January 2007.

[175] R. Fernández Luque and R. Van Beek. Erosion and transport of bedload sediment. *J. Hydraulaul. Res.*, 14:127–144, 1976.

[176] P. Lynett and P. L-F. Liu. A two–layer approach to wave modelling. *Proceedings of the Royal Society of London A: Mathematical, Physical and Engineering Sciences*, 460(2049):2637–2669, 2004.

[177] P.J. Lynett, K. Gately, R. Wilson, L. Montoya, D. Arcas, B. Aytore, Y. Bai, J.D. Bricker, M.J. Castro, K.F. Cheung, C.G. David, G.G. Dogan, C. Escalante, J.M. González-Vida, S.T. Grilli, T.W. Heitmann, J. Horrillo, U. KânoUglu, R. Kian, J.T. Kirby, W. Li, J. Macías, D.J. Nicolsky, S. Ortega, A. Pampell-Manis, Y.S. Park, V. Roeber, N. Sharghivand, M. Shelby, F. Shi, B. Tehranirad, E. Tolkova, H.K. Thio, D. VelioUglu, A.C. Yalçıner, Y. Yamazaki, A. Zaytsev, and Y.J. Zhang. Inter–model analysis of tsunami–induced coastal currents. *Ocean Modelling*, 114:14–32, 2017.

[178] P.J. Lynett and P.L.-F. Liu. Linear analysis of the multi–layer model. *Coastal Engineering*, 51:439–454, 2004.

[179] P.J. Lynett, T.R. Wu, and P.L.-F. Liu. Modeling wave runup with depth–integrated equations. *Coastal Engineering*, 46(2):89–107, jul 2002.

[180] G. Ma, F. Shi, and J. T. Kirby. Shock–capturing non–hydrostatic model for fully dispersive surface wave processes. *Ocean Modelling*, 43:22 – 35, 2012.

[181] G. Ma, F. Shi, and J.T. Kirby. Shock–capturing non–hydrostatic model for fully dispersive surface wave processes. *Ocean Modelling*, 43–44:22–35, 2012.

[182] Jorge Macías, Manuel J. Castro, Sergio Ortega, Cipriano Escalante, and José Manuel González-Vida. Performance benchmarking of tsunami–hysea model for nthmp's inundation mapping activities. *Pure and Applied Geophysics*, 174(8):3147–3183, 2017.

[183] P. A. Madsen, H. B. Bingham, and H. A. Schäffer. Boussinesq–type formulations for fully nonlinear and extremely dispersive water waves: Derivation and analysis. *Proceedings: Mathematical, Physical and Engineering Sciences*, 459(2033):1075–1104, 2003.

[184] P.A. Madsen and O.R. Sorensen. A new form of the boussinesq equations with improved linear dispersion characteristics. part 2: A slowing varying bathymetry. *Coastal Engineering*, 18:183–204, 1992.

[185] R. Manning. On the flow of water in open channels and pipes. *Trans. Inst. Civil Eng. Ireland*, 20:161–207, 1891.

[186] A. Marquina. Local Piecewise Hyperbolic Reconstruction of Numerical Fluxes for Nonlinear Scalar Conservation Laws. *SIAM Journal on Scientific Computing*, 15(4):892–915, July 1994.

[187] R. Maurin, J. Chauchat, and P. Frey. Revisiting slope influence in turbulent bedload transport: consequences for vertical flow structure and transport rate scaling. *arXiv:1701.02665 [physics.geo–ph]*, 2017.

[188] Alireza Mazaheri, Mario Ricchiuto, and Hiroaki Nishikawa. A first–order hyperbolic system approach for dispersion. *Journal of Computational Physics*, 321(Supplement C):593–605, 2016.

[189] C. C. Mei and B. Le Méhauté. Note on the equations of long waves over an uneven bottom. *J. Geophys. Res*, 71:393–400, 1966.

[190] E. Meyer-Peter and R. Müller. Formulas for bedload transport. *ASCE Rep. 2nd Meet. Int. Assoc. Hydraul. Struct. Res., Stockolm*, 107:561–575, 1942.

[191] C. Michoski, C. Dawson, C. Mirabito, E.J. Kubatko, D. Wirasaet, and J.J. Westerink. Fully coupled methods for multiphase morphodynamics. *Advances in Water Resources*, 59:95–110, 2013.

[192] Tomás Morales de Luna, Manuel J. Castro Díaz, Carlos Parés Madroñal, and Enrique D. Fernández Nieto. On a shallow water model for the simulation of turbidity currents. *Communications in Computational Physics*, 6(4):848–882, 2009.

[193] E. Mosselman and T.B. Le. Five common mistakes in fluvial morphodynamic modeling. *Advances in Water Resources*, 93:15–20, 2016.

[194] Lucas O. Müller, Carlos Parés, and Eleuterio F. Toro. Well-balanced High–order Numerical Schemes for One–dimensional Blood Flow in Vessels with Varying Mechanical Properties. *J. Comput. Phys.*, 242:53–85, June 2013.

[195] S. Munkejord, S. Evje, and T. Flatten. A MUSTA Scheme for a Nonconservative Two–Fluid Model. *SIAM Journal on Scientific Computing*, 31(4):2587–2622, January 2009.

[196] C.D. Munz, P. Omnes, R. Schneider, E. Sonnendrücker, and U. Voss. Divergence Correction Techniques for Maxwell Solvers Based on a Hyperbolic Model. *Journal of Computational Physics*, 161:484–511, 2000.

[197] P. Nielsen. Coastal bottom boundary layers and sediment transport. *World Scientific Publishing, Singapore. Advanced Series on Ocean Engineering*, 4, 1992.

[198] Sebastian Noelle, Normann Pankratz, Gabriella Puppo, and Jostein R. Natvig. Well-balanced finite volume schemes of arbitrary order of accuracy for shallow water flows. *Journal of Computational Physics*, 213(2):474–499, 2006.

[199] Sebastian Noelle, Yulong Xing, and Chi-Wang Shu. High–order well–balanced finite volume weno schemes for shallow water equation with moving water. *Journal of Computational Physics*, 226(1):29–58, 2007.

[200] NTHMP. Landslide Tsunami Model Benchmarking Workshop. http://www1.udel.edu/kirby/landslide, Accessed November 2017.

[201] NVIDIA. Cuda home page. http://www.nvidia.com/object/cuda_home_new.html.

[202] O. Nwogu. An alternative form of the boussinesq equations for nearshore wave propagation. *Waterway, Port, Coastal, Ocean Engineering*, 119:618–638, 1994.

[203] Stanley Osher and Fred Solomon. Upwind difference schemes for hyperbolic systems of conservation laws. *Mathematics of Computation*, 38(158):339–374, 1982.

[204] B. Owren and M. Zennaro. Derivation of efficient, continuous, explicit Runge–Kutta methods. *SIAM J. Sci. and Stat. Comput.*, 13:1488–1501, 1992.

[205] C. Parés. Numerical methods for nonconservative hyperbolic systems: a theoretical framework. *SIAM Journal on Numerical Analysis*, 44:300–321, 2006.

[206] C. Parés and M. J. Castro. On the well–balance property of Roe's method for nonconservative hyperbolic systems. Applications to shallow–water systems. *ESAIM: Mathematical Modelling and Numerical Analysis*, 38(5):821–852, 2004.

[207] Carlos Parés. Numerical methods for nonconservative hyperbolic systems: a theoretical framework. *SIAM J. Numer. Anal.*, 44(1):300–321 (electronic), 2006.

[208] Carlos Parés and Manuel Castro. On the well–balance property of Roe's method for nonconservative hyperbolic systems. Applications to shallow–water systems. *M2AN Math. Model. Numer. Anal.*, 38(5):821–852, 2004.

[209] Marica Pelanti, François Bouchut, and Anne Mangeney. A Roe–type scheme for two–phase shallow granular flows over variable topography. *ESAIM: Mathematical Modelling and Numerical Analysis*, 42(5):851–885, September 2008.

[210] D.H. Peregrine. Long waves on a beach. *Fluid Mechanics*, 27(4):815–827, 1967.

[211] B. Perthame and C. Simeoni. A kinetic scheme for the Saint–Venant system with a source term. *CALCOLO*, 38(4):201–231, December 2001.

[212] Benoît Perthame and Chiara Simeoni. Convergence of the Upwind Interface Source Method for Hyperbolic Conservation Laws. In Thomas Y. Hou and Eitan Tadmor, editors, *Hyperbolic Problems: Theory, Numerics, Applications*, pages 61–78. Springer Berlin Heidelberg, 2003.

[213] M. Postacchini, M. Brocchini, A. Mancinelli, and M. Landon. A multi–purpose, intra–wave, shallow water hydro–morphodynamic solver. *Advances in Water Resources*, 38:13–26, 2012.

[214] W. H. Reed and T. R. Hill. Triangular mesh methods for the neutron transport equation. Technical report, University of California, Los Alamos Scientific Laboratory, 1973.

[215] S. Rhebergen, O. Bokhove, and J. J. W. van der Vegt. Discontinuous Galerkin finite element methods for hyperbolic nonconservative partial differential equations. *Journal of Computational Physics*, 227(3):1887–1922, January 2008.

[216] S. Rhebergen, O. Bokhove, and J.J.W. van der Vegt. Discontinuous Galerkin finite element methods for hyperbolic nonconservative partial differential equations. *Journal of Computational Physics*, 227:1887–1922, 2008.

[217] M. Ricchiuto and A.G. Filippini. Upwind residual discretization of enhanced boussinesq equations for wave propagation over complex bathymetries. *Journal of Computational Physics*, 271:306–341, aug 2014.

[218] L. C. Van Rijn. Sediment transport (i): bed load transport. *J. Hydraul. Div. Proc. ASCE*, 110:1431–1456, 1984.

[219] V. Roeber, K. F. Cheung, and M. H. Kobayashi. Shock–capturing boussinesq–type model for nearshore wave processes. *Coastal Engineering*, 57:407–423, 2010.

[220] E.I. Romenski. Hyperbolic systems of thermodynamically compatible conservation laws in continuum mechanics. *Mathematical and computer modelling*, 28(10):115–130, 1998.

[221] J. S. Russell. Report on waves. technical report. *Report of the fourteenth meeting of the British Association for the Advancement of Science*, 1845.

[222] Giovanni Russo and Alexander Khe. High order well balanced schemes for systems of balance laws. In *Hyperbolic problems: theory, numerics and applications*, volume 67 of *Proc. Sympos. Appl. Math.*, pages 919–928. Amer. Math. Soc., Providence, RI, 2009.

[223] C. Sánchez-Linares. *Cuantificación de la incertidumbre en flujos geofísicos mediante el uso de esquemas de volúmenes finitos Monte Carlo multi-nivel.* PhD thesis, Universidad de Málaga, 2018.

[224] C. Sánchez-Linares, T. Morales de Luna, and M. J. Castro Díaz. A HLLC scheme for Ripa model. *Applied Mathematics and Computation*, 272, Part 2:369–384, January 2016.

[225] C. Savary. *Transcritical transient flow over mobile bed. Two–layer shallow–water model.* PhD dissertation, Université catholique de Louvain, 2007.

[226] H. A. Schäffer and P. A. Madsen. Further enhancements of boussinesq–type equations. *Coastal Engineering*, 26(1):1 – 14, 1995.

[227] F. Serre. Contribution à l'étude des écoulements permanents et variables dans les canaux. *La Houille blanche*, 8:374–388, 1953.

[228] Chi-Wang Shu and Stanley Osher. Efficient implementation of essentially non–oscillatory shock–capturing schemes. *Journal of Computational Physics*, 77(2):439–471, August 1988.

[229] Chi-Wang Shu and Stanley Osher. Efficient implementation of essentially non–oscillatory shock–capturing schemes, II. *J. Comput. Phys.*, 83(1):32–78, July 1989.

[230] B. Spinewine. *Two–layer flow behaviour and the effects of granular dilatancy in dam–break induced sheet–flow.* PhD dissertation, Université catholique de Louvain, 2005.

[231] G. Stelling and M. Zijlema. An accurate and efficient finite–difference algorithm for non–hydrostatic free–surface flow with application to wave propagation. *International Journal for Numerical Methods in Fluids*, 43(1):1–23, 2003.

[232] C. Swartenbroekx, S. Soares-Fraz ao, B. Spinewine, V. Guinot, and Y. Zech. Hyperbolicity preserving hll solver for two–layer shallow–water equations applied to dam–break flows. *River Flow 2010, Dittrich, Koll, Aberle & Geisenhainer (eds.), Bundesanstalt fur Wasserbau (BAW), Karlsruhe, Germany*, 2:1379–1387, 2010.

[233] C.E. Synolakis. The runup of solitary waves. *Fluid Mechanics*, 185:523–545, 1987.

[234] Huazhong Tang, Tao Tang, and Kun Xu. A gas–kinetic scheme for shallow–water equations with source terms. *Zeitschrift für angewandte Mathematik und Physik ZAMP*, 55(3):365–382, May 2004.

[235] P. Tassi, S. Rhebergen, C. Vionnet, and O. Bokhove. A discontinuous galerkin finite element model for morphodynamical evolution in shallow flows. *Comp. Meth. App. Mech. Eng.*, 197:2930–2947, 2008.

[236] L.H. Thomas. Elliptic problems in linear difference equations over a network. *Watson Sci. Comput. Lab Report, Columbia University, New York.*, 1949.

[237] V.A. Titarev and E.F. Toro. ADER: Arbitrary high order Godunov approach. *Journal of Scientific Computing*, 17(1–4):609–618, December 2002.

[238] V.A. Titarev and E.F. Toro. ADER schemes for three–dimensional nonlinear hyperbolic systems. *Journal of Computational Physics*, 204:715–736, 2005.

[239] M. Tonelli and M. Petti. Hybrid finite volume – finite difference scheme for 2dh improved boussinesq equations. *Coastal Engineering*, 56(5–6):609–620, may 2009.

[240] E. F. Toro and S. J. Billett. Centred TVD schemes for hyperbolic conservation laws. *IMA Journal of Numerical Analysis*, 20(1):47–79, January 2000.

[241] E. F. Toro and V. A. Titarev. Derivative Riemann solvers for systems of conservation laws and ADER methods. *Journal of Computational Physics*, 212(1):150–165, 2006.

[242] E. F. Toro and V. A. Titarev. MUSTA fluxes for systems of conservation laws. *Journal of Computational Physics*, 216(2):403–429, August 2006.

[243] E.F. Toro and G.I. Montecinos. Advection-diffusion–reaction equations: Hyperbolization and high–order ADER discretizations. *SIAM Journal on Scientific Computing*, 36(5):A2423–A2457, 2014.

[244] E.F. Toro and V. A. Titarev. Solution of the generalized Riemann problem for advection–reaction equations. *Proc. Roy. Soc. London*, pages 271–281, 2002.

[245] Eleuterio F. Toro. *Riemann Solvers and Numerical Methods for Fluid Dynamics: A Practical Introduction, 3rd ed.* Springer Science & Business Media, April 2013.

[246] M. Torrilhon. Krylov–Riemann Solver for Large Hyperbolic Systems of Conservation Laws. *SIAM Journal on Scientific Computing*, 34(4):A2072–A2091, January 2012.

[247] R. Touma, U. Koley, and C. Kingenberg. Well–balanced unstaggered central schemes for the Euler equations with gravitation. *submitted to SIAM J. Sci. Comp.*, 2016.

[248] I. Toumi. A weak formulation of Roe's approximate Riemann solver. *J. Comput. Phys.*, 102(2):360–373, 1992.

[249] A. Treske. Undular bores (favre–waves) in open channels–experimental studies. *Journal of Hydraulic Research*, 32(3):355–370, 1994.

[250] Tatsuhiko Uchida and Shoji Fukuoka. Quasi–3d two-phase model for dam–break flow over movable bed based on a non–hydrostatic depth–integrated model with a dynamic rough wall law. *Advances in Water Resources*, 2017.

[251] M. Ujaldon. High performance computing and simulations on the GPU using CUDA. *2012 International Conference on High Performance Computing & Simulation, HPCS*, pages 1–7, 2012.

[252] P. Ung. *Simulation numérique du transport sédimentaire*. PhD dissertation, Université d'Orléans, 2016.

[253] A. I. Volpert. Spaces BV and quasilinear equations. *Mat. Sb. (N.S.)*, 73 (115):255–302, 1967.

[254] EDANYA web group. *https://edanya.uma.es/hysea.* 2018.

[255] G.B. Whitham and Wiley. Linear and nonlinear waves. *Earthquake Engng. Struct. Dyn.*, 4(5):518–518, 1976.

[256] J.M. Witting. A unified model for the evolution nonlinear water waves. *Journal of Computational Physics*, 56(2):203–236, 1984.

[257] Chin H. Wu, Chih-Chieh Young, Qin Chen, and Patrick J. Lynett. Efficient nonhydrostatic modeling of surface waves from deep to shallow water. *Journal of Waterway, Port, Coastal, and Ocean Engineering*, 136(2):104–118, 2010.

[258] Yulong Xing and Chi-Wang Shu. High order well-balanced finite volume WENO schemes and discontinuous Galerkin methods for a class of hyperbolic systems with source terms. *Journal of Computational Physics*, 214(2):567–598, May 2006.

[259] Y. Yamazaki, Z. Kowalik, and K.F. Cheung. Depth–integrated, non–hydrostatic model for wave breaking and run–up. *Numerical Methods in Fluids*, 61:473–497, 2008.

[260] O. Zanotti and M. Dumbser. Efficient conservative ader schemes based on weno reconstruction and space–time predictor in primitive variables. *Computational Astrophysics and Cosmology*, 3(1):1, 2016.

[261] O. Zanotti, F. Fambri, M. Dumbser, and A. Hidalgo. Space–time adaptive ADER discontinuous Galerkin finite element schemes with a posteriori sub–cell finite volume limiting. *Computers and Fluids*, 118:204–224, 2015.